

Integrating Quantum Optical and Superconducting Circuits with Quantum Acoustics for Scalable Quantum Network and Computation

Thesis by
Jie Luo

In Partial Fulfillment of the Requirements for the
Degree of
Doctor of Philosophy

The logo for the California Institute of Technology (Caltech), featuring the word "Caltech" in a bold, orange, sans-serif font.

CALIFORNIA INSTITUTE OF TECHNOLOGY
Pasadena, California

2020
Defended July 1, 2019

© 2020

Jie Luo

ORCID: 0000-0002-6464-2761

All rights reserved

What I cannot create, I do not understand.

————— Richard Feynman (1988)

ACKNOWLEDGEMENTS

To my family, thank you very much for generously supporting me to pursue my "unrealistic" passion without worrying about other unessential things throughout my education. I am incredibly fortunate to have you in the first place.

To my fiancée, Xueyin (Sherry) Chen, I am so grateful and feel unbelievably fortunate to have you with me since 2013. It has been a fantastic six-year journey together. Thank you so much for the patience and faith in me. Every single moment we share is among my most treasurable life memories. I believe the best is yet to come and I can't wait to convert the great future with you into a reality.

To Oskar, thank you for the guidance and support on various projects from optomechanics to superconducting qubits over the years. Finishing my Ph.D. with you has been a very enriching and educational experience. I am looking forward to crossing path with you in quantum device engineering soon.

To Hengjiang (Jared) Ren who I have shared an office with for five years, thank you so much for being my friend and lab partner. Other than our fruitful collaborations on various projects, it has been enjoyable to have dinners, playing games, and working on amazing things together.

To Prof. Kejie Fang and Greg, thank you both for working with me in the first two years of my time in the group. Hope Kejie all the best in his tenure track at UIUC, and I am looking forward to reconnecting with you in the future. As Greg is already enjoying his real life in a real job, I can only wish Greg all the best in every way.

To the previous generations of the Painter Lab, thank you all so much for building the infrastructure and leaving behind amazing tools. This work wouldn't be possible without the accumulated knowledge from you in device design and fabrication. Particularly, let me thank Johannes for building our first fridge. I am so grateful to be able to overlap with Tim, Justin, and Sean for a short period to learn from them about the group and the projects.

To the current and quasi-current group members, I have enjoyed working with you on various paths. To Michael and Andrew (now at Rigetti), thank you so much for building the superconducting qubit direction's foundation for the rest of the group. We have all benefitted so much from your dedicated work. To Jash, thank you for the inspiring lunch chats. To Vinicius for all the fun and energy, you have brought

into the group. Thank you two so much for the initial stage of the Spidermon project. To Xueyue (Sherry), thank you for being a friend and partner in building the CQIA and commitment to carry it on to the next stage. I hope you are on your way to being a rising star in academia. To Eun-Jong for your patience and generous help in providing us with information on how to properly design and fabricate Spidermon. To Mahmoud and Muhammad for your time in training me on lifting off superconducting structure for the very first generation of quantum acoustic device. To Alp for joining Michael and me on the quantum piezo-acoustics projects and continuing our work in building the quantum acoustic transduction platform. To Szilard for working with me on exploring different ways to grow high-quality AlN via ALD. Those days we spent together on solving material science puzzles are genuinely memorable. To Barry, Michelle, and Jonathan, thank you all for supporting the group over the last five years. Barry has proven to be the most effective person in "nicely asking" vendors to reach a high level of service quality.

To Prof. John Preskill, it has been an honor to work with you to start the exciting CQIA. Hope it can be a platform to provide the whole Caltech community to learn from the quantum talents on campus and seek opportunities to contribute to the rapid development of quantum information science and engineering. I would also thank Google and Rigetti for working with CQIA.

To Prof. Kerry Vahala, Prof. Austin Minnich, and Prof. Andrei Faraon, thank you for being my Ph.D. defense committee. To Prof. David Hsieh and Prof. Jonas Zmuidzinas, thank you for joining my candidacy exam.

The all the others who have helped me in various ways, I am forever grateful for your kindness. Particularly, I would like to thank Honglie Ning for coaching me at the gym, Wenlong Ma for walking me through advanced robotics, Xiang Li for helping me understand more on quantum optomechanics, Tian Zhong for introducing his recent great developments in rare earth ion doped quantum photonic crystals, and Joe Iverson for discussing quantum error correction codes.

ABSTRACT

Due to its high coherence in transmission over a large distance in ambient environment, quantum optical system has been a prevailing platform for long-distance quantum communication, which was recently realized over a continental distance with a low earth orbit satellite and ground stations [102, 70]. However, pure quantum optical system has so far shown weak interactions between photon and matter, which makes it inefficient in carrying out deterministic quantum gates for quantum repeater based scalable quantum network and quantum computing. On the other hand, superconducting quantum systems operating in the microwave domain with Josephson junction transmon qubits have proven to be capable of efficient deterministic quantum operations on quantum states [86, 87, 66]. Nevertheless, such architecture is prone to errors and decoherence due to cross-talk between microwave elements in a large-scale superconducting quantum circuit. Furthermore, superconducting systems, in general, also have large footprint (100s um) elements (resonators and superconducting quantum bits) [92, 60] that limit the ability to scale up a superconducting quantum system. Moreover, microwave quantum circuits require cooling to around 10 mK, making it unsuitable for communicating quantum information outside a dilution refrigerator (DF). Micro- and nano- acoustic elements have been extensively used in conventional integrated information processing systems due to their compactness and high coherence [97]. Acoustic systems in quantum engineering also have the advantage of being a platform for universal couplings between various quantum systems including spins, optical photons, and superconducting circuits. As it will be discussed in this thesis, elements critical to scalable optical quantum network and superconducting quantum circuit can be constructed relying on the cavity optomechanics and piezoelectric interactions.

Optomechanical interaction is concerned with the light pressure coupling of cavity mechanical deformation to a strong optical field. This interaction has allowed the close to mechanical ground state cooling of mechanical resonators using laser and the ultra-sensitive displacement measurement that led to the detection of gravitational waves in the LIGO collaboration [125, 25]. Optomechanical crystals (OMCs) are lithographically patterned devices which contain periodic structure that host bandgaps for both optical band electromagnetic waves and microwave band acoustic waves. A properly engineered defect in the crystal can confine and localize acoustic

and electromagnetic modes of similar wavelengths into a small mode volume [17, 20, 21]. A strong optomechanical coupling, which can be achieved between such strongly confined co-localized optical and acoustic modes, can be used in engineering the quantum state of mechanical motion to realize useful quantum devices such as a high-coherence quantum memory [74] and an optomechanical high efficiency optical isolator for unidirectionally connecting distant optical cavities via an acoustic bus [37].

To strongly couple the mechanical degree of freedom with a superconducting quantum circuit, various methods can be used, ranging from electromechanic coupling (electric coupling to a mechanically compliant capacitor), magnetomechanical coupling (magnetic coupling to a vibrating SQUID loop), and piezoelectric coupling. The recent advent of quantum acoustics [23, 8, 9] was realized with the strong piezoelectric coupling between a superconducting transmon qubit and a high-coherence mechanical resonator. The engineered strong piezoacoustic coupling provides the possibility to carry out deterministic ultra-high fidelity two-qubit quantum gates on non-classical mechanical quantum states [52]. This ability together with the recent demonstration of ultra-long phonon lifetime mechanical resonators show the possibility of integrating the ultra-high quality mechanical resonator as a compact quantum memory element and even a new ultra-compact (10s um) quantum bit architecture for scalable superconducting quantum circuits. Furthermore, the strong piezoelectric coupling that can transduce quantum state in a superconducting circuit into mechanical wave also makes it possible to efficiently transduce a quantum state between a superconducting quantum circuit and a telecommunication band optical channel via a mechanical waveguide connected to an optomechanical crystal cavity.

The Chapter 1 will summarize the theoretical framework for optomechanics, electromechanics, magnetomechanics, and piezoacoustics. The Chapter 2 will introduce the superconducting quantum circuit and Josephson junction transmon qubit used in this work. The Chapter 3 will introduce the the synthetic crystals that tailor the propagation dispersions of optical and mechanical waves. This forms the foundations for the photonic and phononic engineering to guide and confine photons and phonons involved in this work. The Chapter 4 will proceed to discuss optomechanical interaction induced time-symmetry breaking, device design, and characterization details of optomechanical crystals and waveguides used in this work that enabled the con-

struction efficient optomechanical optical isolator. The Chapter 5 will talk about details of characterizing ultra-high quality nano-mechanical microwave resonators demonstrating phonon lifetime approaching one second at 10 mK. The various dissipation mechanisms involved in the pump heating induced elevated mechanical loss and intrinsic dissipation in the absence of pump heating are going to be discussed. This information is important in understanding the potentials of acoustic quantum memories based our ultra-high quality phononic platform. The Chapter 6 introduces the details in design and characterization of piezoacoustic resonators strongly coupled to superconducting electric circuit for the purpose of piezoacoustic transduction that can be further used for building compact an ultra-long lifetime nano-mechanical quantum memory, an ultra-compact anharmonic acoustic qubit architecture, and a microwave to optical transducer (in the appendix). The Chapter 7 presents the efforts of growing Aluminum Nitride (AlN) with both atomic-layer-deposition (ALD) and sputtering. The Chapter 8 will introduce a hardware efficient programmable superconducting quantum logic circuit architecture that opens door to various research directions in quantum floquet engineering, cryogenic high efficiency circulator, topological photonic lattice, and demonstration of small size fault-tolerant protocols requiring a high connectivity graph between qubits and dynamic coupling controls. I will use a four-qubit device to create a synthetic quasi-3D tetrahedron interacting photonic lattice with intrinsic time-reversal symmetry breaking and nontrivial single-photon manifold phases as an example to showcase the flexibility and usefulness of such architecture. The Chapter 9 will conclude the work, with a summary and introduction to future directions on a hardware efficient way for scaling up superconducting quantum circuits and novel experiments in quantum optomechanics.

TABLE OF CONTENTS

Acknowledgements	iv
Abstract	vi
Table of Contents	ix
Chapter I: Frameworks For Coupling Mechanical Motion to Optical and Electric Circuits	1
1.1 Optomechanical Interaction	1
1.1.1 Sideband Unresolved Regime: Measuring Mechanical Dis- placement	3
1.1.2 Sideband Resolved Regime: Photon-Phonon Scattering	3
1.2 Electromechanical Interaction	4
1.3 Magneto-mechanical Interaction	7
1.4 Piezoelectric Interaction	9
Chapter II: Superconducting Quantum Circuit and Josephson Junction Trans- mon Qubit	12
2.1 Josephson Effect and Josephson Junction	13
2.1.1 BCS Theory	14
2.1.2 Superconducting Quantum Interference Device	19
2.2 Superconducting Josephson Junction Qubits	20
2.2.1 Anharmonic Quantum Oscillator	20
2.2.2 Charge Qubits and Transmon Qubits	22
2.2.3 Flux Qubits	24
2.2.4 Phase Qubits	25
2.2.5 Superconducting Qubit Readout	26
2.2.6 Transmon Qubit Controls	32
2.3 Standard Cryogenic System for Measuring and Controlling A Trans- mon Qubit	36
2.3.1 Structure and Cooling Process of a Dilution Refrigerator	36
2.3.2 Cryogenic Setup for Controlling and Measuring Supercon- ducting Qubits	38
Chapter III: Synthesized Crystals for Engineering Propagation of Light and Mechanical Waves	41
3.1 Photonic Crystal	42
3.1.1 Photonic Waveguide and Photonic Defect Cavity	43
3.2 Phononic Crystal	44
3.2.1 Phononic Waveguide	47
3.2.2 Phononic Defect Cavity	47
3.3 Opto-mechanical Crystal	48
Chapter IV: Time Symmetry Breaking with Synthetic Gauge Field For Uni- directional Photon Routing	49

4.1	Device Fabrication and Methods	57
4.1.1	Device fabrication and atomic force microscope nano-oxidation tuning	57
4.1.2	Optical transmission coefficient measurement	58
4.1.3	Device characterization	59
4.2	Theory of optical nonreciprocity	61
4.2.1	Input-output formula	61
4.2.2	Mechanically-mediated coupling	62
4.2.3	Directionality by balancing coherent and dissipative interactions	64
4.2.4	Nonreciprocal optical transmission: two blue-detuned pumps	66
4.2.5	Nonreciprocal optical transmission: two red-detuned pumps	67
4.2.6	Nonreciprocity associated with a single mechanical waveguide mode	68
4.3	Directional flow of quantum and thermal noise	69
4.4	Reciprocal device	71
Chapter V: Ultra-high Quality Nano-mechanical resonator		81
5.1	Phononic bandgap structure	81
5.2	Limits of acoustic damping	83
5.3	Device design and fabrication	83
5.4	Optical Ringdown measurements	84
5.5	Temperature dependent damping	86
Chapter VI: Quantum Acoustics with Piezoelectric Strong Coupling between superconducting circuits and phononic resonances		89
6.1	Phononic piezoelectric transducer	90
6.1.1	Optimizing the piezoacoustic coupling per period of Interdigit electrode	94
6.1.2	Lamb Resonator Coupling Spectrum Cleanup	98
6.2	Ultra-high coherence compact quantum memory for a superconducting transmon qubit	100
6.2.1	2D Phononic Crystal and Defect Cavity	102
6.2.2	Piezoacoustic Cavity	103
6.2.3	Evanescence Mechanical Coupling Between Piezo and Memory Cavities	107
6.2.4	Tunable High Impedance Electric Microwave Resonator Coupled To A Transmon Qubit Via A Tunable Inductive Coupler	111
6.3	On-Demand Coherence Preserving Virtual Coupling Channels	113
6.3.1	Swap-State: Quantum State Transfer	116
6.3.2	Idle-State: Memory and Qubit Coherence Preservation	120
6.3.3	System Parameter Optimization for A Large Asynchronized Quantum Rate	122
6.3.4	Ultra-High Fidelity In-Memory Two-Qubit Quantum Gates	124
6.3.5	Conclusion and Outlook	125
6.4	Stacked Phononic Piezoacoustic Crystal for Nonlinear Phononics And A New Architecture for Phononic Quantum-Bit	125

6.5	Future Directions on Piezoelectric Microwave-Acoustic Transduction	128
Chapter VII: Efforts in Growing and Characterizing Piezoelectric Material		
	Aluminum Nitride	133
7.1	Thin Film Quality Characterization	133
7.1.1	Single Crystalline Thin Film X-ray Diffraction (XRD)	133
7.1.2	Measuring the Film Thickness with Ellipsometry	135
7.1.3	Measuring Oxygen Contamination with X-ray Photoelectron Spectroscopy	136
7.2	Atomic Layer Deposition for Depositing High Quality AlN	137
7.3	Sputtering Deposition of AlN Thin Layer and Electrodes	141
Chapter VIII: Hardware Efficient Programmable Multi-Qubit All-to-All Coupling Architecture: Spidermon		
8.1	Time-reversal Symmetry Broken Interacting Photonic Tetrahedron Lattice	159
8.2	Controlling and Measuring Slightly Hybridized Multiqubit system	162
Chapter IX: Conclusion		
	Bibliography	171
Appendix A: Details on Designing Ultra-high Coherence Microwave Phononic Quantum Random Access Memory		
	Quantum Random Access Memory	182
A.1	Finite-element Simulations and Device Parameters	182
A.1.1	Coupling Rate Via Field Overlap Integral	182
A.1.2	Coupling Strength via Circuit Equivalence	183
A.2	Derivation of Multi-channel Virtual Coupling	185
A.3	Idle-State Noise Propagation and Decoherence Suppression	187
Appendix B: Efficient Optic-Microwave Quantum Transduction Via Acoustic Channel		
	Channel	190

Chapter 1

FRAMEWORKS FOR COUPLING MECHANICAL MOTION TO OPTICAL AND ELECTRIC CIRCUITS

1.1 Optomechanical Interaction

Strong optical field in a high quality optical cavity can impart a large radiation pressure onto the cavity itself. For the simplicity of the discussion, assume that the optical cavity is a Fabry-Perot optical cavity with highly reflective and mechanically compliant mirrors. To further simplify the problem, only one mirror is assumed to be the moving mirror as shown in the Fig. 1.1 with all the system variables involved in the following discussion. The Hamiltonian describing this system with intrinsic losses to environment and coupling to an external optical pump can be written into (1.1).

$$\begin{aligned}
 H = & \hbar(\omega_0 + g_0\hat{x} - \frac{\kappa}{2}i)\hat{a}^\dagger\hat{a} + \hbar(\omega_m - \frac{\gamma_i}{2}i)\hat{b}^\dagger\hat{b} \\
 & - \hbar\sqrt{\kappa_e}i(\hat{a}_{\text{ex}}\hat{a}^\dagger + \hat{a}_{\text{ex}}^\dagger\hat{a}) - \hbar\sqrt{\kappa_i}i(\hat{a}_{\text{env}}\hat{a}^\dagger + \hat{a}_{\text{env}}^\dagger\hat{a}) \\
 & - \hbar\sqrt{\gamma_i}i(\hat{b}_{\text{env}}\hat{b}^\dagger + \hat{b}_{\text{env}}^\dagger\hat{b})
 \end{aligned} \tag{1.1}$$

In this expression, $\hat{a}(\hat{b})$ and $\hat{a}^\dagger(\hat{b}^\dagger)$ are quantum annihilation and creation operators

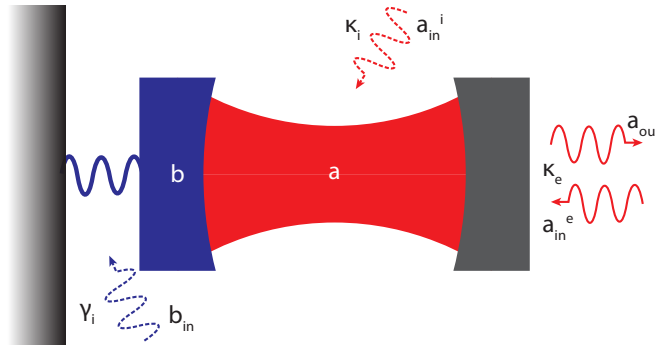


Figure 1.1: A generic optomechanical cavity with an optical cavity radiation pressure coupled to a moving mirror (blue) of the cavity.

for the optical cavity (mechanical resonator) mode of interest. $\hat{x} = \hat{b} + \hat{b}^\dagger$ is the normalized dimensionless displacement quantum operator for the mechanical oscillation. $\kappa = \kappa_i + \kappa_e$ is the total optical loss rate (linewidth) of the optical mode. It is the sum of intrinsic optical cavity loss rate (κ_i) and coupling rate to pump waveguide (κ_e). γ_i is the intrinsic loss rate of the mechanical mode of interest into its environment. As there is no mechanical pump channel, all the mechanical loss is due to intrinsic coupling to acoustic environment. It should be noted that the laser driving term can be expanded into a sum of classical laser driving amplitude and a quantum fluctuation term as $\hat{a}_{\text{ex}} = \alpha_{\text{ex}}(t) + \delta\hat{a}_{\text{ex}}$. Take $\alpha_{\text{ex}}(t) = \alpha_{\text{ex}}^0 e^{-i\omega_1 t}$ for a laser pump with frequency ω_1 . First, to get rid of the time-dependence of the driving laser, transform the (1.1) into a frame rotating with the laser using the unitary transformation $\hat{U}(t) = \exp(i\omega_1 \hat{a}^\dagger \hat{a} t)$ and the obtained rotated Hamiltonian will be (1.2) with $\Delta_0 = \omega_0 - \omega_1$.

$$\begin{aligned} H^R &= \hbar(\Delta_0 + g_0 \hat{x} - \frac{\kappa}{2} i) \hat{a}^\dagger \hat{a} + \hbar(\omega_m - \frac{\gamma_i}{2} i) \hat{b}^\dagger \hat{b} \\ &\quad - \hbar\sqrt{\kappa_e} i (\hat{a}_{\text{ex}}^R \hat{a}^\dagger + \hat{a}_{\text{ex}}^{\dagger R} \hat{a}) - \hbar\sqrt{\kappa_i} i (\hat{a}_{\text{env}}^R \hat{a}^\dagger + \hat{a}_{\text{env}}^{\dagger R} \hat{a}) \\ &\quad - \hbar\sqrt{\gamma_i} i (\hat{b}_{\text{env}} \hat{b}^\dagger + \hat{b}_{\text{env}}^\dagger \hat{b}) \end{aligned} \quad (1.2)$$

Here the optical drive and environment noise in the rotating frame are: $\hat{a}_{\text{ex}}^R = e^{i\omega_1 t} \hat{a}_{\text{ex}} = \alpha_{\text{ex}}^0 + e^{i\omega_1 t} \delta\hat{a}_{\text{ex}}$ and $\hat{a}_{\text{env}}^R = e^{i\omega_1 t} \hat{a}_{\text{env}}$. Absorbing the time factors on the input quantum variables in the rest of the work is equivalent to also transforming the input quantum dynamics into the rotating frame, and thus quantum fluctuations of pump channel and environment can be relabeled as $e^{i\omega_1 t} \delta\hat{a}_{\text{ex}} \rightarrow \delta\hat{a}_{\text{ex}}$ and $e^{i\omega_1 t} \hat{a}_{\text{env}} \rightarrow \hat{a}_{\text{env}}$.

From the Hamiltonian, we can get the master equations of the open quantum system as (1.3) and (1.4).

$$\dot{\hat{a}} = -i(\Delta_0 - \frac{\kappa}{2} i) \hat{a} - ig_0(\hat{b} + \hat{b}^\dagger) \hat{a} + \sqrt{\kappa_e} \hat{a}_{\text{ex}}^R + \sqrt{\kappa_i} \hat{a}_{\text{env}}^R \quad (1.3)$$

$$\dot{\hat{b}} = -i(\omega_m - \frac{\gamma_i}{2} i) \hat{b} - ig_0 \hat{a}^\dagger \hat{a} + \sqrt{\gamma_i} \hat{b}_{\text{env}} \quad (1.4)$$

The above equations of motion are intrinsically nonlinear and a general solution to the problem is not available. However, due to the usual smallness of the vacuum optomechanical coupling rate g_0 , significant optomechanical interaction is only achieved with strong laser pump that creates a relatively large and steady state photon population in the optical cavity mode of interest. Assuming that the laser pump is also long enough to drive the optical cavity into a steady state (ring-up effect ignored), the equation of motion can be linearized with the substitution, $\hat{a} = \alpha + \delta\hat{a}$, where α is the classical coherent amplitude of the cavity mode and $\delta\hat{a}$

describes the small quantum dynamics of the cavity. Expanding the equations with the substitutions for drive and cavity dynamics and ignoring terms corresponding to negligible multi-photon processes ($O(\delta\hat{a}^2)$ and $O(\delta\hat{a}^{\dagger 2})$ in Hamiltonian), we can have linearized equations of motion as (1.5) and (1.6).

$$\delta\dot{\hat{a}} = -i(\Delta_0 - \frac{\kappa}{2}i)\delta\hat{a} - ig_0\alpha(\hat{b} + \hat{b}^\dagger) + \sqrt{\kappa_e}\delta\hat{a}_{\text{ex}} + \sqrt{\kappa_i}\hat{a}_{\text{env}} \quad (1.5)$$

$$\dot{\hat{b}} = -i(\omega_m - \frac{\gamma_i}{2}i)\hat{b} - ig_0(\alpha^*\delta\hat{a} + \alpha\delta\hat{a}^\dagger) + \sqrt{\gamma_i}\hat{b}_{\text{env}} \quad (1.6)$$

The equation above also assumes a steady state condition and a shift of mechanical resonator's harmonic potential coordinate origin that:

$$\alpha = -\frac{\sqrt{\kappa_e}i\alpha_{\text{ex}}^0}{\Delta_0 - \frac{\kappa}{2}i} \quad (1.7)$$

$$\hat{b} - \frac{g_0|\alpha|^2}{\omega_m - \frac{\gamma_i}{2}i} \rightarrow \hat{b} \quad (1.8)$$

It is clear from the (1.5) and (1.6) that the effective optomechanical interaction strength is $G = g_0\alpha$ with intra-cavity photon number defined as $n_c = |\alpha|^2$. Effective interaction rate (G) between quantum dynamics of the optical cavity and the mechanical cavity can be enhanced significantly with a large intra-cavity photon population. Depending on whether $\kappa \gg \omega_m$, optomechanical interactions can be studied in two regimes for different applications.

1.1.1 Sideband Unresolved Regime: Measuring Mechanical Displacement

The sideband unresolved regime corresponds to the case that $\kappa \gg \omega_m$. In this case, optical light field in the cavity responds to the mechanical displacement instantaneously and records the displacement into the phase of light leaving the cavity. The optomechanical displacement measurement is behind the LIGO Scientific Collaboration that used strong optical fields in 4 km long cavities to measure the gravitational displacements of cavity mirrors [125, 25]. This regime can also be used to precisely measure displacement of a micro-mechanical resonator and was used in building quantum-limited optomechanical accelerometers on-chip [67]. It can be used to explore pulsed optomechanics that can potentially generate close to 20 dB optical squeezing and explore transient dynamics and coherence of quantum mechanical motion.

1.1.2 Sideband Resolved Regime: Photon-Phonon Scattering

The sideband resolved regime corresponds to the case where $\kappa \ll \omega_m$. In this regime, long lived optical field in an optical cavity feeds back to the mechanical

displacement dynamically due to retardation in optical response according to the sign of laser-cavity detuning Δ_0 . For red-detuning that $\Delta_0 > 0$, the retardation causes out of phase response of optical field to motion that effectively damps the mechanical oscillator. The effect is most predominant when $\Delta_0 \sim \omega_m$. Then (1.5) and (1.6) can be written using rotation-wave-approximation (RWA) as (1.9) and (1.10).

$$\delta\dot{\hat{a}} = -i(\Delta_0 - \frac{\kappa}{2}i)\delta\hat{a} - ig_0\alpha\hat{b} + \sqrt{\kappa_e}\delta\hat{a}_{\text{ex}} + \sqrt{\kappa_i}\hat{a}_{\text{env}} \quad (1.9)$$

$$\dot{\hat{b}} = -i(\omega_m - \frac{\gamma_i}{2}i)\hat{b} - ig_0\alpha^*\delta\hat{a} + \sqrt{\gamma_i}\hat{b}_{\text{env}} \quad (1.10)$$

The above equations describe that a mechanical quanta can coherently up-convert a pump laser photon into a cavity frequency photon and vice versa. This mechanism was used to efficiently laser cool a 5 GHz nano-mechanical resonator mode to its motional ground state and, as it will be discussed in this work, count mechanical resonator phonon population via detecting the number of photons, leaving the optical cavity at cavity frequency. The phonon-photon scattering rate for $\Delta_0 = \omega_m$ can be shown to be $\gamma_{\text{OM}} = \frac{4G^2}{\kappa}$ and the effective total damping rate of the mechanical resonator is $\gamma = \gamma_i + \gamma_{\text{OM}}$

As the red-detuning can swap phonon and cavity-photon, similarly, the blue-detuned region where $\Delta_0 < 0$ led to spontaneous down-conversion of a laser pump frequency photon into a cavity frequency photon and a mechanical resonator phonon with the frequency of $|\Delta_0|$. The process is also resonantly enhanced if $|\Delta_0| = \omega_m$ and the on-resonance total damping rate of the mechanical resonator is $\gamma = \gamma_i - \gamma_{\text{OM}}$. Optomechanical system under blue-detuned laser drive can lead to lasing when the optomechanical photon-phonon scattering rate is $\gamma_{\text{OM}} > \gamma_i$. This interaction can be used to write-in a quanta from optical pump into the mechanical resonator and entangle it with a cavity-frequency photon.

1.2 Electromechanical Interaction

Electromechanical interaction is normally used to describe the coupling between a mechanically compliant capacitor and an electric circuit as shown in Fig. 1.2. The mechanical motion of the capacitor modulates its capacitance. If the capacitor is part of a LC electric resonator, the motion is transduced into the modulation of the frequency of the electric resonator. It is just like the case of optomechanics where mechanical displacement modulates the optical cavity frequency and leads to optomechanical interaction between light and matter. The LC-resonator with

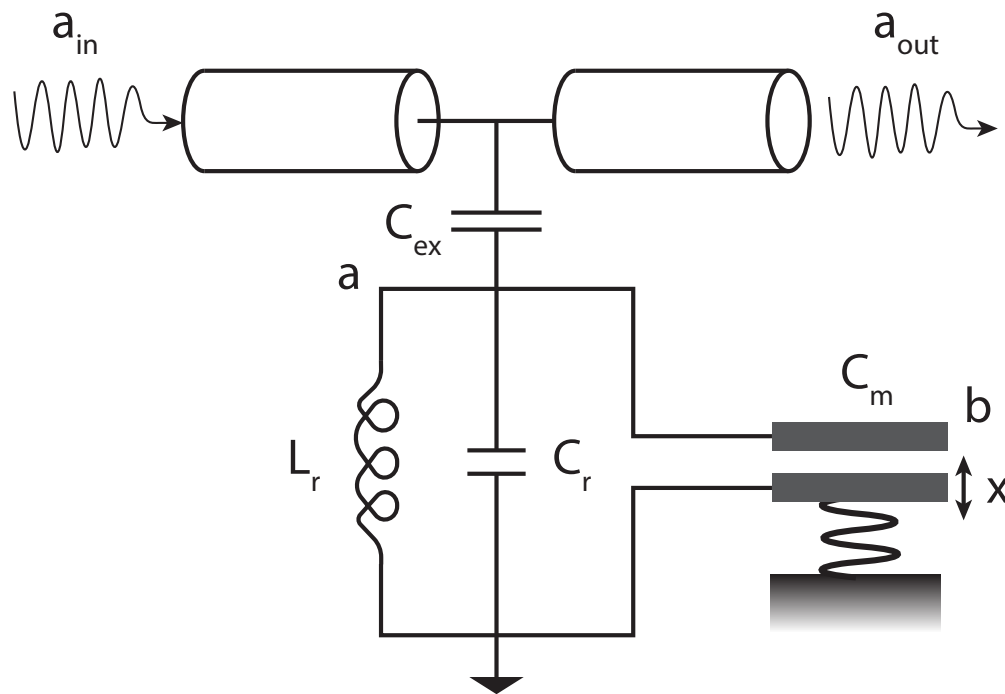


Figure 1.2: Similar to the optomechanical case, electromechanical interaction can be realized in an electric LC-resonator that has a capacitor that is mechanical compliant. Mechanical displacement \hat{x} modulates the capacitance and changes the resonator's frequency.

vibrating capacitor leads to a similar dynamics that couples the microwave electric signal in the circuit to the mechanical mode of the capacitor.

Instead of repeating the discussions in the introduction of optomechanics, the electromechanical interaction can also be extended to describe a system of two electric resonators coupled via a vibrating capacitor shown in Fig. 1.3. In this case, the system is effectively an engineered nonlinear system that causes three-wave-mixing of the mechanical motion with the two electric resonances. The dynamics of the system can be generically written as (1.11).

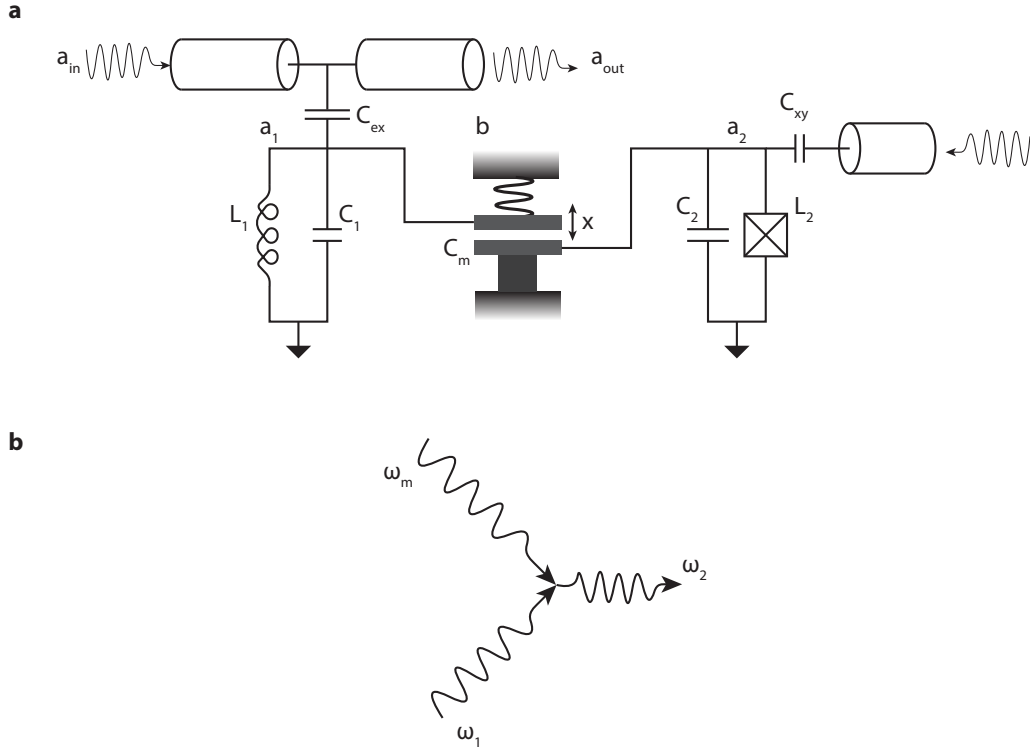


Figure 1.3: **a**, a qubit on the right can be strongly coupled to a mechanical oscillator to swap a quanta between the qubit and a mechanical mode via an engineered three wave mixing shown in **b** using a mechanically compliant capacitor that couples a LC-resonator and a superconducting qubit. The mechanical mode of interest is in the coupling capacitor and its displacement (x) will modulate the coupling between the LC-resonator and qubit. This three wave mixing effectively enhances the coupling between the mechanical mode and the qubit with the LC-resonator driven to a high coherent amplitude.

$$\begin{aligned}
 H = & \sum_{j=1,2} \hbar(\omega_j - \frac{\kappa_j}{2}i) \hat{a}_j^\dagger \hat{a}_j + \hbar(\omega_m - \frac{\gamma_1}{2}i) \hat{b}^\dagger \hat{b} \\
 & + \hbar(J_0 + J_1 \hat{x})(\hat{a}_1 + \hat{a}_1^\dagger)(\hat{a}_2 + \hat{a}_2^\dagger)
 \end{aligned} \tag{1.11}$$

where $\hat{a}_j(\hat{b})$ denotes the annihilation operator for the electric resonances (mechanical resonator). The two electric resonances are coupled via a static coupling J_0 and a varying coupling term $J_1 \hat{x}$ to the first order in displacement $\hat{x} = \hat{b}^\dagger + \hat{b}$. Using the presented coupler design which composed of a vibrating capacitor in parallel to a SQUID loop, the coupling terms can be expressed as (1.12) and (1.13) assuming that $C_m \simeq C_{m,0} + C_{m,1} \hat{x}$ and zero-point-fluctuation in charge amplitudes described

by (1.14). $Z_{1,2} = \sqrt{\frac{L_{1,2}}{C_{1,2}}}$ are the impedance of the electrical resonator 1 and 2.

$$J_0 = \frac{q_1^0 q_2^0}{C_{m,0}} \quad (1.12)$$

$$J_1 = -J_0 \frac{C_{m,1}}{C_{m,0}} \quad (1.13)$$

$$q_{1,2}^0 = \sqrt{\frac{\hbar \omega_{1,2} C_{1,2}}{2}} = \sqrt{\frac{\hbar}{2Z_{1,2}}} \quad (1.14)$$

The three mixing amplitude is characterized by the J_1 in the term involving $(\hat{b}^\dagger + \hat{b})(\hat{a}_1 + \hat{a}_1^\dagger)(\hat{a}_2 + \hat{a}_2^\dagger)$. Assuming that the second electric resonator on the left has a large coherent population α_1 and $\omega_2 = \omega_1 + \omega_m$, the interaction picture Hamiltonian in rotation-wave-approximation (RWA) is (1.15):

$$H_{\text{int}} = \hbar J_1 (\alpha_1^* \hat{a}_2 \hat{b}^\dagger + \alpha_1 \hat{a}_2^\dagger \hat{b}) \quad (1.15)$$

Thus, it can be seen that the swap between electric resonator-1 and the mechanical resonator can be parametrically enhanced with the large photon number $n_1 = |\alpha_1|^2$ in electric resonator-1.

Furthermore, even though electric resonator-2 was described here as a harmonic oscillator with harmonic annihilation and creation operators \hat{a}_2 and \hat{a}_2^\dagger , it is still valid to replace the resonator-2 with a superconducting transmon qubit so that quantum state can be transferred between the qubit and the mechanical resonator at large effective coupling rate enhanced parametrically by populating the other harmonic electric resonator.

This implementation allows the qubit to mechanical resonator coupling to be parametrically enhanced, just like the electromechanical coupling between an electric resonator and a mechanical resonator can be parametrically enhanced by a large detuned pump to the electric resonator. The difference is that the parametric enhancement comes from pumping a second harmonic electric resonator and the coherent single quanta quantum state transfer is between a transmon qubit and a mechanical mode of interest.

1.3 Magneto-mechanical Interaction

Magneto-mechanical coupling is also another form of creating parametrically enhanced coupling between an electric mode and an acoustic mode via having the

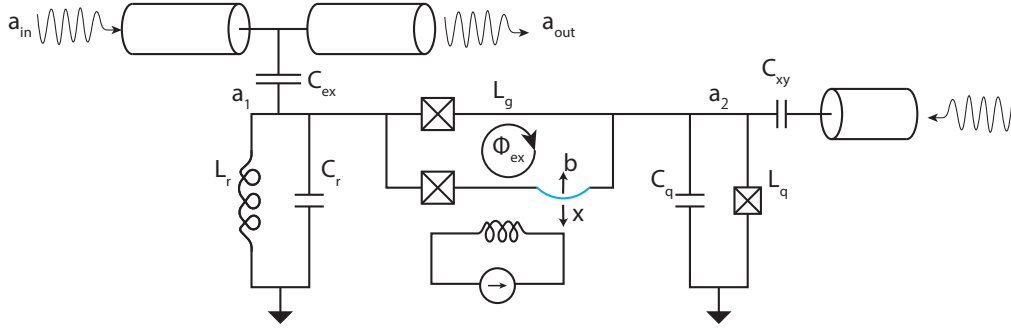


Figure 1.4: Similar engineered three wave mixing used to enhance single photon swap rate between a qubit and a mechanical mode can be realized a SQUID device that couples a highly driven LC-resonator with the superconducting qubit. The SQUID device has a segment that is mechanically compliant and its displacement (x) modulates the magnetic flux through the SQUID loop in a strong magnetic field threading magnetic flux Φ_{ex} through the loop.

mechanical mode to modulate the coupling between the electric mode of interest and another heavily populated harmonic electric resonator illustrated in Fig. 1.4. It is similar to the previous electromechanical case with a mechanically compliant capacitor in the coupler. This design, instead of implementing a moving capacitor, uses a mechanically compliant SQUID loop with part of the loop wire being mechanically compliant schematically shown in Fig. 1.4 as the blue segment. With a strong magnetic field near the moving SQUID edge, motion will be transduced into modulation in the SQUID loop flux which will lead to a modulation of the SQUID effective inductance that creates the coupling between the two electric resonators. The generic form of the Hamiltonian will be the same as (1.11). The static and moving couplings can be expressed as (1.16) and (1.17) with static external flux bias Φ_{ex}^0 .

$$J_0 = \phi_1^0 \phi_2^0 E_J^0 \cos\left(\pi \frac{\Phi_{ex}^0}{\Phi_0}\right) \quad (1.16)$$

$$J_1 = -\phi_1^0 \phi_2^0 E_J^0 \sin\left(\pi \frac{\Phi_{ex}^0}{\Phi_0}\right) \frac{\pi}{\Phi_0} \frac{\partial \Phi_{ex}}{\partial x} \quad (1.17)$$

$$\phi_{1,2}^0 = \frac{\pi}{\Phi_0} \sqrt{\frac{\hbar \omega_{1,2} L_{1,2}}{2}} = \frac{\pi}{\Phi_0} \sqrt{\frac{\hbar Z_{1,2}}{2}} \quad (1.18)$$

The static coupling J_0 can be tuned to zero with external magnetic flux bias $\Phi_{ex}^0 = (0.5 + 2n)\Phi_0$ for $n \in N$. Furthermore, the $|J_1|$ is maximized at these

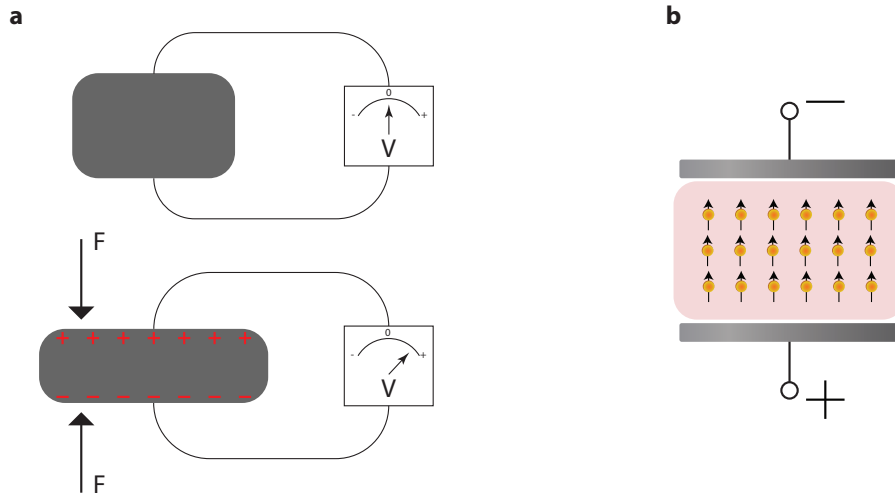


Figure 1.5: **a** shows that the mechanical deformation of a piezoelectric material generates an electric potential and a charge accumulation on its surface. **b** The piezoelectric coupling linearly maps a mechanical mode into the electric domain as vibrating electric dipoles.

$J_0 = 0$ bias points. The ability to turn off the static coupling avoids the large dispersive shifts and decoherence caused by the highly populated electric resonator to the detuned superconducting qubit.

The interaction Hamiltonian under RWA and the assumptions in the electromechanics section will still be (1.15). Thus, replacing the right electric resonator with a superconducting qubit will lead to a strong effective coupling between the qubit and the mechanical mode of interest because this effective single quanta coupling rate is parametrically enhanced by the large population of left electric resonator.

1.4 Piezoelectric Interaction

Piezoelectricity is concerned with a phenomenon that certain materials respond to mechanical deformation with a electric polarization and voltage build-up. A simple figure that illustrates this is shown in Fig. 1.5a. This property of various piezoelectric materials has been extensively utilized over the last century to generate ultra-sound for electric circuits. The strong coupling between the material strain and electric field is due to the broken center symmetry of the material's crystal structure so that strain in the lattice displaces the weighted centers of opposite charges and electrically polarizes the material which is shown in Fig. 1.6 and Fig. 1.5. It should be noted that

there are 20 central symmetry broken crystal classes that have piezoelectric effects. Most commonly used piezoelectric materials can only be polarized by having a non-zero strain-stress field. Such materials belong to 10 of the piezoelectric crystal classes. The rest of the piezoelectric crystal classes are spontaneously polarized even without any deformation.

The mechanical deformation of a piezoelectric material can be effectively mapped into its dual electric domain as an ensemble of electric dipoles like Fig. 1.5b. The mapping can also be quantitatively captured by the coupled field equations in (6.1) and (6.2) with stress (σ_{ij}) induced electric polarization (P_i) described by $P_j = \sum_{kl} d_{jkl} \sigma_{kl}$. The piezoacoustic mode's coupling to a mode of electric circuit can be equivalently treated as the coupling between an electric dipole ensemble to an external electric field. This observation leads to a convenient method for extracting piezoelectric coupling between the electric circuit and a piezoacoustic mode of interest by utilizing the established electromagnetic perturbation method for electric field to polarization field coupling, which can be shown in the later chapter as an overlap integral between the normalized polarization field and the circuit's electric field.

It will be discussed later in detail that coupling cooperativity of a given piezoelectric material to a circuit is fundamentally limited by its piezoelectric coupling coefficient, conventionally denoted as k_{pe}^2 , which is defined as (1.19).

$$k_{pe}^2 = \frac{\text{Energy Stored In Electric Field}}{\text{Energy Stored In Stress Field}} \quad (1.19)$$

This value for the main piezoelectric material (Aluminum Nitride) of interest in this work is between 1% ~ 4%. Other materials like LiNbO₃ and PMN-PT can have larger piezoelectric coupling coefficients for achieving much higher quantum transduction cooperativities.

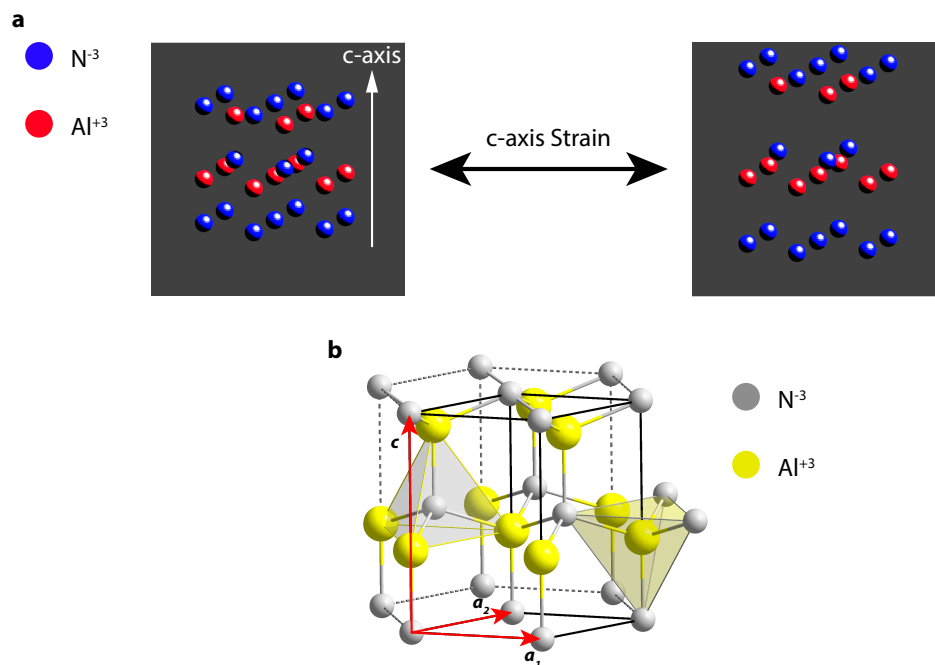


Figure 1.6: **a**, the deformation of a piezoelectric Aluminum Nitride crystal unit cell is shown here. As the unit cell is deformed under c -axis directional strain, the center of opposite charges move in opposite directions due to the lack of inversion symmetry about the c -axis. The deformation is highlighted here with negative Nitrogen ions (blue) and positive Aluminum ions (red). **b**, the AlN crystal unit cell exhibiting hexagonal $6mm$ -symmetry around the c -axis. Primitive lattice vectors are shown in red. The crystal lattice is sited from a web source under public license.

Chapter 2

SUPERCONDUCTING QUANTUM CIRCUIT AND JOSEPHSON JUNCTION TRANSMON QUBIT

Superconductivity is a mesoscopic quantum phenomenon originating from the condensation of cooper-pairs in a superconducting ground state gapped from states containing unpaired electrons. Electrons now share a common wave-function in the ground state and it can be described by a single superconducting phase factor, ϕ , for regions of common potential, V , which can be defined as (2.1).

$$\phi(x, t) = \int_0^t V(x, \tau) d\tau \quad (2.1)$$

Each piece of superconductor in a circuit can be denoted as a node and marked with its superconducting phase variable in a circuit diagram shown in Fig. 2.1. Here, we need to introduce the concept of the spanning-tree in a given circuit. To define a spanning tree, a reference point need to be chosen to be the zero phase point. From the reference point, find a path that traverse all the notes in the circuit without self-intersections that form loops. The path is then called the spanning tree of the circuit. The choice of a spanning tree for a given circuit is not unique. In fact, each choice represents a gauge degree of freedom in circuit dynamics. For example, two different choices of spanning tress are shown in Fig. 2.1 (a) and **b**.

The set of independent phase factors associated with the nodes in the circuit are the degrees of freedom of the system. The classical dynamics of the system can be

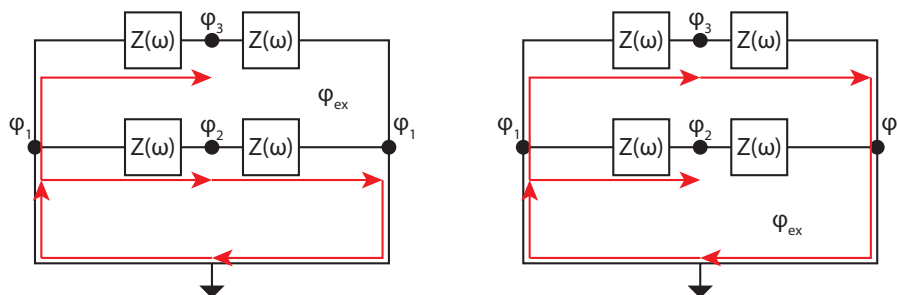


Figure 2.1: Two choices of spanning trees (red) for one physical circuit.

described with a Lagrangian $L(\{\phi_i, \dot{\phi}_i\})$ which is written down noting that $V_i = \dot{\phi}_i$ for a node and each electric element's energy can be written as $E_k = E_k(V_{k+1} - V_k, \phi_{k+1} - \phi_k)$ or $E_k = E_k(V_{k+1} - V_k, \phi_{k+1} - \phi_k + \phi_{\text{ex}})$ if the k -th and $(k+1)$ -th nodes are connected with a path segment that forms a loop with the rest of the choice of spanning tree. The formed loop has an external magnetic flux Φ_{ex} thought it that induces an additional phase difference $\phi_{\text{ex}} = \pi \frac{\Phi_{\text{ex}}}{\Phi_0}$. For example, linear inductance L can contribute inductive energy $E_L = \frac{(\phi_L \Phi_0 / \pi)^2}{2L}$ with a flux quanta $\Phi_0 = \frac{h}{2e}$ and linear capacitor C can contribute capacitive energy $E_C = \frac{1}{2} C \dot{\phi}_C^2$. With the Lagrangian, we can also define conjugated charges for the system with (2.2).

$$q_i = \frac{\partial L(\{\phi_i, \dot{\phi}_i\})}{\partial \dot{\phi}_i} \quad (2.2)$$

Until this point, the circuit is still described classically and the $\{\phi_i, q_i\}$ variables are not operators but numbers. To promote these variables into quantum operators so that the circuit's quantum dynamics can be accurately described in the framework quantum mechanics, we can define the algebra of the variables to follow the canonical commutation relation in (2.3) with $\delta_{i,j}$ being the Kronecker delta function that is 1 when $i = j$ and 0 for other cases.

$$[\hat{\phi}_i, \hat{q}_j] = i\delta_{i,j} \quad (2.3)$$

The Hamiltonian of the system can be obtained via (2.4).

$$\hat{H}(\{\hat{\phi}_i, \hat{q}_i\}) = \sum_i \hat{\phi}_i \hat{q}_i - \hat{L}(\{\hat{\phi}_i, \dot{\hat{\phi}}_i\}) \quad (2.4)$$

2.1 Josephson Effect and Josephson Junction

Josephson effect (Nobel Prize 1973) is concerned with a system composed of two superconductors with a very thin layer of insulator separating them shown in the Fig. 2.2. As electrons in each superconductor pair up as cooper-pairs and condense into a ground state, the thin barrier forms a narrow infinite potential wall between cooper-pairs on both sides. As the wave-function of the electrons on one side has finite amplitude on the other side, there is a finite tunnelling possibility for a cooper pair to tunnel through the barrier into the other side. To have a better understanding of the effect that is in the core of superconducting Josephson junction qubits, we begin with a brief introduction of the BCS theory (Nobel Prize 1957) and then use a simple delta-potential model to derive the responses of the Josephson junction.

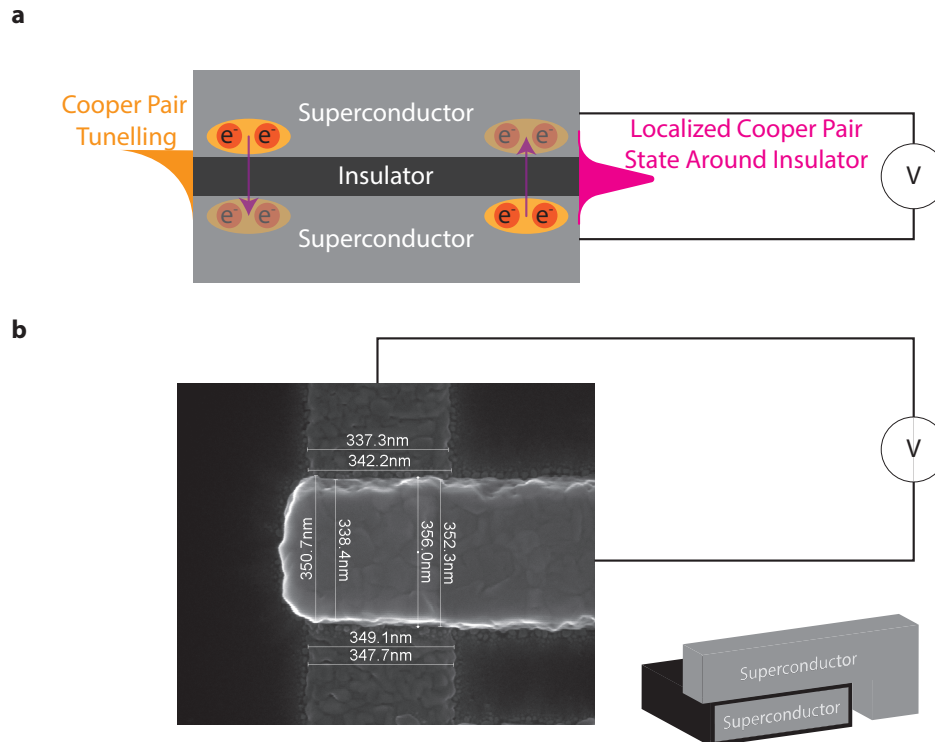


Figure 2.2: **a**, Cooper-pair tunneling between the two superconductors due to extended electronic wave-functions across the potential barrier from the thin insulator. This tunneling term introduces localized cooper-pair state around the insulator. This is the origin of the Josephson energy E_J and lossless Josephson junction current under an external voltage. **b**, the SEM image of a Josephson junction used in this work. The metal and insulator composition is shown in the lower right corner with the black layer representing a layer of insulating oxide. The superconductors used are evaporated Aluminum and the insulating layer was created in a self-limited way via oxidizing the lower Aluminum layer before depositing the upper layer Aluminum.

2.1.1 BCS Theory

BCS theory is named after John Bardeen, Leon Cooper, and John Robert Schrieffer who proposed that electrons in a Fermi sea due to exchange of phonon via the crystal lattice can form a bound state of two electrons as the so-called cooper-pair. To understand the superconducting ground state formed with condensed cooper-pairs, an anza wave-function for the superconducting ground state with zero net electron cooper-pair momentum was proposed to be (2.5) and illustrated in Fig. 2.3.

$$|\Psi\rangle = \prod_{\vec{k}} (u_{\vec{k}} + v_{\vec{k}} e^{i\phi_{\vec{k}}} \hat{c}_{\vec{k}}^{\dagger} \hat{c}_{-\vec{k}}^{\dagger}) |0\rangle \quad (2.5)$$

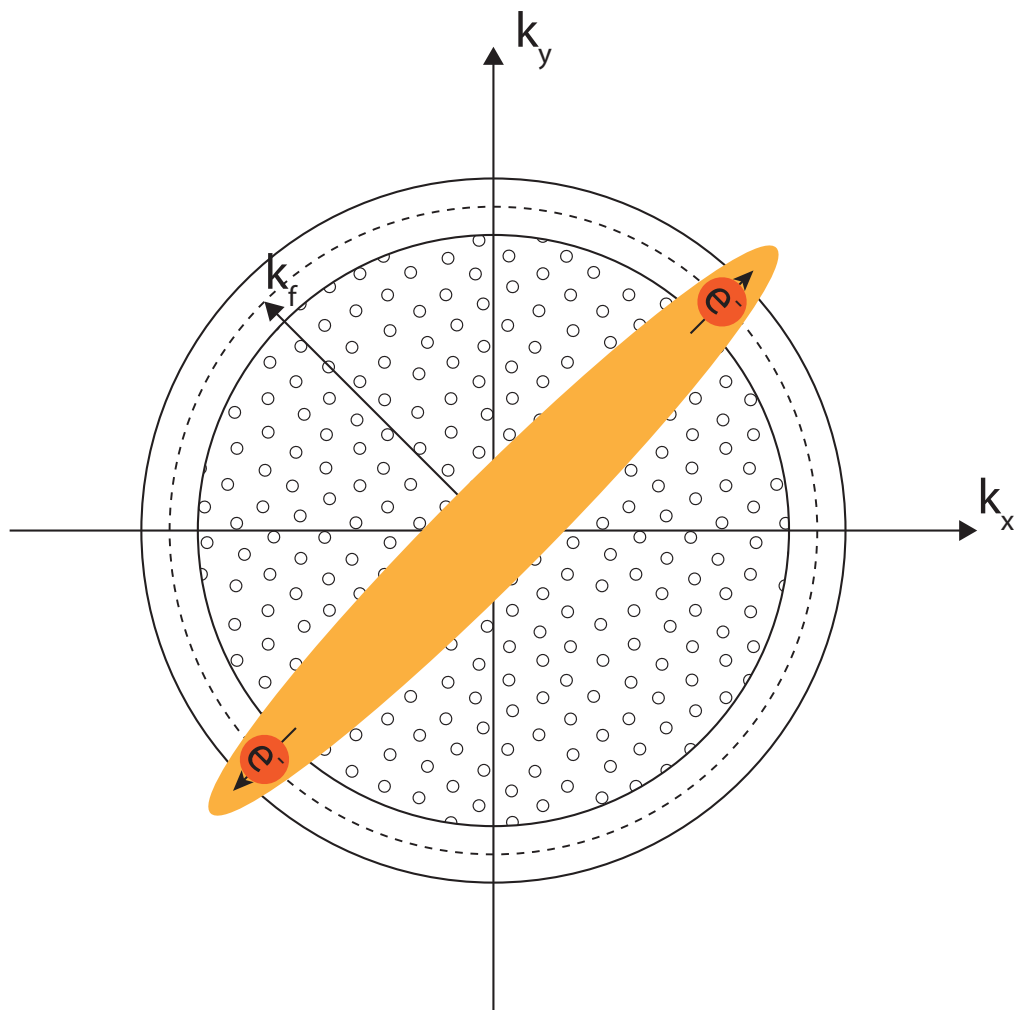


Figure 2.3: The zero net-momentum Cooper-pair formed near the Fermi-surface that has energy slightly below the Fermi-level in the condensed superconducting ground state.

The $|0\rangle$ is the Fermi sea without any cooper-pair and $\{\hat{c}_{\vec{k}}^\dagger\}$ are single electron fermionic creation operators for an electron with momentum \vec{k} . Since each cooper-pair's Hilbert Space in the above proposed ground-state form has two possible basis states, each pair can be represented using a spin, and the ground state becomes a direct product of states of spins as (2.6) and (2.7).

$$(u_{\vec{k}} + v_{\vec{k}} e^{i\phi_{\vec{k}}} \hat{c}_{\vec{k}}^\dagger \hat{c}_{-\vec{k}}^\dagger) |0\rangle \rightarrow \begin{bmatrix} u_{\vec{k}} \\ v_{\vec{k}} e^{i\phi_{\vec{k}}} \end{bmatrix} \quad (2.6)$$

$$\Psi = \bigotimes_{\vec{k}} \begin{bmatrix} u_{\vec{k}} \\ v_{\vec{k}} e^{i\phi_{\vec{k}}} \end{bmatrix} \quad (2.7)$$

The above spin representation of BCS ground state allows the use of Pauli matrices for each cooper-pair's sub Hilbert Space. Assuming that each electron has energy $\epsilon_{\vec{k}}$ relative to the Fermi energy, we can have the kinetic part of the cooper-pairs Hamiltonian in (2.8). The condensation of cooper-pairs has to do with an attractive potential due to the phonon exchange interaction between unbounded electrons. The detailed dynamics that generated the critical attractive potential is beyond the scope of this work. Phenomenologically, this effect can be incorporated into the effective Hamiltonian as an attractive potential term with constant potential V favoring condensation. As a result, the effective Hamiltonian can be written into (2.8).

$$H = - \sum_{\vec{k}} \epsilon_{\vec{k}} \hat{\sigma}_{z, \vec{k}} - \frac{V}{2} \sum_{\vec{p}, \vec{q}} (\hat{\sigma}_{x, \vec{p}} \hat{\sigma}_{x, \vec{q}} + \hat{\sigma}_{y, \vec{p}} \hat{\sigma}_{y, \vec{q}}) \quad (2.8)$$

As can be seen from the potential term of (2.8), the spins in the system have ferromagnetic interaction with each other in the XY-plane. This means that in ground state, their average polarization will be aligned in XY-plane. The average polarization of each spin in XY-plane are (2.9) and (2.10).

$$\langle \hat{\sigma}_{x, \vec{q}} \rangle = 2u_{\vec{q}} v_{\vec{q}} \cos \phi_{\vec{q}} \quad (2.9)$$

$$\langle \hat{\sigma}_{y, \vec{q}} \rangle = 2u_{\vec{q}} v_{\vec{q}} \sin \phi_{\vec{q}} \quad (2.10)$$

The ferromagnetic interaction will result in $\phi_{\vec{q}}$ for the whole ground state to become the same and we can define a single phase variable, ϕ , to characterize the whole condensation of superconducting electrons.

The mean field approximation on the potential term significantly simplifies dynamics of the problem and makes the solution obvious. Taking the mean field approximation, a mean field Hamiltonian becomes (2.11) with the definition $\Delta = V \sum_{\vec{q}} u_{\vec{q}} v_{\vec{q}}$

$$\begin{aligned}
H &= - \sum_{\vec{k}} \epsilon_{\vec{k}} \hat{\sigma}_{z, \vec{k}} - \frac{V}{2} \sum_{\vec{p}, \vec{q}} (\hat{\sigma}_{x, \vec{p}} \langle \hat{\sigma}_{x, \vec{q}} \rangle + \hat{\sigma}_{y, \vec{p}} \langle \hat{\sigma}_{y, \vec{q}} \rangle) \\
&= - \sum_{\vec{k}} (\hat{\sigma}_{x, \vec{k}}, \hat{\sigma}_{y, \vec{k}}, \hat{\sigma}_{z, \vec{k}}) \cdot (\Delta \cos \phi, \Delta \sin \phi, \epsilon_{\vec{k}})
\end{aligned} \tag{2.11}$$

The above equation is just describing non-interacting spins in a magnetic field whose z-component depends the location. Since in this mean field approximation region spins are decoupled, a simple solution for eigenvalues and eigenstates of each spin can be obtained as (2.12) - (2.15)

$$E_{\pm, \vec{k}} = \pm \sqrt{\Delta^2 + \epsilon_{\vec{k}}^2} \tag{2.12}$$

$$\Psi_- = \begin{bmatrix} \sin \frac{\theta}{2} \\ -e^{i\phi_{\vec{k}}} \cos \frac{\theta}{2} \end{bmatrix} \tag{2.13}$$

$$\Psi_+ = \begin{bmatrix} \cos \frac{\theta}{2} \\ e^{i\phi_{\vec{k}}} \sin \frac{\theta}{2} \end{bmatrix} \tag{2.14}$$

$$\theta = 2 \arctan \left(\frac{1 + \frac{\epsilon_{\vec{k}}}{|E_{\pm, \vec{k}}|}}{1 - \frac{\epsilon_{\vec{k}}}{|E_{\pm, \vec{k}}|}} \right) \tag{2.15}$$

The solution can be used to solve for the energy gap Δ self-consistently by using $\Delta = V \sum_q u_{\vec{q}} v_{\vec{q}}$.

Furthermore, beyond the lower energy ground state corresponding to $|\Psi_-\rangle$, we also have single electron excitation of the Fermi sea $\hat{c}_{\pm \vec{k}}^\dagger |0\rangle$ which can be related to the so-called quasi-particle excitation of the cooper-pair ground state as show below with two independent types of quasi-particle creation operators $\gamma_{0, \vec{k}}^\dagger$ and $\gamma_{1, \vec{k}}^\dagger$ defined as (2.16).

$$\begin{aligned}
\gamma_{0, \vec{k}}^\dagger &= u_{\vec{k}} \hat{c}_{\vec{k}}^\dagger - e^{-i\phi} v_{\vec{k}} \hat{c}_{-\vec{k}} \\
\gamma_{1, \vec{k}}^\dagger &= u_{\vec{k}} \hat{c}_{-\vec{k}}^\dagger + e^{-i\phi} v_{\vec{k}} \hat{c}_{\vec{k}}
\end{aligned} \tag{2.16}$$

It can be checked that $\gamma_{0, \vec{k}}^\dagger |\Psi_-\rangle = \hat{c}_{\vec{k}}^\dagger |0\rangle$ and $\gamma_{1, \vec{k}}^\dagger |\Psi_-\rangle = \hat{c}_{-\vec{k}}^\dagger |0\rangle$.

The above derivations are for cooper-pairs of zero net moment that corresponds to a stationary ground state of minimal energy. BCS condensation can also have

non-zero momentum and thus may also be described by a planar travelling wave-function as in the case of a free electron. Here for the simplicity of the discussion, we took a simple planar travelling wave-function and it can be shown in a more general Hamiltonian to have the forms (2.17) and (2.18) for the incident wave from the left and transmitted wave on the right respectively.

$$\Psi_L = Ae^{i\kappa x} \begin{bmatrix} u \\ e^{i\phi_L v} \end{bmatrix} + Be^{i\kappa x} \begin{bmatrix} v \\ e^{i\phi_L u} \end{bmatrix} + Ce^{-i\kappa x} \begin{bmatrix} u \\ e^{i\phi_L v} \end{bmatrix} \quad (2.17)$$

$$\Psi_R = De^{-i\kappa x} \begin{bmatrix} v \\ e^{i\phi_R u} \end{bmatrix} + Ee^{i\kappa x} \begin{bmatrix} u \\ e^{i\phi_R v} \end{bmatrix} \quad (2.18)$$

Using this together with the continuity boundary conditions for wave scattering off a delta-potential, we can obtain two quasi-particle bound states around the barrier with eigenenergies as (2.19) and the current for them as (2.20) with phase difference across the junction as $\delta = \phi_R - \phi_L$.

$$E_{\pm,J} = \pm\Delta\sqrt{1 - \eta \sin^2 \delta} \quad (2.19)$$

$$I_{\pm,J} = \frac{2\pi}{\Phi_0} \frac{\partial E_{\pm,J}}{\partial \delta} \quad (2.20)$$

The total current through the junction is (2.21) where f_{\pm} are Fermion occupation numbers for the upper (forward,+) and lower (backward,-) bound states of cooper-pair condensation wave-functions near the potential barrier.

$$\begin{aligned} I_J &= I_{-,J}f_- - I_{+,J}f_+ \\ &= I_{-,J}(f_- - f_+) \\ &= \frac{\pi}{2} \frac{\Delta(T)}{eR_N} \tanh \frac{\Delta(T)}{2k_bT} \sin \delta \\ &= I_{Jc} \sin \delta \end{aligned} \quad (2.21)$$

This shows that the current flowing through the junction is $\propto \sin \delta$. Comparing it with a linear inductive element that $I_L = \frac{\Phi_0}{\pi L} \delta \propto \delta$, it is clear that a Josephson Junction is a nonlinear inductor which forms the foundation for all superconducting Josephson junction qubits as it can be used to create anharmonic resonators in the circuit that are effectively two level systems if we only care about the excitation between the ground state and the first excited state.

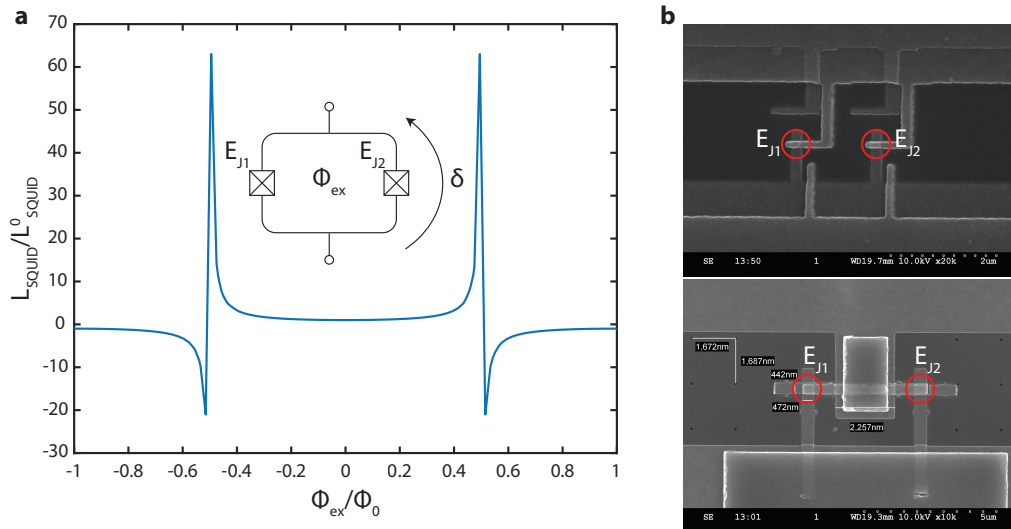


Figure 2.4: The inset of **a** shows schematically a superconducting quantum interference device (SQUID). It is composed of two Josephson junctions connected together in parallel. This device can be regarded as one Josephson junction with tunable Josephson energy tuned by an external magnetic flux Φ_{ex} threaded by an external circuit. **a** shows the effective Josephson inductance tuned by the external flux corresponding to different levels of asymmetry (defined in the text) in the pair of Josephson junctions. **b**, SEM images of SQUID devices with Dolan Bridge and Manhattan Josephson junctions (red circles) used in our superconducting transmon qubits.

2.1.2 Superconducting Quantum Interference Device

A superconducting quantum interference device (SQUID) has been widely used in the community of superconducting quantum circuit electrostatics. It is composed of a pair of Josephson junctions shown in Fig. 2.4a. The two junctions may not be the same and their asymmetry is characterized by a dimensionless parameter d in (2.22) with Josephson junction energies E_{J1} and E_{J2} . The SQUID energy with a phase difference δ across it is (2.23). For a negligible asymmetry ($d \sim 0$), the SQUID can be regarded as a nonlinear inductance just like a single Josephson junction would be. The effective Josephson junction inductance for a SQUID with $d = 0$ is (2.24) with tunability curve shown in Fig. 2.4b. SQUID has been widely used in a variety of applications for the flexibility offered by its tunable effective Josephson junction inductance. For example, tunable transmon qubits use SQUID as their nonlinear inductance to achieve a wide variety of frequency tuning so that they can avoid resonant coupling to TLSs and perform fast two qubit gates on demand. SQUIDs are also serially connected to form a serial SQUID resonator that can be regarded as a high impedance tunable electrical resonator for applications involving quantum

acoustic transductions.

$$d = \frac{|E_{J1} - E_{J2}|}{E_{J1} + E_{J2}} \quad (2.22)$$

$$E_{\text{SQUID}} = -(E_{J1} + E_{J2}) \left[\cos \left(\pi \frac{\Phi_{\text{ex}}}{\Phi_0} \right) \cos \delta + d \sin \left(\pi \frac{\Phi_{\text{ex}}}{\Phi_0} \right) \sin \delta \right] \quad (2.23)$$

$$L_{\text{SQUID}} = \frac{\Phi_0^2}{\pi^2 (E_{J1} + E_{J2}) \cos \left(\pi \frac{\Phi_{\text{ex}}}{\Phi_0} \right)} = \frac{L_{\text{SQUID}}^0}{\cos \left(\pi \frac{\Phi_{\text{ex}}}{\Phi_0} \right)} \quad (2.24)$$

2.2 Superconducting Josephson Junction Qubits

2.2.1 Anharmonic Quantum Oscillator

As it was found out in the previous section that potential energy stored in the Josephson junction region is not, in general, quadratic. The $\cos \delta$ dependent potential can be used to create highly nonlinear electric resonators as illustrated in the circuit diagram in Fig. 2.5 where a box with a cross in the circuit diagram is used to describe the Josephson junction. The Hamiltonian can thus be written as (2.25).

$$\hat{H} = \frac{\hat{q}^2}{2C} - E_J \cos \hat{\delta} \quad (2.25)$$

This Hamiltonian can also be used to describe the motion of a quantum pendulum since both systems' potentials are cos-dependent. In terms of a quantum oscillator, its displacement amplitude corresponding to a low level excitation is characterized by the oscillator's zero-point-fluctuation amplitude $\phi_{\text{zpf}} = \left(\frac{2E_C}{E_J} \right)^{\frac{1}{4}}$ where $E_C = \frac{e^2}{2C}$ is called the "Charging Energy" of the qubit. In the case of a small zero-point-fluctuation amplitude, the nonlinear harmonic oscillator can be approximated by a aharmonic oscillator with a slightly perturbed parabolic potential. Linear harmonic oscillator has equally spaced energy levels and aharmonic oscillator will have energy levels with nonuniform spacings due to the perturbation. This feature in the energy structure allows selective addressing of transitions and effective truncation of its Hilbert space to the lowest relevant levels. We can treat such aharmonic resonators in a superconducting circuit as artificial atoms and two level systems when the system is sufficiently cooled to its ground state in a dilution refrigerator (DF). Such artificial atoms and superconducting two level systems are called superconducting Josephson Junction qubits in the context of quantum computing based on superconducting circuits.

There are a large variety of Josephson junction qubits utilizing the $\cos \delta$ -potential provided by the Josephson junctions. The difference is mainly characterized by

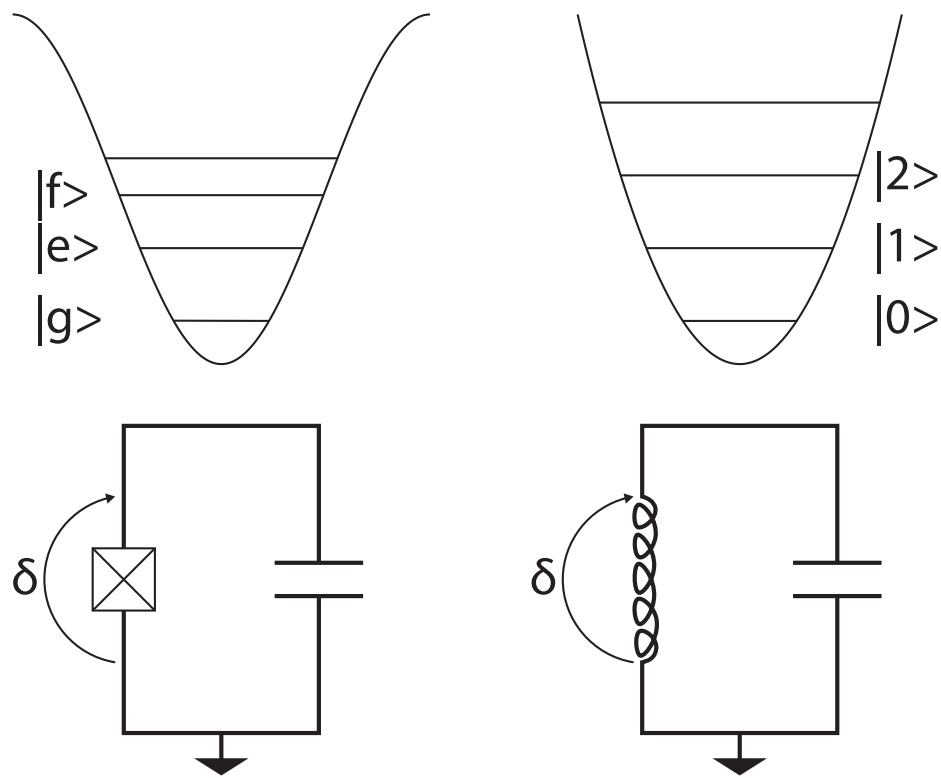


Figure 2.5: The left is a linear electric resonator represented with a LC-resonator. It has a parabolic potential with phase difference δ cross the capacitor as the potential position variable. The right is the anharmonic resonator that forms the foundation of Josephson junction qubits. The anharmonic resonator potential will create the unevenly spaced energy levels indicated in the figure.

the shape of the superconducting phase potential in the neighborhood of a chosen linearization point (phase difference bias across a Josephson junction). In this way, Josephson junction qubits can be separated into different categories including flux qubits, phase qubit, charge qubits, and transmon qubits. The rest of the section will focus on discussing the different superconducting qubits systems.

2.2.2 Charge Qubits and Transmon Qubits

Charge qubits and transmon qubits are forms of a so-called Cooper pair box qubit category [66]. The cooper-pair box qubits have phase bias point $\delta_0 = 0$. A charge qubit has a large zero-point-fluctuation amplitude that makes the qubit extremely nonlinear since the phase oscillation of an excitation covers most of the nonlinear $\cos \delta$ -potential making the oscillator a strictly nonlinear oscillator. It can be described by a circuit in Fig. 2.6a with phase variable potential described by in Fig. 2.6b. The system's Hamiltonian can be written as (2.26).

$$\hat{H} = E_C(\hat{n} - n_g)^2 - E_J \cos \hat{\delta} \quad (2.26)$$

In the expression, the classical variable n_g is the residual number of charges accumulated across the capacitor which is also commonly called the "bias charge" in literature. This variable can be controlled and tuned via an external voltage source (the blue part in Fig. 2.6). The energy levels of the system can be solved analytically according to (2.27) from [64] with Mathieu's characteristic value $A_\alpha(\beta)$ and numerically. The influence of the bias charge on the levels can be easily seen from (2.27). This indicates that a charge qubit's frequency can be externally tuned with an external DC voltage and also that the energy levels are sensitive to the charge number fluctuation on the capacitor. As charge is long range coupled to the electromagnetic environment, its environmental noises will jitter the bias charge, which will in term jitter the transition frequency of the qubit. The frequency jittering leads to dephasing of the qubit. A charge qubit needs to be charge biased to its charge insensitive point at each $\frac{1}{2}$ -charge point to eliminate the bias charge dependence to the first-order [64]. These points are also called the degeneracy points as the charging energies for a cooper pair to exist on both sides of the capacitor are the same. In other words, the two charge states $|n = n_g - \frac{1}{2}\rangle$ and $|n = n_g + \frac{1}{2}\rangle$ have the same charging energies.

$$E_k(n_g) = E_C A_{2[n_g + s(k, n_g)]} \left(-\frac{E_J}{2E_C} \right), \quad (2.27)$$

$$(2.28)$$

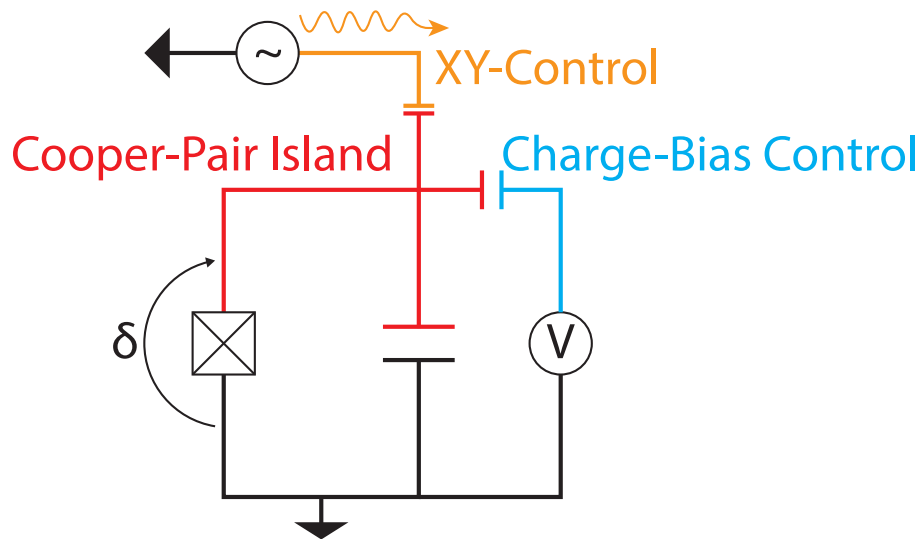


Figure 2.6: An illustration of controls on a single junction charge qubit. For a charge qubit, its strong energy charge dispersion can be utilized to tune its frequency over a large range via a capacitor and external voltage source (blue) that control the number of residual cooper-pairs in the Cooper-pair island (red). This control can thus be viewed as a Z-control for charge qubits. There can also be an XY-control (yellow) for a charge qubit implemented with a near resonant external AC voltage source that drive the qubit via a small capacitor. This AC drive induces Rabi oscillation of the qubit between states having energy difference matching the driving frequency. If the driving frequency is around the spacing between the lowest energy levels, the qubit can be rotated on the Bloch sphere spanned by the two lowest states.

Due to the sensitivity to unavoidable environmental charge noise, charge qubits often have very short coherence time. However, the transmon qubit which is another type of cooper-pair box qubit with phase bias around $\delta_0 = 0$ is designed to significantly suppress the charge sensitivity of these qubits at a relatively small cost of reduced anharmonicity. This qubit is differentiated from a charge qubit by its much smaller phase zero-point-fluctuation amplitude. This makes the qubit a slightly perturbed harmonic oscillator. More specifically, the qubit is shunted with a large capacitor between the cooper-pair island and the ground so that $\phi_{zpf} = \left(\frac{2E_C}{E_J}\right)^{\frac{1}{4}}$ is small. This large capacitance at a given qubit transition frequency leads to a large $\frac{E_J}{E_C} \gg 1$ which exponentially suppresses the bias charge dependence of the qubit energy levels and polynomially suppresses the anharmonicity ($|\omega_{ge} - \omega_{ef}|$) of the qubit. This type of qubit has demonstrated energy relaxation time $T_1 \sim 40 \mu\text{s}$ and phase coherence time $T_2 \sim 20 \mu\text{s}$. Due to high reproducibility, relatively long coherence time, and high

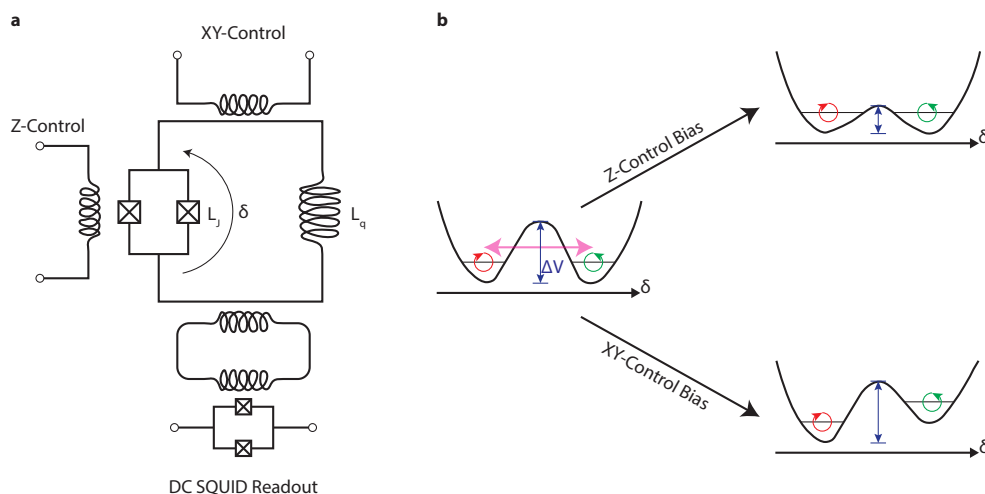


Figure 2.7: **a** A realization of a flux-qubit with controls and the readout circuit. **b** shows the phase variable double-well potential which can be tuned by external controls.

controllability, transmon qubits have been the most popular type of qubits recently in literature and are frequently used in this work.

2.2.3 Flux Qubits

Flux qubits can be constructed with a circuit diagram shown in Fig. 2.7a. In this structure, the potential energy landscape and energy levels are shown in Fig. 2.7b. The potential of the flux qubit is a double-well where the phase of the qubit can tunnel between the two wells through the finite wall. This tunneling process produces a higher energy bounding state and a lower energy anti-bounding state. They correspond to symmetric and anti-symmetric combinations of localized ground state wave-function in each well. Each localized ground state of the double well corresponds to either a clockwise (red) or an anti-clockwise (green) circulation of superconducting current in the flux qubit loop. The spacing between the two lowest levels is determined by the tunnelling amplitude between the two wells. By selectively addressing the transition between the ground state and first excited state, we can treat the multi-level system effectively as an engineered two level system. This system's Hamiltonian can be described in (2.29). For a large anharmonicity, the system is constructed in a way that the linear inductance of L_q cancels the negative effective Josephson junction inductance of the SQUID loop. The SQUID loop is biased to negative inductance by an externally applied Z-Control magnetic flux through the small SQUID loop. The balance of the potential well can also be

tuned by a DC flux through the rest of flux qubit circuit loop. This control flux is applied via the XY-Control loop. As the ground state and first excited states are formed by the hybridized clockwise and anti-clockwise superconducting currents, an operating flux qubit requires the double well to be balanced with an appropriately high potential barrier. The system can be viewed as a dual to the charge qubit system and this time the number of external flux quanta through the circuit become the bias constant that can be used to tune the potential to be a symmetric double well where localized ground states have the same energy in either well. The degeneracy point notion is similar to the degeneracy point in the case of a charge qubit. This point also provides the qubit with protection against flux noise to the first order. The charge noises' detrimental impact on qubit coherence is eliminated, as the flux qubit has a large zero-point-fluctuation charge amplitude and is thus not sensitive to the environmental perturbation in charge degree of freedom. Near the flux degeneracy point of the device, the effective Hamiltonian can again be reduced into a spin in external magnetic field similar to the charge qubit case. The minimal energy splitting between the lowest states is determined by the tunneling amplitude, which depends exponentially on the barrier height. This value needs to be determined numerically for a give set of circuit parameters and analytical solution is not available.

Even though flux qubits are insensitive to charge noise and should to the first order be insensitive to flux noise, flux fluctuation in the environment also causes detrimental effects in the coherence of the qubit. The sources of the flux noises can be flux trapping or critical current fluctuation in junctions.

$$H = E_C \hat{n}^2 + \frac{\Phi_0^2 \hat{\delta}^2}{2L} - E_J \cos \hat{\delta} \quad (2.29)$$

2.2.4 Phase Qubits

Typical phase qubits can be achieved with a circuit diagram shown in Fig. 2.8a. This circuit will give a potential illustrated in Fig. 2.8b together with the lowest energy levels for the bounded states when the Josephson junction is current biased closed to its critical current using a high impedance current source connected to it. Just like the flux qubit, this type of qubit is not sensitive to charge noises due to its large charge zero-point-fluctuation amplitude for a given frequency with a large $\frac{E_J}{E_C}$ ratio. For a bias current I_b , the Hamiltonian of the system can written as (2.30). The titled washboard potential shown in Fig. 2.8b has a tilting slope given by the ratio $\frac{I_b}{I_J}$ where I_J is the Josephson junction critical current. For an external bias current close to the critical current, the potential near $\phi \sim \frac{\pi}{2}$ can be approximated with a qubit potential shown in (2.31). The potential has a well with

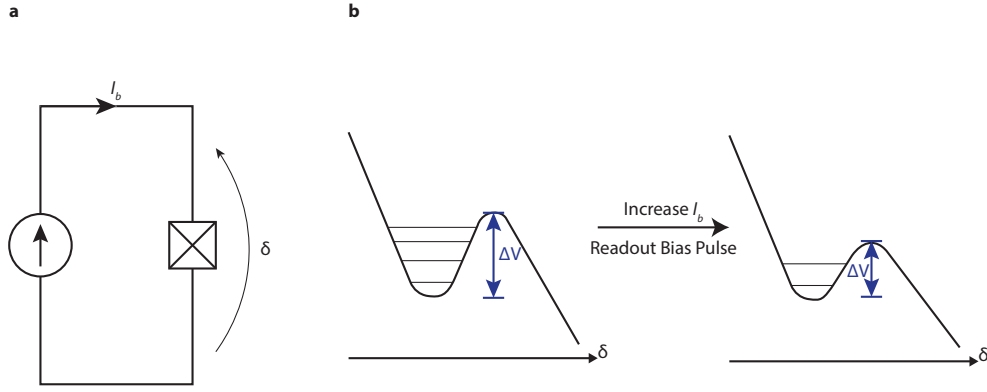


Figure 2.8: **a**, an example of phase qubit which is current (I_b) biased just below the Josephson junction's critical current (I_J) to generate the potential shown in **b**. The potential barrier can also be controlled by increasing the bias current.

a finite potential barrier that can confine a few low level states in it. The barrier height is $\Delta V = \frac{2\sqrt{2}}{3} I_J \phi_0 (1 - \frac{I_b}{I_J})^{\frac{3}{2}}$. The ground state to first excited state transition frequency is shown in (2.33). As the localized energy levels in the well are not uniformly spaced, the qubit's Hilbert space can be truncated to the ground state and the first excited state. The effective Hamiltonian can be written with Pauli operators for spins as in (2.32) with $\chi = \sqrt{\frac{\hbar \omega_{ge}}{3\Delta V}}$ and $\Delta I = I_b - I_J$.

$$H = E_C \hat{n}^2 - I_b \Phi_0 \delta - I_J \Phi_0 \cos \delta \quad (2.30)$$

$$V = \Phi_0 \left(-\Delta I \left(\delta - \frac{\pi}{2} \right) - \frac{I_J}{6} \left(\delta - \frac{\pi}{2} \right)^3 \right) \quad (2.31)$$

$$H_{\text{eff}} = \frac{\omega_{ge}}{2} \hat{\sigma}_z + \sqrt{\frac{\hbar}{2\omega_{eg} C_q}} \Delta I (\hat{\sigma}_x + \chi \hat{\sigma}_z) \quad (2.32)$$

$$\omega_{ge} \simeq 0.95 \frac{1}{\sqrt{L_{J0} C_J}} \left[1 - \left(\frac{I_b}{I_J} \right)^2 \right]^{\frac{1}{4}} \quad (2.33)$$

2.2.5 Superconducting Qubit Readout

The previous section has introduced the three major types of superconducting Josephson junction qubits that can effectively be treated as two level systems and store quantum states as superpositions of their ground states and first excited states. The next important question other than how information is stored is how information

can be extracted by measurement with minimal perturbation. The readout part in a circuit should have the property that it can measure the state of the qubit on-demand. This means that the readout circuit does not decohere or measure the qubit when the qubit is going through quantum gate operations and high fidelity qubit state measurement can be turned on on-demand to distinguish the ground state and the first excited state. Furthermore, the back-action of the measurement should be weak enough to avoid relaxing the qubit. There are four parameters that characterize a readout scheme. They are listed here for reference:

1. Measurement Time τ_{meas} : The time needed to accumulate information for reaching signal-to-noise of one in the determining the state of the measured qubit in one shot.
2. Measurement Decoherence Rate Γ_{meas} : The decoherence rate caused when the qubit is being measured.
3. Parasitic Decoherence Rate Γ_{RO} : The decoherence rate when the qubit is not being measured and the decoherence is caused by qubit coupling to the measurement circuit.
4. Measurement Dead Time τ_d : The time needed for the measurement circuit and possibly the qubit to be reset for the next round of repeated measurement.

It is desirable to simultaneously minimize these parameters for achieving ideal readout. However, the conflicting nature between these parameters prohibits this ideal optimization and leaves a bound in how well a given scheme can do. The merit of a readout scheme can also be measured with the so-called readout fidelity. This is qualitatively defined as the probability of obtaining the correct measurement of a qubit in either the ground state or the first excited state. If for a qubit in the ground state (first excited state), the measurement indicates an outcome corresponding to a ground state (first excited state) with probability $P_{gg}(P_{ee})$, the readout fidelity is $F_R = P_{gg} + P_{ee} - 1$.

The fidelity and speed of the readout, usually not discussed in the context of quantum algorithms because they enter marginally in the evaluation of their complexity, are actually key to experiments studying the coherence properties of qubits and gates. A very fast and sensitive readout will gather at a rapid pace information on the imperfections and drifts of qubit parameters, thereby allowing the experimenter to design

fabrication strategies to mitigate them during the construction or even correct them in real time. For single-shot readout to have high fidelity close to unity, the qubit shouldn't be relaxed by the measurement which demands that $\Gamma_{\text{meas}}\tau_{\text{meas}} \ll 1$. For the measurement circuit to have minimal detrimental effect on the qubit coherence when measurement is not needed, the system should also satisfy $\Gamma_{\text{RO}} \ll \Gamma_2$ where Γ_2 is the intrinsic dephasing rate of the qubit.

Over the time, various different methods for reading out different qubits were developed and the recently developed dispersive readout schemes are the most popular ones. Unlike other schemes that require on-chip amplification and switching elements which introduce loss channels and heat load in the neighborhood of a qubit, dispersive readout measurement can be turned on via a readout pump applied to the readout circuit and information regarding the measured state of the qubit can be obtained by a series of amplifiers from the low temperature stages to room temperature electronics. This type of readout combined hardware simplicity, qubit coherence protection, and the ability to turn ON/OFF measurement (and its back-action) on demand. Fig. 2.9 shows a circuit diagram for a transmon qubit coupled to a readout system composed of a far detuned resonator and a transmission line used to probe the resonator. As the readout resonator is coupled to the qubit via a capacitor, the coupling slightly hybridizes the readout resonator and the qubit despite of the large detuning between them that $\Delta_{\text{RO}} \gg J_{\text{RO}}$. This slight hybridization leads to a resonator-like mode having almost all of its energy in the resonator and a qubit-like mode having almost most of its energy in the qubit. If we ignore the qubit and only look at the frequency response of the resonator as probed by the transmission line, the readout resonator's frequency will appear to be shifted as it is now slightly dressed with the qubit. If the qubit is in its ground state, this shift is often regarded as a form of Lamb-shift. If the qubit is in its excited state, the shift of the frequency will be different and this change of frequency can be probed with either the phase or amplitude responses of the pump pulse with frequency aligned with the resonator frequency when the qubit is in its ground state. It has to be noted that the state dependant frequency shift of the readout resonator is absent in a system with two coupled harmonic resonators as it will be shown later that the dispersive shift is related to the anharmonicity directly.

The Hamiltonian describing a transmon qubit coupled to a resonator can be written

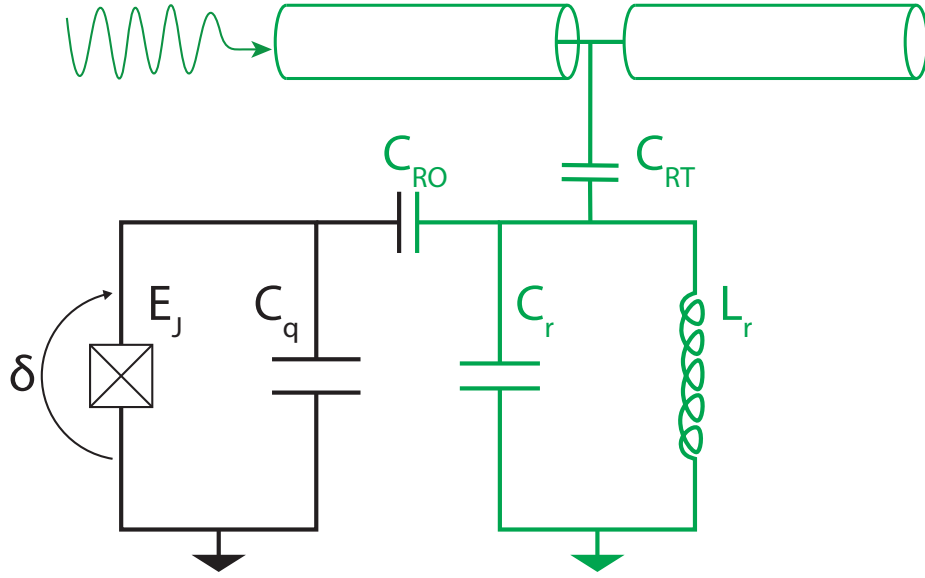


Figure 2.9: A standard transmon dispersive readout circuit (green) without Purcell filters.

as (2.34). The Hamiltonian can be diagonalized to the second order in $(\frac{g}{\Delta})^2$ by first rotating the basis via an unitary transformation defined as (2.36) with (2.37).

$$\hat{H} = \hbar\omega_q(\hat{c}^\dagger\hat{c} + \frac{1}{2}) - E_J - \frac{E_C}{12}(\hat{c} + \hat{c}^\dagger)^4 + \hbar\omega_r\hat{a}^\dagger\hat{a} + \hbar g(\hat{c} - \hat{c}^\dagger)(\hat{a} - \hat{a}^\dagger) \quad (2.34)$$

$$g_{k,k+1} = g \langle k | (\hat{c}^\dagger - \hat{c}) | k + 1 \rangle \quad (2.35)$$

$$\hat{U} = \exp(\hat{S} - \hat{S}^\dagger) \quad (2.36)$$

$$\hat{S} = \sum_k \beta_k \hat{a} |k + 1\rangle \langle k| \quad (2.37)$$

$$\beta_k = \frac{g_{k,k+1}}{\omega_{k,k+1} - \omega_{RO}} = \frac{g_{k,k+1}}{\Delta_k} \quad (2.38)$$

Using the Baker-Campbell-Hausdorff (BCH) formula which describes $\exp(\hat{A})\exp(\hat{B}) = \exp(\hat{A} + \hat{B} + [\hat{A}, \hat{B}]/2 + \dots)$ and keep the transformed Hamiltonian to the second order as stated previously will yield the effective Hamiltonian in this transformed

frame as (2.39).

$$\begin{aligned} \hat{H}_{\text{eff}} = \hat{U} \hat{H} \hat{D}^\dagger \simeq & \sum_k \hbar \omega_k |k\rangle \langle k| + \sum_k \hbar \chi_{k,k+1} |k+1\rangle \langle k+1| \\ & + \hbar \left(\omega_{\text{RO}} - \chi_{01} |0\rangle \langle 0| + \sum_{k=1} (\chi_{k-1,k} - \chi_{k,k+1}) |k\rangle \langle k| \right) \hat{a}^\dagger \hat{a} \\ & + \sum_k \hbar \eta_k \hat{a}^2 |k+2\rangle \langle k+2| + \sum_k \hbar \eta_k^* \hat{a}^{\dagger 2} |k\rangle \langle k+2| \end{aligned} \quad (2.39)$$

$$\eta_k = \frac{g_{k,k+1} g_{k,k+2} [(\omega_{k+1} - \omega_{k+2}) - (\omega_k - \omega_{k+1})]}{2(\omega_{k+1} - \omega_k - \omega_{\text{RO}})(\omega_{k+2} - \omega_{k+1} - \omega_{\text{RO}})} \quad (2.40)$$

$$\chi_{ij} = \frac{g_{ij}^2}{\omega_{ij} - \omega_{\text{RO}}} \quad (2.41)$$

$$\omega_{ij} = \omega_j - \omega_i \quad (2.42)$$

As it can be noticed in the second line of (2.39), the effective dressed readout resonator frequency depends on the number state of the transmon qubit. More precisely, the effective readout resonator frequency can be treated as a projective measurement operator for the qubit state. This forms the basis of the dispersive readout schemes and the dispersive shifts are closely related to the anharmonicity of the qubit energy levels. If we truncate the Hilber space for the qubit into the lowest energy levels, the system Hamiltonian can be written as (2.43).

$$\hat{H}_{\text{eff}} \simeq \hbar(\omega'_{\text{RO}} - \chi \hat{\sigma}_z) \hat{a}^\dagger \hat{a} + \frac{\hbar \omega_{\text{q}}}{2} \hat{\sigma}_z \quad (2.43)$$

$$\chi = \left(\frac{g_{\text{RO}}^2}{\omega_{\text{RO}} - \omega_{\text{q}}} \right) \quad (2.44)$$

If the qubit was replaced with a linear resonator, the state dependent dispersive shifts would be zero as mentioned earlier.

It should also be mentioned that this readout can still introduce a qubit decay channel even though the qubit is coupled to a far detuned resonator, which can in principle act as a filter that protects the qubit from environmental noises in the readout transmission line. The decay channel is called Purcell loss [115]. It is fundamentally a second order effect that virtual coupling between the qubit and the electromagnetic continuum in the transmission line can be mediated by virtual photon processes in the readout resonator as shown in Fig. 2.10a. The Purcell loss

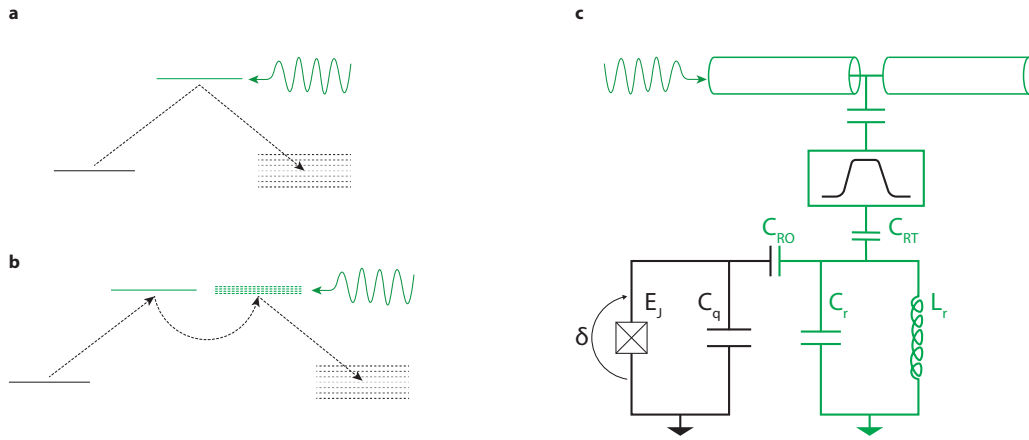


Figure 2.10: **a** The Purcell loss process due to virtual coupling between the transmon qubit (black-solid line) and the electromagnetic continuum (black-dotted lines) in the transmission line coupled to the readout resonator (green-solid line) far detuned from the qubit. The green wiggling line is the readout tone. The black-dotted arrow is the quantum path via which a qubit photon tunnels into the transmission line continuum. **b**, the Purcell loss is significantly suppressed by introducing a Purcell filter that modifies the electromagnetic density of states (green-dotted lines) coupled to the readout resonator. **c** is a modified readout circuit (green) with an addition of Purcell filter that suppresses the Purcell loss significantly.

rate is $\kappa_{\text{purcell}} \simeq \left(\frac{g_{\text{RO}}}{\Delta_{\text{QR}}} \right)^2 \kappa_{\text{RO}}$ where g_{RO} is the coupling rate between the readout resonator and the qubit. $\Delta_{\text{QR}} = \omega_{\text{q}} - \omega_{\text{RO}}$ and κ_{RO} is the damping total rate of the readout resonator. This loss mechanism can be strongly suppressed with an on-chip Purcell filter in the readout transmission line to block the electromagnetic wave with qubit frequency from propagating in and out of the chip via the readout ports [115, 57]. The filtered process is shown in Fig. 2.10**b**. The new circuit diagram with the filter is shown in Fig. 2.10**c**. This does not influence the propagation of the readout pump since the readout pump aligned with the readout resonator frequency well within the bandpass window of the Purcell filter. This filter should ideally have a wide pass-band covering the readout resonator frequencies and stop-band for all qubit frequencies if there are multiple qubits and readout resonators. A wide bandpass Purcell filter with a high stop-band attenuation can be achieved with the superconducting microwave photonic crystal [83].

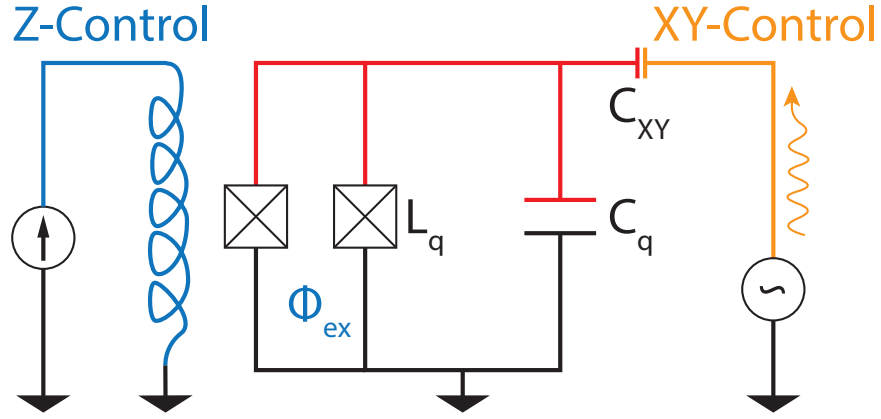


Figure 2.11: The resonant XY-Control (yellow) circuit of a standard transmon qubit with qubit frequency tuning implemented with a blue Z-Control circuit (blue) that tune the qubit frequency by threading external magnetic flux Φ_{ex} through the qubit SQUID loop.

2.2.6 Transmon Qubit Controls

As this work only used transmon qubits, I will discuss about the basics in controlling this type of qubit using classical electric signals. An image of a superconducting transmon qubit and a corresponding circuit diagram is shown in Fig. 2.11. There are two types of controls for the qubit called XY-Control and Z-Control on a qubit Hamiltonian that describe its dynamics in (2.45)

2.2.6.1 XY-Control

XY-Control couples the qubit charge degree of freedom to an oscillating external voltage drive. This control is used to drive the transition between qubit energy levels. For the truncated Hilbert space containing only the lowest energy levels of interest, the qubit state can be represented on the so-called Bloch-Sphere as shown in Fig. 2.12 as a vector pointing to a point on the sphere. A XY-Control drive can be characterized with a detuning $\delta_{XY} = \omega_{XY} - \omega_q$ and a so-called Rabi amplitude $\hbar\Omega_{XY} = C_{XY} \frac{(8E_c^3 E_J)^{\frac{1}{4}}}{e} \tilde{V}_d$ proportional to the driving port voltage amplitude \tilde{V}_d . It can lead to a driving interaction Hamiltonian as (2.46) under a driving voltage described by $V_d(t) = \tilde{V}_d \cos(\omega_{XY}t)$. This causes the spin state vector to precess around an axis with direction along (2.47) with rate (2.48).

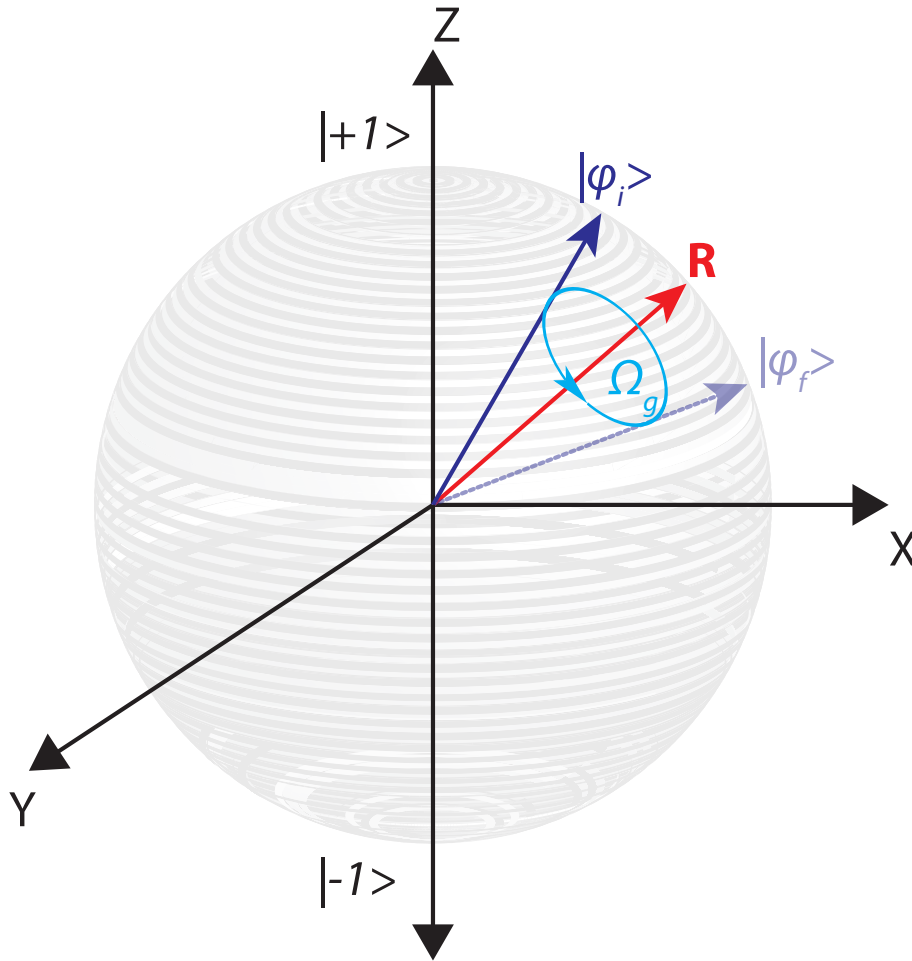


Figure 2.12: The Bloch sphere showing the state vector at $|\phi_i\rangle$ to $|\phi_f\rangle$ around the “laser vector“ with Rabi frequency Ω_R

$$H_{\text{transmon}} = \frac{\hbar\omega_q}{2}\hat{\sigma}_z + H_d \quad (2.45)$$

$$H_d = \hbar\Omega_{XY} \cos(\omega_{XY}t)\sigma_x \quad (2.46)$$

$$\vec{R} = \left(\frac{\Omega_{XY}}{\Omega_R}, 0, \frac{\delta_{XY}}{\Omega_R} \right) \quad (2.47)$$

$$\Omega_R = \sqrt{\delta_{XY}^2 + \Omega_{XY}^2} \quad (2.48)$$

The XY-Control potentially provides the a relaxation channel for the qubit as it directly couples the charge degree of freedom to a classical drive line going off the chip. This loss channel can be suppressed greatly by designing the XY-Control’s coupling to the qubit as small as possible and fast XY-Control rotation can still be

obtained via a stronger drive on the control line.

2.2.6.2 Z-Control

Z-Control is used to control the transition frequency of the shown transmon qubit with a SQUID as its nonlinear inductance by threading magnetic flux into the SQUID loop. The frequency of a typical superconducting qubit can be tuned with external flux Φ_{ex} following the $\omega_{01} = \omega_{01}^{\text{max}} \sqrt{\cos(\pi \frac{\Phi_{\text{ex}}}{\Phi_0})}$. The ability to tune the frequency of a qubit can be used to control relative phase of the quantum state and turn-on/off resonant coupling between another coupled qubit at a given frequency. As the current in the Z-Control changes the qubit frequency, this control channel also transduces the current noise into frequency jittering of the qubit. This random jittering leads to a phase random walk and dephasing of the qubit. For protecting the qubit coherence, a stable DC-bias in the Z-Control can be used to tune to qubit into its flux noise insensitive point corresponding to an extremum in qubit frequency.

Moreover, a Z-Control with fast oscillation can also be used to generate side-bands of a qubit so that the qubit can be accessed at multiple frequencies without having to move the qubit out of its flux noise insensitive point. This AC frequency tuning of a qubit can be further used to generate phase and amplitude controlled qubit-qubit coupling between detuned qubits via their side-bands with a relative phase difference in oscillating Z-Controls. Details of the side-band generation can be understood in the following simple model. Assume that the external magnetic field flux $\Phi_{\text{ex}}(t) = \Phi_{\text{ex}}^0 + A_{\Phi} \cos(\omega_d t)$, the absorption spectrum of the qubit can be derived below from (2.49) to (2.54). Multiple sidebands will be generated at locations detuned by multiples of the driving frequency ω_d . If $\Phi_{\text{ex}}^0 = 0$, with modulation around the flux insensitive point, the sidebands will be at even integer multiples of the flux driving frequency. This parametric modulation of the qubit frequency can be used to quickly tune two qubits into near resonance and perform two qubit gates between two far detuned qubits. This is useful as parametric frequency modulation generates sidebands detuned from the main qubit frequency with detuning depending on the driving frequency instead of the driving amplitude. This makes it possible to access the qubit at frequencies outside the tunability range based on DC flux tuning of the qubit SQUID (even above the maximum qubit frequency at flux insensitive point). The amplitude can be used to tune the coupling rate between two detuned qubits during near resonant interaction. It has also been shown in experiments that para-

metric modulation of the qubit frequency does not significantly degrade the qubit coherence as compared with the degradation caused by DC tuning of the qubit away from its flux insensitive point. The technique can also be used to generate qubit absorption/emission sideband near the readout resonator frequency for an ultra-fast high fidelity readout of the qubit.

$$H(t) = \frac{\hbar}{2} \omega_q(t) \hat{\sigma}_z \quad (2.49)$$

$$\dot{\rho}_q(t) = -\frac{i}{\hbar} [H(t), \rho_q] + \frac{\Gamma_1}{2} (2\sigma_- \rho \sigma_+ - \sigma_+ \sigma_- - \rho \sigma_+ \sigma_-) - \frac{\Gamma_\phi}{4} [\hat{\sigma}_z, [\hat{\sigma}_z, \rho(t)]] \quad (2.50)$$

$$\frac{d}{dt} \langle \sigma_-(t) \rangle = \text{Tr}(\dot{\rho}(t) \sigma_-(t=0)) = \left(-i\omega_q(t) - \frac{\Gamma_1}{2} - \Gamma_\phi \right) \langle \sigma_-(t) \rangle \quad (2.51)$$

Putting (2.49) into (2.50) will lead to (2.51). Following the Quantum Regression Theorem, we can have (2.52).

$$\frac{d}{dt} \langle \sigma_-(t) \sigma_+(0) \rangle = \left(-i\omega_q(t) - \frac{\Gamma_1}{2} - \Gamma_\phi \right) \langle \sigma_-(t) \sigma_+(0) \rangle \quad (2.52)$$

$$\langle \sigma_-(t) \sigma_+(0) \rangle = \exp\left(\left(-\left(\frac{\Gamma_1}{2} + \Gamma_\phi \right) |t| - i \int_0^t \omega_q(\tau) d\tau \right) \right) \quad (2.53)$$

The absorption/emission noise spectrum of the qubit can be shown to be (2.54) with (2.53).

$$\begin{aligned} S[\omega] &= \frac{1}{2\pi} \int_{-\infty}^{\infty} e^{i\omega\tau} \langle \sigma_-(\tau) \sigma_+(0) \rangle \\ &= \frac{1}{2\pi} \int_{-\infty}^{\infty} \exp\left(\left(i\omega\tau - \Gamma_2 |\tau| - i \int_0^\tau \omega_q(s) ds \right) \right) d\tau \end{aligned} \quad (2.54)$$

The final form in (2.54) with $\Gamma_2 = \frac{\Gamma_1}{2} + \Gamma_\phi$ which is the total dephasing rate cannot be further simplified analytically in general. However, the last integration can be easily done numerically for any given form of $\omega_q(t)$ caused by fast Z-Control modulation of the qubit frequency. An example of modulation with $\Phi_{\text{ex}}(t) = A_\Phi \cos(\omega_d t)$ can be calculated to have absorption peaks shown in Fig. 2.13.

The XY-Control and Z-Control together can be used to produce any single qubit gates. Combining single qubit operations together with pulsed frequency control that bring two qubits into resonance for a short time can generate arbitrary two qubit gates. The ability to create arbitrary single and two-qubit gates forms the foundation for universal quantum computing with superconducting transmon qubits.

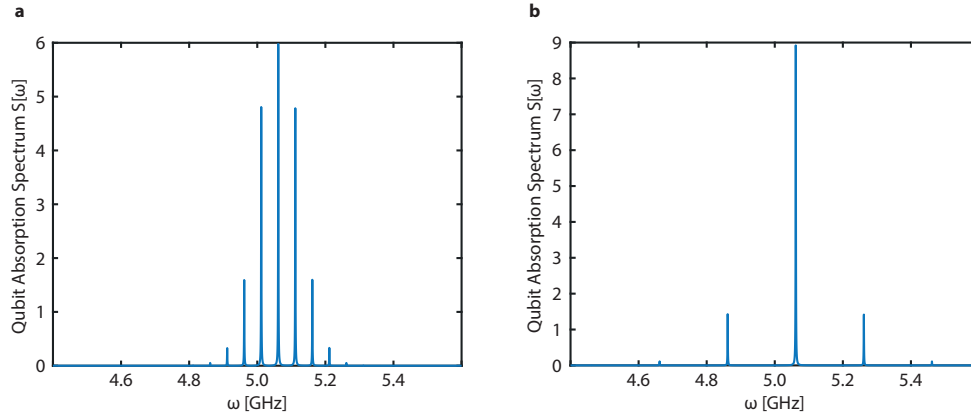


Figure 2.13: **a**, the qubit absorption spectrum with frequency flux modulation tone $\omega_d = 25$ MHz. **b**, the qubit absorption spectrum with frequency flux modulation tone $\omega_d = 100$ MHz.

2.3 Standard Cryogenic System for Measuring and Controlling A Transmon Qubit

2.3.1 Structure and Cooling Process of a Dilution Refrigerator

Superconducting quantum circuits involved in this work operate in the GHz microwave region and have to be cooled to mK temperatures for lowering the thermal microwave photon noise in its environment. In this work, we used the commercial dilution refrigerator (DF) from BlueFors Cryogenics Oy. As it can be seen in this figure, the refrigerator has multiple stages that can be sequentially cooled to different temperatures with different cooling powers. The cooling process for different stages can be better seen in the Fig. 2.14. In this system, the first two stages are directly connected to two cooling stages of a Pulse Tube (PT) cooling system respectively. The cold plate and the mixing chamber plate are thermally connected to the second PT stage with switchable thermal switches. These thermal connections can be disconnected during the cooling process.

Initially, the low temperature stages are thermally connected with the switches to the first two plates connected to the PT. The first stage can be cooled to around 50 K and second stage and lower temperature parts can be further cooled to around 4 K. After the plates and lines in the system are cooled to around 4 K, the thermal switches disconnect lower temperature plates from the 4 K plate connected to the PT. Then, the condensation of gaseous He³/He⁴ mixture starts with starting the compressed gas flow into the Still Line (SL) below the 4 K plate. There is a main flow impedance in the line to partly condense the pressurized gas mixture using the Joule-Thomson

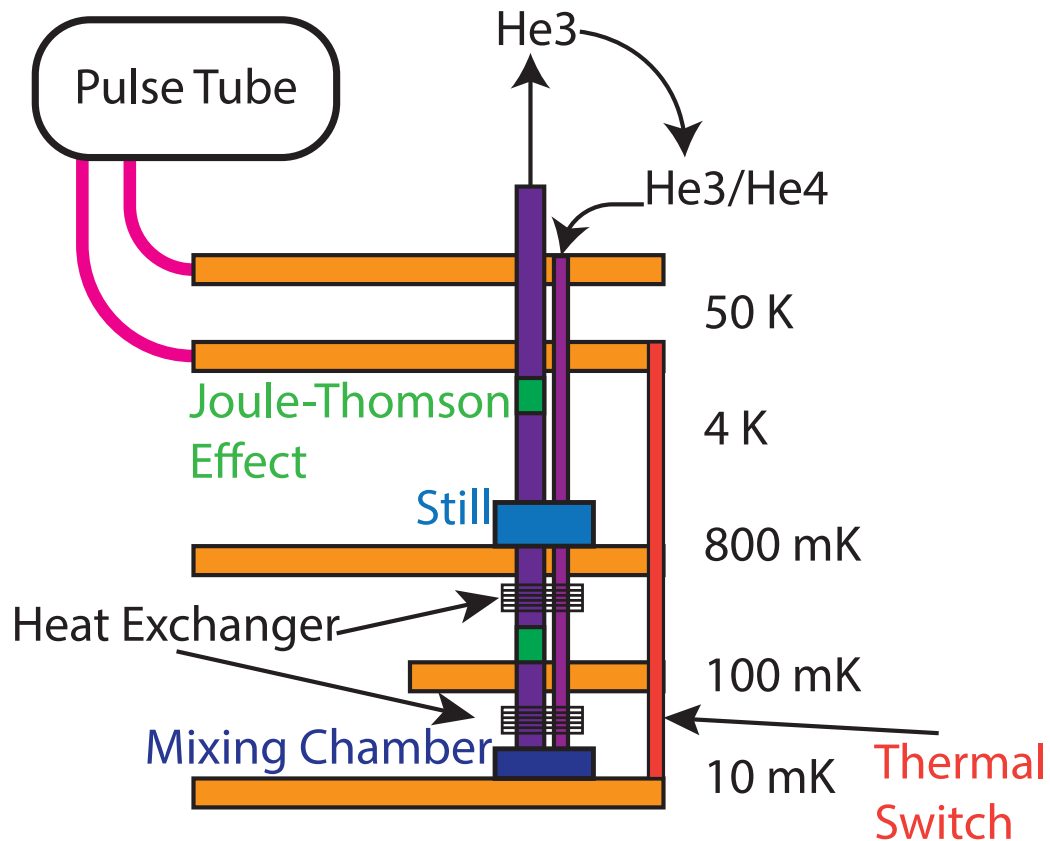


Figure 2.14: The cooling system of a dilution refrigerator.

effect before arriving at the still plate. The condensed liquid He³/He⁴ mixture fills the condensation line and still line below the still plate and mixing chamber. After the condensation is complete with sufficient liquid He³/He⁴ mixture to fill the lines and mixing chamber below the still chamber. The still pumping starts to remove He³ from the system. This evaporative cooling cools the still plate to around 800 mK. At this temperature, the phase separation between He³ and He⁴ phases occurs in the mixing chamber (MC). Due to gravity, heavier pure He⁴ phase liquid region forms at the bottom of the mixing chamber. The He³ phase liquid forms above the He⁴ rich region in the still line. Due to the pumping on the still chamber, He³ constantly diffuses across the phase boundary between the He⁴ and He³ condensed regions in MC. The He³ then replenishes the still chamber and gets pumped away by still

pumping. The pumped He3 is returned back into the condensation line and dilution unit of the fridge so that the cooling cycle is completed. The He3 diffusion across the boundary into He4 region takes away the thermal energy and cools the mixing chamber to below 10 mK.

2.3.2 Cryogenic Setup for Controlling and Measuring Superconducting Qubits

A typical circuit diagram for controlling and measuring a superconducting qubits is shown in Fig. 2.15. For all the control lines, attenuators were used to attenuate noises propagating from room temperature environment into the fridge. They serve as thermal anchoring points that dump high temperature electromagnetic noises onto the cooled plates along the way. They also re-emit Johnson–Nyquist electronic noises at their ambient temperature down the line into the lower temperature stages where other attenuators are located. Here are also band-pass filters on the lines to filter out thermal noises with irrelevant frequencies. The XY-Drive line has a band-pass filter around the qubit resonance and is heavily attenuated as electromagnetic waves resonant with the qubit can propagate on the line and this can be a direct energy relaxation channel for the controlled qubit. The cost for having larger attenuation on the XY line is increased signal power which may cause heating issues, as the attenuators also dissipate the excess energy into its environment that has finite cooling power. The low pass filter on the Z-control line is used to block higher frequency noises that may act as dephasing noise to the qubit. The readout input line is also heavily attenuated and filtered around the readout resonator frequency. Thermal photon population in the readout resonator can also dephase qubit via the dispersive coupling effect. A larger readout pump is thus needed to achieve sufficient readout photon number in order to have fast and high fidelity readout. The output line of the readout loop goes through amplifiers instead of attenuators because projective measurement quantum signals are weak and sufficient photons need to be collected to achieve acceptable signal-noise-ratio (SNR). The amplifier is like the attenuators that also add its own thermal noise to its output line. Thus it is ideal to achieve the smallest added noise power as possible. The smallest added noise power is half quanta of photon energy at the readout frequency. The amplifier needs to be located to low temperature stages near the superconducting chip. In our system, as the first amplifier, we used a Traveling-Wave-Parametric-Amplifier from the Lincoln Lab to amplify the output readout signal to the quantum limit at the mixing chamber plate. There is also a low temperature High Electron Mobility Transistor (HEMT) amplifier located at the 50 K stage. Even though it is ideal to

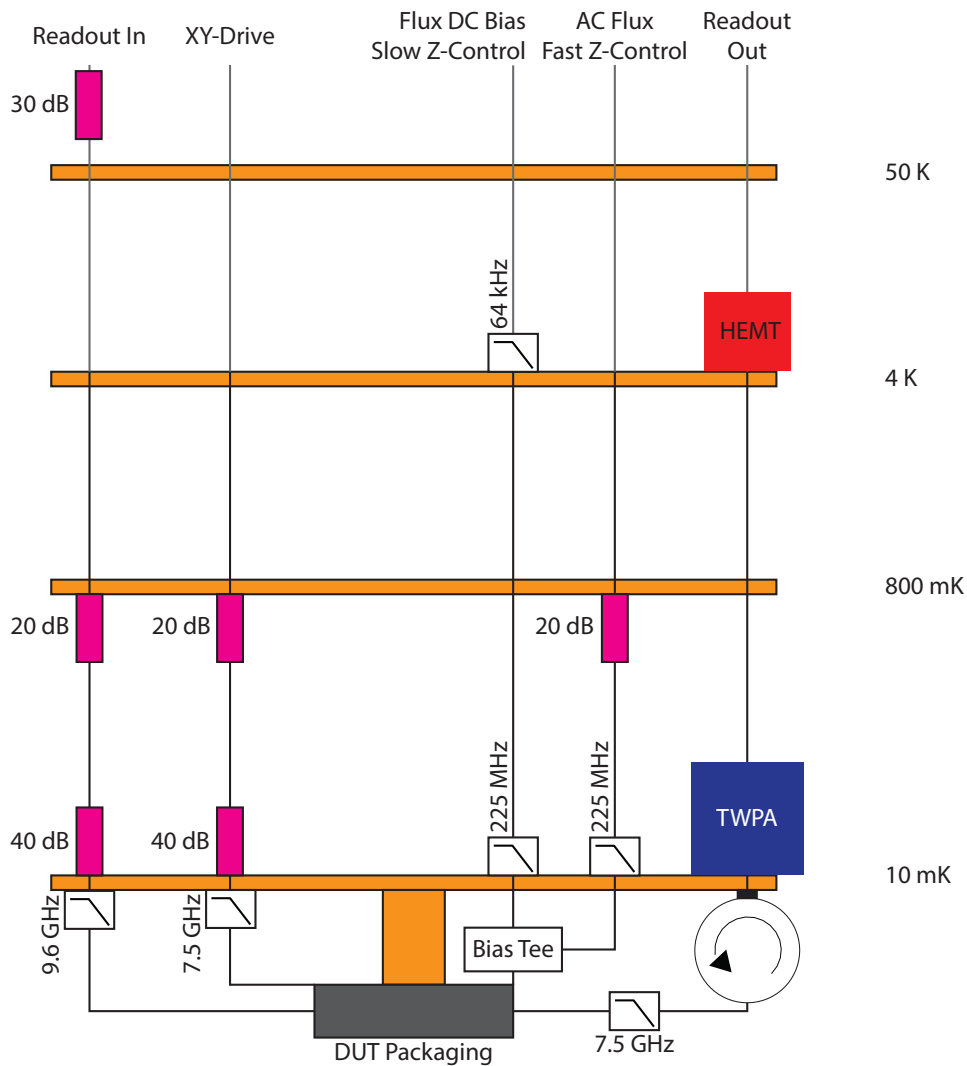


Figure 2.15: The standard wiring of microwave and DC lines used to control and measure superconducting qubits used. The pink boxes are attenuators that are used to dissipate higher temperature radiation noises propagating from higher temperature stages and room temperature electronics. They absorb the incoming noise and re-emit Johnson–Nyquist noise corresponding to their ambient temperatures down the line into lower temperature stages. There are also filters used to filter out noise power outside the frequency range of interest. The circulator on the mixing chamber stage forbids the backward transmission of high temperature noise back into the device under test while allowing the readout signal to be transmitted out. The output readout signal is then amplified by the Traveling-Wave-Parametric-Amplifier (TWPA) from Lincoln Lab to amplify the signal to the quantum limit. This significantly increases the signal-to-noise (SNR) of the qubit measurements for a given number of averages. The quantum-limit amplified readout out signal then goes through a low temperature High-Electron-Mobility-Transistor Amplifier (HEMT) on the 4 K stage before leaving the DF and being further amplified by room temperature amplifiers and digitized.

locate the amplifiers at lower temperature stages to minimize added thermal noise, the cooling power at lower temperature stages is significantly lower. Amplifiers also dissipate a larger amount of heat to its environment, a higher cooling power is needed to avoid heating up the stage. The output readout signal is further amplified by room temperature amplifiers before being digitized by our digitizer. The readout output line also back propagates noise into the lower temperature stages. This noise power is also blocked from going back to the superconducting quantum chip by the circulators that unidirectionally transmit the output readout signal and dump inversely propagating noise into their cryogenic ambient environment.

Chapter 3

**SYNTHESIZED CRYSTALS FOR ENGINEERING
PROPAGATION OF LIGHT AND MECHANICAL WAVES**

It has long been known that electronic waves in a periodic potential can have a nontrivial dispersion relation that processes gaps in allowed frequencies for the propagating waves. Such gaps are often called electronic bandgaps and dielectric materials that processes such gaps are called semiconductors, widely used in building today's electronics. The electronic wave dispersion can be calculated by solving the Schrodinger's equation for electrons in a solid, shown in (3.1).

$$\left(-\frac{\hbar^2}{2m_e}\nabla^2 + V(\vec{r})\right)\Psi(\vec{r}) = E\Psi(\vec{r}) \quad (3.1)$$

This equation has a periodic potential term $V(\vec{r}) = V(\vec{r} + \vec{R})$, where \vec{R} is a displacement vector that the crystal structure is invariant with respect to it. The discrete translation symmetry can be utilized to simplify the Schrodinger's equation using the Bloch's theorem that the solutions of (3.1) can be written into the form in (3.2).

$$\Psi(\vec{r}) = \psi(\vec{r}) \exp(-i\vec{k} \cdot \vec{r}) \quad (3.2)$$

$$\vec{k} \cdot \vec{R} = 2\pi n \text{ where } n \in Z \quad (3.3)$$

$$\psi(\vec{r}) = \psi(\vec{r} + \vec{R}) \quad (3.4)$$

(3.1) can be reduced into (3.5) with periodic boundary conditions on the boundaries of an unit cell which is the basic repeating structure of a crystal.

$$\left(\frac{\hbar^2}{2m_e}(-i\nabla + \vec{k})^2 + V(\vec{r})\right)\psi(\vec{r}) = E(\vec{k})\psi(\vec{r}) \quad (3.5)$$

For each given \vec{k} , there is a series of eigen-energies corresponding to eigen-solutions of (3.5). These eigen-energies can be labelled from the lowest energy up with an integer $n \in Z$ such that the n-th eigen-mode of (3.5) for a given \vec{k} has energy $E_n(\vec{k})$. This means that the n-th mode's energy is a function of \vec{k} as a continuous variable. The continuous curve formed by the n-th eigen-mode corresponding to different \vec{k}

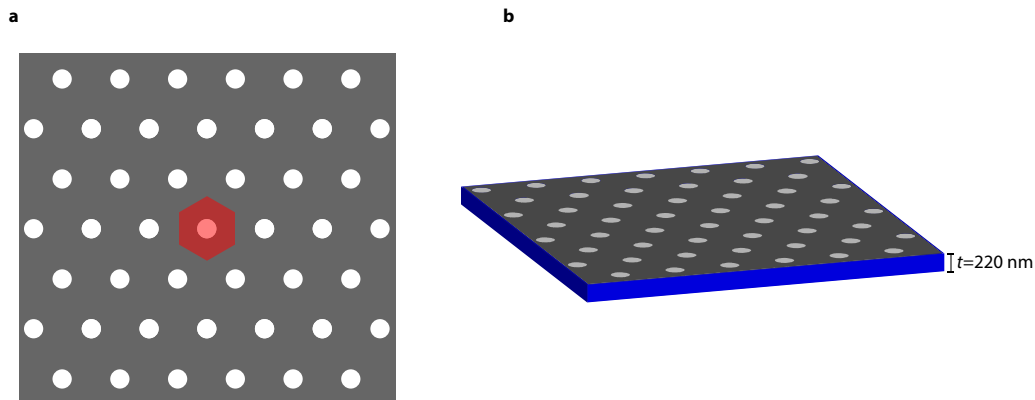


Figure 3.1: **a**, a 2D photonic crystal with hexagonal unit cell highlighted in the red region. **b**, the photonic crystal is created with by etching holes in a suspended silicon membrane with thickness $t = 220$ nm.

is called a band. All the bands formed by all the eigen-modes collectively form the electronic bandstructure of the material. As it has already been seen in various semiconductor materials, bandstructures of certain periodic potentials can host gaps in the energy meaning that no eigen-modes can be found for range of electron energy. These gaps intuitively indicate that electronic waves with certain energy are not allowed to propagate in the crystal.

Moreover, this phenomena is not unique to electronic waves in crystals with periodic potentials and it is fundamentally a result of discrete translation symmetry of the Hamiltonian. This means that other waves propagating in a medium with discrete translation symmetry can also process nontrivial dispersion relation (bandstructure) with bandgaps.

3.1 Photonic Crystal

Electromagnetic waves in a periodically patterned dielectric structure like the periodically patterned suspended silicon membrane in Fig. 3.1 is engineered to tailor the dispersion of electromagnetic waves in optical domain to have bandgap that prohibit propagation of light in certain frequency range. This artificially synthesized material which is also called photonic crystal and the electromagnetic wave equation in such periodic structures can be described by (3.8) in a unit cell highlighted as the

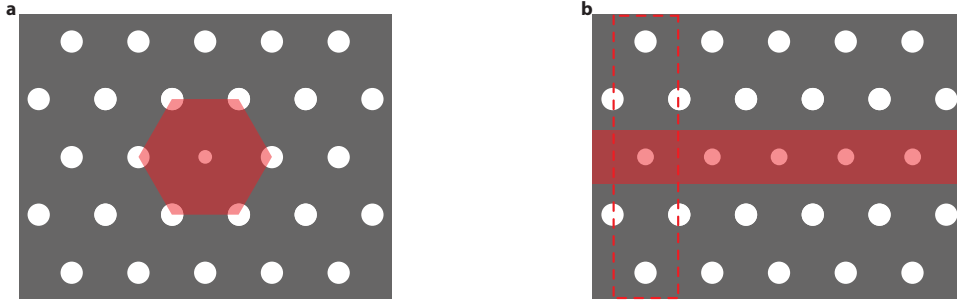


Figure 3.2: **a**, photonic point defect cavity with the defect cavity region highlighted in red. **b**, a periodic translation of the defect region in one direction can create a photonic waveguide that route the optical waves with a tailored dispersion.

red region in Fig. 3.1a with Bloch waves for electromagnetic fields in (3.7).

$$\nabla \times \frac{1}{\epsilon(\vec{r})} (i\vec{k} + \nabla) \times \vec{H} = \left(\frac{\omega}{c}\right)^2 \vec{H} \quad (3.6)$$

$$\vec{H} = \vec{h}(\vec{r}) \exp(-i\vec{k} \cdot \vec{r}) \quad (3.7)$$

$$(-i\nabla + \vec{k}) \times \frac{1}{\epsilon(\vec{r})} (-i\nabla + \vec{k}) \times \vec{h} = -\left(\frac{\omega(\vec{k})}{c}\right)^2 \vec{h} \quad (3.8)$$

Structure in Fig. 3.1 has a bandstructure with a wide gap. This gap indicates that optical wave with frequency inside the gap can not propagate in the membrane. Photonic crystals with locally broken translation symmetry can be used to guide and trap light on a microchip. Light can be trapped in the crystal by creating a small region on the crystal that breaks the translation symmetry locally. This small region, if designed properly, can support modes of light with frequency forbidden from propagation in the bulk of the crystal. In this way, an optical cavity is created in this region with the rest of the photonic crystal acting as mirrors. As can be seen, this confinement can be engineered easily with current nanofabrication techniques to only hold a single fundamental mode of light with an ultra-small mode volume that can be used to strongly couple light to matters like atoms and mechanical mode in the cavity region.

3.1.1 Photonic Waveguide and Photonic Defect Cavity

A waveguide for routing light with engineered dispersion can be made by breaking the discrete translation symmetry in a region to support wave propagation at a certain frequency in the bandgap of the bulk of the crystal as shown in Fig. 3.2b with

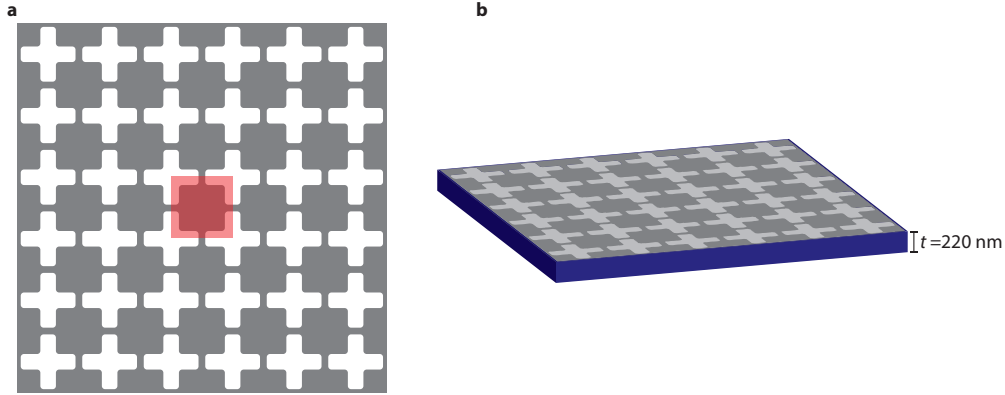


Figure 3.3: **a**, a 2D phononic crystal with a square unit cell highlighted in the red region. **b**, the photonic crystal is created with by etching the unit cell patterns in a suspended silicon membrane with thickness $t = 220$ nm.

the red region. The waveguide band structure can be obtained by looking at an unit cell with periodicity along the propagation direction as highlighted by the dashed red box in Fig. 3.2**b**. By changing the hole dimensions in the middle of the unit cell, a specific band can be moved into the bandgap.

Similar to engineering the photonic waveguide in a photonic crystal where a waveguide is built by locally breaking the crystal's discrete translation symmetry in one direction, an optical cavity can be created by breaking the crystal's discrete translation symmetry in all directions as in the red region of Fig. 3.2**a**. The cavity is introduced with an intentionally introduced point defect region.

3.2 Phononic Crystal

An engineered periodic structure can also be used in trapping and guiding mechanical waves propagating in solids. Periodically patterned solid can also have nontrivial bandstructure and bandgaps that prohibits the propagation of strain wave in certain frequency range. The dynamics and bandstructure of mechanical waves in the structure can be calculated with the frequency domain strain wave eigen-equation in (3.10) derived from the time-domain strain-wave equation in (3.9).

$$\frac{1}{\rho(\vec{r})} \nabla_j C_{ijmn}(\vec{r}) \nabla_n Q_m(\vec{r}, t) = \frac{\partial^2}{\partial t^2} Q_i(\vec{r}, t) \quad (3.9)$$

$$\frac{1}{\rho(\vec{r})} \nabla^T \left(C(\vec{r}) \nabla \vec{Q}(\vec{r}) \right) = \omega^2 \vec{Q}(\vec{r}) \quad (3.10)$$

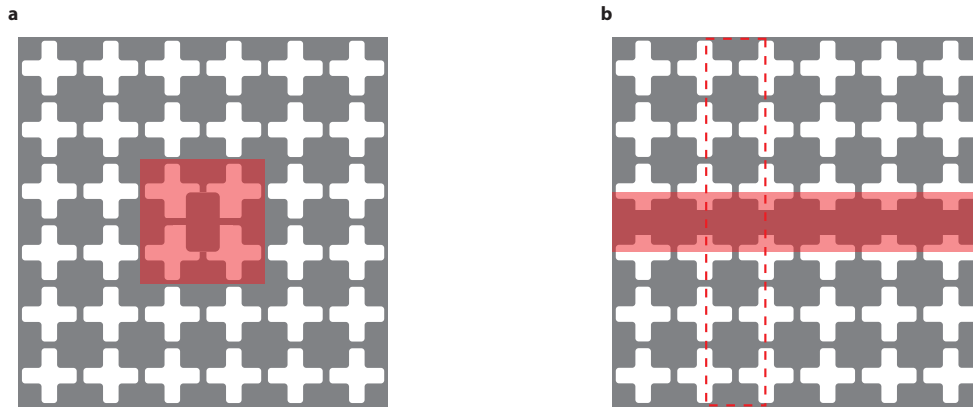


Figure 3.4: **a**, phononic point defect cavity with the defect cavity region highlighted in red. **b**, a periodic translation of the defect region in one direction can create a mechanical waveguide that route the optical waves with a tailored dispersion.

This type of engineered material is called phononic crystal and an example of it is shown in Fig. 3.3 which is a patterned suspended silicon membrane. For the suspended silicon membrane used in this work, its thickness is 220 nm and this is effectively a two-dimensional material for mechanical wave with frequency below 10 GHz as such waves' wavelength is much larger than the membrane thickness. The shown two-dimensional phononic crystal with a square unit cell highlighted in the red region has a two-dimensional acoustic phonon bandstructure illustrated in Fig. 3.5a. The region highlighted in the Fig. 3.5a is a phononic bandgap around 5 GHz. If a defect region is created in the phononic crystal that can support mechanical vibration with frequency in the bandgap as shown with a red region in Fig. 3.4a, this defect region forms a phononic crystal defect cavity and the surrounding bulk of the phononic crystal acts as mechanical mirror that confines the mode into the defect region. In contrary to the photonic crystal cavity case where loss due to photon scattering off the two-dimensional structure into free space is possible, as there is a continuum of three-dimensional electromagnetic density of states around the structure, bandgap for the mechanical waves is truly three-dimensional as mechanical waves of any frequency can not propagate in vacuum around the structure. This true three-dimensional confinement forms the basis of realizing nano-mechanical GHz resonators with unprecedented quality factor around 50 billion at cryogenic environment which will be discussed later in this work.

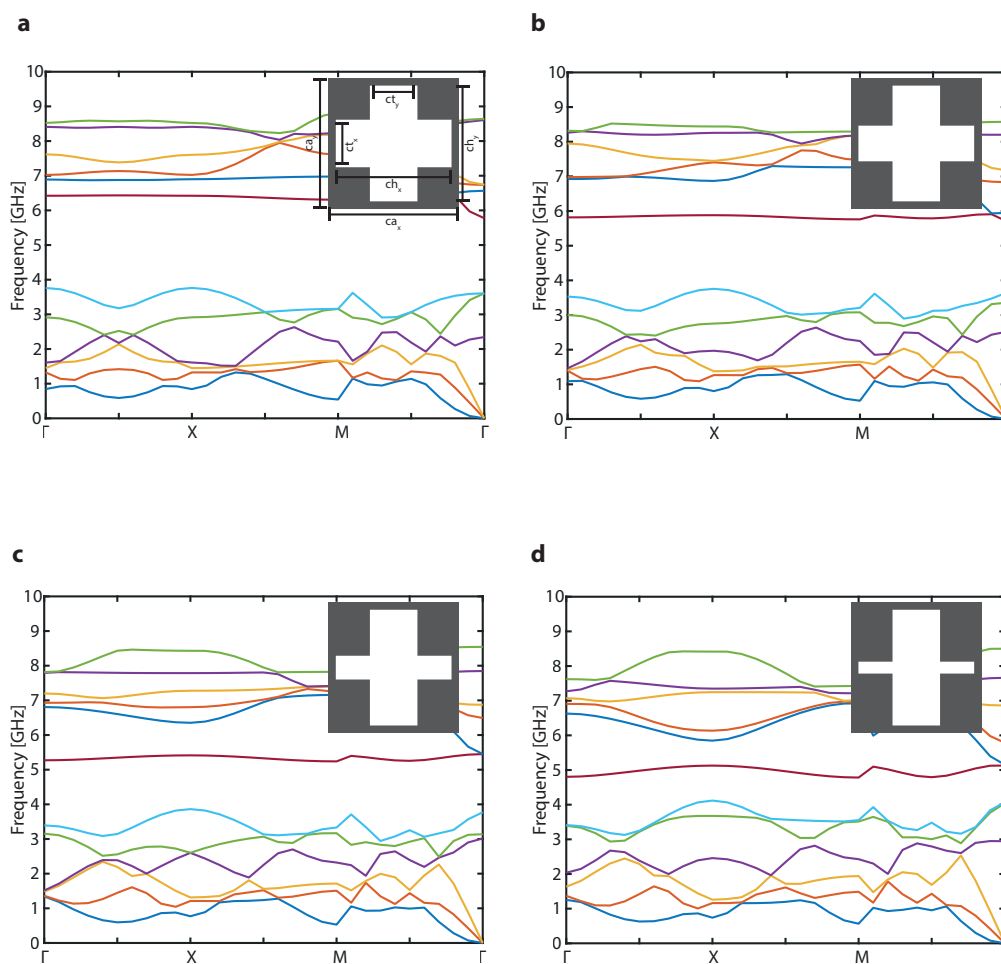


Figure 3.5: **a** The phononic bandstructure corresponding to the nominal phononic unit cell in the inset. For the nominal unit cell we have $ct_{x,y} = 200$ nm, $ch_{x,y} = 487$ nm, $ca_{x,y} = 550$ nm. The other unit cells in **b** – **d** have different ct_x values. **b**, the phononic bandstructure with $ct_x = 150$ nm. **c**, the phononic bandstructure with $ct_x = 100$ nm. **d**, the phononic bandstructure with $ct_x = 50$ nm. It can be seen that the red-band is moved down into the bandgap region of the nominal phononic crystal in the bulk of the membrane. Mechanical modes with frequency around 5 GHz can be supported by a defect region in a nominal phononic crystal for applications in constructing phononic waveguides and defect cavities.

3.2.1 Phononic Waveguide

Just like the methods used for designing a waveguide in a photonic crystal, a phononic waveguide that guides the on-chip propagation of mechanical waves with tailored dispersion can be realized via breaking the discrete translation symmetry of the phononic crystal in direction orthogonal to the desired propagation direction as in the example shown in Fig. 3.4b with the red dashed box highlighted unit cell that preserves the discrete translation symmetry along the desired mechanical wave propagation direction. The ability to engineering mechanical waveguides on a chip enables wiring various different quantum objects on a chip via mechanical waves as mechanical coupling is a type of universal coupling for creating hybrid quantum systems. For example, coupling between two optical cavities can be mediated via a mechanical waveguide.

As mechanical waves in GHz have short wavelengths in micrometers and phononic waveguides confine the propagation to only the waveguide region, this also provides the possibility of scaling up spin based quantum computing chips without increasing cross talks between qubits that ultimately limit the fidelity of quantum operations on a scaled up chip with more than a hundred integrated qubits.

3.2.2 Phononic Defect Cavity

A cavity that localizes mechanical vibration modes can be realized by breaking all translation symmetry of the crystal bulk in a local region as in the red region of Fig. 3.4a. The region, similar to the photonic case, is called the defect region of the photonic crystal and the cavity formed in this way is always called photonic defect cavity. To understand the symmetry, size, and frequency of the modes localized in the defect region, it is helpful to study the "bandstructure" of the phononic defect region. This means that we can start by looking at the bandstructure corresponding to a phononic crystal formed by periodic translation of the defect region on the suspended membrane. The "bandstructure" of the phononic crystal defect region can be seen in Fig. 3.5 with the bandgap of the bulk of the phononic crystal outside the defect region highlighted in the red. The parts of the defect region bands in the bulk bandgap region forms the localized modes in the cavity. Qualitatively, each localized mode can be viewed as a standing wave formed by the superposition of the propagating modes of a certain band trapped in the bulk bandgap region. Thus, as more of a defect band get trapped in the bandgap region, the smaller and more localized the defect cavity mode corresponding to that band is going to be.

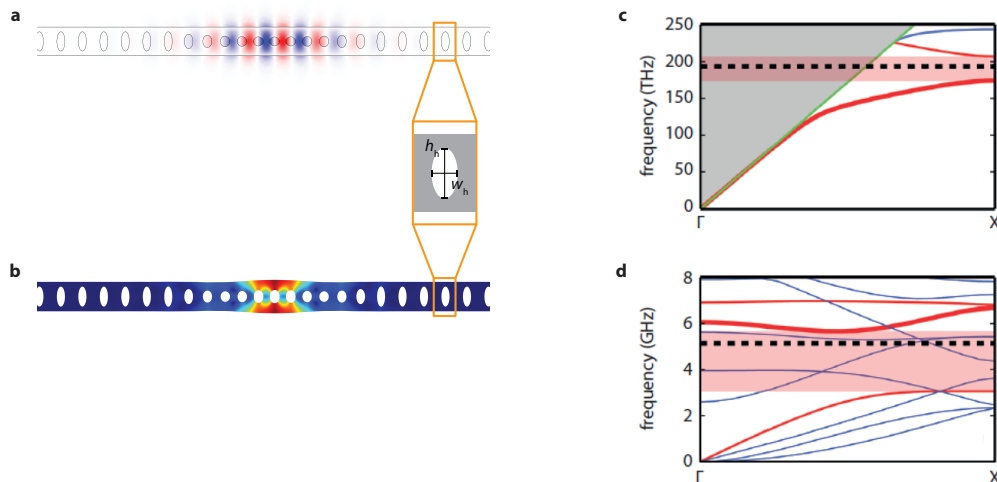


Figure 3.6: These are examples from Jasper Chan’s Ph.D. thesis. **a**, the fundamental optical mode (195 THz) field that is co-localized with the fundamental mechanical mode around 5.1 GHz with the breathing deformation profile in **b**. **c**, the optical bandstructure of the 1D photonic crystal in the mirror (bulk) region of the 1D photonic nanobeam. **d**, the mechanical bandstructure of the 1D phononic crystal in the mirror (bulk) region of the 1D phononic nanobeam realized with the same unit cell shown in **a** and **b**. The bandgaps are highlighted in the red regions of **c** and **d**. The optical and mechanical cavities mode frequencies are highlighted in **c** and **d** in the bandgap regions with dashed black lines.

This can be argued from the perspective that the real space trapped mode profile is qualitatively a Fourier transform from the trapped band in the momentum space (\vec{k} -space) to the real position space.

3.3 Opto-mechanical Crystal

As mentioned previously, optical and mechanical waves can be localized by properly designed periodically patterned structures. In particular, in this work, a two-dimensional silicon based membrane can be used to co-localize light and mechanical waves in a defect region if their wavelengths are comparable. For example, a 5 GHz mechanical wave has wavelength around $2 \mu\text{m}$ and a C-band optical field in the silicon photonic substrate has wavelength around $1 \mu\text{m}$. Since the optomechanical interaction is a radiation pressure interaction that is proportional to the intensity of the optical field and displacement of the mechanical oscillator. A fundamental mechanical mode is about a half-wavelength long that matches the full wavelength fundamental optical mode as shown in the Fig. 3.6 [17].

TIME SYMMETRY BREAKING WITH SYNTHETIC GAUGE FIELD FOR UNIDIRECTIONAL PHOTON ROUTING

Synthetic magnetism has been used to control charge neutral excitations for applications ranging from classical beam steering to quantum simulation. In optomechanics, radiation-pressure-induced parametric coupling between optical (photon) and mechanical (phonon) excitations may be used to break time-reversal symmetry, providing the prerequisite for synthetic magnetism. Here we design and fabricate a silicon optomechanical circuit with both optical and mechanical connectivity between two optomechanical cavities. Driving the two cavities with phase-correlated laser light results in a synthetic magnetic flux, which in combination with dissipative coupling to the mechanical bath leads to nonreciprocal transport of photons with 35 dB of isolation. Additionally, optical pumping with blue-detuned light manifests as a particle non-conserving interaction between photons and phonons, resulting in directional optical amplification of 12 dB in the isolator through direction. These results indicate the feasibility of utilizing optomechanical circuits to create a more general class of nonreciprocal optical devices, and further to enable novel topological phases for both light and sound on a microchip.

Synthetic magnetism involving charge neutral elements such as atoms [26], polaritons [65, 105, 118], and photons [127, 50, 36, 101, 126] is an area of active theoretical and experimental research, driven by the potential to simulate quantum many-body phenomena [71], reveal new topological wave effects [100, 72], and create defect-immune devices for information communication [50, 126]. Optomechanical systems [11], involving the coupling of light intensity to mechanical motion via radiation pressure, are a particularly promising venue for studying synthetic fields, as they can be used to create the requisite large optical nonlinearities [103]. By applying external optical driving fields time-reversal symmetry may be explicitly broken in these systems. It was predicted that this could enable optically tunable nonreciprocal propagation in few-port devices [76, 49, 48, 132], or in the case of a lattice of optomechanical cavities, topological phases of light and sound [95, 114]. Here we demonstrate a generalized form of optical nonreciprocity in a silicon optomechanical crystal circuit [38] that goes beyond simple directional propagation; this is achieved using a combination of synthetic magnetism, reservoir engineering,

and parametric squeezing.

Distinct from recent demonstrations of optomechanical nonreciprocity in degenerate whispering-gallery resonators with inherent nontrivial topology [62, 116, 107], we employ a scheme similar to that proposed in Refs. [48, 114] in which a synthetic magnetic field is generated via optical pumping of the effective lattice formed by coupled optomechanical cavities. In such a scenario, the resulting synthetic field amplitude is set by the spatial variation of the pump field phase and the field lines thread optomechanical plaquettes between the photon and phonon lattices (see Fig. 4.1). To achieve nonreciprocal transmission of intensity in the two-port device of this work i.e., bonafide phonon or photon transport effects, not just nonreciprocal transmission phase – one can combine this synthetic field with dissipation to implement the general reservoir engineering strategy outlined in Ref. [82]. This approach requires one to balance coherent and dissipative couplings between optical cavities. In our system the combination of the optical drives and mechanical dissipation provide the “engineered reservoir” which is needed to mediate the required dissipative coupling.

To highlight the flexibility of our approach, we use it to implement a novel kind of nonreciprocal device exhibiting gain [2, 3]. By using an optical pump which is tuned to the upper motional sideband of the optical cavities, we realize a two-mode squeezing interaction which creates and destroys photon and phonon excitations in pairs. These particle non-conserving interactions can be used to break time-reversal symmetry in a manner that is distinct from a standard synthetic gauge field. In a lattice system, this can enable unusual topological phases and surprising behavior such as protected chiral edge states involving inelastic scattering [94] and amplification [93]. Here, we use these interactions along with our reservoir-engineering approach to create a cavity-based optical directional amplifier: backward propagating signals and noise are extinguished by 35 dB relative to forward propagating waves which are amplified with an internal gain of 12 dB (1 dB port-to-port).

The optomechanical system considered in this work is shown schematically in Fig. 4.1a and consists of two interacting optomechanical cavities, labeled L (left) and R (right), with each cavity supporting one optical mode $O_{L(R)}$ and one mechanical mode $M_{L(R)}$. Both the optical and mechanical modes of each cavity are coupled together via a photon-phonon waveguide, resulting in optical and mechanical inter-cavity hopping rates of J and V , respectively (here we choose a local definition of the cavity amplitudes so both are real). The radiation pressure interaction between

the co-localized optical and mechanical modes of a single cavity can be described by a Hamiltonian $\hat{\mathcal{H}} = \hbar g_0 \hat{a}^\dagger \hat{a} (\hat{b} + \hat{b}^\dagger)$, where $\hat{a}(\hat{b})$ is the annihilation operator of the optical (mechanical) mode and g_0 is the vacuum optomechanical coupling rate [11] (here we have omitted the cavity labeling).

To enhance the effective photon-phonon interaction strength each cavity is driven by an optical pump field with frequency relatively detuned from the optical cavity resonance by the mechanical frequency ($\Delta \equiv \omega_p - \omega_c \approx \pm\omega_m$), with a resulting intra-cavity optical field amplitude $|\alpha|e^{i\phi}$. In the good-cavity limit, where $\omega_m \gg \kappa$ (κ being the optical cavity linewidth), spectral filtering by the optical cavity preferentially selects resonant photon-phonon scattering, leading to a linearized Hamiltonian with either a two-mode squeezing form $\hat{\mathcal{H}}_{\text{ent}} = \hbar G (e^{i\phi} \hat{d}^\dagger \hat{b}^\dagger + e^{-i\phi} \hat{d} \hat{b})$ (blue detuned pumping) or a beamsplitter form $\hat{\mathcal{H}}_{\text{ex}} = \hbar G (e^{i\phi} \hat{d}^\dagger \hat{b} + e^{-i\phi} \hat{d} \hat{b}^\dagger)$ (red detuned pumping). Here $G = g_0 |\alpha|$ is the parametrically enhanced optomechanical coupling rate and $\hat{d} = \hat{a} - \alpha$ contains the small signal sidebands of the pump. For both cases the phase of the resulting coupling coefficient is nonreciprocal in terms of the generation and annihilation of photon-phonon excitations. As has been pointed out before, such a nonreciprocal phase resembles the Peierls phase that a charged particle accumulates in a magnetic vector potential [35]. Crucially, the relative phase $\Phi_B = \phi_L - \phi_R$ is gauge independent (i.e. independent of local redefinitions of the \hat{a} and \hat{b} cavity amplitudes), implying it should have an observable effect. In the simple case of $\Delta = -\omega_m$, Φ_B is formally equivalent to having a synthetic magnetic flux threading the plaquette formed by the four coupled optomechanical modes (two optical and two mechanical) [36, 48, 114]. For $\Delta = +\omega_m$, a non-zero Φ_B still results in the breaking of time-reversal symmetry, though the lack of particle number conservation means that it is not simply equivalent to a synthetic gauge field. Nonetheless, we will refer to it as a flux in what follows for simplicity.

To detect the presence of the effective flux Φ_B , consider the transmission of an optical probe signal, on resonance with the optical cavity resonances and coupled in from either the left or the right side via external optical coupling waveguides as depicted in Fig. 4.1b. The probe light can propagate via two different paths simultaneously: (i) direct photon hopping between cavities via the connecting optical waveguide, and (ii) photon-phonon conversion in conjunction with intervening phonon hopping via the mechanical waveguide between the cavities. As in the Aharonov-Bohm effect for electrons [5], the synthetic magnetic flux set up by the phase-correlated optical pump beams in the two cavities causes a flux-dependent

interference between the two paths. We define the forward (backward) transmission amplitude as $T_{R \rightarrow L(L \rightarrow R)} \equiv d_{\text{out},L(R)}/d_{\text{in},R(L)}$, where $d_{\text{out(in)}}$ is the amplitude of the outgoing (incoming) electromagnetic signal field in the corresponding coupling waveguide in units of square root of photon flux. The optical transmission amplitude in the forward direction has the general form

$$T_{L \rightarrow R}[\omega; \Delta = \pm\omega_m] = A_{\pm}[\omega] \left(J - \Gamma_{\pm}[\omega] e^{-i\Phi_B} \right), \quad (4.1)$$

where $\omega \equiv \omega_s - \omega_p$ and ω_s is the frequency of the probe light. Γ_{\pm} is the amplitude of the effective mechanically-mediated coupling between the two optical cavities, and is given by

$$\Gamma_{\pm}[\omega] = \frac{VG_L G_R}{(-i(\omega \pm \omega_{mL}) + \frac{\gamma_{iL}}{2})(-i(\omega \pm \omega_{mR}) + \frac{\gamma_{iR}}{2}) + V^2}. \quad (4.2)$$

The prefactor $A_{\pm}[\omega]$ in Eq. (4.1) accounts for reflection and loss at the optical cavity couplers, as well as the mechanically-induced back-action on the optical cavities. This prefactor is independent of the transmission direction, and for the reverse transmission amplitude $T_{R \rightarrow L}$, only the sign in front of Φ_B changes.

The directional nature of the optical probe transmission may be studied via the frequency-dependent ratio

$$\left(\frac{T_{L \rightarrow R}}{T_{R \rightarrow L}} \right) [\omega; \Delta = \pm\omega_m] = \frac{J - \Gamma_{\pm}[\omega] e^{-i\Phi_B}}{J - \Gamma_{\pm}[\omega] e^{+i\Phi_B}}. \quad (4.3)$$

Although the presence of the synthetic flux breaks time-reversal symmetry, it does not in and of itself result in nonreciprocal photon transmission magnitudes upon swapping input and output ports [28, 82]. In our system, if one takes the limit of zero intrinsic mechanical damping (i.e. $\gamma_{ik} = 0$), the mechanically-mediated coupling amplitude $\Gamma_{\pm}[\omega]$ is real at all frequencies. This implies $|T_{L \rightarrow R}| = |T_{R \rightarrow L}|$, irrespective of the value of Φ_B . We thus find that non-zero mechanical dissipation will be crucial in achieving any non-reciprocity in the magnitude of the optical transmission amplitudes.

The general reservoir-engineering approach to nonreciprocity introduced in Ref. [82] provides a framework for both understanding and exploiting the above observation. It demonstrates that nonreciprocity is generically achieved by balancing a direct (Hamiltonian) coupling between two cavities against a dissipative coupling of the

cavities; such a dissipative coupling can arise when both cavities couple to the same dissipative reservoir. The balancing requires both a tuning of the magnitude of the coupling to the bath, as well as a relative phase which plays a role akin to the flux Φ_B . In our case, the damped mechanical modes can play the role of the needed reservoir, with the optical drives controlling how the optical cavities couple to this effective reservoir. One finds that at any given frequency ω , the mechanical modes induce both an additional coherent coupling between the two cavities (equivalent to an additional coupling term in the Hamiltonian) as well as a dissipative coupling (which is not describable by a Hamiltonian). As is shown explicitly in App. 4.2, in the present setting these correspond directly to the real and imaginary parts of $\Gamma_{\pm}[\omega]$. Hence, the requirement of having $\text{Im } \Gamma[\omega] \neq 0$ is equivalent to requiring a non-zero mechanically-mediated dissipative coupling between the cavities.

Achieving directionality requires working at a frequency where the dissipative coupling has the correct magnitude to balance the coherent coupling J , and a tuning of the flux Φ_B . For $|\Gamma_{\pm}[\omega]| = J$ and $\arg(\Gamma_{\pm}) = -\Phi_B (\neq 0, \pi)$, one obtains purely uni-directional transport where the right optical cavity is driven by the left optical cavity but not vice versa. One finds from Eq. (4.3) that the mechanically-mediated dissipative coupling between the cavities is maximized at frequencies near the mechanical normal mode frequencies $\omega \approx -\omega_m \pm V$; to achieve the correct magnitude of coupling, the optical pumping needs to realize a many-photon optomechanical coupling $G_k \approx (J\gamma_{ik})^{1/2}$ (see App. 4.2 for details). Note that our discussion applies to both the choices of red-detuned and blue-detuned pumping. While the basic recipe for directionality is the same, in the blue-detuned pump case the effective reservoir seen by the cavity modes can give rise to negative damping, with the result that the forward transmission magnitude can be larger than one. We explore this more in what follows.

In order to realize the optomechanical circuit depicted in Fig. 4.1 we employ the device architecture of optomechanical crystals [33, 108, 44], which allows for the realization of integrated cavity-optomechanical circuits with versatile connectivity and cavity coupling rates [109, 38]. Figure 4.2a shows the optomechanical crystal circuit fabricated on a silicon-on-insulator microchip. The main section of the circuit, shown zoomed-in in Fig. 4.2b, contains two optomechanical crystal nanobeam cavities, each of which has an optical resonance of wavelength $\lambda \approx 1530$ nm and a mechanical resonance of frequency $\omega_m/2\pi \approx 6$ GHz. The two optical cavities can be excited through two separate optical coupling paths, one for coupling to the left

cavity and one for the right cavity. Both the left and right optical coupling paths consist of an adiabatic fiber-to-chip coupler which couples light from an optical fiber to a silicon waveguide, and a near-field waveguide-to-cavity reflective coupler. This allows separate optical pumping of each cavity and optical transmission measurements to be carried out in either direction. The two nanobeam cavities are physically connected together via a central silicon beam section which is designed to act as both an optical waveguide and an acoustic waveguide. The central beam thus mediates both photon hopping and phonon hopping between the two cavities even though the cavities are separated by a distance much larger than the cavity mode size [112, 38]. The numerically simulated mode profiles for the localized cavities and the connecting waveguide are shown in Fig. 4.2c and 4.2d, respectively. The hopping rate for photons and phonons can be engineered by adjusting the number and shape of the holes in the mirror section of the optomechanical crystal cavity along with the free-spectral range of the connecting waveguide section [38]. Here we aim for a design with $J/2\pi \approx 100$ MHz and $V/2\pi \approx 3$ MHz so that nonreciprocity can be realized at low optical pump power, yet still with high transmission efficiency.

As will be presented elsewhere [39], the optical and mechanical frequencies of the optomechanical cavities are independently trimmed into alignment post-fabrication using an atomic force microscope to oxidize nanoscale regions of the cavity. After nano-oxidation tuning, the left (right) cavity has optical resonance wavelength $\lambda_{L(R)} = 1534.502$ (1534.499) nm, total loaded damping rate $\kappa_{L(R)}/2\pi = 1.03$ (0.75) GHz, and intrinsic cavity damping rate $\kappa_{iL(R)}/2\pi = 0.29$ (0.31) GHz (c.f. Fig. 4.2e). Note that hybridization of the optical cavity resonances is too weak to be observable in the measured left and right cavity spectra due to the fact that the optical cavity linewidths are much larger than the designed cavity coupling J . The thermal mechanical spectra, as measured from the two cavities using a blue-detuned pump laser (see App. 4.1), are shown in Fig. 4.2f where one can see hybridized resonances M_{\pm} which are mixtures of the localized mechanical cavity modes M_L and M_R . A nearby phonon waveguide mode (M_W) is also observable in both left and right cavity spectra. The optomechanical coupling rate and mechanical dissipation rate of $M_{L(R)}$ were measured before nano-oxidation tuning, yielding $g_{0,L(R)}/2\pi = 0.76$ (0.84) MHz and $\gamma_{iL(R)}/2\pi = 4.3$ (5.9) MHz.

The experimental apparatus used to drive and probe the optomechanical circuit is shown schematically in Fig. 4.3a. As indicated, an optical pump field for the left and right cavities is generated from a common diode laser. The phase difference of

the pump fields at the input to the cavities, and thus the synthetic magnetic flux, is tuned by a stretchable fiber phase shifter and stabilized by locking the interference intensity of the reflected pump signals from the cavities. To highlight the unique kinds of nonreciprocal transport possible in our setup, we present results for an experiment performed with blue-detuned pump fields with frequency $\omega_p \approx \omega_c + \omega_m$; as discussed, this will enable non-reciprocal transport with gain. An input optical probe signal is generated from either of the left or right cavity pump beams by sending them through an electro-optic modulator (EOM). A vector network analyzer (VNA) is used to drive the EOMs at modulation frequency ω_{mod} and detect the photocurrent generated by the beating of the transmitted probe and reflected pump signals, thus providing amplitude and phase information of the transmitted probe signal. Owing to the spectral filtering of the cavities, only the generated lower sideband of the blue-detuned pump at $\omega = -\omega_{\text{mod}}$ is transmitted through the circuit as a probe signal.

Figure 4.3b shows the ratio of the forward and backward optical power transmission coefficients of the probe light ($|T_{L \rightarrow R}/T_{R \rightarrow L}|^2$) for several magnetic flux values between $\Phi_B = 0$ and π . For these measurements the pump powers at the input to the left and right cavity were set to $P_{\text{pL}} = -14.2$ dBm and $P_{\text{pR}} = -10.8$ dBm, respectively, corresponding to intra-cavity photon numbers of $n_{\text{cL}} = 1000$ and $n_{\text{cR}} = 1420$. So as to remove differences in the forward and reverse transmission paths external to the optomechanical circuit, here the $|T_{L \rightarrow R}/T_{R \rightarrow L}|^2$ ratio is normalized to 0 dB for a modulation frequency $\omega_{\text{mod}}/2\pi \approx 5.74$ GHz, detuned far from mechanical resonance in a frequency range where reciprocal transmission is expected. Closer to mechanical resonance, strong nonreciprocity in the optically transmitted power is observed, with a peak and a dip in $|T_{L \rightarrow R}/T_{R \rightarrow L}|^2$ occurring roughly at the resonance frequencies of the hybridized mechanical modes M_+ and M_- , respectively (c.f. Fig. 4.2c). The maximum contrast ratio between forward and backward probe transmission – the isolation level – is measured to be 35 dB for $\Phi_B = 0.34\pi$ near the M_+ resonance. The forward transmission is also amplified in this configuration (blue-detuned pump, $\Delta = +\omega_m$), with a measured peak probe signal amplification of 12 dB above the background level set by photon hopping alone ($J/|\Gamma_{\pm}| \gg 1$). The corresponding port-to-port net gain is only 1 dB due to impedance mismatching ($J \neq \kappa/2$) and intrinsic optical cavity losses (see SI for details).

From a two-parameter fit to the measured optical power transmission ratio spectra using Eq. 4.3 (see blue curves in Figs. 4.3b and 4.3c), we obtain a waveguide-

mediated optical and mechanical hopping rate of $J/2\pi = 110$ MHz and $V/2\pi = 2.8$ MHz, respectively, consistent with our design parameters. Figure 4.3d shows the theoretical calculation of $|T_{L\rightarrow R}/T_{R\rightarrow L}|^2$ for a full 2π range of Φ_B with the measured and fit optomechanical circuit parameters. The pattern is seen to be odd symmetric with respect to $\Phi_B = \pi$. Inserting an additional magnetic flux π into the measurements performed in Fig. 4.3b yields the spectra shown in Fig. 4.3c which displays a switch in the isolation direction as predicted by the model. The pump power dependence of the peak (in frequency) forward signal amplification and the corresponding backward signal attenuation relative to the background level far from mechanical resonance are shown in Fig. 4.3e for a fixed magnetic flux of $\Phi_B = 0.28\pi$. Good correspondence with the theoretical power dependence (solid curves) is observed, with nonreciprocal amplification vanishing at low pump power.

One can also obtain nonreciprocal optical power transmission utilizing an even simpler system involving a single mechanical cavity. This is the situation we have for the Fabry-Perot-like mechanical resonances that exist in the central coupling waveguide (see M_W resonance of Fig. 4.2c). As depicted in Fig. 4.4a, the mode configuration in this case consists of two optical cavity modes (O_L and O_R) coupled together via the optical waveguide, one mechanical waveguide mode M_W which is parametrically coupled to each of the optical cavity modes, and the synthetic magnetic flux $\Phi_B = \phi_L - \phi_R$ due to the relative phases of the optical pump fields threading the triangular mode space. In Fig. 4.4b and 4.4c we show the measurement of $|T_{L\rightarrow R}/T_{R\rightarrow L}|^2$ for a series of different flux values Φ_B with blue-detuned pumping ($\Delta \approx +\omega_{M_W}$) at levels of $n_{cL} = 770$ and $n_{cR} = 1090$. In this single mechanical mode case the direction of the signal propagation is determined by the magnitude of the flux; $\Phi_B \leq \pi$ leads to backward propagation and $\Phi_B \geq \pi$ to forward propagation. The lower contrast ratio observed is a result of the weaker coupling between the localized optical cavity modes and the external waveguide mode, which for the modest pump power levels used here ($\lesssim 100 \mu\text{W}$) does not allow us to reach the parametric coupling required for strong directional transmission.

While our focus has been on the propagation of injected coherent signals through the optomechanical circuit, it is also interesting to consider the flow of noise. As might be expected, the induced directionality of our system also applies to noise photons generated by the upconversion of both thermal and quantum fluctuations of the mechanics; see App. 4.3 for detailed calculations. One finds that for the system of Fig. 4.2, the spectrally-resolved photon noise flux shows high directionality, but

that the sign of this directionality changes as a function of frequency (analogous to what happens in the transmission amplitudes). In contrast, in the single-mechanical mode setup of Fig. 4.4 the sign of the directionality is constant with frequency, and thus the total (frequency-integrated) noise photon flux is directional depending upon the flux magnitude. The laser pump fields can thus effectively act as a heat pump, creating a temperature difference between the left and right waveguide output fields. The corresponding directional flow of quantum noise is especially useful for quantum information applications, as it can suppress noise-induced damage of a delicate signal source like a qubit [82, 3].

The device studied in this work highlights the potential for optomechanics to realize synthetic gauge fields and novel forms of nonreciprocity enabled by harnessing mechanical dissipation. Using just a few modes, it was possible to go beyond simply mimicking the physics of an isolator and realize a directional optical amplifier. By adding modes, an even greater variety of behaviours could be achieved. For example, the simple addition of a third optical cavity mode, tunnel-coupled to the first two cavities but with no mechanical coupling, would realize a photon circulator similar to the phonon circulators considered in Ref. [48]. Scaling the synthetic gauge field mechanism realized here to a full lattice of optomechanical cavities would allow the study of topological phenomena in the propagation of both light and sound. Predicted effects include the formation of back-scattering immune photonic [114] and phononic [95] chiral edge states, topologically nontrivial phases of hybrid photon-phonon excitations [95], dynamical gauge fields [131], and, in the case of non-particle-conserving interactions enabled by blue-detuned optical pumping, topologically protected inelastic scattering of photons [94] and even protected amplifying edge states [93].

4.1 Device Fabrication and Methods

4.1.1 Device fabrication and atomic force microscope nano-oxidation tuning

The devices were fabricated from a silicon-on-insulator wafer with a silicon device layer thickness of 220 nm and buried-oxide layer thickness of 2 μm . The device geometry was defined by electron-beam lithography followed by inductively coupled plasma reactive ion etching to transfer the pattern through the 220 nm silicon device layer. The devices were then undercut using an HF:H₂O solution to remove the buried oxide layer and cleaned using a piranha etch.

After device fabrication, we used an atomic force microscope to draw nanoscale

oxide patterns on the silicon device surface. This process modifies the optical and mechanical cavity frequencies in a controllable and independent way with the appropriate choice of oxide pattern. The nano-oxidation process was carried out using an Asylum MFP-3D atomic force microscope and conductive diamond tips (NaDiaProbes) in an environment with relative humidity of 48%. The tip was biased at a voltage of -11.5 V, scanned with a velocity of 100 nm/s, and run in tapping mode with an amplitude of 10 nm. The unpassivated silicon device surface was grounded.

4.1.2 Optical transmission coefficient measurement

To measure the optical power transmission through the optomechanical circuit we used a vector network analyzer (VNA). The VNA outputs a microwave tone from port 1 with frequency ω_{mod} to an electro-optic modulator which modulates the optical pump to generate an optical sideband corresponding to the optical probe. In the case of a blue-detuned pump from the optical cavity resonance, the probe field corresponds to the lower sideband (selected by the filtering properties of the cavity itself). Both the optical probe and pump are launched into one optomechanical cavity in the circuit. At the other cavity, the transmitted optical probe combines with a second pump and the beating of the two is detected by a high-speed photodetector (both the first and second pump beams are from the same laser source, and thus phase coherent). The photocurrent signal from the photodetector is sent into port 2 of the VNA to measure the microwave signal transmission coefficient T_μ . Fig. 4.5 shows $|T_\mu|^2$ for forward (right-propagating; blue curve) and backward (left-propagating; red curve) directions through the optomechanical circuit as a function of the modulation frequency ω_{mod} . In Fig. 4.5a the synthetic flux value is locked to $\Phi_B = 0.34\pi$ whereas in Fig. 4.5b $\Phi_B = 1.34\pi$. In both flux settings the optical pumping levels were such that the left and right cavity photon numbers were $n_{cL} = 1000$ and $n_{cR} = 1420$, respectively.

While absolute optical transmission is not directly measured, the ratio of the optical transmission coefficients for forward and backward propagation can be obtained from the normalized microwave signal transmission coefficient \bar{T}_μ ,

$$|T_{L \rightarrow R}/T_{R \rightarrow L}|^2 = |\bar{T}_{\mu R}/\bar{T}_{\mu L}|^2, \quad (4.4)$$

where $|\bar{T}_\mu|^2$ is normalized using the value of $|T_\mu|^2$ away from all mechanical resonances to remove all the external asymmetry in the experimental setup for left and right propagation paths. These external asymmetries include modulator efficiency,

cable/fiber loss, etc. In our analysis the normalization level is the average value of $|T_\mu|^2$ in the frequency range of 5.74-5.76 GHz. To be clear, the reason this calibration is necessary is because we do not actually physically swap the source and detector in our measurements. Rather, for the left-to-right transmission path we have one modulator on the left side which generates the probe tone and one detector on the right side which measures the transmission through to the right side. When we measure right-to-left transmission we have a different modulator on the right side to generate the probe tone and a different detector on the left side to detect the transmitted probe. If the modulator on the left side is different from the modulator on the right side, then for the same microwave drive that excites the modulators we would get different a different optical probe power in the sidebands of the pump. Similarly if the left and right detectors have different efficiencies then they would produce a different photocurrent for the same transmitted optical probe power. Since we measure in practice the ratio of the microwave drive to the detected microwave photocurrent, this could cause an inherent asymmetry in the measured transmission for left-to-right and right-to-left transmission even if the *optical* transmission was perfectly symmetric.

4.1.3 Device characterization

To determine the components of optical cavity loss (intrinsic decay rate κ_i , external waveguide-to-cavity coupling κ_e , total cavity decay rate κ) of both the left and right optical cavities we used a pump-probe scheme similar to that used to measure the nonreciprocity of the optomechanical circuit. The pump beam in this case, however, is set to be very weak so as to not resonantly excite the mechanics as the probe signal is swept across the optical cavity resonance. The cavity scans are plotted in Fig. 4.6a and 4.6b for the left and right cavities, respectively. We fit the phase response curves and get $\kappa_{iL(R)}/2\pi = 0.29$ (0.31) GHz, $\kappa_e/2\pi = 0.74$ (0.44) GHz, and $\kappa_{L(R)}/2\pi = 1.03$ (0.75) GHz. The intrinsic and external optical cavity rates are used to determine the intra-cavity photon number for a given optical pump power (specified at the input to the cavity).

Thermal mechanical spectra of the two cavities are measured with a weak blue-detuned optical pump so as to avoid back-action; a single pump is used for each of the left and right cavity measurements. The reflected pump light from the cavity contains modulation sidebands from the thermal mechanical motion, which upon detection with a high-speed photodetector creates a photocurrent with the thermal motion of the mechanical cavity modes imprinted on it. Since the mechanical

modes can be hybridized between left-cavity, right-cavity, and waveguide modes, a measurement with the left-side pump produces a local measurement of the cavity modes as measured by the localized left optical cavity mode, and similarly for the right-side pump and cavity. The intrinsic decay rate of the mechanical modes is inferred from the linewidth of the Lorentzian mechanical spectrum.

Measurements of the mechanical mode spectra were performed both before and after the cavities were nano-oxidized to tune their localized optical and mechanical modes into resonance. Measurements prior to nano-oxidation allowed us to determine the local (left and right) mechanical and optical cavity mode properties (i.e., the bare, uncoupled mode properties). Knowing the left and right cavity mode properties from independent measurements allowed us to fit with fewer fitting parameters the measured forward and backward transmission curves of the hybridized cavities presented in the main article text. Note that after nano-oxidation the left and right optical cavity modes were only very weakly hybridized so as to maintain their left-cavity and right-cavity character. The mechanical modes were tuned to be strongly hybridized as evidenced in Fig. 4.6f. Figures 4.6c and 4.6d show the measured linewidth of the mechanical cavity modes $M_{L(R)}$ versus optical pumping power. In Fig. 4.6c the left cavity was pumped with a blue detuning $\Delta = +\omega_{mL}$; in Fig. 4.6d the right cavity was pumped with a blue detuning of $\Delta = +\omega_{mR}$. By fitting the measured data with formula $\gamma = \gamma_i - 4g_0^2 n_c / \kappa$ (n_c corresponding to the intra-cavity photon number determined from the $O_{L(R)}$ measured cavity properties), we obtain $g_{0,L(R)}/2\pi = 0.76$ (0.84) MHz and $\gamma_{iL(R)}/2\pi = 4.3$ (5.9) MHz for the left (right) localized cavity modes.

The optical (J) and mechanical (V) hopping rates between the two optomechanical cavities via the connecting waveguide are determined from a global fitting using Eq. (1) for the group of measured transmission coefficient ratio curves in Figs. 3c and 3d with varying Φ_B . The intra-cavity cavity photon number, optomechanical coupling rates, and intrinsic mechanical decay rates are all taken as fixed and equal to the independently measured values as described above.

With the fit value of J from forward and reverse transmission measurements versus Φ_B , and the measured cavity coupling rates (κ , κ_i) from the left and right optical cavity modes prior to nano-oxidation tuning, we fit the measured optical reflection spectra of the two weakly coupled optical cavity modes after nano-oxidation. This allows us to determine the uncoupled left and right optical cavity mode frequencies. The measured and fit spectra as measured from the left and right cavities are shown

in Fig. 4.6e. As noted earlier, the measured spectra after nano-oxidation are still predominantly given by uncoupled left and right cavity modes. Based on the theoretical fit to the measured optical reflection spectra, we also calculate the transmission of an optical probe signal through the optomechanical circuit in the absence of a pump beam (i.e., no coupling to phonons, just pure optical transmission)

$$\eta = \frac{J\sqrt{\kappa_{eL}\kappa_{eR}}}{\left| J^2 + \kappa_L\kappa_R/4 - (\omega - \omega_{cL})(\omega - \omega_{cR}) - i\kappa_L(\omega - \omega_{cL})/2 - i\kappa_R(\omega - \omega_{cR})/2 \right|}. \quad (4.5)$$

Fig. 4.6f shows the numerical result, and the minimum insertion loss for transmission from one port to the other port is found to be about 11 dB for a probe signal frequency in between the two cavity resonances. This is the estimated port-to-port optical transmission efficiency in absence of optomechanical amplification.

4.2 Theory of optical nonreciprocity

4.2.1 Input-output formula

We provide theoretical analysis of optical nonreciprocity in the coupled optomechanical cavity system. We first consider the case with two optical and two mechanical cavity modes. The Hamiltonian of this system can thus be written as follows,

$$\begin{aligned} \hat{H} = & \sum_{k=L,R} \hbar\omega_{ck}\hat{a}_k^\dagger\hat{a}_k + J(\hat{a}_L^\dagger\hat{a}_R + \hat{a}_L\hat{a}_R^\dagger) + \sum_{k=L,R} \hbar\omega_{mk}\hat{b}_k^\dagger\hat{b}_k \\ & + V(\hat{b}_L^\dagger\hat{b}_R + \hat{b}_L\hat{b}_R^\dagger) \\ & + \sum_{k=L,R} \hbar g_{0k}(\hat{b}_k^\dagger + \hat{b}_k)\hat{a}_k^\dagger\hat{a}_k + \sum_{k=L,R} i\hbar\sqrt{\kappa_{ek}}\alpha_{pk}e^{-i\omega_{pk}t-i\phi_k}(\hat{a}_k - \hat{a}_k^\dagger), \end{aligned} \quad (4.6)$$

where J and V are the waveguide mediated optical and mechanical coupling strength (we gauged out the phase of J and V and take both of them to be real), and the last two terms are the optical driving fields (pumps) which have the same frequency and correlated phases. We consider the situation where the optical cavities are nearly degenerate, i.e., $\omega_{cL} \simeq \omega_{cR} \equiv \omega_c$ and both optomechanical systems are driven with a blue-detuned laser ($\omega_{pk} = \omega_c + \omega_{mk}$). We perform a displacement transformation $\hat{a}_k = \alpha_k + \hat{d}_k$, separating the classical steady state amplitude of the local optical cavity field from its fluctuations. With this we can linearize the optomechanical interaction in the Hamiltonian of Eq. 4.6 in the usual manner. Assuming the good cavity limit (sideband resolved, $\omega_{mk} \gg \kappa_k$), we apply a rotating wave approximation

and obtain for the equations of motions ($\hbar = 1$)

$$\begin{aligned}
\frac{d}{dt}\hat{d}_L &= \left(i\Delta_L - \frac{\kappa_L}{2}\right)\hat{d}_L - \sqrt{\kappa_{eL}}\hat{d}_{L,in} - \sqrt{\kappa_{iL}}\hat{\xi}_{L,in} - iJ\hat{d}_R - iG_L\hat{b}_L^\dagger e^{i\phi_L}, \\
\frac{d}{dt}\hat{d}_R &= \left(i\Delta_R - \frac{\kappa_R}{2}\right)\hat{d}_R - \sqrt{\kappa_{eR}}\hat{d}_{R,in} - \sqrt{\kappa_{iR}}\hat{\xi}_{R,in} - iJ\hat{d}_L - iG_R\hat{b}_R^\dagger e^{i\phi_R}, \\
\frac{d}{dt}\hat{b}_L &= -\left(i\omega_{mL} + \frac{\gamma_{iL}}{2}\right)\hat{b}_L - \sqrt{\gamma_{iL}}\hat{b}_{L,in} - iV\hat{b}_R - iG_L\hat{d}_L^\dagger e^{i\phi_L}, \\
\frac{d}{dt}\hat{b}_R &= -\left(i\omega_{mR} + \frac{\gamma_{iR}}{2}\right)\hat{b}_R - \sqrt{\gamma_{iR}}\hat{b}_{R,in} - iV\hat{b}_L - iG_R\hat{d}_R^\dagger e^{i\phi_R},
\end{aligned} \tag{4.7}$$

with the total damping rates $\kappa_k = \kappa_{ek} + \kappa_{ik}$, the detunings $\Delta_k = \omega_p - \omega_{ck}$ and the many-photon optomechanical couplings $G_k = g_{0k}\alpha_k$. The latter contains the steady state amplitude of the local optical cavity field $\alpha_k e^{i\phi_k}$, which is related to the pump amplitudes through

$$\alpha_{L(R)} e^{i\phi_{L(R)}} = \frac{(i\Delta_{R(L)} - \kappa_{R(L)}/2)\sqrt{\kappa_{eL(R)}}\alpha_{pL(R)}e^{-i\varphi_{L(R)}} + iJ\sqrt{\kappa_{eR(L)}}\alpha_{pR(L)}e^{-i\varphi_{R(L)}}}{(i\Delta_L - \kappa_L/2)(i\Delta_R - \kappa_R/2) + J^2}. \tag{4.8}$$

We find the steady state amplitude is approximately $\sqrt{\kappa_{ek}}\alpha_{pk}e^{-i\varphi_k}/i\Delta_k$ under the condition $\Delta_k \approx \omega_{mk} \gg \kappa_k, J$, which means each cavity is effectively only driven by its own optical pump. Thus, each pump-enhanced optomechanical coupling and its phase can be independently controlled. The intrinsic noise operators $\hat{\xi}_{k,in}$ and $\hat{b}_{k,in}$ in the coupled mode equations 4.7 describe thermal and vacuum fluctuations impinging on the the cavities and the mechanical modes respectively. The associated noise of a possible input signal is described via $\hat{d}_{k,in}$.

4.2.2 Mechanically-mediated coupling

We perform a Fourier transform ($\hat{b}[\omega] \equiv \int dt \hat{b}(t)e^{+i\omega t}$; $\hat{b}(t) \equiv \int \frac{d\omega}{2\pi} \hat{b}[\omega]e^{-i\omega t}$) of the coupled mode equations Eqs. 4.7 and insert the resulting solution for $\hat{b}_{L,R}^\dagger[\omega]$ into the equations of the cavity operators. Ignoring the intrinsic noise terms $\hat{\xi}_{in,k}$ and $\hat{b}_{in,k}$ for the moment, we obtain for the cavity operators in frequency space ($\Phi_B = \phi_L - \phi_R$)

$$\begin{aligned}
\tilde{\chi}_{L,+}^{-1}[\omega]\hat{d}_L[\omega] &= -\sqrt{\kappa_{eL}}\hat{d}_{L,in}[\omega] - i\left(J - \Gamma_+[\omega]e^{+i\Phi_B}\right)\hat{d}_R[\omega], \\
\tilde{\chi}_{R,+}^{-1}[\omega]\hat{d}_R[\omega] &= -\sqrt{\kappa_{eR}}\hat{d}_{R,in}[\omega] - i\left(J - \Gamma_+[\omega]e^{-i\Phi_B}\right)\hat{d}_L[\omega],
\end{aligned} \tag{4.9}$$

with the modified susceptibility $\tilde{\chi}_{k,+}^{-1}[\omega] = (-i(\omega + \Delta_k) + \frac{\kappa_k}{2} + i\Sigma_{k,+}[\omega])$. The frequency dependent coupling $\Gamma_+[\omega]$ and the self-energy $\Sigma_{k,+}[\omega]$ are defined as

$$\begin{aligned}\Gamma_+[\omega] &= \frac{VG_R G_L}{[-i(\omega + \omega_{mL}) + \frac{\gamma_{iL}}{2}] [(-i(\omega + \omega_{mR}) + \frac{\gamma_{iR}}{2})] + V^2} \\ \Sigma_{k,+}[\omega] &= \frac{iG_k}{VG_{\bar{k}}} \left[-i(\omega + \omega_{m\bar{k}}) + \frac{\gamma_{i\bar{k}}}{2} \right] \Gamma_+[\omega],\end{aligned}\quad (4.10)$$

here the coupling $\Gamma_+[\omega]$ coincides with Eq. (2). After eliminating the mechanical degrees of freedom, one finds both a "local" modification of each cavity (described by the self energy $\Sigma_{k,+}[\omega]$) and an induced coupling between the cavities. The self-energies lead to damping (or anti-damping) of each cavity resonance as well as a frequency shift of the resonance. Here the subscript + indicates blue-detuning ($\Delta_k = \omega_{pk} - \omega_c \approx +\omega_{mk}$). The poles of the self energy read

$$\begin{aligned}\omega_{\pm} &= -\frac{i}{4}(\gamma_{iL} + \gamma_{iR}) - \frac{1}{2}(\omega_{mL} + \omega_{mR}) \\ &\pm \sqrt{V^2 - \left[\frac{1}{4}(\gamma_{iL} - \gamma_{iR}) - \frac{i}{2}(\omega_{mL} - \omega_{mR}) \right]^2}.\end{aligned}\quad (4.11)$$

The induced coupling has a coherent and a dissipative aspect. To illustrate this we separate the coupling into real and imaginary parts $\Gamma_+[\omega] \equiv \Gamma_{\text{Re}}[\omega] + i\Gamma_{\text{Im}}[\omega]$. The real and imaginary parts of this frequency-dependent coupling have completely different physical interpretations. We see this, by considering again the coupling terms in Eq. (4.9). We have

$$\begin{aligned}\hat{d}_L[\omega] &\sim \left[-i \left(J - \Gamma_{\text{Re}}[\omega] e^{+i\Phi_B} \right) - \Gamma_{\text{Im}}[\omega] e^{+i\Phi_B} \right] \hat{d}_R[\omega] \\ &\equiv \left[-i\tilde{J}[\omega] - \Gamma_{\text{Im}}[\omega] e^{+i\Phi_B} \right] \hat{d}_R[\omega], \\ \hat{d}_R[\omega] &\sim \left[-i \left(J - \Gamma_{\text{Re}}[\omega] e^{-i\Phi_B} \right) - \Gamma_{\text{Im}}[\omega] e^{-i\Phi_B} \right] \hat{d}_L[\omega] \\ &\equiv \left[-i\tilde{J}^*[\omega] - \Gamma_{\text{Im}}[\omega] e^{-i\Phi_B} \right] \hat{d}_L[\omega].\end{aligned}\quad (4.12)$$

For the given frequency of interest, we see that the real part of the induced coupling is completely equivalent to having a Hamiltonian, coherent tunneling term between the cavities; we can absorb it into a redefinition of the coherent hopping strength J , i.e., $J \rightarrow \tilde{J}[\omega]$. In contrast, the coupling mediated by the imaginary part $\Gamma_{\text{Im}}[\omega]$ is *not* equivalent to some effective coherent tunneling interaction between the cavities, i.e., the $\Gamma_{\text{Im}}[\omega]$ terms in \hat{d}_L and \hat{d}_R Eqs.(4.12) cannot be incorporated into a definition of J . The terms involving $\Gamma_{\text{Im}}[\omega]$ instead represent a *dissipative* coupling between the two cavities mediated by the mechanics. Such dissipative interactions

(if we ignore their frequency dependence) can be obtained in a master equation formalism via an effective Lindblad dissipator of the form $2\Gamma_{\text{Im}}\mathcal{L}\left[d_L^\dagger + e^{-i\Delta\phi}d_R^\dagger\right]$, where $\mathcal{L}[\hat{\rho}]\hat{\rho} = \hat{\rho}\hat{\rho}^\dagger - 1/2\hat{\rho}^\dagger\hat{\rho} - 1/2\hat{\rho}\hat{\rho}^\dagger$ is the standard Lindblad superoperator.

4.2.3 Directionality by balancing coherent and dissipative interactions

The dissipative coupling is crucial for directionality: by balancing the dissipative interaction against the coherent interaction we obtain a nonreciprocal system (following the general recipe outlined in Ref.[82]). For example, if we aim for a directional transport from the left to the right cavity, we want to decouple the left cavity from the right cavity (while still having the right cavity influenced by the left cavity). This is accomplished by balancing coherent and dissipative interactions, i.e.,

$$\tilde{J}[\omega] \stackrel{!}{=} i\Gamma_{\text{Im}}[\omega]e^{i\Phi_{\text{B}}}, \quad (4.13)$$

in which case the coupling from the left to right cavity vanishes, cf. Eq. (4.12), and we obtain a unidirectional coupling where the right cavity is driven by the left cavity but not vice versa. Crucially, this would not be possible without the dissipative interaction, i.e., we need $\Gamma_{\text{Im}}[\omega] \neq 0$. Note, for the situation that $\Gamma_{\text{Im}}[\omega] = 0$, i.e., $\gamma_{ik} = 0$, but finite Φ_{B} , we still obtain a directional dependent phase. However, to use this as the basis for nonreciprocal transmission additional interference processes have to be implemented.

The directionality condition Eq. (4.13) can be reformulated in terms of the original J and the phase difference Φ_{B} as used in Eq. (4.9). This translates to the condition

$$J = |\Gamma_+[\omega]|, \quad \Phi_{\text{B}} = -\arg(\Gamma_+[\omega]), \quad (4.14)$$

where we still aim for unidirectional behavior from left to right. For the case of a purely real coupling $\Gamma_+[\omega] = \Gamma_{\text{Re}}[\omega]$ these conditions could still be satisfied, i.e., for $\Phi_{\text{B}} = 0$ and $\Gamma_{\text{Re}}[\omega] = J$. However, this means that there is effectively no coupling between the cavities, and thus no forward transport either. Note that a sign change in $\arg(\Gamma_+[\omega])$ would lead to the opposite situation, where the propagation direction would be from right to left.

In general, the directionality balancing condition obtained here is frequency dependent, for the simple reason that the mechanically-mediated cavity-cavity coupling is frequency-dependent. If we could somehow fulfill the directionality condition in Eq. (4.14) at every frequency, the cavity output field operators would be given by

(using the standard input-output relation $\hat{d}_{k,out} = \hat{d}_{k,out} + \sqrt{\kappa_{ek}}\hat{a}_k$)

$$\begin{aligned}\hat{d}_{L,out}[\omega] &= [1 - \kappa_{eL}\tilde{\chi}_{L,+}[\omega]] \hat{d}_{L,in}[\omega], \\ \hat{d}_{R,out}[\omega] &= [1 - \kappa_{eR}\tilde{\chi}_{R,+}[\omega]] \hat{d}_{R,in}[\omega] \\ &\quad - i\sqrt{\kappa_{eR}\kappa_{eL}}\tilde{\chi}_{R,+}[\omega]\tilde{\chi}_{L,+}[\omega] |\Gamma_+[\omega]| \left(e^{i2\arg(\Gamma_+[\omega])} - 1 \right) \hat{d}_{L,in}[\omega],\end{aligned}\quad (4.15)$$

where we neglected the noise contributions originating from the mechanical modes, i.e., the coupling to $\hat{b}_{n,in}$ in Eq. (4.9), and the intrinsic cavity noise $\xi_{in,k}$ for simplicity. Here, we see again that the dissipative interaction is crucial as we need $\arg(\Gamma_+[\omega]) \neq n\pi$, $n \in \mathbb{Z}$, i.e., we need a finite imaginary part of $\Gamma_+[\omega]$.

The experimentally relevant situation is where dissipative and coherent interactions are only balanced at a single frequency (by appropriate tuning of phase and J). Achieving this condition close to the normal modes resonance frequencies is favorable given the resonantly-enhanced transmission. Enforcing directionality at $\omega = -\omega_m \pm V$ for equal mechanical resonance frequencies, results in the directionality conditions

$$\omega_{mL} = \omega_{mR} : \Phi_B = \mp \arctan \frac{2V(\gamma_{iL} + \gamma_{iR})}{\gamma_{iL}\gamma_{iR}}, \quad J = \frac{VG_R G_L}{\sqrt{\frac{1}{4}V^2(\gamma_{iL} + \gamma_{iR})^2 + \frac{\gamma_{iL}^2\gamma_{iR}^2}{16}}}, \quad (4.16)$$

where the upper (lower) sign in the phase difference Φ_B realizes directionality at $\omega = -\omega_m + V(-\omega_m - V)$. Directionality here means that an input signal injected on the left cavity is transmitted to the right cavity, whereas the backward propagation path, i.e., from right to left, is blocked.

On the other side, if we assume identical bare mechanical damping of the mechanical modes ($\gamma_{iL} = \gamma_{iR} = \gamma_i$), but unequal bare mechanical frequencies ($\omega_{mL} \neq \omega_{mR}$), then we find that at the frequencies of the hybridized mechanical modes $\Omega_{\pm} = -\frac{1}{2}(\omega_{mL} + \omega_{mR}) \pm \sqrt{V^2 + \frac{1}{4}(\omega_{mL} - \omega_{mR})^2}$ the directionality condition is modified to

$$\gamma_{iL} = \gamma_{iR} : \Phi_B = \mp \arctan \frac{4\sqrt{V^2 + \frac{1}{4}(\omega_{mL} - \omega_{mR})^2}}{\gamma}, \quad J = \frac{VG_L G_R}{\gamma\sqrt{V^2 + \frac{\gamma^2}{16} + \frac{1}{4}(\omega_{mL} - \omega_{mR})^2}}. \quad (4.17)$$

where the upper (lower) sign in the phase difference Φ_B realizes directionality at $\omega = \Omega_{+(-)}$. The directionality conditions for a perfectly symmetric device, i.e., for equal mechanical resonance frequencies (ω_m) and decay rates (γ), can simply be read off from either Eq. 4.17 or Eq. 4.16.

4.2.4 Nonreciprocal optical transmission: two blue-detuned pumps

From the equations for the cavity operators in Eqs. 4.9 we can calculate the transmission coefficients via input/output theory. Note that although Eqs. 4.9 are formulated on the basis of noise operators, they also describe the dynamics of the cavity field amplitudes d_k around their steady state solution. The right transmission coefficient $T_{L \rightarrow R} \equiv d_{R,out}/d_{L,in}$ and left transmission coefficient $T_{R \rightarrow L} \equiv d_{L,out}/d_{R,in}$ are given by

$$T_{R \leftrightarrow L}[\omega] = \frac{i\sqrt{\kappa_{eL}\kappa_{eR}} [J - \Gamma_+[\omega]e^{\mp i\Phi_B}]}{\tilde{\chi}_L^{-1}[\omega]\tilde{\chi}_R^{-1}[\omega] + [\Gamma_+[\omega]^2 + J^2 - 2\Gamma_+[\omega]J \cos(\phi)]} \quad (4.18)$$

$$\equiv A_+[\omega] [J - \Gamma_+[\omega]e^{\mp i\Phi_B}],$$

with the modified susceptibilities $\tilde{\chi}_k[\omega]$ as defined after Eq. (4.9). The prefactor $A_+[\omega]$ is the same for both transmission amplitudes, it accounts for the mechanically-induced back-action on the optical cavities, cf. after Eq. (2). Note, that the corresponding prefactor for two red-detuned pumps is simply $A_-[\omega] = -A_+^*[-\omega]$.

We now assume a completely symmetric pair of mechanical cavities ($\omega_{mL} = \omega_{mR} = \omega_m$ and $\gamma_{iL} = \gamma_{iR} = \gamma_i$) and apply the corresponding directionality direction for symmetric parameters, cf. Eq. 4.17 or Eq. 4.16. The transmission coefficient for the through direction (\rightarrow) under these conditions of perfect nonreciprocity is given by,

$$T_{\rightarrow}[-\omega_m \pm V] = \sqrt{\frac{\kappa_{eL}\kappa_{eR}}{\kappa_R\kappa_L}} \sqrt{\frac{1 \pm i\frac{\gamma_i}{4V}}{1 \mp i\frac{\gamma_i}{4V}}} \times \frac{8i\sqrt{C_L C_R}}{\left[C_L \left(1 \pm i\frac{\gamma_i}{2V} \right) - \left(1 \mp i\frac{2V}{\kappa_L} \right) \left(2 \pm i\frac{\gamma_i}{2V} \right) \right]} \times \left[C_R \left(1 \pm i\frac{\gamma_i}{2V} \right) - \left(1 \mp i\frac{2V}{\kappa_R} \right) \left(2 \pm i\frac{\gamma_i}{2V} \right) \right], \quad (4.19)$$

introducing the single cavity cooperativity $C_k \equiv 4G_k^2/\gamma_i\kappa_k$. Considering as well symmetric optical cavities ($\kappa_{eL} = \kappa_{eR} = \kappa_e$; $\kappa_L = \kappa_R = \kappa$) with symmetric optical pumping ($G_L = G_R = G$) the transmission coefficient simplifies to

$$T_{\rightarrow}[-\omega_m \pm V] \stackrel{V \ll \kappa}{\simeq} \frac{8iC \frac{\kappa_e}{\kappa}}{\left[2 - C \pm i\frac{\gamma_i}{2V} (1 - C) \right]^2}, \quad (4.20)$$

with $C \equiv 4G^2/\gamma_i\kappa$ and under the realistic assumption that the hopping rate V is much lower than the cavity decay rate κ . Here we work with blue-detuned pumping of both optical cavities ($\Delta \approx +\omega_m$), which results in parametric amplification of each of the left and right mechanical modes and leads to amplification of the optical

probe signal. This becomes apparent for the situation that the mechanical hopping rate is much faster than the intrinsic mechanical decay rate ($V/\gamma_i \gg 1$). In this case the gain diverges for $C \rightarrow 2$ (this is twice as large as for a single cavity instability because the mechanical modes are hybridized and thus the effective optomechanical coupling from the left or right optical cavity is reduced by a factor of $\sqrt{2}$, hence the cooperativity by a factor of 2). Note, for the situation $V/\gamma_i \gg 1$, the directionality conditions at the hybridized mechanical modes $\omega = -\omega_m \pm V$ simplifies to $J \simeq G_L G_R / \gamma_i$ and $\Phi_B \rightarrow \mp \pi/2$.

4.2.5 Nonreciprocal optical transmission: two red-detuned pumps

The analysis for the the case of two red detuned pumps is similar to the blue-detuned case. The cavity operators in Eq.(4.7) couple now to the mechanical lowering operators \hat{b}_k and vice versa, while the detuning between the cavity resonances and the external pump tones yields $\Delta_k = -\omega_{mk}$. The ratio of transmission coefficients is found to be given by the following expression

$$\frac{T_{L \rightarrow R}}{T_{R \rightarrow L}} = \frac{J - \Gamma_-[\omega] e^{-i\Phi_B}}{J - \Gamma_-[\omega] e^{+i\Phi_B}} = \frac{J - \frac{VG_L G_R}{[-i(\omega - \omega_{mL}) + \frac{\gamma_{iL}}{2}][-i(\omega - \omega_{mR}) + \frac{\gamma_{iR}}{2}] + V^2} e^{-i\Phi_B}}{J - \frac{VG_L G_R}{[-i(\omega - \omega_{mL}) + \frac{\gamma_{iL}}{2}][-i(\omega - \omega_{mR}) + \frac{\gamma_{iR}}{2}] + V^2} e^{+i\Phi_B}} \quad (4.21)$$

where we have $\Gamma_-[\omega] = \Gamma_+^*[-\omega]$, and thus the ratio $|T_{L \rightarrow R}/T_{R \rightarrow L}|$ is the same for blue and red detuned pumps evaluated at corresponding frequencies. The reason for this is that the transmission is either amplified or suppressed simultaneously for both directions and thus their ratio stay unchanged. Comparing to the blue detuned case, the perfect nonreciprocity condition remains the same in the red detuned case, while the transmission coefficient for the through direction the hybridized mechanical modes $\Omega_{\pm} = \omega_m \pm V$ is given by (assuming $\omega_{mL} = \omega_{mR}$, $\gamma_{iL} = \gamma_{iR} = \gamma_i$ and $V \ll \kappa_k$)

$$T_{\rightarrow}[\omega_m \pm V] \simeq \sqrt{\frac{\kappa_{eL} \kappa_{eR}}{\kappa_R \kappa_L}} \frac{8i \sqrt{C_L C_R}}{[C_L + 2 \pm i \frac{\gamma_i}{2V} (C_L + 1)] [C_R + 2 \pm i \frac{\gamma_i}{2V} (C_R + 1)]}. \quad (4.22)$$

From Eq. 4.22, we note in general an attenuated transmission for the red detuned case as $T_{\rightarrow} \leq \sqrt{\kappa_{eL} \kappa_{eR} / (\kappa_L \kappa_R)} < 1$. For the case of a fast hopping rate $V/\gamma_i \gg 1$ equality is achieved when $C_k = 2$ and/or $\kappa_k/2 = \frac{G_L G_R}{\gamma_i}$. Comparing the latter to Eq. 4.16 we see the maximal through transmission efficiency is achieved when the optical cavity loss rate $\kappa_k/2$ is matched to the inter-cavity photon hopping rate J for both cavities (impedance matching condition).

4.2.6 Nonreciprocity associated with a single mechanical waveguide mode

In our optomechanical circuits, we also observed optical nonreciprocity with a single mechanical waveguide mode. In this case, the Hamiltonian describing the interaction between two optical cavity modes and one mechanical waveguide mode is given by,

$$\begin{aligned} \hat{H} = & \sum_{k=L,R} \hbar + J(+)+ \hbar\omega_{M_W} \hat{b}_W^\dagger \hat{b}_W \\ & + \sum_{k=L,R} \hbar \left(\hat{b}_W + {}^* \hat{b}_W^\dagger \right) + \sum_{k=L,R} i\hbar\sqrt{\kappa_{ek}} \alpha_{pk} e^{-i\omega_p t - i\phi_k(-)}. \end{aligned} \quad (4.23)$$

Going through a similar calculation using coupled mode equations, we find that the ratio of right and left optical transmission coefficients is

$$\frac{T_{L \rightarrow R}}{T_{R \rightarrow L}} = \frac{J \pm i \frac{|G_{WL} G_{WR}|}{-i(\omega \pm \omega_{M_W}) + \frac{\gamma_{iW}}{2}} e^{-i(\Phi_B \pm \Phi_W)}}{J \pm i \frac{|G_{WL} G_{WR}|}{-i(\omega \pm \omega_{M_W}) + \frac{\gamma_{iW}}{2}} e^{+i(\Phi_B \pm \Phi_W)}}, \quad (4.24)$$

where the upper (lower) sign corresponds to the blue (red) detuned case and $\Phi_W = \arg(G_{WL}^* G_{WR})$. The corresponding conditions for perfect directionality from left to right and at $\omega = \mp \omega_{M_W}$ are

$$J = \frac{2|G_{WL} G_{WR}|}{\gamma_{iW}}, \quad \Phi_B = \pm \frac{\pi}{2} \mp \Phi_W. \quad (4.25)$$

This in turn leads to the transmission coefficients

$$T_{\rightarrow[\mp \omega_{M_W}]} = \sqrt{\frac{\kappa_{eL} \kappa_{eR}}{\kappa_L \kappa_R}} \frac{4i\sqrt{C_{WL} C_{WR}}}{(C_{WL} \mp 1)(C_{WR} \mp 1)}. \quad (4.26)$$

In the case of blue detuned tones an input signal is amplified and the corresponding gain increases for $C_{Wk} \rightarrow 1$.

Note in Eq. 4.25 we included the phase of the product $G_{WL}^* G_{WR}$. This addition comes from the fact that we have already chosen definitions for the local cavity mode amplitudes ($a_{L,R}$ and $b_{L,R}$) such that the phase of the optomechanical couplings of the localized cavity modes – $G_L \equiv |\alpha_L|g_{0,L}$ and $G_R \equiv |\alpha_R|g_{0,R}$ – are both zero. With these same definitions for amplitudes a_L and a_R we are not then free to set the phases of *both* G_{WL} and G_{WR} to be zero; not at least for the same set of pump phases ϕ_L and ϕ_R chosen for the localized cavity mode coupling. A simple example helps to illustrate this. The mode M_W can be viewed as a hybridization between the localized left and right cavity modes and a delocalized waveguide mode [38]. Using

perturbation theory, we have for the mechanical mode amplitude of the hybridized mode M_W ,

$$b_W = b_{W'} + \frac{t_L}{-\omega_{mL}} b_L + \frac{t_R}{-\omega_{mR}} b_R, \quad (4.27)$$

where $b_{W'}$ is the unperturbed delocalized waveguide mode amplitude and $\omega_{W'}$ is the unperturbed frequency of the delocalized waveguide mode. $t_{L(R)}$ is the coupling coefficient between the delocalized waveguide mode and the localized cavity mode $M_{L(R)}$. The phases of t_L and t_R are determined by the field distribution of the hybridized mode M_W in the left and right cavities, respectively, and cannot be (both) chosen arbitrarily. Using the mode decomposition of Eq. 4.27, we have that $\arg(g_{0,WL}^* g_{0,WR}) = \arg(t_L^* t_R)$ as we have already chosen a local cavity mode amplitude basis such that $\arg(g_{0,L}) = \arg(g_{0,R}) = 0$ and $\omega_{mL}, \omega_{mR} > 0$ (this assumes of course that the left (right) optical cavity mode only couples to the portion of b_W which is due to b_L (b_R), which is a good approximation due to the fact that the optical cavities are in the far field of each other). Thus, by *simultaneously* measuring the flux-dependent transmission near the resonance of the localized mechanical cavity modes and the hybridized mechanical waveguide mode we can determine the $\arg(g_{0,WL}^* g_{0,WR})$ in this mode basis (see Fig. 4.8 for example). For the M_W mode in our experiment, we find $\arg(g_{0,WL}^* g_{0,WR}) \approx \pi$, which means for this hybridized mode and chosen localized cavity mode basis the mechanical motion in the left cavity as seen by the left cavity optical mode is approximately 180 degrees out of phase with the motion in the right cavity as seen by the right cavity optical mode.

4.3 Directional flow of quantum and thermal noise

Besides the nonreciprocal optical signal transmission, the flow of quantum and thermal noise in the optomechanical circuit is directional. This is a natural consequence of the system's scattering matrix having a directional form; the scattering matrix determines both the transmission of coherent signals, as well as noise properties. To show this, we calculate the symmetrized output noise spectral density via

$$\bar{S}_{k,out}[\omega] = \frac{1}{2} \int \frac{d\Omega}{2\pi} \left\langle \left\{ \hat{d}_{k,out}[\omega], \hat{d}_{k,out}^\dagger[\Omega] \right\} \right\rangle, \quad (4.28)$$

defined in the standard manner [24]. The mechanical and optical noise operators introduced in Eqs. 4.7 have zero mean and satisfy the canonical correlation relations:

$$\begin{aligned} \langle \hat{o}_{k,in}[\omega] \hat{o}_{k',in}^\dagger[\Omega] \rangle &= \langle \hat{o}_{k,in}^\dagger[\omega] \hat{o}_{k',in}[\Omega] \rangle + \delta_{k,k'} \delta(\omega + \Omega) \\ &= \left(n_{o_k}^{th} + 1 \right) \delta_{k,k'} \delta(\omega + \Omega), \end{aligned} \quad (4.29)$$

$$\hat{o}_{k,in} = \hat{d}_{k,in}, \hat{\xi}_{k,in}, \hat{b}_{k,in}. \quad (4.30)$$

where n_{ok}^{th} is the thermal occupation of each bath. In what follows, we assume that we have no thermal occupation of the optical field. This is justified as we work with a very high optical frequency.

Figure 4.7a-d depicts the output spectra for the situation that both pumps are blue detuned from the cavity by ω_m . Here we assumed equal mechanical frequencies $\omega_{mL} = \omega_{mR} = \omega_m$ and work in a rotating frame where the uncoupled mechanical resonance frequencies are shifted to zero. The remaining parameters are as used in the experiment, i.e., we take $\gamma_{iL}/2\pi = 4.3$ MHz, $\gamma_{iR}/2\pi = 5.9$ MHz, $\kappa_L/2\pi = 1.03$ GHz, $\kappa_R/2\pi = 0.75$ GHz, $\kappa_{iL}/2\pi = 0.29$ GHz, $\kappa_{iR}/2\pi = 0.31$ GHz, $V/2\pi = 2.8$ MHz, $J/2\pi = 110$ MHz. The multiphoton couplings $G_L = G_R$ used in the calculation are determined from Eq. 4.16.

Figure 4.7a shows the result for zero temperature mechanical baths and a finite phase $\Phi_B = 0.36\pi$ (determined from Eq. 4.16). As expected, the L and R output spectra are not identical: while each has a double-peaked structure (corresponding to the two normal mode resonances), the right output spectra $\bar{S}_{R,out}[\omega]$ has the upper-frequency peak larger than the lower-frequency peak, while the situation is reversed for the left output spectra. This does not lead to any asymmetry in the total output photon number fluxes (i.e., intergrated over all frequencies). It does however lead to an asymmetry in the energy fluxes (i.e., as the higher energy peak is bigger for the right output spectrum, and the low energy peak is bigger for the left spectrum). Thus, the "quantum heating" of zero-point fluctuations preferentially cause an energy flow to the right (rather than to the left) for this choice of phase.

It is also worth noting that if all dissipative rates are equal for the R and L cavities, then the L output spectrum is just the frequency-mirrored R output spectrum. The latter is visible in Fig. 4.7c, where we plotted the output spectra for symmetric parameters, i.e., we set $\gamma_{iR}/2\pi = \gamma_{iL}/2\pi = 4.3$ MHz, $\kappa_R/2\pi = \kappa_L/2\pi = 1.03$ GHz, $\kappa_{iR}/2\pi = \kappa_{iL}/2\pi = 0.31$ GHz and $\Phi_B = 0.38\pi$ (determined from Eq. 4.16 for the new γ_{iR}). However, having unequal decay rates, i.e., $\gamma_R \neq \gamma_L$ and $\kappa_R \neq \kappa_L$, leads to a slight asymmetry even if the phase is set to zero, i.e., $\Phi_B = 0$, as visible in Fig. 4.7b. In Fig. 4.7g we plot the asymmetry $\bar{S}_{L,out}[\omega] - \bar{S}_{R,out}[\omega]$ for all the four cases corresponding to Fig. 4.7a-d.

For finite temperature, we find that the output spectrum has a roughly linear dependence on the mechanical bath temperature: $\bar{S}_{k,out}(T) = c_k n^{th} + \bar{S}_{k,out}(0)$ (assuming $n_{bL}^{th} = n_{bR}^{th} \equiv n^{th}$). This linear dependence is visible if we compare Fig. 4.7c,d and Fig. 4.7e,f, where the latter show the output noise spectra for $n^{th} = 10$ with sym-

metric cavity parameters. Additionally, we also calculate the added noise quanta to the transmitted signal

$$\bar{n}_{k,add}[\omega] \equiv \frac{\bar{S}_{k,out}[\omega]}{|T_k[\omega]|^2} - \frac{1}{2}, \quad (4.31)$$

where $\frac{1}{2}$ is the half quanta noise of the vacuum optical fields injected from the coupler. Fig. 4.7h shows the added noise for left-right propagation with $\Phi_B = 0.36\pi$ (and asymmetric experimental cavity parameters). The mechanical baths n^{th} are varied as denoted in each graph. Even if the cavities and the mechanics are only driven by vacuum noise the standard quantum limit (SQL) of half a quanta is not achieved. This is due to the limited amount of gain achieved in the experiment, i.e., the transmission coefficient is not high enough to suppress the noise contributions. Moreover, even in the large gain limit the added noise would be roughly one quanta due to the finite amount of intrinsic optical cavity loss.

4.4 Reciprocal device

Realizing optical nonreciprocity in the optomechanical circuits studied in this work is not simple or easy as just creating a circuit with optical and mechanical coupling between two optomechanical cavities. One is limited by the practical realities of device power handling capability, finite optical and mechanical Q -factors, etc. As such, not all the circuits that were tested exhibited nonreciprocal transmission and amplification; the effects were too weak to observe in some circuits. This, however, was a useful test of our set-up as nonreciprocity could be effectively turned on and off by looking at different circuits with only slightly different parameters.

Eq. 4.17 sets the desired circuit parameters in order to achieve significant nonreciprocity, which for the optomechanical coupling, optical and mechanical Q -factors, and the power handling capabilities of the nanobeam cavities requires optical hopping rate between cavities to be less than $J/2\pi \approx 500$ MHz. Devices with larger coupling rates can simply not be pumped hard enough to satisfy $G_k \approx (J\gamma_{ik})^{1/2}$. To confirm this, here we show another optomechanical crystal circuit with bare cavity wavelengths of $\lambda_{L(R)} = 1535.051$ (1535.060) nm and inter-cavity photon hopping rate of $J/2\pi = 1.4$ GHz (more than ten times larger than the device studied). The mechanical spectra of this device as measured from both the left and right optical cavities is shown in Fig. 4.8a. Figure 4.8b shows the normalized transmission coefficient for forward and reverse optical signal propagation for a blue-detuned pump wavelength of $\lambda_p = 1534.99$ nm and synthetic flux of $\Phi_B = \pi/2$. Even at the largest pump powers ($P_p \approx 100 \mu\text{W}$; $n_c \approx 1.5 \times 10^3$) this device does not satisfy the

condition of Eq. 4.17 due to the large J , resulting in nearly perfect reciprocity in the optical signal transmitted power. These measurements were performed on the exact same set-up as the circuit studied.

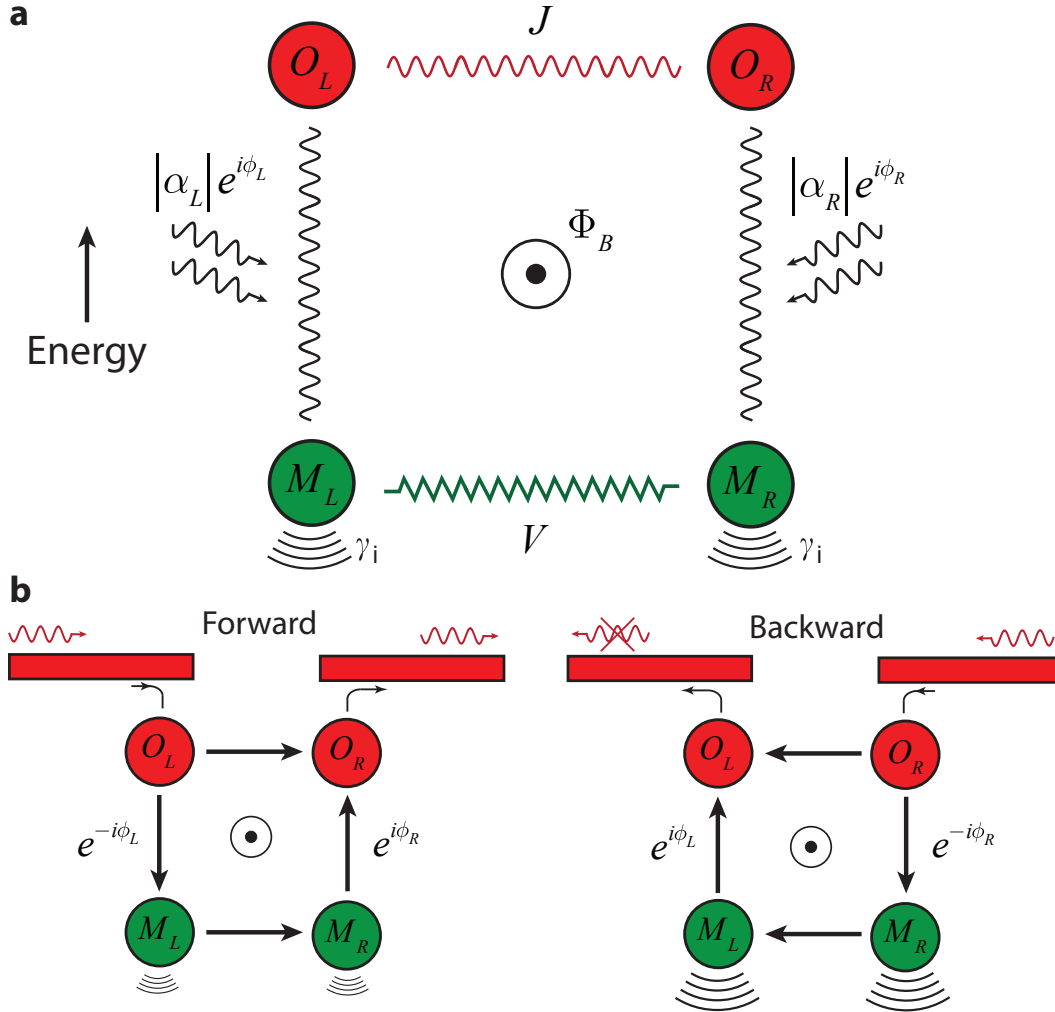


Figure 4.1: **Synthetic magnetic field in an optomechanical cavity system.** **a**, In this scheme consisting of only two optomechanical cavities, a two-dimensional plaquette can be formed from the synthetic dimension [114] created by radiation pressure coupling from the optical modes to the mechanical modes. Photon hopping at rate J and phonon hopping at rate V occurs between the optical and mechanical cavities, respectively, with J and V real for appropriate choice of gauge. Pumping of the optomechanical cavities with phase correlated laser light ($|\alpha_L|e^{i\phi_L}$ for the left cavity and $|\alpha_R|e^{i\phi_R}$ for the right cavity) results in a synthetic flux $\Phi_B = \phi_L - \phi_R$ threading the 4-mode plaquette. **b**, Scheme for detecting the synthetic flux through nonreciprocal power transmission of an optical probe laser field. For forward (L \rightarrow R) propagation, constructive interference set by the flux-dependent phase $\Phi_B \approx \pi/2$ of the dissipative phonon coupling path results in efficient optical power transmission. The accumulated phase in the phonon coupling path is reversed for the backward (R \rightarrow L) propagation direction resulting in destructive interference and reduced optical power transmission in the left output waveguide. The power in this case is sunk into the mechanical baths.

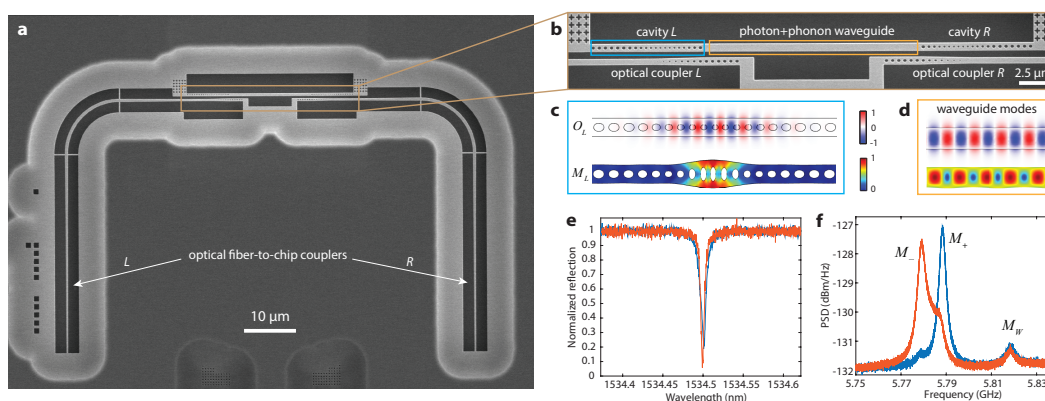


Figure 4.2: **Silicon optomechanical crystal circuit.** **a**, Scanning electron microscopy (SEM) image of the optomechanical crystal circuit studied in this work. The circuit is fabricated from a silicon-on-insulator microchip (see App. 4.1). **b**, SEM of the main part of the circuit, which consists of a left and a right nanobeam optomechanical crystal cavity with a central unpatterned nanobeam waveguide connecting the two cavities. A left and right optical coupler, which are each fed by an adiabatic fiber-to-chip coupler [46], are used to evanescently couple light into either of the two optical cavities. **c**, FEM simulated electrical field E_y and magnitude of the displacement field for the localized optical and mechanical cavity modes, respectively, of the nanobeam. **d**, FEM simulated section of the corresponding optical and mechanical modes of the connecting waveguide. **e**, Optical reflection spectrum of the left (blue) and right (orange) optical cavities. **f**, Optically transduced mechanical power spectral density (PSD) measured from the left (blue) and right (orange) optical cavities. M_{\pm} are the two hybridized mechanical cavity modes with frequency $\omega_{M_{+(-)}}/2\pi = 5788.4$ (5779.1) MHz and M_W is a mechanical waveguide mode with frequency $\omega_{M_W}/2\pi = 5818.3$ MHz.

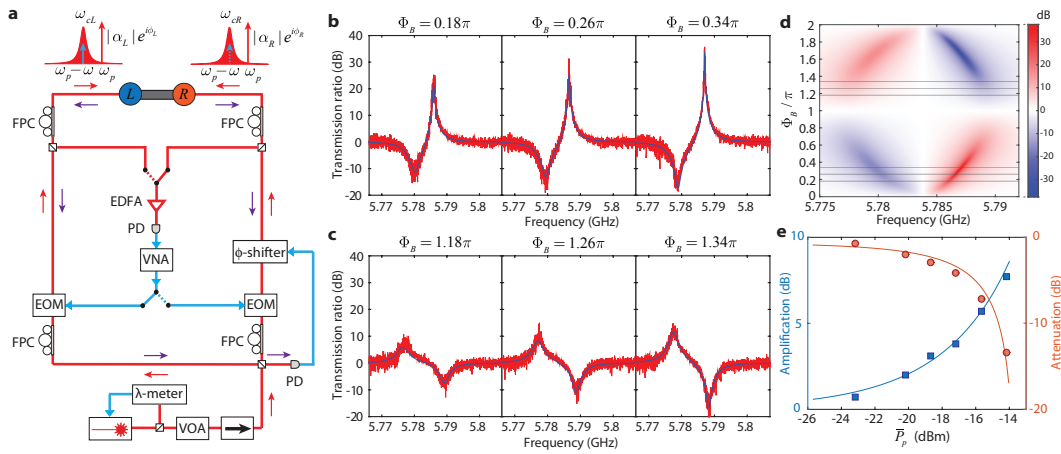


Figure 4.3: Measurement of optical nonreciprocity. **a**, Experiment set-up. Red (blue) lines are optical (electronic) wiring. Blue-detuned pump light from a tunable diode laser is split into two paths and fed into the two cavities (red arrows). Part of the reflected pump laser light from the cavities (purple arrows) is collected by a photodetector (PD) and fed into a stretchable fiber phase shifter (ϕ -shifter) to tune and lock the phase difference of the optical pumps. Each optical path can be modulated by an electro-optic modulator (EOM) to generate an optical sideband which we use as the optical probe signal. The microwave modulation signal with frequency ω_{mod} is generated by port 1 of a vector network analyzer (VNA). After optical amplification and photodetection, the transmitted optical probe signal through the optomechanical circuit is sent back to port 2 of the VNA to measure the phase and amplitude of the optical probe transmission coefficient. EDFA: Erbium doped fiber amplifier, FPC: fiber polarization controller, λ -meter: wavelength meter. **b**, The ratio of optical power transmission coefficients for right- and left-propagation versus modulation frequency ($\omega_{\text{mod}} = -\omega = \omega_p - \omega_s$), for three different synthetic flux values $\Phi_B/\pi = 0.18, 0.26$, and 0.34 . The blue curves correspond to the fit of the theoretical model (c.f. Eq. 4.3) to the measured spectra. **c**, The power transmission coefficient ratio for Φ_B with an additional π flux relative to those in **b**. **d**, Theoretical calculation of the power transmission coefficient ratio for $0 \leq \Phi_B \leq 2\pi$, where the six grey lines correspond to the six measured Φ_B values in **b** and **c**. **e**, Peak forward signal amplification above background level (blue squares) and corresponding signal attenuation in the reverse direction (red circles) versus average optical pump power ($\bar{P}_p = \sqrt{P_{pL}P_{pR}}$) for fixed flux value of $\Phi_B = 0.28\pi$. The solid curves are theoretical calculations based upon the theoretical model (c.f. Eq. 4.3 and SI) fit to the data in **b** and **c**.

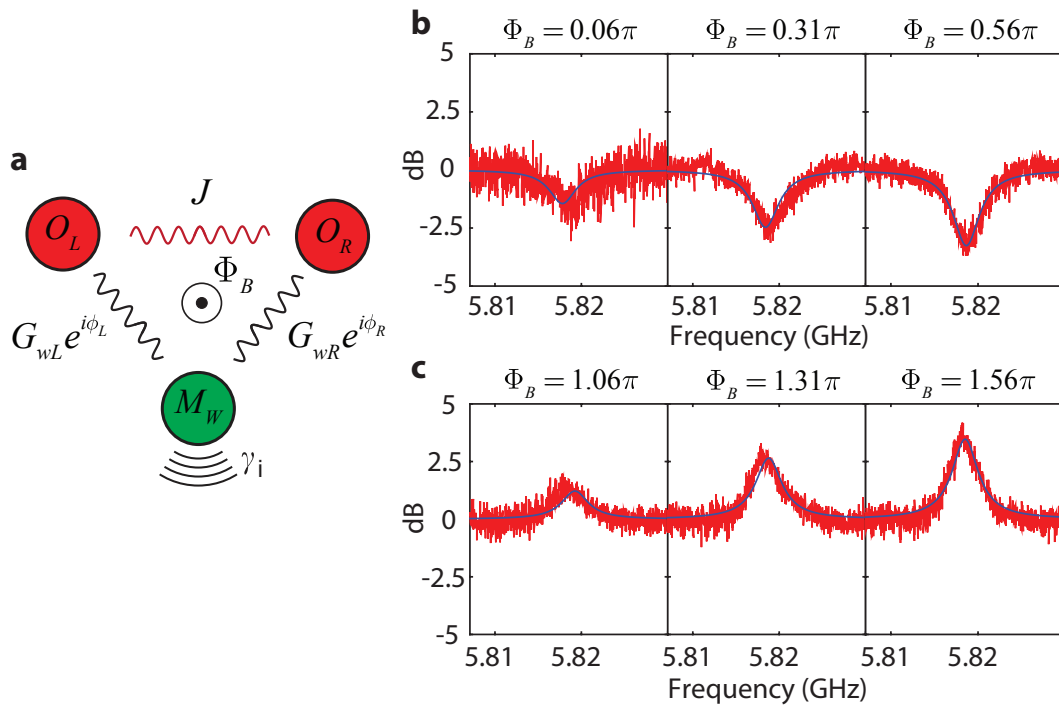


Figure 4.4: **Synthetic magnetic field with a single mechanical cavity.** **a**, Physical configuration for generation of a synthetic magnetic field and optical nonreciprocity with two optical modes parametrically coupled with a common dissipative mechanical waveguide mode. **b,c** The ratio of optical power transmission coefficients for right and left propagation versus modulation frequency ω_{mod} around the frequency of the waveguide mode M_W for various Φ_B . The blue curves correspond to a fit of the theoretical model (see App. 4.2) to the measured data.

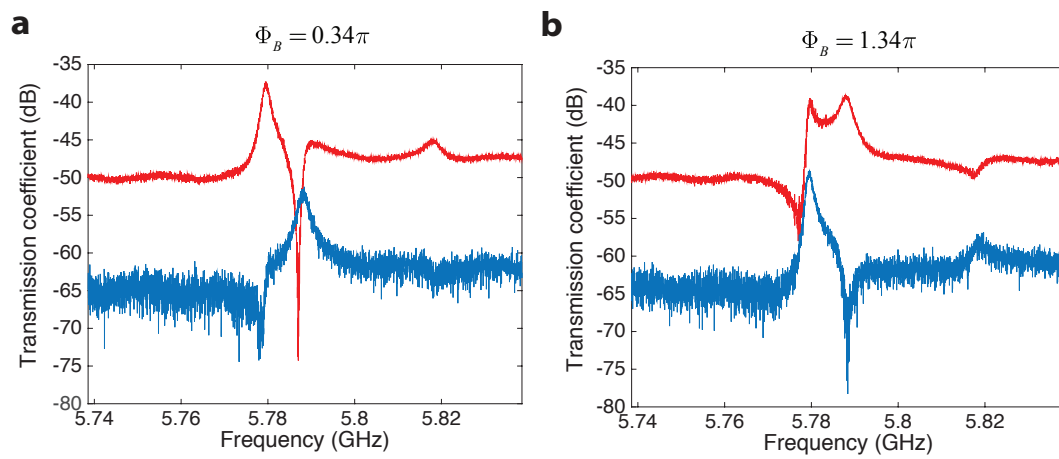


Figure 4.5: **a** Microwave signal power transmission through the optomechanical circuit for forward (right-propagation; blue) and backward (left-propagation; blue curve) directions, with flux set to $\Phi_B = 0.34\pi$ and cavity photon number $n_{cL} = 1000$ and $n_{cR} = 1420$. **b** Same as **a** but with $\Phi_B = 1.34\pi$.

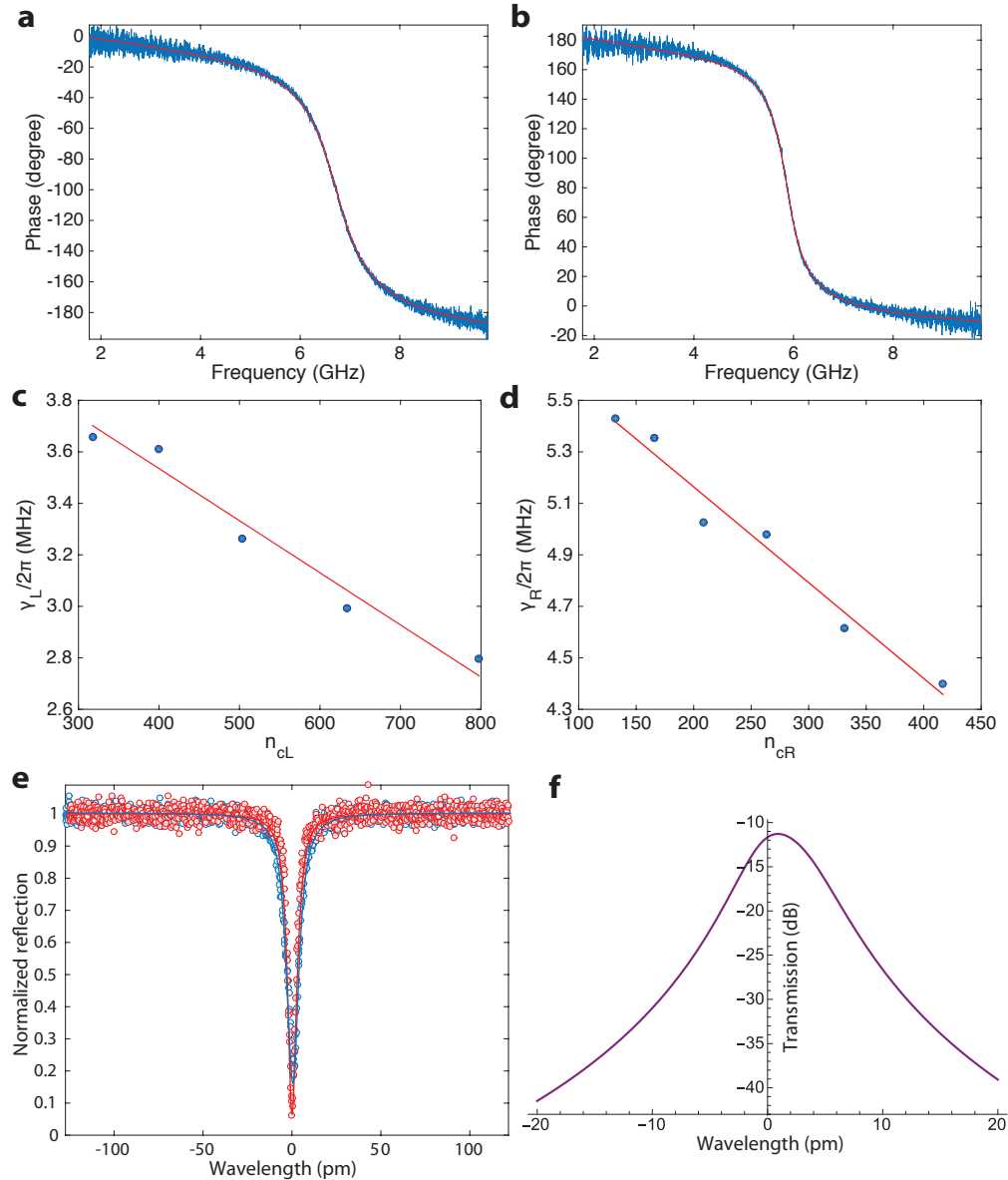


Figure 4.6: **a**, Left optical cavity phase response as measured by scanning the probe signal across the cavity resonance with weak blue-detuned pump. **b**, Same as in **a** for the right optical cavity. **c**, Measured back-action modified mechanical linewidth versus intra-cavity pump photon number for the left optical cavity. Here only left cavity pump beam is applied, and the pump is tuned to the upper motional sideband of the cavity (blue-detuned with $\Delta = +\omega_{mL}$). **d**, Same as in **c** for the right-side cavity and right-side pump. Measurements in **a** – **d** were performed prior to nano-oxidation tuning. **e** Measured (circles) and theoretical (solid curves) optical reflection spectra using a left-cavity (blue) and right-cavity (red) optical pump. These measurements are taken after nano-oxidation and the theoretical calculation includes the fit coupling ($J/2\pi = 110$ MHz) between the left and right optical cavity modes and a splitting between the uncoupled modes. The wavelength origin is taken to correspond to the right optical cavity resonance. **f** Calculated optical transmission power from one optical port to the other of an optical probe signal near resonance of the coupled optical cavity modes. Here there is no pump beam, and so no coupling to phonons. The parameters of the optical cavity modes are taken from the fit to the measured optical reflection spectra in **e**.

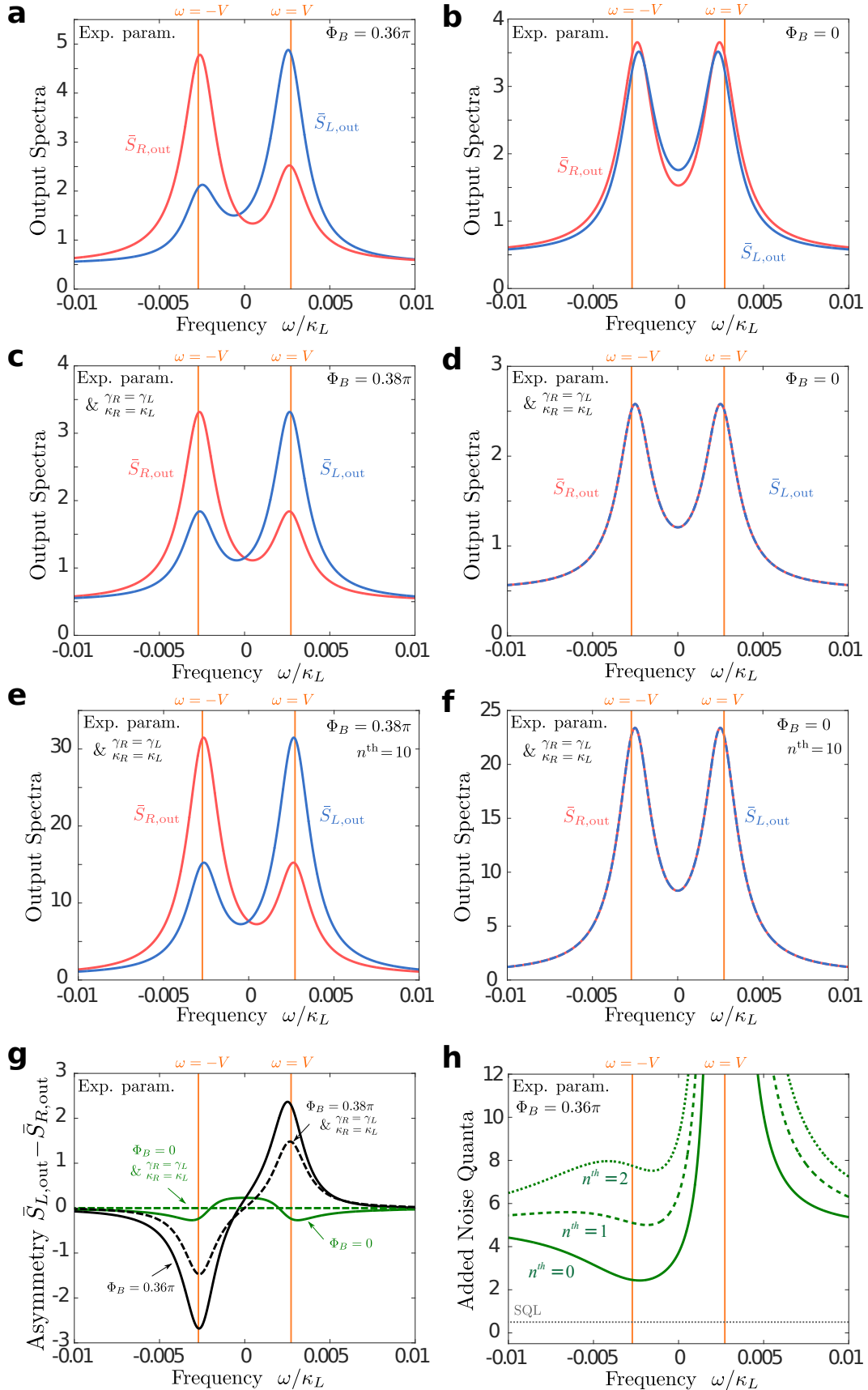


Figure 4.7: **a-d** Output noise spectra at zero temperature for a set of parameters given in the text. **e-f** Output noise spectra at finite temperature with thermal phonon occupation of $n^{th} = 10$. **g** Difference of the left and right output spectra for **a-d**. **f** Added noise for right-propagation signal.

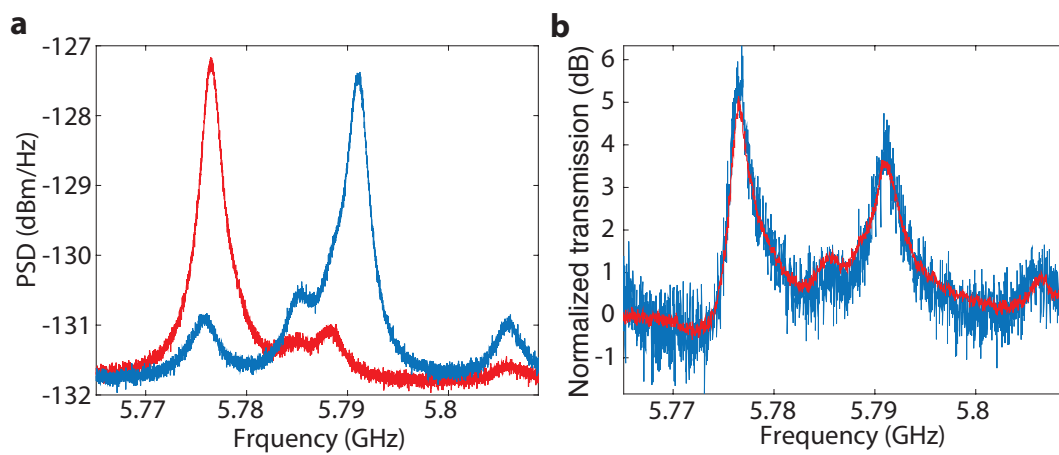


Figure 4.8: Optical reciprocity in a circuit with large optical cavity coupling, J . **a** Mechanical spectra measured from the left (red) and right (blue) optical cavities. **b** Normalized optical signal power transmission coefficient for forward (red) and reverse (blue) optical signal propagation.

ULTRA-HIGH QUALITY NANO-MECHANICAL RESONATOR

With the rapid progress of quantum science and technologies in recent years, the need for a high quality quantum memory device for various applications has driven efforts in developing systems from trapped cold atoms, high quality 3 dimensional microwave cavity, nuclear spins in nitrogen centers, and topological materials. Nano-mechanical resonators have shown in many cases to be a promising platform for storing energy over a relatively long time. This Chapter will present our work on creating a 5 GHz nano-mechanical resonator that can have energy relaxation time around 1 second in 10 mk environment. Such ultra-high quality nano-mechanical resonators can be integrated with a superconducting quantum circuit as quantum memory elements.

5.1 Phononic bandgap structure

Phononic bandgap structures, similar to their electromagnetic counterparts, can be used to modify the emission or scattering of phonons. These ideas have recently been explored in quantum optomechanics [6, 18, 138, 134, 43] and electromechanics [58] experiments to greatly reduce the mechanical coupling to the thermal environment through acoustic radiation. At ultrasonic frequencies and below, one can combine phononic bandgap clamping with a form of ‘dissipation dilution’ in high stress films [128] to realize quality (Q) factors in excess of 10^8 in two-dimensional nanomembranes [134] and approaching 10^9 in one-dimensional strain-engineered nanobeams [43]. At higher, microwave frequencies the benefit of stress-loading of the film fades as local strain energy dominates [43] and one is left once again to deal with intrinsic material absorption.

To date, far less attention has been paid to the impact of geometry and phononic bandgaps on acoustic material absorption [15, 54]. Fundamental limits to sound absorption in solids are known to result from the anharmonicity of the host crystal lattice [69, 121, 133]. At low temperatures T , in the Landau-Rumer regime ($\omega\tau_{\text{th}} \gg 1$) where the thermal phonon relaxation rate (τ_{th}^{-1}) is much smaller than the acoustic frequency (ω), a quantum model of three-phonon scattering can be used to describe phonon-phonon mixing that results in damping and thermalization of acoustic modes [69, 121]. Landau-Rumer damping scales approximately as T^α ,

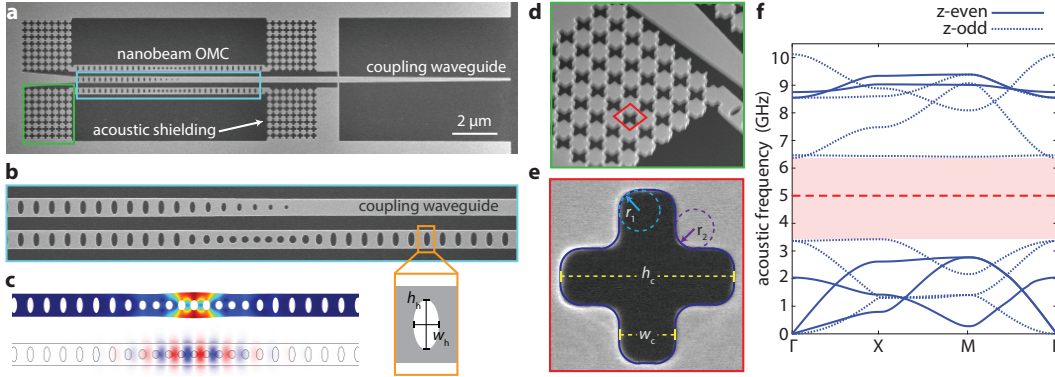


Figure 5.1: Nanobeam optomechanical crystal and phononic shield design. **a**, Scanning electron microscope (SEM) image of a full nanobeam optomechanical crystal (OMC) device fabricated on SOI with $N = 7$ periods of acoustic shielding. A central coupling waveguide allows for fibre-to-chip optical coupling as well as side-coupling to individual nanobeam OMC cavities. **b**, SEM image of an individual nanobeam OMC and the coupling waveguide, with enlarged illustration of an individual unit cell in the end-mirror portion of the nanobeam. **c**, FEM simulations of the mechanical (top; total displacement) and optical (bottom; transverse electric field) modes of interest in the nanobeam. Distortion of the mechanical displacement profile is exaggerated for clarity. **d**, SEM image showing the nanobeam clamping geometry. **e**, SEM image of an individual unit cell of the cross-crystal acoustic shield. The dashed lines show fitted geometric parameters used in simulation, including cross height ($h_c = 474$ nm), cross width ($w_c = 164$ nm), inner fillet radius (r_1), and outer fillet radius (r_2). **f**, Simulated acoustic band structure of the realized cross-crystal shield unit cell, with the full acoustic bandgap highlighted in pink. Solid (dotted) lines correspond to modes of even (odd) symmetry in the direction normal to the plane of the unit cell. The dashed red line indicates the mechanical breathing-mode frequency at $\omega_m/2\pi = 5.0$ GHz.

where $\alpha \approx 4$ depends upon the phonon dispersion and density of states (DOS) [121]. At the very lowest lattice temperatures ($\lesssim 10$ K), where Landau-Rumer damping has dropped off, a residual damping emerges due to material defects. These two-level system (TLS) defects [96], typically found in amorphous materials, correspond to a pair of nearly degenerate local arrangements of atoms in the solid which can have both an electric and an acoustic transition dipole, and couple to both electric and strain fields. Recent theoretical analysis shows that TLS interactions with acoustic waves can be dramatically altered in a structured material [15].

5.2 Limits of acoustic damping

Here we explore the limits of acoustic damping and coherence of a microwave acoustic nanocavity with a phononic crystal shield that possesses a wide bandgap for all polarizations of acoustic waves. Our nanocavity, formed from an optomechanical crystal (OMC) nanobeam resonator [32, 18], supports an acoustic breathing mode at $\omega_m/2\pi \approx 5$ GHz and a co-localized optical resonant mode at $\omega_c/2\pi \approx 195$ THz ($\lambda_c \approx 1550$ nm) which allows us to excite and readout mechanical motion using radiation pressure from a pulsed laser source. This minimally invasive pulsed measurement technique avoids a slew of parasitic damping effects – typically associated with electrode materials and mechanical contact [41], or probe fields for continuous readout – and allows for the sensitive measurement of motion at the single phonon level [81]. The results of acoustic ringdown measurements at millikelvin temperatures show that damping due to radiation is effectively suppressed by the phononic shield, with breathing mode quality factors reaching $Q = 4.9 \times 10^{10}$, corresponding to an unprecedented frequency- Q product of $f \cdot Q = 2.6 \times 10^{20}$. The temperature and amplitude dependence of the residual acoustic damping is consistent with relaxation damping of non-resonant TLS, modeling of which indicates that not only does the phononic bandgap directly eliminate the acoustic radiation of the breathing mode but it also reduces the phonon damping of TLS in the host material.

5.3 Device design and fabrication

The devices studied in this work are fabricated from the 220 nm device layer of a silicon-on-insulator (SOI) microchip. Details of the fabrication process are provided in [74]. In Figs. 5.1(a-b) we show scanning electron microscope images of a single fabricated device, which consists of a coupling optical waveguide, the nanobeam OMC cavities that support both the microwave acoustic and optical resonant modes, and the acoustic shield that connects the cavity to the surrounding chip substrate. Fig. 5.1c shows finite-element method (FEM) simulations of the microwave acoustic breathing mode and fundamental optical mode of the nanobeam cavity. We use the on-chip coupling waveguide to direct laser light to the nanobeam OMC cavities. A pair of cavities with slightly different optical mode frequencies are evanescently coupled to each waveguide. An integrated photonic crystal back mirror in the waveguide allows for optical measurement in a reflection geometry. The design of the OMC cavities, detailed in Ref. [18], uses a tapering of the etched hole size and shape in the nanobeam to provide strong localization and overlap of the breathing mode and the fundamental optical mode, resulting in a vacuum optomechanical

coupling rate [12] between photons and phonons of $g_0/2\pi \approx 1$ MHz.

In order to minimize mechanical clamping losses, the nanobeam is anchored to the Si bulk with a periodic cross structure which is designed to have a complete phononic bandgap at the breathing mode frequency [18]. Through tuning of the cross height h_c and width w_c (c.f., Figs. 5.1(d-e)), bandgaps as wide as ~ 3 GHz can be achieved as shown in Fig. 5.1. We analyze SEM images of realized structures to provide accurate structure dimensions for our FEM models, and in particular we include in our modeling a filleting of the inner and outer corners (r_1 and r_2 in Fig. 5.1e) of the crosses arising from technical limitations of the patterning of the structure. To investigate the efficacy of the acoustic shielding we fabricate and characterize arrays of devices with a scaling of the cross period number from $N_{\text{shield}} = 0$ to 10, with all other design parameters held constant. FEM modeling indicates (see [74]) that the addition of the cross shield provides significant protection against nanometer-scale disorder which is inherently introduced during device fabrication.

5.4 Optical Ringdown measurements

Optical measurements of the acoustic properties of the OMC cavity are performed at millikelvin temperatures in a dilution refrigerator. The sample containing an array of different OMC devices is mounted directly on a copper mount attached to the mixing chamber stage of the fridge, and a single lensed optical-fiber is positioned with a 3-axis stage to couple light into and out of each device [81]. In a first set of measurements of acoustic energy damping, we employ a single pulsed laser scheme to perform both excitation and readout of the breathing mode. In this scenario, depicted in Fig. 5.2a, the laser frequency (ω_l) is tuned to the red motional sideband of the OMC cavity optical resonance, $\Delta \equiv \omega_c - \omega_l \approx +\omega_m$, and is pulsed on for a duration T_{pulse} and then off for a variable time T_{off} . This produces a periodic train of photon pulses due to anti-Stokes scattering of the probe laser which are on-resonance with the optical cavity. The anti-Stokes scattered photons are filtered from the probe laser and sent to a single photon detector producing a photon count rate proportional to the number of phonons in the acoustic resonator (see [74] for details of the measurement set-up and phonon number calibration methods).

We display in Fig. 5.2b a typical readout signal, showing the normalized phonon occupancy during and immediately after the application of a $4 \mu\text{s}$ pulse. The initial optomechanical back-action cooling of the acoustic breathing mode is followed by a slower turn-on of heating of the mode during the pulse. After the pulse,

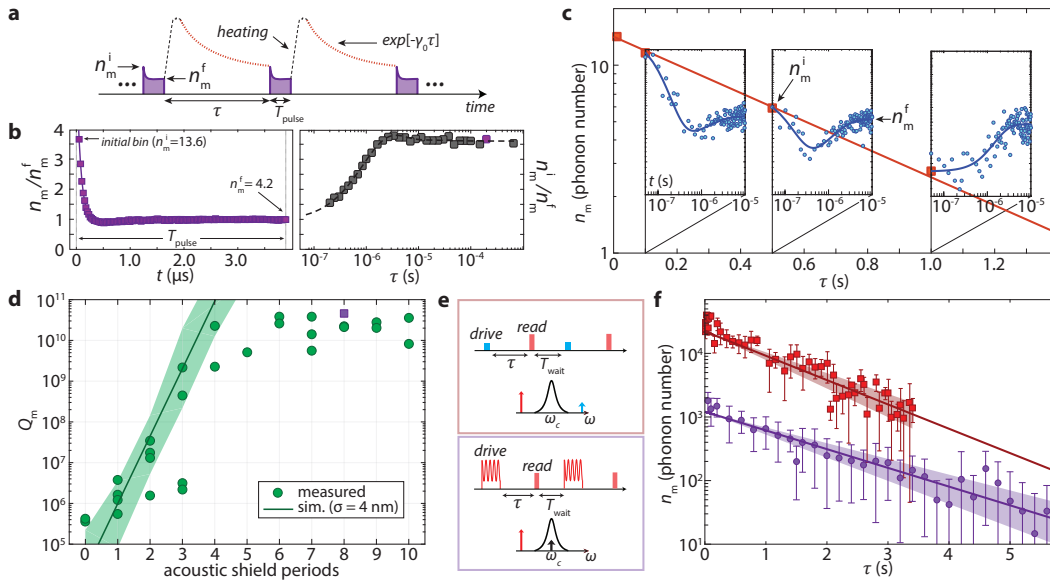


Figure 5.2: Ringdown measurements of the acoustic breathing mode. **a**, Illustration of the ringdown measurement performed using a red-detuned ($\Delta = +\omega_m$) pulsed laser for excitation and readout. **b**, Normalized phonon occupancy measured during (left) and after (right) the laser readout pulse ($n_c = 569$; optomechanical back-action rate $\gamma_{\text{OM}}/2\pi = 1.07$ MHz) for a 6-shield device (device B). Squares are measured data points. Solid and dashed lines are a best fit to the dynamical model of the hot bath (see [74]). The displayed pulse-on-state plot (left) corresponds to a delay of $T_{\text{off}} = 200 \mu\text{s}$, with $n_m^i = 4.2$ and $n_m^f = 13.6$ phonons. **c**, Ringdown measurements of a 7-shield device (device C) for readout pulse amplitude of $n_c = 320$. The series of inset panels show the measured (and fit; solid blue curve) anti-Stokes signal during the optical pulse at a series of pulse delays. **d**, Plot of the measured breathing mode Q -factor versus number of acoustic shield periods N_{shield} . The solid green line is a fit to the corresponding simulated radiation-limited Q -factor (see [74]) for devices with standard deviation (SD) $\sigma = 4$ nm disorder in hole position and size, similar to the value measured from device SEM image analysis. The shaded green region corresponding to the range of simulated Q values (ensemble size 10) within one SD of the mean. The square purple data points represents the measured Q in **(f)**. **e**, Acoustic excitation is performed coherently by using either a blue-detuned pump (upper diagram) to drive the breathing mode into self-oscillation, or using an RF-modulated red-detuned pump [110] (lower diagram). See [74] for details of the coherent excitation and readout parameters. **f**, Ringdown measurements performed on an eight-shield device (device D) at large phonon amplitude. For blue-detuned driving (red squares) the fit decay rate is $\gamma_0/2\pi = (0.122 \pm 0.020)$ Hz. For modulated-pump driving (purple circles) the fit decay rate is $\gamma_0/2\pi = (0.108 \pm 0.006)$ Hz. The error bars are 90% confidence intervals of the measured values of n_m^i . The shaded regions are the 90% confidence intervals for the exponential fit curves.

with the back-action cooling turned off, a transient heating of the acoustic mode occurs over several microseconds. The parasitic heating is attributable to very weak optical absorption of the probe pulse in the Si cavity which produces a hot bath coupled to the breathing mode [81]. Here we use the transient heating of the acoustic mode to perform ringdown measurements of the stored phonon number. A phenomenological model of the dynamics of the induced damping (γ_p) and effective occupancy (n_p) of the hot bath (see [74]) allows us to fit the anti-Stokes decay signal. Plotting the initial mode occupancy at the beginning of the fit readout pulse (n_m^i) versus delay time T_{off} between pulses (c.f., Fig. 5.2a), we plot the ringdown of the stored phonon number in the the breathing mode as displayed in Fig. 5.2c for a device with $N_{\text{shield}} = 7$.

Performing a series of ringdown measurements over a range of devices with varying N_{shield} , and fitting an exponential decay curve to each ringdown we produce the Q -factor plot in Fig. 5.2d. We observe an initial trend in Q -factor versus shield number which rises on average exponentially with each additional shield period, and then saturates for $N_{\text{shield}} \geq 5$ to $Q_m \gtrsim 10^{10}$. As indicated in Fig. 5.2c these Q values correspond to ringdown of small, near-single-phonon level amplitudes. We also perform ringdown measurements at high phonon amplitude using two additional methods displayed schematically in Fig. 5.2e and described in detail in [74]. These methods use two laser tones to selectively excite the acoustic breathing mode using a $\times 1000$ weaker excitation and readout optical pulse amplitude ($n_c \lesssim 0.3$). The measured ringdown curves, displayed in Fig. 5.2f, show the decay from initial phonon occupancies of 10^3 - 10^4 of an 8-shield device (device D; square purple data point in Fig. 5.2d). The two methods yield similar breathing mode energy decay rates of $\gamma_0/2\pi = 0.108$ Hz and 0.122 Hz, the smaller of which corresponds to a Q -value of $Q_m = 4.92_{-0.26}^{+0.39} \times 10^{10}$ and a phonon lifetime of $\tau_{\text{ph},0} = 1.47_{-0.08}^{+0.09}$ s. Comparing all three excitation methods with widely varying optical-absorption-heating and phonon amplitude, we consistently measure $Q_m \gtrsim 10^{10}$ for devices with $N_{\text{shield}} \geq 5$.

5.5 Temperature dependent damping

In order to understand the origin of the residual damping for large N_{shield} we also measured the temperature dependence of the energy damping rate, breathing mode frequency, and full width at half maximum (FWHM) linewidth of the breathing mode for the highest Q 8-shield device (device D). In Fig. 5.3a we plot the energy damping rate which shows an approximately linear rise in temperature up to $T_f \approx 100$ mK,

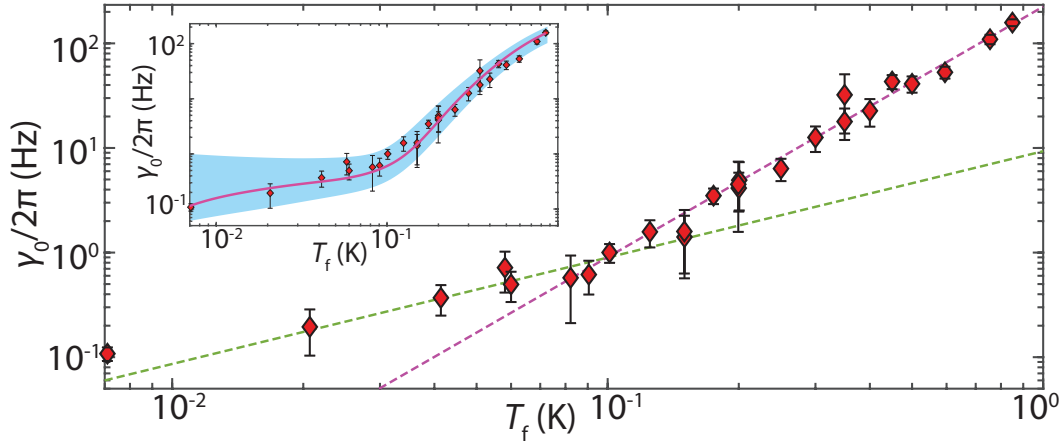


Figure 5.3: **Temperature dependence of acoustic damping, frequency, and frequency jitter.** Plot of the measured breathing mode energy damping rate, $\gamma_0/2\pi$, as a function of fridge temperature (T_f). Dashed green (magenta) curve is a fit with temperature dependence $\gamma_0 \sim T_f^{1.01}$ ($\gamma_0 \sim T_f^{2.39}$). Error bars are 90% confidence intervals of the exponential fit to measured ring down curves. Inset: Plot of measured damping data with estimated energy damping from a TLS model (see [74]). The shaded blue region corresponds to the standard deviation of $\log(\gamma_0/2\pi)$ for 100 different random TLS distributions.

and then a much faster $\sim (T_f)^{2.4}$ rise in the damping.

Estimates of the magnitude of Landau-Rumer damping of the breathing mode (see [74]) indicate that 3-phonon scattering in Si is far too weak at $T_f \lesssim 1$ K to explain the measured damping. Analysis of the interactions of TLS with the localized acoustic modes of the confined geometry of the OMC cavity structure, however, show that TLS interactions can explain all of the observed breathing mode behavior. In this analysis, detailed in [74], FEM simulation is used to find the frequencies and radiation-limited damping rates of the acoustic quasi-normal modes of the OMC cavity structure. An estimate of the spectral density of TLS within the breathing mode volume ($V_m \approx 0.11 (\mu\text{m})^3$) is ascertained from estimated surface oxide (~ 0.25 nm [135]) and etch-damage (~ 15 nm [91]) layer thicknesses in the Si device, and bulk TLS density found in amorphous materials [63, 96]. Using the resulting effective spectral density of interacting TLS, $n_{0,m} \approx 20 \text{ GHz}^{-1}$, and average TLS transverse and longitudinal deformation potentials of $\bar{M} \approx 0.04$ eV and $\bar{D} \approx 3.2$ eV, respectively, yields breathing mode damping and frequency shifts which are in excellent agreement with the measured data (see Fig. 5.3). The estimated level of frequency jitter is also found in agreement with the measured value, assuming all

TLS are being pumped via the same optical absorption that drives the hot bath.

Several key observations can be drawn from the TLS damping modeling. The first is that the typical T^3 dependence of TLS relaxation damping of acoustic waves is dependent on the phonon bath DOS into which the TLS decay [15, 54]. In the OMC cavity the phonon DOS is strongly modified from a three-dimensional bulk material. This directly results in the observed weak temperature dependence of the acoustic damping for $T_f \lesssim 100$ mK, where the thermally activated TLS interact resonantly with an approximately one-dimensional phonon DOS. A second point to note is that the TLS resonant damping is strongly suppressed due to the phononic bandgap surrounding the OMC cavity. Estimates of the phonon-induced spontaneous decay rate of TLS in the bandgap is on the order of Hz; combined with the discrete number of TLS in the small mode volume of the breathing mode, acoustic energy from the breathing mode cannot escape via resonant coupling to TLS. The observed lack of saturation of the breathing mode energy damping with either temperature or phonon amplitude is further evidence that non-resonant relaxation damping – due to dispersive coupling to TLS – is dominant [96]. Finally, the small average number of estimated TLS in V_m which are thermally activated at the lowest temperatures (~ 2), leads to significant variation in the simulated TLS relaxation damping at $T_f \sim 10$ mK (see shaded blue region of the inset to Fig. 5.3). This is consistent with the observed fluctuations from device-to-device in the low-temperature Q_m for devices with $N_{\text{shield}} > 5$ (see Fig. 5.2d).

Utilizing the advanced methods of nanofabrication and cavity optomechanics has provided a new toolkit to explore quantum acoustodynamics in solid-state materials. Continued studies of the behavior of TLS in similar engineered nanostructures to the OMC cavity of this work may lead to, among other things, new approaches to modifying the behavior of quasi-particles in superconductors [104], mitigating decoherence in superconducting [42, 79] and color center [119, 13] qubits, and even new coherent TLS-based qubit states in strong coupling with an acoustic cavity [99]. The extremely small motional mass ($m_{\text{eff}} = 136$ fg [18]) and narrow linewidth of the OMC cavity also make it ideal for precision mass sensing [51] and in exploring limits to alternative quantum collapse models [88]. Perhaps most intriguing is the possibility of creating a hybrid quantum architecture consisting of acoustic and superconducting quantum circuits [29, 98, 47, 23, 75, 113, 84, 10], where the small scale, reduced cross-talk, and ultralong coherence time of quantum acoustic devices may provide significant improvements in performance of current quantum hardware.

*Chapter 6***QUANTUM ACOUSTICS WITH PIEZOELECTRIC STRONG COUPLING BETWEEN SUPERCONDUCTING CIRCUITS AND PHONONIC RESONANCES**

As shown in the last chapter, nano-mechanical cavity isolated from the environment with two-dimensional phononic crystal shield can achieve a strikingly long energy relaxation time approaching one second for a mode frequency around 5 GHz. Furthermore, the high quality phononic resonator is a small footprint ($\sim 10 \mu\text{m}$) planar structure in a suspended silicon membrane. Considering that mode frequency of this resonator is compatible with the state of art superconducting quantum circuit, it provides an attractive way to integrate multiple high quality phononic cavities with a qubit as a multi-mode quantum memory bank that can be used to realize a Von Neumann architecture for scalable quantum computing. In order to enable the state transfer between a superconducting microwave circuit and the mechanical degree of freedom efficiently, piezoelectric materials can be used to construct the transduction interface. Piezoelectric materials have inversion symmetry broken crystal structure that can be electrically polarized in response to a strain field in the crystal as in Fig. 1.6 and Fig. 1.5. This transduction mechanism can directly map a mechanical mode's strain profile into a coherently vibrating electrical dipole ensemble. In the following subsections, I will first introduce the piezo-phononic transducer we created to efficiently transduce between an microwave photon in the electric circuit and an mechanical phonon in a mechanical mode of interest. After introducing the interface we built to bridge the gap between the electric domain and acoustic domain, I will present a viable architecture that can be used to efficiently couple a high coherence superconducting transmon qubit to an ultra-high coherence phononic cavity via an engineered hybrid virtual coupling channel which is composed of a tunable electric resonator and a high coupling piezoacoustic cavity on a two-dimensional phononic crystal. In the end, I will introduce the efficient quantum optical-microwave transducer that can be enabled by the piezoelectric transducer and opportunities in adopting new materials for close to unity efficiency microwave field to acoustic field transduction. In the end, I will also talk about the work we did on designing an ultra-high efficiency phononic piezoacoustic transduction waveguide to probe the ultra-small piezoelectric coefficients potentially present in the surface

layer of a silicon substrate due to surface inversion symmetry breaking.

6.1 Phononic piezoelectric transducer

In order to transduce a quantum state from a qubit into the mechanical degree of freedom, it is important that we can engineer an efficient transducer made out of a piezoelectric material. Here we chose a piezoelectric material called Aluminum Nitride (AlN). This material has the Wurtzite crystal lattice structure shown in Fig. 1.6 with labeled c-axis as the main inversion symmetry broken axis. As the electric dipole is generated between the positive charge center of Al-ions and weighted negative charge center of N-ions, the dominant piezoelectric conversion effect comes from the strain along the c-axis which includes the dilation (compression) along this axis. The piezoelectric coupling equations of motion are described in (6.1) that describes the electric field transduction to strain-field and (6.2) that describes the transduction from stress to electric displacement field and contributes the material polarization, $P_i = \sum_{jk} d_{ijk} \sigma_{jk}$.

$$s_{ij} = \sum_{kl} c_{ijkl} \sigma_{kl} + \sum_k d_{kij} E_k \quad (6.1)$$

$$D_i = \sum_{jk} d_{ijk} \sigma_{jk} + \sum_j \epsilon_{ij} E_j \quad (6.2)$$

Here, c_{ijkl} is the elastic matrix connecting strain-stress for a solid material and ϵ_{ij} is the linear polarization dielectric permittivity. We can write strain-stress tensors (s_{ij} and σ_{ij}) as vectors to unwrap the piezoelectric coupling coefficient tensor d_{ijk} into a matrix form $[d]_{3 \times 6}$. This matrix representation for AlN can be further simplified to include only five non-vanishing independent parameters due to its $6mm$ symmetry around its c-axis.

$$\vec{\sigma} = \begin{bmatrix} \sigma_{11} \\ \sigma_{22} \\ \sigma_{33} \\ \sigma_{13} \\ \sigma_{23} \\ \sigma_{12} \end{bmatrix} \quad (6.3)$$

$$[d] = \begin{bmatrix} 0 & 0 & 0 & 0 & d_{15} & 0 \\ 0 & 0 & 0 & d_{24} & 0 & 0 \\ d_{31} & d_{32} & d_{33} & 0 & 0 & 0 \end{bmatrix} \quad (6.4)$$

The electric field component, E_3 , align the c-axis direction can be coupled to dilation strain fields in directions normal to the c-axis (d_{31} , d_{32}) and parallel to the c-axis (d_{33}). The electric field components in the plane normal to the c-axis are coupled to the shear strains σ_{13} and σ_{23} via d_{15} and d_{24} respectively. The shear deformation coupling can be readily utilized to couple the electric field of an inter-digit array of planar electrodes on a surface of the piezoelectric material shown in Fig. 6.1. Even though the dilation motion along the c-axis provides stronger piezoelectric coupling, electric field coupling to motion in this direction is realized with a sandwich structure schematically shown in Fig. 6.9b. This type piezoacoustic resonator can be commonly found in various applications to obtain strong piezoelectric interaction and high conversion efficiency. However, a precise fabrication of such a stack multi-layer structure for constructing a nano-mechanical resonator is challenging. As a result, we first attempted the inter-digit (IDT) architecture for realizing high efficiency microwave to mechanics transduction and will move towards realizing stacked piezoacoustic phononic crystal in the future as it will be discussed in other sections of this chapter.

As an initial attempt, we designed the IDT resonator shown in Fig. 6.1. The resonator is called Lamb resonator in literature and is clamped onto the nearby substrate via the two-dimensional phononic crystal shield on a suspended silicon membrane and one full device looks like this Fig. 6.3. The mechanical mode of this shown structures can be simulated using COMSOL to be Fig. 6.1c and d. The larger the size, the larger the electric energy participation ratio of the coupled electric microwave resonator at a given mode frequency in the piezoelectric coupling since the IDT region's contribution to the total electric resonator capacitance scales linearly with the size of this region (i.e. the number of periods of the Lamb resonator unit cell and lateral length of the unit cell). This scaling trend with the number of periods in the Lamb resonator shown in Fig. 6.2. It shows an expected scaling of $g = g_u \sqrt{N_{\text{idt}}}$ with g_u being the single unit cell piezoacoustic coupling rate and this can continue until all the capacitance of the superconducting qubit at a given frequency is contributed to completely by the IDT capacitance.

The method to scale up the coupling by creating a larger Lamb resonator soon encounters the difficulty of having denser spectrum since more modes around the frequency of the superconducting resonator and the desired Lamb mode of interest.

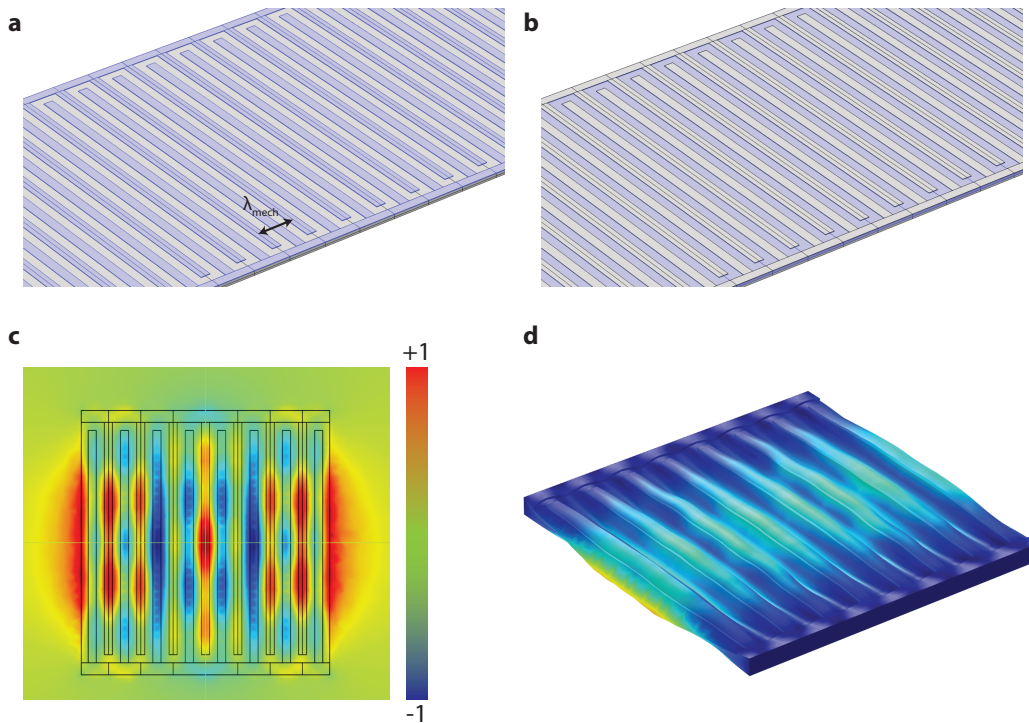


Figure 6.1: **a**, the Lamb resonator we designed with electrodes highlighted in blue. **b**, the AlN layer below the electrodes and above the suspended silicon membrane. **c**, the normalized mechanical mode piezoelectric potential near the top surface of the AlN. This potential profile is a direction transduction from the strain-stress field of the mechanical mode into its dual electric domain and an optimal coupling between this mode and the electric field of the electrodes can be achieved with aligning the positive and negative electrodes with the positive potential and negative potential nodes respectively. **d**, the displacement field and deformation profile of the mechanical mode of interest that is optimally coupled to the electrodes.

If the other modes' detuning from the superconducting qubit frequency are smaller than their coupling strength to the qubit, these modes will be hybridized to the qubit, which makes the system evolution dynamics complicated. If the modes are of high coherence, quantum state may still be stored in and extracted by from the ensemble of modes via a re-phasing pulse on the qubit to reverse the free evolution ballistic diffusion of quantum state among multiple mechanical modes. To achieve single mode interaction between the qubit and a piezoacoustic mode, we can tailor the density of acoustic modes and eliminate spurious piezoacoustic modes near the Lamb mode of interest via phononic engineering and careful design of the resonator dimensions.

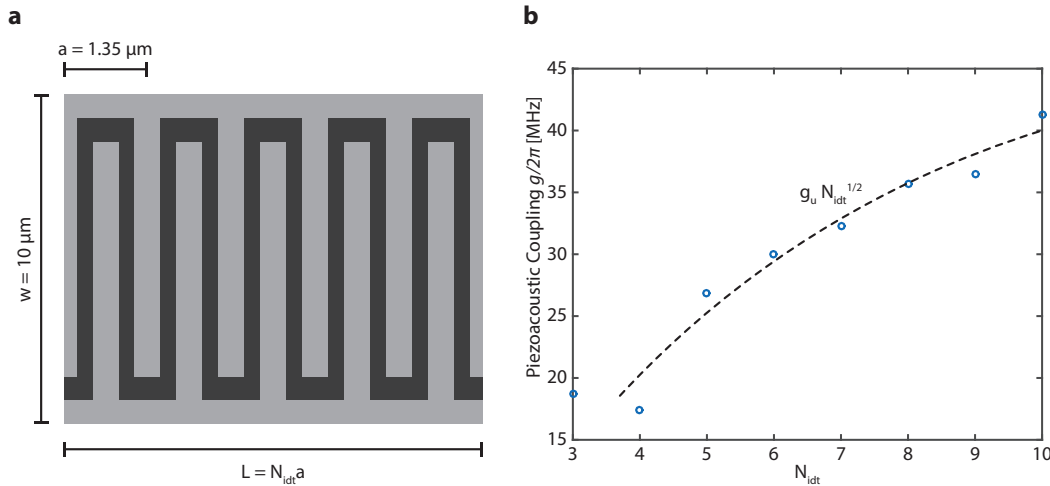


Figure 6.2: **a**, we kept the length (w) of each IDT unit cell to be $10 \mu\text{m}$ and swept the number of IDT unit cells N_{idt} in the Lamb resonator. **b**, the simulated piezoacoustic coupling rate $\frac{g}{2\pi}$ between the high coupling mechanical mode of interest around 3 GHz with a resonant electric resonator with capacitance $C_{\mu} = 60 \text{ fF}$ as a function of number of periods (N_{idt}) in the Lamb resonator. The trend of the coupling rate for a large enough number of periods scales as $g = g_u \sqrt{N_{\text{idt}}}$ with g_u being the single unit cell piezoacoustic coupling rate to a resonant electric resonator with $C_{\mu} = 60 \text{ fF}$.

The phononic crystal we have discussed so far is implemented in a single layer of suspended bare silicon membrane. In order to integrate this silicon phononic crystal with aluminum nitride (AlN) and electrodes, it is desirable to understand the influence of these added materials on the phononic gap and slight redesigns may be needed in the cases where the phononic gaps can not efficiently confine the mechanical mode of interest in the resonator region.

A 60 nm thick layer of Al can be deposited on the phononic crystal as shown in Fig. 6.4a and b. Their corresponding bandstructures are shown in Fig. 6.4c and d as dashed red lines. Solid lines in Fig. 6.4c and d are bandstructures of a bare silicon phononic crystal with bandgap between 4 GHz and 6 GHz.

If a 300 nm layer of AlN is deposited on the phononic crystal as shown in Fig. 6.5a, its phononic bandstructure is shown in b as dashed red lines. In practice, we use over-etch to remove the AlN residual on the silicon surface, this over etch can reduce the silicon thickness to around 170 nm. This over-etch's perturbation can be understood through the thinned phononic unit cell in c and its phononic bandstructure in d as

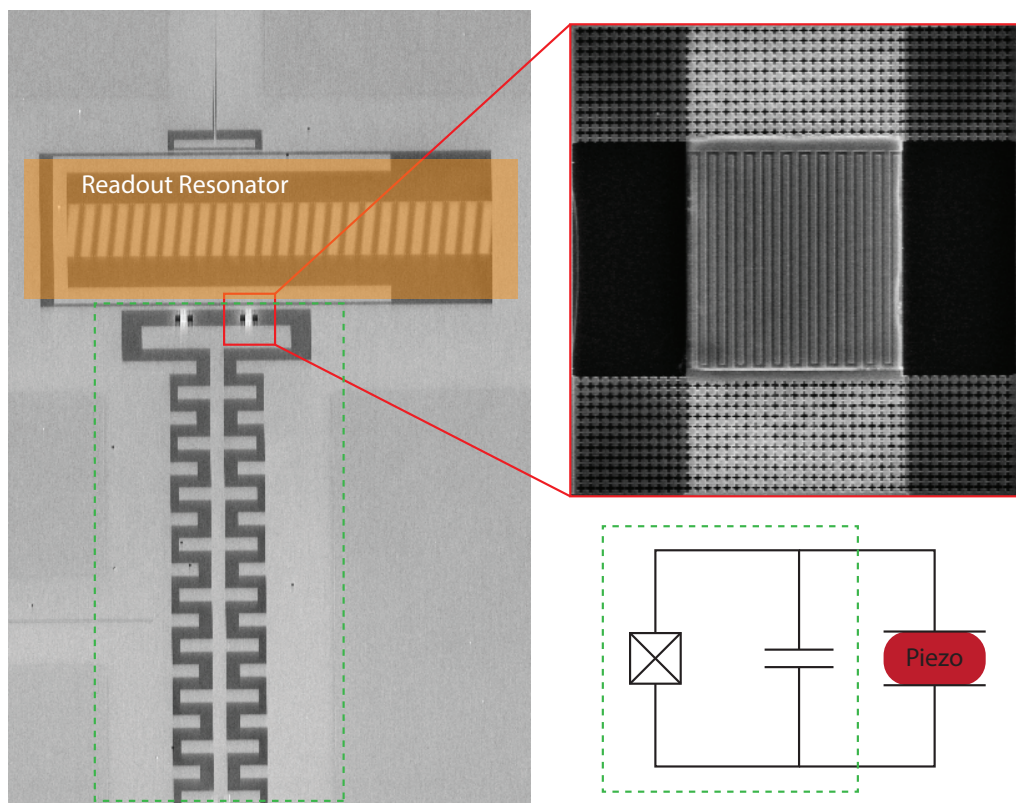


Figure 6.3: The SEM image of the first generation Lamb resonator (red box) and its coupled superconducting transmon qubit (dashed green box). The yellow region corresponds to the readout resonator attached to the qubit for measuring the Rabi oscillation between the qubit and the piezoacoustic mode.

dashed red lines. In both Fig. 6.5**b** and **d**, the bare 220 nm thick silicon phononic crystal bandstructure is shown as the solid blue lines with bandgap between 2.5 GHz and 3.8 GHz.

It can be observed that the bandstructure is perturbed by the additional layer of materials. Nevertheless, the resulting bandgaps are still wide enough and roughly centered at the frequency of interest.

6.1.1 Optimizing the piezoacoustic coupling per period of Inter-digit electrode

As discussed previously in the introduction that piezoacoustic coupling can be readily extracted from Finite-Element-Method (FEM) simulations that calculate the piezoacoustic resonator's normal modes' strain-stress field together with their strain induced electric polarization field in terms of piezoacoustic displacement field \vec{D}_{pa} . The simulated electric field corresponding to the Lamb resonance mode of interest is shown in Fig. 6.1**c** and its mechanical deformation is shown in Fig. 6.1**d**. The

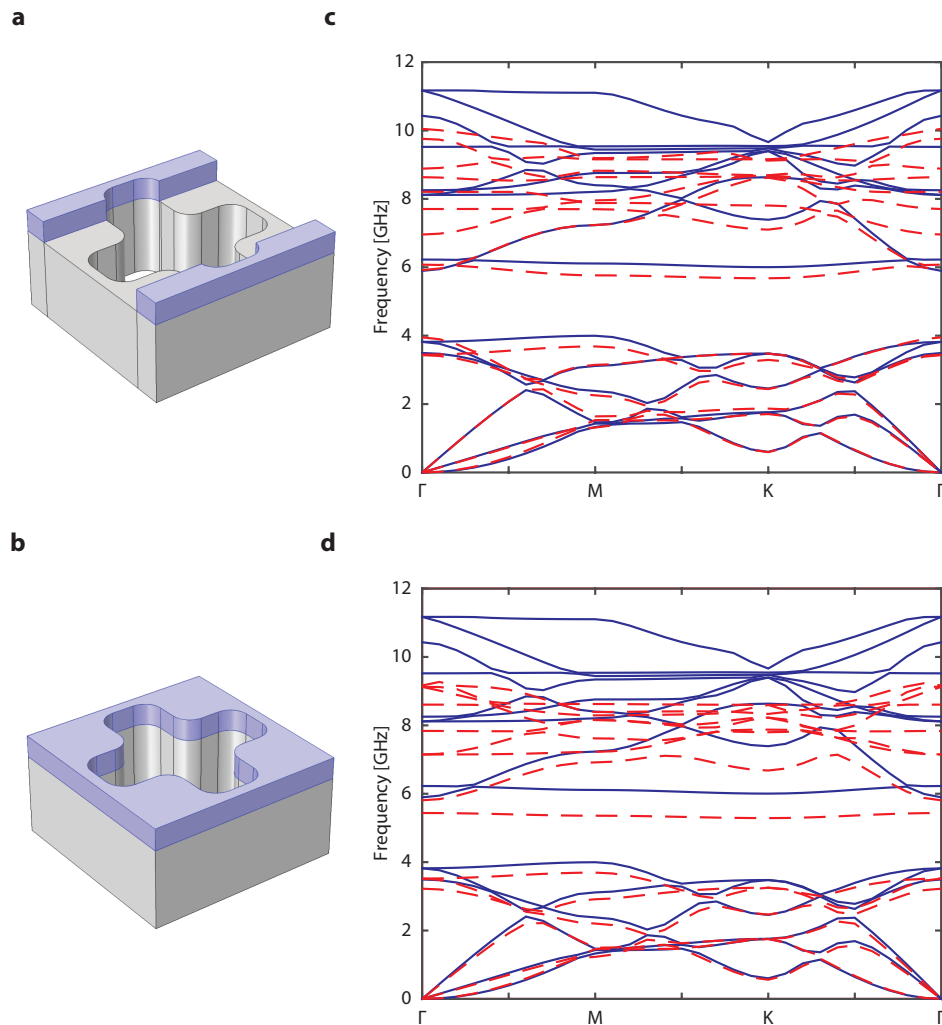


Figure 6.4: **a**, the phononic crystal unit cell with the blue part corresponds to 150 nm thick Al wires running on the phononic crystal. This type of perturbation leads to a phononic bandstructure shown in **c** with dashed lines. Similarly, **b** is the phononic crystal unit cell with blue part representing a 150 nm thick Al layer uniformly deposited on top of the etched silicon layer. This type of Al deposition leads to a phononic bandstructure shown in **d** with dashed lines. The solid lines in **c** and **d** represent the bandstructure of the unperturbed phononic crystal with a bandgap between 4 GHz and 6 GHz.

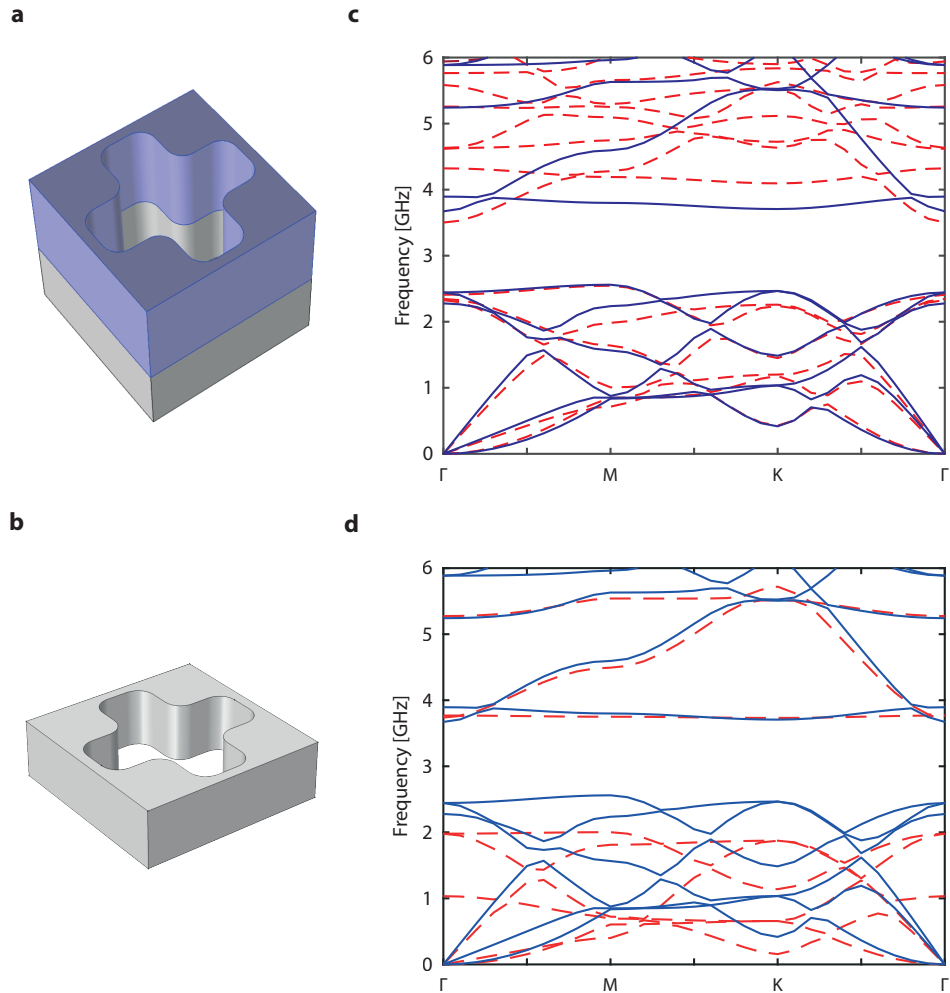


Figure 6.5: **a**, the phononic crystal unit cell with the blue part corresponds to 300 nm thick AlN layer uniformly deposited on the phononic crystal. This type of perturbation leads to a phononic bandstructure shown in **c** with dashed lines. **b** is the silicon phononic crystal unit cell which is over etched to have a thickness around 170 nm. This reduction in silicon thickness leads to a phononic bandstructure shown in **d** with dashed lines. The solid lines in **c** and **d** represent the bandstructure of the unperturbed phononic crystal with a bandgap between 2.5 GHz and 3.8 GHz.

FEM simulation of piezoacoustic normal modes also yields those normal modes' as-simulated energies E_{pa} which can be used to normalize each mode's piezoacoustic polarization field to the electric quadrature amplitude of the mode's zero-point-energy motion. This normalized amplitude can be then used to calculate the zero-point-energy normalized electric field of coupled electric circuit. As the electromagnetic wave in GHz range near the mechanical resonance has wavelength near centimeter which is much larger than the typical size ($\sim 10\mu\text{m}$) of the piezoacoustic resonator, it suffices to simulate the static electric field corresponding to the electric circuit's voltage amplitude on the electrodes to calculate the coupling between the electric circuit to the piezoacoustic modes via overlap integrals between the simulated normal modes' piezoelectric displacement fields and the simulated static electrodes' electric field for a given voltage. As the overlap integral is bilinear in the piezoelectric field and the electrodes' electric field, we can simulate the static field by numerically assign one volt of potential difference between the coupling electrodes to obtain the per-volt-piezoelectric-coupling (J_{pvpa}) strength of the piezoacoustic mode to an external circuit. Then, the J_{pvpa} can then be translated to the coupling to any type of external circuit by multiplying it with the external circuit's properly normalized voltage amplitude on the coupling electrodes.

For example, if the piezoacoustic resonator is coupled to a transmission line with characteristic impedance of Z_0 , the coupling rate of the resonator to the transmission line is $\sqrt{\kappa_{\text{pa}}^e} = J_{\text{pvpa}}\sqrt{\frac{\hbar\omega_p Z_0}{2}}$ where ω_p is the resonant frequency of the piezoacoustic resonator as the zero-point-fluctuation voltage in a transmission line is $V_{\text{T,zpf}}(\omega) = \sqrt{\frac{\hbar\omega Z_0}{2}}$ with quantized transmission line voltage $\hat{V}(t) = V_{\text{T,zpf}}(\hat{a}_{\text{ex}}(t) + \hat{a}_{\text{ex}}^\dagger(t))$ and normalization such that $\langle \hat{a}_{\text{ex}}^\dagger(t)\hat{a}_{\text{ex}}(t) \rangle = \dot{n}$ for a traveling photon number rate of \dot{n} in the transmission line. In the case where this piezoacoustic resonator is coupled to an electric resonator of impedance $Z_r = \sqrt{\frac{L_r}{C_r}}$ at frequency ω_r with resonator inductance L_r and capacitance C_r , the coupling strength is $J_{\text{pa}} = J_{\text{pvpa}}\sqrt{\frac{\hbar\omega_r^2 Z_r}{2}}$.

With the physical intuition built upon the above understanding of the coupling, it immediately leads to the conclusion that electrodes need to be placed at the anti-nodes of the Lamb resonator deformation profile to maximize the electrodes' electric field overlap with the piezoelectric displacement field for achieving optimal coupling efficiency. This optimization done for the shown Lamb resonator predicts that the coupling to a transmission line of $Z_0 = 50 \Omega$ is $\kappa_{\text{pa}}^e/2\pi \simeq 10 \text{ kHz}$ and the coupling to a $\omega_r/2\pi = 3 \text{ GHz}$ electric resonator having $Z_r = 430 \Omega$ is $J_{\text{pa}}/2\pi \simeq 16 \text{ MHz}$.

6.1.2 Lamb Resonator Coupling Spectrum Cleanup

As briefly discussed previously, spurious modes that can also be reasonably coupled to the electrodes will appear as the Lamb resonator size scales up. Most of these spurious modes are a hybridization of other modes of different polarisation to the mode of interest. Those other modes appear as a result of the denser density of states in the frequency range of interest due to the increasing resonator size. More specifically, a simplified model shown below can be used to understand the increase in the number of modes near the Lamb resonance frequency of interest.

Consider an infinite two-dimensional suspended membrane surface whose thickness is much smaller than wavelength of an elastic wave in our interested frequency range. The elastic wave equation can be written as (6.5). As X-translation commutes with Y-translation in this system, wave function can be written into a product of an x-dependent part and an y-dependent part like (6.6) that are eigen functions of X-translation and Y-translation operators respectively. Furthermore, due to the translation invariance in both directions, both X-dependent and Y-dependent components can be written as plane waves in (6.7) and (6.8). In the case of a broken translation symmetry with a finitely sized Lamb resonator structure, the basis functions (6.6) formed with (6.7) and (6.8) still completely span the whole Hilbert space of the elastic wave equation with finite boundary conditions. However, they are not in general orthogonal. Considering a finite rectangle membrane shown in Fig. 6.6a, the X-translation still commutes with Y-translation since the boundaries are orthogonal in this ideal rectangle box. The eigen-function can still be written as a product of an X-dependent part and a Y-dependent part. Meanwhile, each part is a superposition of two counter propagating plane waves that form a standing wave in that direction. The eigen modes should look like (6.6) with (6.9) and (6.10). The allowed states form a two-dimensional point lattice shown in Fig. 6.6c and d for two rectangle sizes. The density of states increases as the system size become larger. An increase of dimension in Y-axis increases the number of modes that have the same wavelength in X-dependent part of the eigen function. As for a Lamb resonator coupled to the IDT, the periodicity of the electrodes in X-axis should match that of the X-dependent part of the eigen functions to achieve optimal coupling between the electric field and the elastic wave. This means that for a given IDT periodicity in X-axis, the larger the Y-dimension size of the Lamb resonator the more modes

are going to be efficiently coupled to the electrodes near the frequency of interest.

$$\hat{\Theta}\vec{u} = \omega^2\vec{u} \quad (6.5)$$

$$\vec{u} = \begin{bmatrix} u_1 \\ u_2 \end{bmatrix} = \begin{bmatrix} u_{X1}(x)u_{Y1}(y) \\ u_{X2}(x)u_{Y2}(y) \end{bmatrix} \quad (6.6)$$

$$\vec{u}_X(x) = \vec{a}_x e^{ik_x x} \quad (6.7)$$

$$\vec{u}_Y(y) = \vec{a}_y e^{ik_y y} \quad (6.8)$$

$$\vec{u}_X(x) = \vec{a}_x \sin(k_{x,n}(x + \frac{Lx}{2})) \quad (6.9)$$

$$\vec{u}_Y(y) = \vec{a}_y \sin(k_{y,n}(y + \frac{Ly}{2})) \quad (6.10)$$

$$k_{\mu,n} = \frac{n\pi}{L_\mu}, \mu = x, y \quad (6.11)$$

Realistically, the device boundaries look like the Fig. 6.6b where the X-Y translation symmetry is broken, meaning that X-translation and Y-translation is not commutative. This broken symmetry means that eigen functions of the resonator can no longer be a simple product of X-dependent component and Y-dependent component and the previously mentioned infinite surface plane wave basis of the Hilbert space will be mixed into inseparable eigen functions satisfying the rough boundary conditions. This creates the complicated mode profiles seen in a large Lamb resonator whose spectrum is convoluted. Furthermore, the modes of the same frequency and wavelength in one direction can be broken into multiple parts as the randomness in the metal electrodes and AlN material in-uniformity may have already broken the translation symmetry in the bulk of the resonator far from the boundaries. Thus, the larger the device the harder it gets to clean the spectrum so that we have a single mechanical mode of interest that is strongly coupled to the electrodes and external circuit at a given frequency.

As the ideal rectangle density of states have suggested, the lateral length (Y-axis length) of the resonator should be made small enough to exclude mode distribution in the Y-dependent part of the eigen function. This direction should be smaller than half-wavelength of the acoustic frequency of interest in the material.

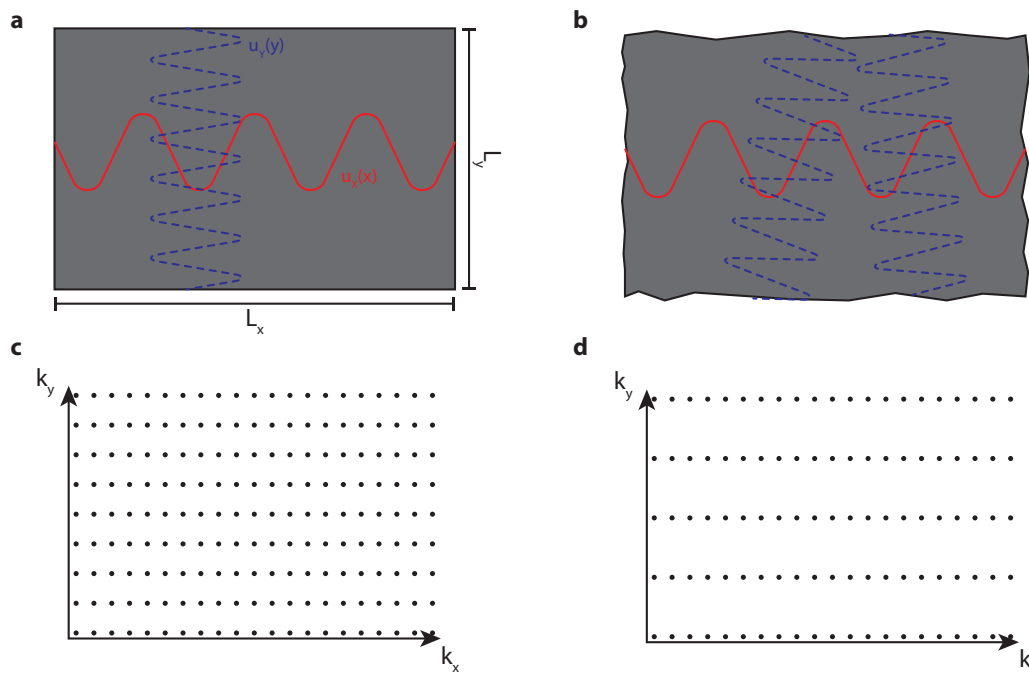


Figure 6.6: **a**, the rectangle box that mixes two counter propagation planar wave in one direction. The plane wave basis functions are not orthogonal in the inner product space defined on this finite two-dimensional space. However, as the box edges are orthogonal, the X-dependant component and Y-dependant component are still separable. **b**, the edges of the finite space is rough and the inner product space defined in this space does mix the X-dependant component and the Y-dependant component. **c**, the quantized density of states (DOS) for a rectangle box shown in **a**. **d**, the DOS of a 2D finite surface that are narrower in Y-direction as compared to the case in **c**. The narrower one dimension gets, the sparser the states are in that direction.

6.2 Ultra-high coherence compact quantum memory for a superconducting transmon qubit

As indicated in the previous section that a silicon phononic cavity coupled to a transmon qubit via a piezoelectric material can be used as a compact high-coherence quantum memory for a quantum electric circuit. However, a large coupling between the electric circuit and the silicon mode also comes with the cost of significantly elevated loss due to large electric and acoustic energy participation ratios in the extremely lossy the piezoelectric material [89]. Moreover, a large coupling is necessary for achieving high fidelity state transfer as it requires a high cooperativity interface between the transmon qubit and high quality silicon phononic mode of interest. Thus, it appears contradictory to require on-demand high fidelity quantum state transfer between the memory and qubit in a swap-state, high coherence super-

conducting qubit in an idle-state, and ultra-high coherence silicon memory acoustic mode in an idle-state for one device. In this section, I will present a way we propose to achieve the three goals in one device that can switch between the swap-state and the idle-state. This device can be turned to a swap-state where a quantum state can be swapped with a high cooperativity ($\sim 10^5$) between a superconducting transmon qubit and a high coherence phononic quantum memory cavity. After the completion of the swap operation, the system can be turned into an idle-state where the high coherence of the transmon qubit and the ultra-high coherence of the bare silicon phononic quantum memory mode can be preserved. More specifically, we expect the silicon memory mode to achieve an energy relaxation time in millisecond during the idle-state with realistic system loss rates.

The idea behind this device that almost combines the best of both worlds is illustrated in Fig. 6.7a. Instead of having the transmon qubit (red) and the quantum memory mode (blue) in direct contact with piezoelectric material, the device contains three subsystems, as illustrated in Fig. 6.7c. Shown on the left in the red box is a superconducting transmon qubit on silicon-on-insulator (SOI) substrate with the buried oxide etched away [60]. The blue box corresponds to the defect phononic crystal cavity on a bare suspended silicon membrane. These two subsystems are coupled to an intermediate hybrid system (green box) with pure electric coupling, J_q , and pure mechanical piezo-memory coupling, J_m , respectively. The intermediate hybrid system has a tunable electromagnetic resonator (I_{em}) with frequency, ω_{em} , and a piezoacoustic resonator (I_{pa}) with frequency, ω_{pa} . They are strongly coupled with piezoelectric coupling strength, J_p . As mentioned previously, the system can switch between an idle-state and a swap-state. The state of operation depends on how the intermediate system is hybridized and how qubit frequency (ω_q) is tuned to align with the memory frequency (ω_m). In the swap-state, intermediate resonators are tuned resonant ($\omega_{em} = \omega_{pa}$) and strongly hybridized into symmetric and anti-symmetric superpositions of the microwave resonator mode and the piezoacoustic mode at frequencies $\omega_{\pm} = \omega_{pa} \pm J_p$. In qubit-memory coupling (J_{vc}) in the swap-state is implemented with a virtual coupling process mediated by the hybridized intermediate system super-modes.

We can also draw a not-to-scale illustration in Fig. 6.7d to show the layout of the device. The blue box in the figure highlights the region containing the phononic region. It has the piezoacoustic resonator and memory cavity embedded in a two-

Component	w [nm]	l [nm]	t [nm]		Freq.[GHz]
Piezo.	685	1118	Top Mo	100	5.15
			AlN Act.	100	
			Bot. Mo	90	
			AlN Seed	30	
Memory	440	780			5.0
Unit Cell	w [nm]	h [nm]	a [nm]		Gap. [GHz]
	200	488	550		4 – 6

Table 6.1: The table listing a set of experimentally achievable mechanical structure design parameters that can satisfy the requirements for realizing the proposed architecture’s desired operations.

dimensional phononic crystal. Even though the illustration is not-to-scale, it can still be seen that the mechanical region has an extremely small footprint, as compared with all the other electric components in the system. This means that multiple mechanical memory cavities can be coupled to one transmon qubit in parallel so that one qubit can have a memory bank consisting of a large number of ultra-high coherence quantum registers. In this architecture, ultra high fidelity in-memory two-qubit gates can be carried out [52]. In the rest of this section, I will discuss each part of the device designed for realizing this Quantum Random Access Memory (QRAM). Moreover, I will elaborate on design optimizations, operation protocols, and potential applications in building near-term engineering feasible fault-tolerant quantum computers.

6.2.1 2D Phononic Crystal and Defect Cavity

Periodically patterned solid mechanical structure on 2D silicon membrane with a gaped mechanical wave bandstructure can be used to manipulate the propagation of mechanical waves (phonons). A complete 3D phononic bandgap between 4 GHz–6 GHz (Fig. 6.8b) is realized in the phononic crystal depicted in Fig. 6.8a using the unit cell structure illustrated as an inset.

A point defect in the 2D phononic crystal can localize a mechanical mode to form a cavity [111, 6, 18]. Previous studies have shown that this type of GHz mechanical cavities can demonstrate outstanding quality factor (Q-factor) around fifty-billion leading to a phonon lifetime about one second at a refrigerated temperature around 10 mK [74]. Fig. 6.8c depicts a 5 GHz 2D phononic cavity design that can be

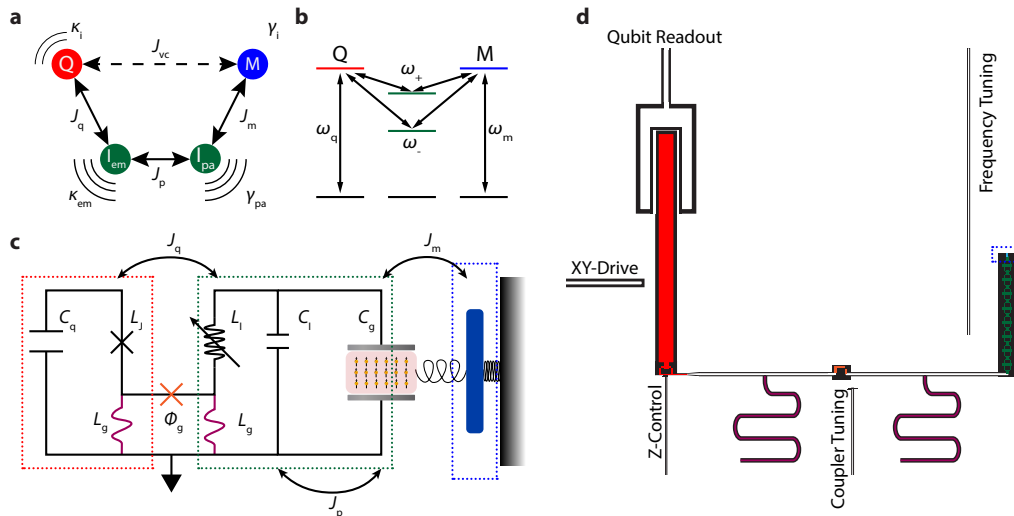


Figure 6.7: **a**, The virtual coupling model used in this work. mode-Q, mode-M, and mode- $I_{em,pa}$ stand for qubit mode (red), acoustic memory mode (blue), and intermediate electric and piezoacoustic modes (green). The intermediate system decay rates (κ_{em} and γ_{pa}), the qubit intrinsic decay rate (κ_i), and memory intrinsic decay rate (γ_i) are shown in this figure. The acoustic memory mode is assumed to be almost lossless ($\gamma_i/2\pi \sim 1$ Hz) in the system dynamics of interest. **b**, The system energy levels of different parts of **a** with corresponding colors. **c**, The proposed circuit diagram of the system has three parts. The part highlighted in the red box represents the qubit, and the part highlighted in the green box represents the high-Q memory resonator. They are each coupled to the intermediate system highlighted in the green box with pure electric and mechanical couplings J_q and J_m respectively. The intermediate microwave and the piezoacoustic resonators are strongly piezoelectrically coupled with rate, J_p . **d** The illustration (not to scale) of the proposed device layout with different elements colored corresponding to **c**.

mechanically coupled to a piezoacoustic resonator on the same 220 nm thin phononic crystal membrane. The memory's frequency (ω_m) can be tuned around 5 GHz by changing its width (w_m) and length (l_m) in design. The dependence on these parameters is illustrated in Fig. 6.8e. It can be seen that the significant tuning dimension is the length of the cavity. This observation is consistent with the planar memory mode profile in Fig. 6.8d revealing major deformation in the cavity length.

6.2.2 Piezoacoustic Cavity

In order for the scheme to protect the memory in idle-state and achieve high state transfer cooperativity in swap-state, the piezoacoustic cavity that transduces quan-

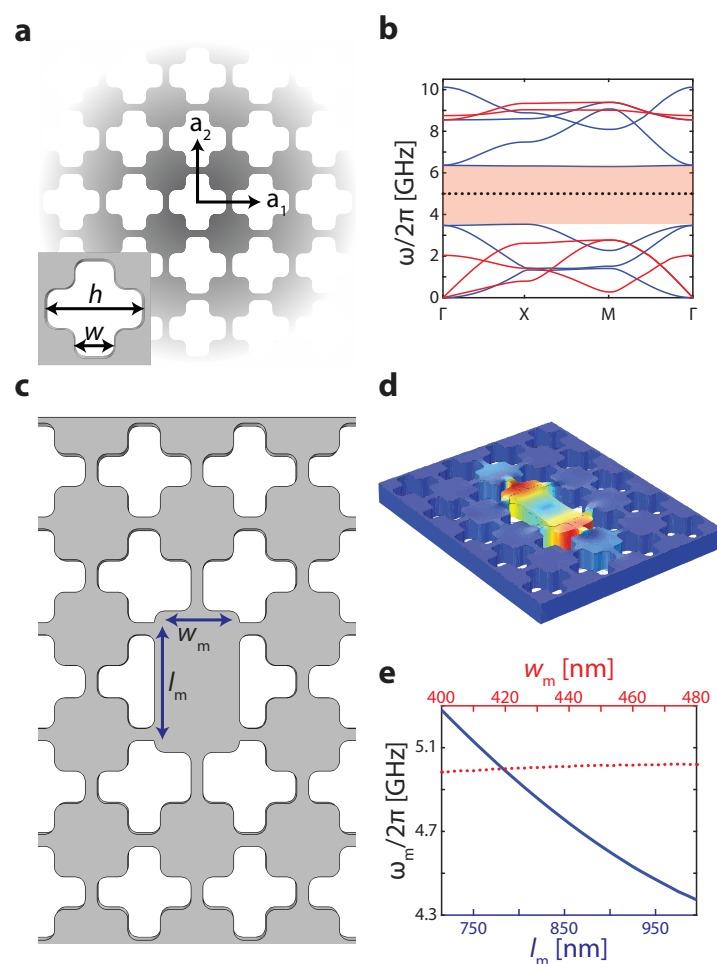


Figure 6.8: **a**, A periodically patterned 2D square lattice phononic crystal with primitive vectors $\vec{a}_{1,2}$. Its unit cell structure is depicted in the lower-left corner inset. **b**, The wide microwave bandgap phononic bandstructure of the phononic crystal membrane using unit cell design parameters taken from Table 6.1. The large bandgap in allowed mechanical wave frequency between 4 GHz and 6 GHz is highlighted in orange. The black-dotted line in the middle of the gap corresponds to the memory cavity mode frequency $\omega_m/2\pi \sim 5$ GHz. **c**, The structure of the proposed high-Q acoustic memory cavity which is realized as a phononic defect cavity embedded in a phononic crystal. **d**, Fundamental mode displacement field profile of the memory cavity in **c**. **e**, The design parameter dependence of the target mechanical resonator mode. The mode frequency has little dependence on the width (w_m) of the mechanical cavity width (red axis and dotted curve). This mode's frequency can be tuned (blue axis and solid line) in design by changing the cavity length (l_m).

tum signal between the electric and acoustic domains needs to be strongly coupled to the tunable electric resonator with a large J_p . Furthermore, the piezoacoustic structure should be extremely compact such that frequency spacings between nearby piezoacoustic modes are wide enough to avoid lossy parasitic modes' couplings to the high-Q mechanical memory mode. The compactness requires the use of a thin-film piezoelectric material that has a small loss tangent and reasonable piezoelectric coupling coefficient. The piezoelectric material of choice is Aluminum Nitride (AlN) as it has a relatively low microwave loss tangent ($\tan \delta_{\text{AlN}} \sim 5 \times 10^{-4}$) [137, 31, 30, 120, 78, 77] and well established nano-fabrication processes [122, 31, 123]. Furthermore, a large field overlap efficiency between piezoacoustic mode inverse piezoelectric displacement field (\vec{D}_p) and the electrodes' electric field (\vec{E}_μ) is necessary to maximize the piezoelectric coupling. Such efficient field overlap is commonly realized with a structure having AlN sandwiched between two electrodes [90] depicted in Fig. 6.9b. In order to further improve the thin-film material quality and confine elastic energy in the piezoelectric material, the heavy superconducting metal, Molybdenum (Mo), is often used as electrodes [122, 31, 123]. To allow evaporation of superconducting wires with the lift-off process, we use Al as the metal leads connecting the Mo electrodes to the external circuit. Al can be evaporated to the selected area after patterning the thin layers of Si, sputtered Mo, and sputtered AlN. The desired high coupling piezoacoustic mode mechanical displacement profile (Fig. 6.9c) and inverse piezoelectric displacement field (\vec{D}_p) in the z-direction (Fig. 6.9g) are plotted for the cross-section indicated in Fig. 6.9b. Fig. 6.9h further shows the electromagnetic mode's electric field (\vec{E}_μ) component in the z-direction. Fig. 6.9g and h highlight that this design achieves the optimal piezoelectric field overlap for a piezoacoustic mode $\omega_{\text{pa}}/2\pi \simeq 5.15$ GHz.

The high-coupling piezoacoustic mode frequency (ω_{pa}) and piezoelectric coupling rate (J_p) depend on the resonator's length (l_p), block width (w_p), and AlN active layer thickness (t_p) as can be observed in Fig. 6.9d–f. They indicate that the mode frequency depends dominantly on the width of the cavity. Noticeably, there are dips in the piezoelectric coupling rate even though the mode frequency curves are smooth. These dips are the direct consequences of the high-coupling mode hybridizing with other low-coupling modes. Fig. 6.9d and Fig. 6.9e correspond to the case where the frequency (ω_{pa}) of the high-coupling mode is tuned to resonance with low-coupling modes. Fig. 6.9f illustrates that the low-coupling modes are tuned to be resonant with the high-coupling mode since the high-coupling mode frequency (ω_{pa}) is not

sensitive to the length (l_p) of the resonator. An appropriate design will avoid the parameter regions that lead to these parasitic degeneracies.

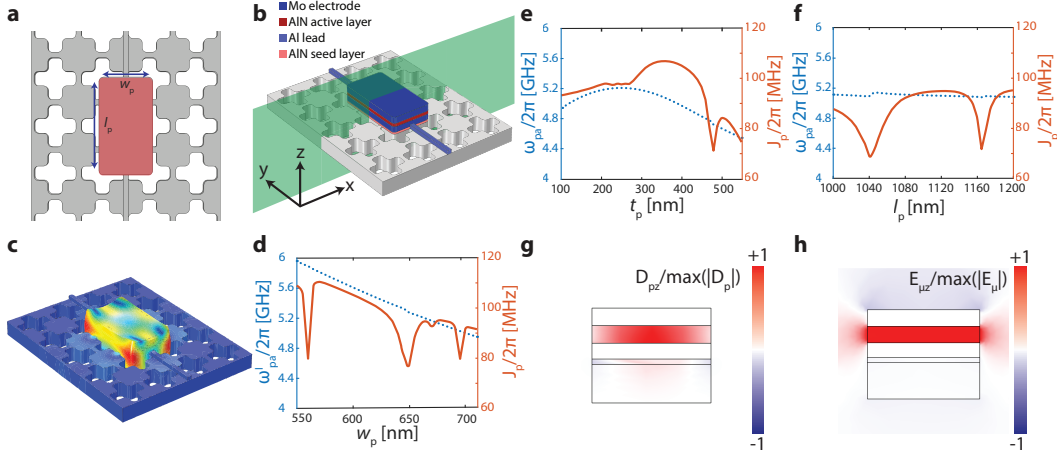


Figure 6.9: **a**, Top view of piezoacoustic resonator. **b**, The stack composition of the piezoacoustic resonator. The transparent green plane indicates the cross-section taken for plotting **g** and **h**. **c**, The high piezoelectric coupling mode's simulated mechanical displacement field profile. **d–f**, Design parameter dependence of the high-coupling mode frequency, ω_{pa} (blue axis and curve), and piezoelectric coupling rate, J_p (red axis and curve). The piezoelectric coupling rate, J_p , is calculated assuming the piezoacoustic resonator is coupled to a resonant high-impedance electric resonator with total shunted capacitance $C_\mu = (C_1 + C_g) \sim 5$ fF. **g**, Normalized inverse piezoelectric displacement field's (\vec{D}_p) z-component. **h**, Normalized electrode electric field's (\vec{E}_μ) z-component. We plot the z-components in **g** and **h** to highlight piezoelectric coupling to the dominant piezoelectric axis (z-axis) of AlN.

There are two ways the piezoelectric coupling can be extracted from finite-element-method (FEM) simulated mechanical deformation of piezoacoustic modes. The first method utilizes the fact that deformation of a piezoelectric material generates electric dipole moment [130]. This inverse piezoelectric effect can be viewed as a direct mapping of the mechanical deformation into the electric domain. Coupling between a piezoacoustic mode and an electromagnetic mode of an external circuit can then be extracted via an overlap integral of the piezoacoustic mode's normalized inverse piezoelectric displacement field (\vec{D}_p) and the normalized electromagnetic mode's electric field (\vec{E}_μ). The piezoelectric coupling rate can thus be calculated as (6.12),

$$\hbar J_p = \int \vec{D}_P(\vec{r}) \cdot \vec{E}_\mu(\vec{r}) d\vec{r}^3, \quad (6.12)$$

with \vec{D}_P is normalized according to (6.13),

$$\vec{D}_P = \sqrt{\frac{\hbar\omega_p}{4E_p}} \vec{D}_P^{\text{fem}}, \quad (6.13)$$

where \vec{D}_P^{fem} is the as-simulated field. The as-simulated piezoacoustic mode's field has total energy, E_p . The normalization scales the displacement field (\vec{D}_P^{fem}) such that the normalized field (\vec{D}_P) contains the mode's zero-point energy. The normalized external circuit electromagnetic mode's electric field (\vec{E}_μ) can be obtained by simulating the electric field distribution according to the prescribed zero-point-fluctuation potential (V_{zpf}) between the electrodes. The zero-point voltage fluctuation amplitude is $V_{\text{zpf}} = \sqrt{\frac{\hbar\omega_\mu}{2C_\mu}}$ where ω_μ is the resonant frequency of the coupled electromagnetic mode and $C_\mu = (C_I + C_g)$ is the total capacitance of the electric resonator.

On the other hand, piezoelectric resonators have been widely used in microwave engineering for compact electric filtering applications [97]. In those applications, the compact piezoacoustic devices are commonly modeled as equivalent circuits that manifest identical electrical responses [130]. By fitting a serial-LC resonator model (Fig. A.1) to numerically simulated device electric admittance, equivalent circuit elements (C_g , C_{pa} , L_{pa}) can be extracted. The coupling between the external circuit and piezoacoustic mode can then be understood in the standard circuit dynamics framework. The admittance simulation and corresponding fitting are described in Appendix A.1.2. For the piezoelectric resonator design parameters shown in Table 6.1, the extracted equivalent circuit model elements are $L_{\text{pa}} = 141 \mu\text{H}$, $C_{\text{pa}} = 6.45 \text{ aF}$, and $C_g = 1.3 \text{ fF}$. The direct dielectric capacitance, C_g , is the result of the AlN linear dielectric permittivity. It can be independently calculated without considering the piezoelectric response of AlN.

Thus, the piezoacoustic mode designed according to Table 6.1 can have frequency, $\omega_{\text{pa}}/2\pi \simeq 5.15 \text{ GHz}$, and realize a large piezoelectric coupling, $J_p/2\pi \sim 100 \text{ MHz}$.

6.2.3 Evanescent Mechanical Coupling Between Piezo and Memory Cavities

The piezoacoustic resonator and the memory cavity are located on the same phononic crystal membrane with complete mechanical bandgap between 4 GHz–6 GHz.

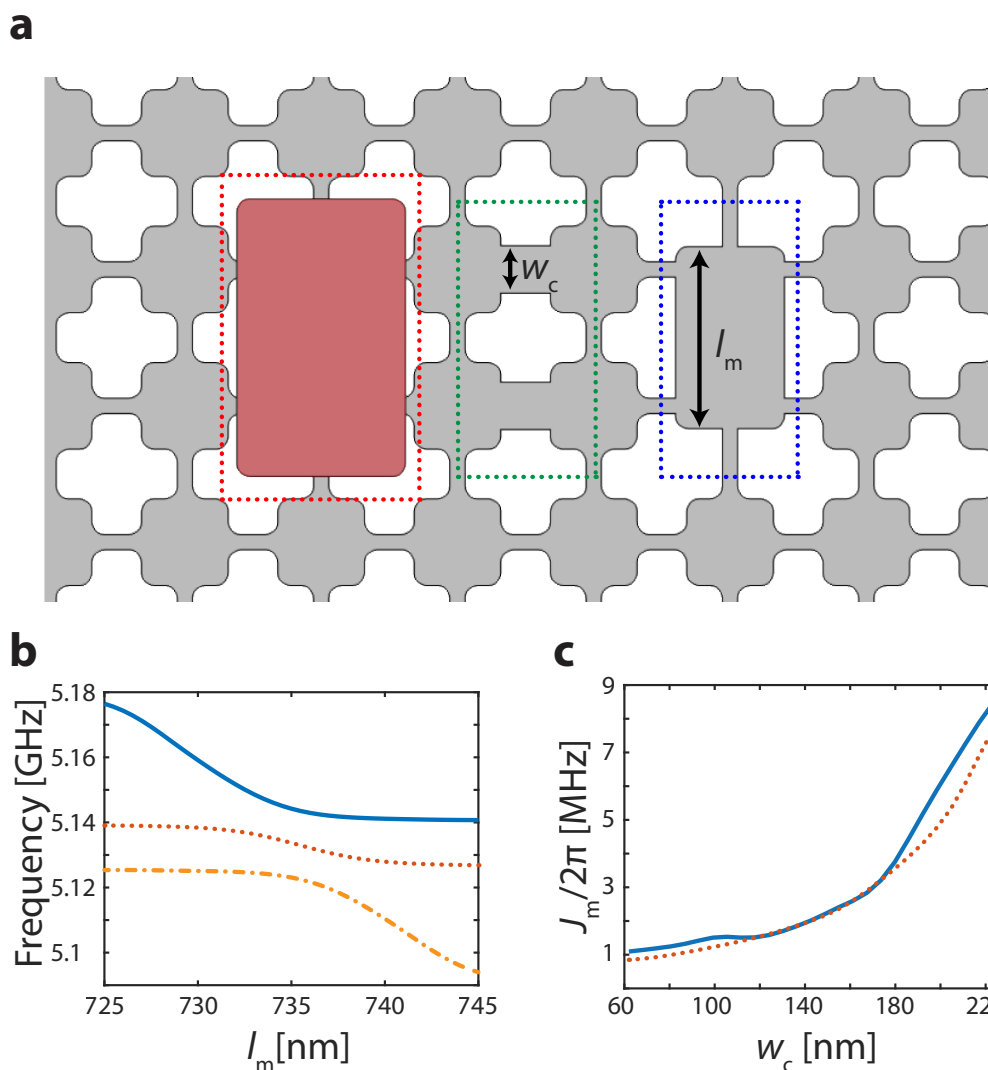


Figure 6.10: **a**, The double cavity layout on a phononic silicon membrane. The left side cavity is piezoacoustic resonator, and the right side is high-Q memory cavity. The parameter relevant to fine-tuning mechanical coupling strength (J_m) is the width (w_c) of the narrow “bridge“ connecting nearby phononic crystal squares between the two acoustic cavities. Desired coupling rate, $J_m/2\pi \sim 5$ MHz, can be achieved with $w_c = 186$ nm. **b**, System mechanical frequency spectrum as a function of the memory cavity length with other parameters fixed to values in Table 6.1. The blue-solid line is the frequency of the memory cavity mode, and red-dashed line is the high piezoelectric coupling piezoacoustic mode (mode of interest). The yellow-dotted line is a parasitic mode of the piezoacoustic resonator that has negligible piezoelectric coupling. Mechanical coupling rate can be extracted from fitting the avoided crossing in system mechanical spectrum. **c**, Calculated mechanical coupling rate (J_m) as a function of w_c using evanescent field overlap integral method (blue-solid) and fitting avoided crossing in the spectrum (red-dashed line).

Nearby mechanical cavities with frequencies around 5 GHz can be coupled through their evanescent mechanical fields in the vicinity. Two methods are used to extract the mechanical coupling rate from FEM simulations. The most straightforward one is sweeping the memory cavity length (l_m) such that the double cavity system exhibits avoided crossing in the simulated mechanical spectrum, as shown in Fig. 6.10b. Fig. 6.11b and c illustrate the hybridized modes near the avoided crossing. The avoided crossing in Fig. 6.10b is fitted to obtain the mechanical coupling rate $J_m/2\pi \sim 5$ MHz between memory cavity (blue-solid curve) and piezoacoustic cavity (red-dashed curve). The yellow-dotted line in Fig. 6.10b corresponds to a piezoacoustic resonator mode next to the piezoacoustic mode of interest. It has negligible piezoelectric coupling due to its anti-symmetric mode shape. Tuning of mechanical coupling rate, J_m , can be achieved by perturbing the width (w_c) of the narrow bridge region connecting nearby phononic crystal squares between the two cavities indicated in the green box of Fig. 6.10a.

Despite the conceptual simplicity demonstrated in the above method, it is very time-consuming for design parameter sweeps and inaccurate for extracting a small coupling rate due to numerical errors. This method also relies on observing avoided crossing, which is not the case for designing far detuned cavities. Alternatively, a more efficient and accurate method based on perturbation theory similar to the coupled mode theory in optics was developed. To arrive at the correct formalism for calculating weak evanescent field coupling on a discrete phononic crystal, it is important to properly define an inner-product as in (6.14). This inner-product is properly defined for the displacement field, $\vec{q}_{1,2}(\vec{r})$, linear space of the given phononic crystal. The crystal's material property and dielectric distribution are characterized by the discontinuous density, $\rho(\vec{r})$, over a spatial region, T , of interest. The constructed inner-product space ensures that the acoustic eigenmodes' displacement fields are orthogonal and normalizable in the phononic crystal region.

$$\langle \vec{q}_1 | \vec{q}_2 \rangle \equiv \int_T \vec{q}_1(\vec{r})^* \cdot \vec{q}_2(\vec{r}) \rho(\vec{r}) d\vec{r}^3 \quad (6.14)$$

The method requires independent simulations of bare piezoacoustic mode displacement field ($\vec{u}^{p,\text{fem}}$), bare memory cavity mode field ($\vec{v}^{m,\text{fem}}$), and the piezoacoustic mode profile in a full-geometry configuration ($\vec{w}^{\text{mp},\text{fem}}$). They are further normalized according to (6.15), (6.16), and (6.17), respectively. These fields are normalized

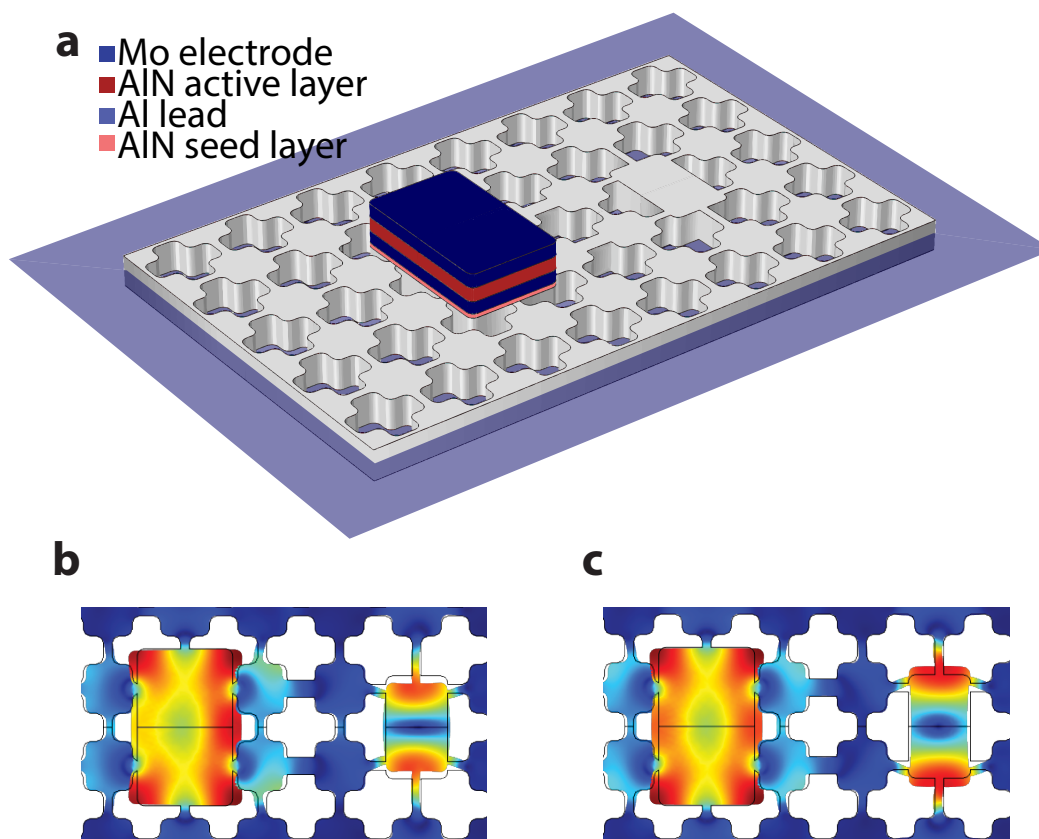


Figure 6.11: **a**, The asymmetric view of the two mechanical resonators. The piezoelectric resonator has different function layers highlighted in colors corresponding to Fig. 6.9**b**. The blue plane is the cross-section where mechanical super-modes' displacement fields are plotted in the two following figures. **b** and **c**, The symmetric and anti-symmetric mode profiles respectively when the two mechanical cavities hybridize near the avoided crossing point.

to their corresponding zero-point-fluctuation energies in a quadrature ($\frac{\hbar\omega_\zeta}{4}$) from as-simulated total elastic energies, E_ζ , $\zeta = p, m, mp$.

$$\vec{u} = \sqrt{\frac{\hbar\omega_p}{4E_p}} \vec{u}^{p,\text{fem}} \quad (6.15)$$

$$\vec{v} = \sqrt{\frac{\hbar\omega_m}{4E_m}} \vec{v}^{m,\text{fem}} \quad (6.16)$$

$$\begin{aligned} \vec{w} &= \sqrt{\frac{\hbar\omega_{mp}}{4E_{mp}}} \vec{w}^{mp,\text{fem}} \\ &\simeq \alpha \vec{u} + \beta \vec{v} \end{aligned} \quad (6.17)$$

Perturbatively, the simulated piezoacoustic mode displacement field can be expanded into a superposition of bare piezoacoustic mode and memory mode fields as indicated by the second equal sign in (6.17). Overlap integrals of the fields can be carried as in (6.18) and (6.19) to get the expansion coefficients in (6.17),

$$\alpha = \frac{-\langle \vec{v} | \vec{u} \rangle \langle \vec{w} | \vec{v} \rangle + \langle \vec{v} | \vec{v} \rangle \langle \vec{w} | \vec{u} \rangle}{\langle \vec{u} | \vec{u} \rangle \langle \vec{v} | \vec{v} \rangle} \quad (6.18)$$

$$\beta = \frac{\langle \vec{v} | \vec{v} \rangle \langle \vec{w} | \vec{v} \rangle - \langle \vec{u} | \vec{v} \rangle \langle \vec{w} | \vec{u} \rangle}{\langle \vec{u} | \vec{u} \rangle \langle \vec{v} | \vec{v} \rangle}, \quad (6.19)$$

The piezo-memory mechanical coupling rate (J_m) can be calculated as (6.20),

$$J_m = \beta(\omega_p - \omega_m). \quad (6.20)$$

The mechanical coupling rate dependence on the narrow region width is shown in Fig. 6.10c. The blue-solid (red-dashed) curve is the mechanical coupling rate calculated with perturbation (fitting avoided crossing). Two methods agree reasonably with each other. However, the perturbation method reduced the time needed for obtaining the curve by almost 40 times and can be readily applied to more general cases involving multiple acoustic cavities in any configuration.

6.2.4 Tunable High Impedance Electric Microwave Resonator Coupled To A Transmon Qubit Via A Tunable Inductive Coupler

A high zero-point-fluctuation voltage amplitude (V_{zpf}) on the piezoelectric resonator electrodes is needed for achieving a large piezoelectric coupling. Furthermore, the electric microwave resonator frequency (ω_{em}) needs to be tunable for a better

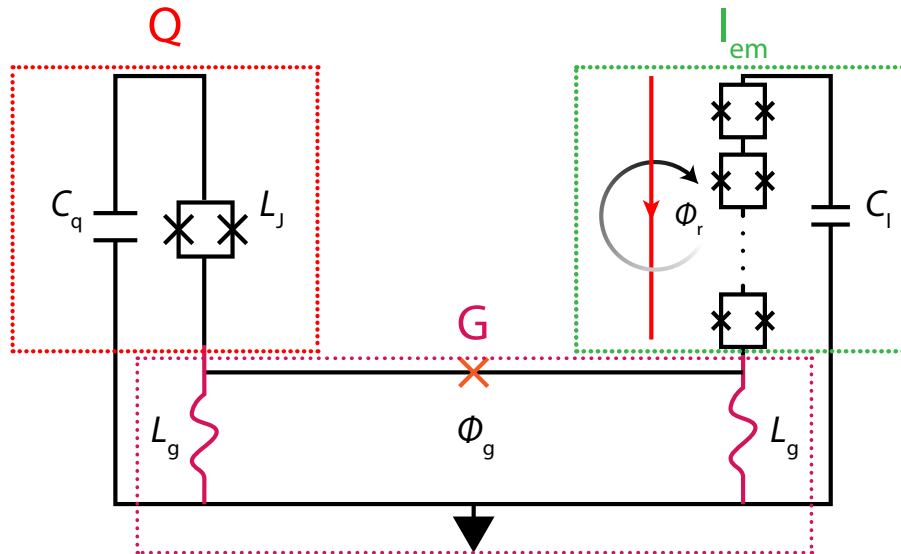


Figure 6.12: Circuit diagram for a transmon qubit labeled with Q coupled inductively to the intermediate tunable high impedance electromagnetic resonator with eight serial SQUIDs labeled with I_{em} . The intermediate electromagnetic mode frequency (ω_{em}) can be tuned by an external current (red arrow) that threads a total magnetic flux of Φ_r through the SQUIDs. The coupler labeled with G between the transmon qubit and the electromagnetic resonator is tunable, and the coupling rate, J_q , depends on the external magnetic field flux (Φ_g) through the ground loop.

swap-state frequency alignment with the piezoacoustic resonator considering the fabrication uncertainty. Such a tunable high-impedance electric microwave resonator can be realized with a series of SQUIDs [8] shown in the green box of Fig. 6.12. Its frequency can be tuned by adjusting externally applied magnetic flux (Φ_r). A single compact SQUID loop with maximum inductance ~ 11 nH was achieved in [60]. Fifteen such SQUIDs can be serially connected to provide the necessary linear inductance. Stray capacitance of this serial SQUID inductance is negligible leading to a high impedance electric resonator ~ 5 GHz with a shunted total capacitance $C_\mu = (C_I + C_g) \sim 5$ fF.

As shown in Fig. 6.12, the inductive coupling (J_q) between transmon qubit and the serial SQUID resonator was realized with a “gmon” coupler [22] in the red box. The coupling between the transmon qubit and the serial-SQUID resonator can be continuously tuned, as shown in (6.21),

$$J_q = -\frac{\sqrt{\omega_q \omega_{em}}}{2\sqrt{(L_g + L_I)(L_g + L_J)}} \frac{L_g^2}{2L_g + L_{g0}/\cos \delta_g}, \quad (6.21)$$

where the L_{g0} is the single junction inductance of the tunable coupler and $\delta_g \equiv \pi\Phi_g/\Phi_0$. Φ_g is the externally applied magnetic flux through the coupler loop and $\Phi_0 \equiv \frac{h}{2e}$ is a magnetic flux quanta. The swap-state electric coupling can be tuned to optimize the state transfer fidelity. This coupling can also be turned off during idle-state to protect the superconducting transmon qubit from decoherence noises in the intermediate system.

6.3 On-Demand Coherence Preserving Virtual Coupling Channels

A desired acoustic quantum memory integrated with a superconducting quantum logic circuit needs to implement a swap-state and an idle-state. In the swap-state, it needs to perform a high-fidelity quantum state transfer. In the idle-state, it preserves the memory's ultra-high coherence and strongly suppresses the parasitic decoherence introduced into the superconducting quantum circuit.

Direct quantum state transduction between a superconducting qubit and a mechanical resonator using a piezoelectric material always induces large fixed parasitic decoherence to both superconducting and mechanical resonators due to the static couplings between the lossy piezoelectric material and the acoustic mode of interest and superconducting qubit [137, 31, 30, 120, 78, 77, 90, 23]. Efforts in the literature have been focused on maximizing the cooperativity of the piezoelectric transduction in the system to maximize the quantum state transfer fidelity. This can be done with optimal designs that maximize the ratio of the qubit electric energy and acoustic energy directly involved in the piezoelectric transduction. However, such optimization is fundamentally limited by the ratios of the chosen piezoelectric material's piezoelectric coupling coefficient k -factor [27, 56] over its intrinsic material loss tangents in elastic and electric domains. For example, the commonly used low-loss thin-film piezoelectric material Aluminum Nitride (AlN) has k -factor $k_{\text{AlN}}^2 \sim 1\%$ [90]. It indicates that this material can transduce at most 1% of its mechanical energy into electric energy. The realizable piezoelectric coupling rate, J_p , is bounded according to (6.22).

$$J_p \leq J_{\text{AlN}} \equiv k_{\text{AlN}} \frac{\omega_m}{2} \quad (6.22)$$

This leads to a coupling rate at most $J_p/2\pi = J_{\text{AIN}}/2\pi \sim 250$ MHz between a qubit and a piezoacoustic resonator for a resonance $\omega_q/2\pi = \omega_m/2\pi \sim 5$ GHz.

On the other hand, a phononic microwave resonator made out of AlN was shown to have a quality factor of $Q_{\text{AIN}} \sim 20000$ [129] (a decay rate of $\gamma_{\text{AIN}}/2\pi \sim 255$ kHz). Furthermore, AlN has microwave loss tangent of $\tan \delta_{\text{AIN}} \sim 5 \times 10^{-4}$ ($\kappa_{\text{AIN}}/2\pi \sim 2.5$ MHz) [137, 31, 30, 120, 78, 77]. The maximal cooperativity in a directly coupled qubit-acoustic system is $C_{\text{AIN}}^{\text{max}} = \frac{4J_{\text{AIN}}^2}{\gamma_{\text{AIN}}\kappa_{\text{AIN}}} \sim 3.8 \times 10^5$. A similar analysis can be done to show that the maximum cooperativity achievable in a coupled qubit-piezoacoustic system using piezoelectric material LiNbO₃ is $\sim 10^6$ with parameters from recent works on defect phononic cavity made with LiNbO₃ [9]. Despite the possibility for realizing high fidelity quantum state transfer as promised by the potentially significant cooperativity, electric and the acoustic modes are susceptible to significant piezoelectric material losses that can not be turned off after switching into the idle-state.

To mitigate the idle-state parasitic mechanical loss in the memory mode, it can be designed such that a small participation ratio of the mechanical energy (η_m) exists in piezoelectric material. The reduction will in principle not change the maximal cooperativity of the transduction process. This is true when the qubit total loss (κ_q) is dominated by the parasitic loss due to its energy participation (η_q) in the lossy piezoelectric material. It is easy to show that $J_p \leq \sqrt{\eta_m \eta_q} k_{\text{AIN}} \frac{\omega_m}{2}$ with total mechanical damping rate $\gamma_m = \eta_m \gamma_{\text{AIN}}$ and total qubit relaxation rate $\kappa_q = \eta_q \kappa_{\text{AIN}} + \kappa_i$. Note that energy participation ratios only limit the upper bound on the obtainable piezoelectric coupling rate (J_p). The obtained piezoelectric coupling rate also relies on the field overlap efficiency between the piezoelectric field of an acoustic mode of interest and the external circuit's electric field in the material. Nevertheless, a smaller mechanical participation ratio reduces the coupling rate $\propto \sqrt{\eta_m}$ given the same field overlap.

For coherent quantum acoustic transduction, the state swapping rate should be larger than the total qubit damping rate (κ_q). The later can be reduced with lower electrical participation ratio η_q and is bounded below by the intrinsic qubit loss of a good qubit with relaxation time $\sim 30 \mu\text{s}$ ($\kappa_i/2\pi \sim 5$ kHz) assumed for the rest of this work. With these constraints, the smallest qubit energy participation ratio for keeping the previously estimated high cooperativity independent of the change in participation ratios

is $\eta_q^{\min} \sim \frac{\kappa_i}{\kappa_{\text{AIN}}}$ such that $\eta_q \kappa_{\text{AIN}} > \kappa_i$. To have $J_p > \kappa_i$ in this limit, we then require $\eta_m \gtrsim \frac{\kappa_{\text{AIN}} \kappa_i}{J_{\text{AIN}}^2}$ where J_{AIN} is the greatest piezoelectric coupling rate achievable with unity participation ratios. This leads to a minimal parasitic mechanical damping of acoustic memory in a direct piezoelectric transduction scheme, $\gamma_m^{\min} \simeq \frac{4\kappa_i}{C_{\text{AIN}}^{\max}}$ which can be comparable to the state-of-art intrinsic acoustic damping $\gamma_m/2\pi \sim 1$ Hz [74] for cooperativity $C_{\text{piezo}}^{\max} \sim 10^6$ with either AlN or LiNbO₃ shown previously.

Even though the best performance achievable with simple direct coupling scheme is promising, engineering such a piezoacoustic device providing maximal field overlap for reaching optimal transduction ($J_p = \sqrt{\eta_m \eta_q} k_{\text{AIN}} \frac{\omega_m}{2}$) is very challenging. This is because design parameters are coupled and constraint by nano-fabrication capabilities and piezoelectric material crystal axis orientations. Other practical limitations such as complicated wiring directly on the phononic memory with mechanically lossy materials can also significantly degrade memory quality and reduce the yield of device fabrication. Moreover, even if the conditions can be satisfied with design and fabrication, the coupling rate will be close to the transmon intrinsic relaxation rate. Such a slow SWAP-gate between the superconducting system and acoustic memory limits the usefulness of utilizing the quantum memory to boost the scalability of a superconducting quantum circuit.

The device proposed here separates the directly coupled system into two parts so that different parts can be optimized for different tasks with more design freedom. The intermediate hybrid piezoelectric system that efficiently transduces electric field into acoustic vibration and the high-coherence system that is composed of an ultra-high quality acoustic memory cavity and high coherence superconducting qubit. This device also contains various in-situ controls that can not only switch the device between two operation states but also optimize their performance in both states. The swap-state ensures that the qubit quantum state can be written into (readout of) the memory cavity with high fidelity and the idle-state minimizes the influence of the coupling to preserve high qubit and memory phonon bare coherence. It can be shown that the overall swap-state transfer cooperativity is still bounded by the optimal cooperativity achievable with direct coupling. However, achieving optimal piezoelectric coupling does not need to further complicate the piezoacoustic resonator and compromise ultra-high quality acoustic memory cavity. Moreover, it is possible to swap a quantum state faster than the direct coupling scheme for the same

level of the idle-state qubit and memory coherence. Different parameter regions in J_q , ω_m , and ω_{em} for a fixed $\omega_{pa}/2\pi = 5.15$ GHz can be explored to identify the best parameter set that optimizes the performance of the device in both swap-state and idle-state.

6.3.1 Swap-State: Quantum State Transfer

For a coupled four-cavity system shown in Fig. 6.7a, the overall Hamiltonian can be written as (6.23),

$$\begin{aligned} \hat{H} = & \hbar \frac{\omega_q}{2} \hat{\sigma}_z + \hbar \omega_{em} \hat{b}_{em}^\dagger \hat{b}_{em} + \hbar \omega_{pa} \hat{b}_{pa}^\dagger \hat{b}_{pa} \\ & + \hbar \omega_m \hat{a}^\dagger \hat{a} + \hat{H}_{int}, \end{aligned} \quad (6.23)$$

with the four-cavity interaction part in (6.24),

$$\begin{aligned} \hat{H}_{int} = & \hbar J_q (\hat{\sigma}_+ \hat{b}_{em} + \hat{\sigma}_- \hat{b}_{em}^\dagger) + \hbar J_m (\hat{b}_{pa} \hat{a}^\dagger + \hat{b}_{pa}^\dagger \hat{a}) \\ & + \hbar J_p (\hat{b}_{em} \hat{b}_{pa}^\dagger + \hat{b}_{em}^\dagger \hat{b}_{pa}), \end{aligned} \quad (6.24)$$

where $\hat{\sigma}_\pm$ are the raising (+) and lowering (−) operators of the superconducting qubit, and $\{\hat{a}, \hat{a}^\dagger\}$ are the bosonic operators of the memory resonator mode. $\{\hat{b}_{em,pa}, \hat{b}_{em,pa}^\dagger\}$ are intermediate electric resonator (I_{em}) and piezoacoustic resonator (I_{pa}) modes' bosonic operators, respectively.

The intermediate resonators are tuned resonant with frequency $\omega_{em} = \omega_{pa}$ and hybridized into symmetry (+) and anti-symmetric (−) modes (WLOG, we assume that $\omega_\pm = \omega_{pa} \pm J_p$) as shown in Fig. 6.7b during the swap-state, the intermediate system can be diagonalized with (6.25) leading to (6.26),

$$\hat{b}_\pm = (\hat{b}_{em} \pm \hat{b}_{pa})/\sqrt{2}, \quad (6.25)$$

$$\hat{H} = \hbar \frac{\omega_q}{2} \hat{\sigma}_z + \sum_{k=\pm} \hbar \omega_k \hat{b}_k^\dagger \hat{b}_k + \hbar \omega_m \hat{a}^\dagger \hat{a} + \hat{H}_{int}, \quad (6.26)$$

where the interaction part of the Hamiltonian is transformed into (6.27),

$$\hat{H}_{int} = \sum_{k=\pm} \left(\begin{array}{c} \hbar \frac{J_q}{\sqrt{2}} (\hat{\sigma}_+ \hat{b}_k + \hat{\sigma}_- \hat{b}_k^\dagger) \\ + \hbar \frac{k J_m}{\sqrt{2}} (\hat{a}^\dagger \hat{b}_k + \hat{a} \hat{b}_k^\dagger) \end{array} \right). \quad (6.27)$$

To adiabatically eliminate the far-detuned intermediate system degrees of freedom ($\{\hat{b}_{em,pa}, \hat{b}_{em,pa}^\dagger\}$) and focus on the effective coupling between the qubit ($\hat{\sigma}_\pm$) and

memory ($\{\hat{a}, \hat{a}^\dagger\}$), we can define the following unitary transformation, \hat{U}_{vc} , in (6.28),

$$\hat{U}_{\text{vc}} = \exp \left(\sum_{k=\pm} k \frac{(J_{\text{m}}\hat{a}^\dagger + J_{\text{q}}\hat{\sigma}_+) \hat{b}_k - (J_{\text{m}}^*\hat{a} + J_{\text{q}}^*\hat{\sigma}_-) \hat{b}_k^\dagger}{\sqrt{2}(\omega_k - \omega_{\text{m}})} \right). \quad (6.28)$$

Apply it to (6.26) and (6.27), it can be shown that the final effective Hamiltonian after ignoring higher order terms involving $O\left(\left(\frac{J_{\text{q,m}}}{\omega_{\pm} - \omega_{\text{q,m}}}\right)^2\right)$ has the form (6.29) assuming $\omega_{\text{q}} \simeq \omega_{\text{m}}$ and $J_{\text{q}}, J_{\text{m}} \ll \sqrt{2}|\omega_{\pm} - \omega_{\text{q,m}}|$.

$$\hat{H}_{\text{eff}} = \hbar \frac{\omega'_{\text{q}}}{2} \hat{\sigma}_z + \hbar \omega'_{\text{m}} \hat{a}^\dagger \hat{a} + \hbar J_{\text{vc}} (\hat{\sigma}_+ \hat{a} + \hat{\sigma}_- \hat{a}^\dagger) \quad (6.29)$$

$$J_{\text{vc}} = \frac{J_{\text{q}} J_{\text{m}}}{2} \left(\frac{1}{\omega_+ - \omega_{\text{m}}} - \frac{1}{\omega_- - \omega_{\text{m}}} \right) \quad (6.30)$$

$$\omega'_{\text{q,m}} = \omega_{\text{q,m}} - \frac{J_{\text{q,m}}^2}{2} \left(\frac{1}{\omega_+ - \omega_{\text{q,m}}} - \frac{1}{\omega_- - \omega_{\text{q,m}}} \right) \quad (6.31)$$

where J_{vc} is the effective virtual coupling rate between the transmon qubit and memory mode. ω'_{q} and ω'_{m} are renormalized frequencies of the qubit and the memory cavity after diagonalizing and eliminating the intermediate system degrees of freedom in the far-detuned limit. The bare qubit and memory cavity frequencies ($\omega_{\text{q,m}}$) are Lamb shifted by the detuned intermediate system as seen in (6.31). The virtual coupling process can be understood to contain two quantum channels connecting the qubit with acoustic memory cavity. Each channel is formed with a super-mode of the intermediate system that mediates the virtual coupling, as expressed with $J_{\text{vc},\pm} = \pm \frac{J_{\text{q}} J_{\text{m}}}{2(\omega_{\pm} - \omega_{\text{m}})}$.

The swap-state requires degenerate intermediate resonators ($\omega_{\text{em}} = \omega_{\text{pa}}$) and matched renormalized qubit and memory frequencies ($\omega'_{\text{q}} = \omega'_{\text{m}}$). For a given $J_{\text{p}}/2\pi = 100$ MHz and $J_{\text{m}}/2\pi = 5$ MHz, the parameters requiring optimization are design and fabrication defined piezo-memory detuning, $\Delta_{\text{pa}} \equiv \omega_{\text{pa}} - \omega_{\text{m}}$, and external flux tunable electric coupling, J_{q} , for achieving high state-transfer fidelity with a small piezo-memory coupling, J_{m} , that is needed to suppress idle-state memory piezoelectric material damping (γ_{pm}). The state transfer fidelity dependence on Δ_{pa} and J_{q} is shown in Fig. 6.13a assuming $\kappa_{\text{em}}/2\pi = 600$ kHz, $\gamma_{\text{pa}}/2\pi = 200$ kHz, and $\kappa_{\text{i}}/2\pi = 5$ kHz that can be achieved with state-of-art device fabrication and known material properties [9]. As high state transfer fidelity requires the effective

frequencies of the qubit and the memory are the matched ($\omega'_q = \omega'_m$), the qubit bare frequency ω_q needs to be tuned appropriately. The fine-tuning of the qubit frequency leads to the near-unity state-transfer fidelity shown Fig. 6.13a over a wide range of parameters (J_q and Δ_{pa}). Thus, even with realistic fabrication randomness in acoustic resonators' detuning (Δ_{pa}), it is always possible to perform a high-fidelity SWAP-Gate between the qubit and memory.

A red-dotted line cutting Fig. 6.13a leads to Fig. 6.13b. The later figure contains an oscillating region around $\Delta_{pa}/2\pi \simeq J_p/2\pi = 100$ MHz. This region corresponds to the case where the memory cavity is almost resonant with a super-mode of the intermediate system ($\omega_m \sim \omega_-$). If we take $\Delta_{pa} = J_p$ as indicated by the black-dashed vertical line in Fig. 6.13a and b, we can obtain the time-domain evolution of the first excited state populations of the four coupled modes in the system shown in Fig. 6.13c.

As will be discussed in the next section, a large $|\Delta_{pa}|$ is preferred in this virtual coupling scheme to suppress the idle-state parasitic mechanical loss in the memory cavity while maintaining a high state-transfer fidelity. We also need to avoid memory cavity hybridization with the intermediate system super-modes in the swap-state around $|\Delta_{pa}| \sim J_p$. Consequently, the large detuned region ($|\Delta_{pa}| > J_p$) in Fig. 6.13a is the region of interest. Further discussion on optimizing system operating parameters will be presented in a later section. In order to characterize the performance of this class of quantum memory that operates in two distinct functional states, we will introduce a new figure of merit called the Asynchronized Quantum Efficiency (AQE) that can be optimized against an external flux tunable J_q and design-fabrication defined Δ_{pa} .

Taking device parameters as $\omega_m/2\pi \sim 5$ GHz, $\omega_{pa}/2\pi \sim 5.15$ GHz, $J_m/2\pi \sim 5$ MHz, and $J_p/2\pi \sim 5$ MHz, the swap-state can have a virtual coupling rate $J_{vc}/2\pi \sim 200$ kHz. The effective virtual coupling leads to a quantum state transfer time ~ 1.25 μ s. The faster swap-state rate can be obtained with larger J_q as the state transfer fidelity is close to unity over a wide range of J_q according to Fig. 6.13a. However, a larger J_q increases the superconducting qubit's total damping (κ_q) in the swap-state. It is straightforward to show that the qubit-memory cooperativity will be the independent of J_q in the dispersive limit ($J_q \ll \sqrt{2}|\Delta_{pa} \pm J_p|$). This is true if the qubit total damping rate κ_q is dominated by the parasitic loss introduced

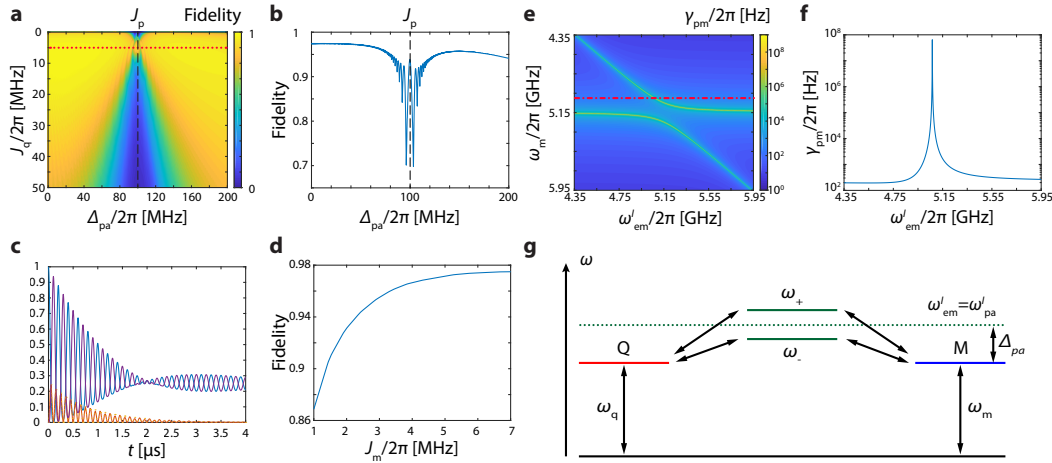


Figure 6.13: **a**, Qubit-memory state transfer fidelity during device swap-state transfer assuming qubit intrinsic damping rate $\kappa_i/2\pi = 5$ kHz, memory damping rate $\gamma_i/2\pi = 1$ Hz, intermediate electric resonator damping rate $\kappa_{em}/2\pi = 600$ kHz, intermediate piezoacoustic resonator damping rate $\gamma_{pa}/2\pi = 200$ kHz, piezo-memory coupling rate $J_m/2\pi = 5$ MHz, resonant intermediate system resonators $\omega_{em}/2\pi = \omega_{pa}/2\pi = 5.15$ GHz. For this plot, the qubit bare frequency is fine-tuned such that effective qubit and memory frequencies are matched ($\omega'_q = \omega'_m$). The fidelity here is defined as the state transfer fidelity ($F_{pa} \equiv |\langle e, 0 | \hat{U}_{pa}(t_{pa}) |g, 1\rangle|^2$) for transferring a quantum state ($|\psi\rangle_{q,m}$ are quantum states of the qubit (q) and memory (m) subspace respectively) $|\phi_i\rangle = |e, 0\rangle = |e\rangle_q |0\rangle_m$ to $|\phi_f\rangle = |g, 1\rangle = |g\rangle_q |1\rangle_m$ via the system propagator $\hat{U}_{pa}(t_{pa})$ with t_{pa} chosen to maximize the fidelity in time-domain evolution. **b**, Fidelity as a function of ($\Delta_{pa} = \omega_{pa} - \omega_m$) for $J_q/2\pi = J_m/2\pi \approx 5$ MHz corresponding to the red-dotted line in **a**. The oscillation near $\Delta_{pa}/2\pi \sim J_p/2\pi = 100$ MHz is caused by the hybridization of the qubit and memory cavity with the intermediate system's lower super-mode (ω_-). **c**, The time-domain evolution of the first excited state populations of the four coupled modes in the system including the qubit (blue-solid), intermediate electric resonator (red-solid), intermediate piezoacoustic resonator (yellow-dotted), and memory cavity (purple-solid), if $\Delta_{pa} = J_p$. **d**, Maximum state transfer fidelity as a function of J_m . The state transfer fidelity illustrated here was optimized with respect to Δ_{pa} , J_q , and ω_q . Other parameters such as the intrinsic damping rates are fixed to the values in obtaining **a** for each given J_m . **e**, Induced memory cavity's piezoelectric material parasitic loss γ_{pm} due to its coupling to the intermediate piezoacoustic resonator as a function of intermediate tunable electromagnetic resonator frequency (ω_{em}) and designed memory cavity frequency (ω_m) when the qubit is decoupled in the device idle-state. **f**, Induced memory cavity loss due to coupling to the intermediate system for the choice that $\omega_m/2\pi = 5$ GHz corresponding to the red-dotted line in **e**. **g**, swap-state energy level diagram of the system with $\omega_m/2\pi \sim 5$ GHz which is about 50 MHz below the lower super-mode of the intermediate system.

via J_q in the swap-state ($\kappa_q \gg \kappa_i$). If $J_q \gtrsim |\Delta_{pa} \pm J_p|$, the swap-state qubit and memory hybridize with a super-mode of the extremely lossy intermediate system, this hybridization leads to a triangular region with significantly reduced fidelity centered around $\Delta_{pa} \sim J_p$ for a large J_q in Fig. 6.13a.

6.3.2 Idle-State: Memory and Qubit Coherence Preservation

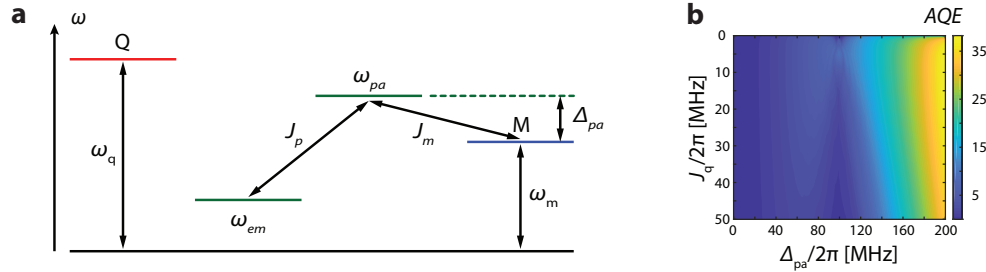


Figure 6.14: **a**, the idle-state energy levels. To reach the idle-state indicated here, we can far detune the qubit frequency (ω_q) such that it is tuned to its flux-insensitive point away from the memory cavity frequency (ω_m). Furthermore, we can turn off the electric coupling (J_q) between the qubit and the intermediate electric resonator so that the superconducting qubit can be further protected. We also far detune the tunable electric resonator in the system such that the intermediate system is no longer hybridized. In this case, the piezoacoustic cavity is now dispersively coupled to the memory cavity at its bare frequency (ω_{pa}). The bare frequency is about $J_p/2\pi \approx 100$ MHz higher than the lower super-mode (ω_-) in the swap-state. Thus, the piezoacoustic mode is further detuned from the memory mode by Δ_{pa} . The parasitic damping (γ_{pm}) introduced into the memory cavity via the fabrication defined mechanical coupling $J_m/2\pi \sim 5$ MHz is strongly suppressed by this detuning (Δ_{pa}) and can be lower than ~ 100 Hz as can be seen in Fig. 6.13e and **f**. **b**, the Asynchronous Quantum Efficiency (AQE) as a product of the swap-state transfer fidelity (F_{pa}) and memory enhancement factor (G_{qm}). It is introduced to characterize the performance of the class of quantum memory devices that can switch between a swap-state and an idle-state. A large AQE is preferred for a good device that operates in this asynchronous way.

Quantum state swap is turned off during the idle-state of the device. The idle-state corresponds to the energy levels shown in Fig. 6.14a. In this state, the qubit is tuned to its flux insensitive point far from the memory frequency. Moreover, the qubit to intermediate electric resonator coupling, J_q , can be tuned to zero in this state to further isolate the qubit from losses.

For simplicity of analyzing decoherence of the memory cavity due to coupling

to the intermediate system, it can be assumed that the intermediate system and the memory cavity effectively form a linearly coupled three-cavity system. The amount of decoherence noise introduced into the memory cavity due to J_m can be understood with the bare noise power spectrum of the lossy piezoacoustic mode ($\hat{b}_{pa}, \hat{b}_{pa}^\dagger$) strongly coupled to a lossy electromagnetic resonator mode ($\hat{b}_{em}, \hat{b}_{em}^\dagger$). The power spectral functions can be shown as in Appendix A.3 to be (6.32) and (6.33),

$$S_{\hat{b}_{pa}^\dagger \hat{b}_{pa}^\dagger}[\omega] = \frac{(\langle n_2 \rangle + 1) \gamma_{pa} + \frac{\langle n_1 \rangle + 1 J_p^2 \kappa_{em}}{(\omega_{em} - \omega)^2 + \frac{\kappa_{em}^2}{4}}}{\left(\omega_{pa} - \omega - \frac{J_p^2 (\omega_{em} - \omega)}{(\omega_{em} - \omega)^2 + \frac{\kappa_{em}^2}{4}} \right)^2 + \left(\frac{\gamma_{pa}}{2} + \frac{J_p^2 \frac{\kappa_{em}}{2}}{(\omega_{em} - \omega)^2 + \frac{\kappa_{em}^2}{4}} \right)^2}, \quad (6.32)$$

$$S_{\hat{b}_{pa} \hat{b}_{pa}}[\omega] = \frac{\langle n_2 \rangle \gamma_{pa} + \frac{\langle n_1 \rangle J_p^2 \kappa_{em}}{(\omega_{em} + \omega)^2 + \frac{\kappa_{em}^2}{4}}}{\left(\omega_{pa} + \omega - \frac{J_p^2 (\omega_{em} + \omega)}{(\omega_{em} + \omega)^2 + \frac{\kappa_{em}^2}{4}} \right)^2 + \left(\frac{\gamma_{pa}}{2} + \frac{J_p^2 \frac{\kappa_{em}}{2}}{(\omega_{em} + \omega)^2 + \frac{\kappa_{em}^2}{4}} \right)^2}. \quad (6.33)$$

The noise in piezoacoustic mode can perturb and decohere the memory cavity via mechanical coupling J_m . The induced memory mode piezoelectric material decay rate is shown in equation (6.34),

$$\begin{aligned} \gamma_{pm} &= J_m^2 \left(S_{\hat{b}_{pa}^\dagger \hat{b}_{pa}^\dagger}[\omega_m] - S_{\hat{b}_{pa} \hat{b}_{pa}}[-\omega_m] \right) \\ &= \frac{J_m^2 \left(\gamma_{pa} + \frac{J_p^2 \kappa_{em}}{(\omega_{em} - \omega_m)^2 + \frac{\kappa_{em}^2}{4}} \right)}{\left(\omega_{pa} - \omega_m - \frac{J_p^2 (\omega_{em} - \omega_m)}{(\omega_{em} - \omega_m)^2 + \frac{\kappa_{em}^2}{4}} \right)^2 + \left(\frac{\gamma_{pa}}{2} + \frac{J_p^2 \frac{\kappa_{em}}{2}}{(\omega_{em} - \omega_m)^2 + \frac{\kappa_{em}^2}{4}} \right)^2}, \end{aligned} \quad (6.34)$$

where κ_{em} (γ_{pa}) is the intrinsic decay rate of the intermediate electromagnetic cavity (piezoacoustic cavity) and ω_{em} (ω_{pa}) is the frequency of the intermediate electromagnetic resonator (piezoacoustic cavity). $\langle n_1 \rangle$ ($\langle n_2 \rangle$) is the equilibrium thermal occupation of the photon (phonon) bath at a refrigerated temperature $T_{env} \sim 10$ mK. The noise power in the piezoacoustic mode degree of freedom ($\hat{b}_{pa}, \hat{b}_{pa}^\dagger$) is contributed by the noise of piezoacoustic cavity's intrinsic loss channel (γ_{pa}) and the

noise from the intermediate electromagnetic resonator mode's intrinsic loss channel (κ_{em}) via the piezoelectric coupling J_p .

Idle-state memory cavity coherence can be protected by far detuning the intermediate electromagnetic resonator such that the memory cavity only suffers the small parasitic loss from a far detuned piezoacoustic resonator. Given $\omega_{pa}/2\pi = 5.15$ GHz and $J_m/2\pi = 5$ MHz, the induced memory cavity piezoelectric material loss rate (γ_{pm}) as a function of memory cavity's designed frequency (ω_m) and intermediate electromagnetic cavity frequency (ω_{em}) is shown in Fig. 6.13e. Designing the memory cavity such that $\omega_m/2\pi \simeq 5$ GHz will lead to an induced loss curve in Fig. 6.13f corresponding to the red-dashed cut line in Fig. 6.13e. If the intermediate tunable electromagnetic resonator is tuned to a low frequency in idle-state, the memory cavity can preserve its high coherence as γ_{pm} is minimized. The residual induced memory cavity loss due to the fixed coupling J_m to the piezoacoustic resonator will limit the memory phonon lifetime $\tau_m = \frac{1}{\gamma_i + \gamma_{pm}} \simeq \frac{1}{\gamma_{pm}} \sim 1$ ms assuming a large piezoacoustic resonator damping rate $\gamma_{pa}/2\pi \simeq 200$ kHz. Note that the residual induced memory mode loss is $\propto J_m^2$. As a result, it is preferable to take a small J_m . Meanwhile, the swap-state state transfer fidelity decreases rapidly with smaller J_m as illustrated in Fig. 6.13d. The chosen $J_m/2\pi \sim 5$ MHz is small enough to suppress the additional loss in idle-state while still offerings close to unity (~ 0.97) state transfer fidelity during swap-state in the presence of large intermediate system loss.

6.3.3 System Parameter Optimization for A Large Asynchronized Quantum Rate

A good figure of merit that can be defined for evaluating such class of asynchronized quantum logic devices is the Asynchronized Quantum Efficiency (AQE) expressed in (6.35),

$$\zeta_{AQE} \equiv F_{pa}(J_q, \Delta_{pa})G_{qm}(\Delta_{pa}), \quad (6.35)$$

as a product of the swap-state state transfer fidelity (F_{pa}) and idle-state memory enhancement factor, $G_{qm, idle}(\Delta_{pa})$. The enhancement factor is the ratio of idle-state memory relaxation time ($\tau_m = 1/\gamma_{m, idle}$) over bare qubit relaxation time ($\tau_q = 1/\kappa_i$) as in (6.36),

$$G_{qm}(\Delta_{pa}) \equiv \kappa_i/\gamma_{m, idle}(\Delta_{pa}), \quad (6.36)$$

where the idle-state memory damping rate is expressed in (6.37),

$$\gamma_{m,\text{idle}}(\Delta_{\text{pa}}) = \gamma_i + \frac{J_m^2 \gamma_{\text{pa}}}{\Delta_{\text{pa}}^2 + \frac{\gamma_{\text{pa}}^2}{4}}. \quad (6.37)$$

A high AQE indicates that the quantum memory can be accessed by a superconducting quantum circuit with a high fidelity and store quantum resources over an extended period.

The ζ_{AQE} can be optimized with respect J_q and Δ_{pa} seen in Fig. 6.14b for the previously chosen realistic system parameters in obtaining Fig. 6.13a. It can be seen that, for this proposed scheme with a high-quality qubit having bare energy relaxation time $\sim 30 \mu\text{s}$, a larger piezo-memory detuning ($|\Delta_{\text{pa}}|$) is generally preferred for $J_{\text{vc}}(\Delta_{\text{pa}}) \gg \kappa_{q,\text{swap}}(\Delta_{\text{pa}})$ and $\kappa_{q,\text{swap}}(\Delta_{\text{pa}}) \gg \kappa_i \simeq 2\pi \times 5 \text{ kHz}$ where $\kappa_{q,\text{swap}}$ is the swap-state qubit total damping rate in (6.38),

$$\kappa_{q,\text{swap}}(\Delta_{\text{pa}}) = \kappa_i + \frac{J_q^2 \left(\kappa_{\text{em}} + \frac{J_p^2 \gamma_{\text{pa}}}{\Delta_{\text{pa}}^2 + \frac{\gamma_{\text{pa}}^2}{4}} \right)}{\left(\Delta_{\text{pa}} - \frac{J_p^2 \Delta_{\text{pa}}}{\Delta_{\text{pa}}^2 + \frac{\gamma_{\text{pa}}^2}{4}} \right)^2 + \left(\frac{\kappa_{\text{em}}}{2} + \frac{J_p^2 \gamma_{\text{pa}}}{\Delta_{\text{pa}}^2 + \frac{\gamma_{\text{pa}}^2}{4}} \right)^2}. \quad (6.38)$$

This condition can be satisfied for $|\Delta_{\text{pa}}|/2\pi \leq 1 \text{ GHz}$. Since $J_{\text{vc}}(\Delta_{\text{pa}}) \gg \gamma_{m,\text{swap}}(\Delta_{\text{pa}}) \gg \gamma_i \sim 2\pi \times 1 \text{ Hz}$ is true for an ultra-wide range of $|\Delta_{\text{pa}}|$ with swap-state memory damping rate expressed in (6.39),

$$\gamma_{m,\text{swap}}(\Delta_{\text{pa}}) = \gamma_i + \frac{J_m^2 \left(\gamma_{\text{pa}} + \frac{J_p^2 \kappa_{\text{em}}}{\Delta_{\text{pa}}^2 + \frac{\kappa_{\text{em}}^2}{4}} \right)}{\left(\Delta_{\text{pa}} - \frac{J_p^2 \Delta_{\text{pa}}}{\Delta_{\text{pa}}^2 + \frac{\kappa_{\text{em}}^2}{4}} \right)^2 + \left(\frac{\gamma_{\text{pa}}}{2} + \frac{J_p^2 \kappa_{\text{em}}}{\Delta_{\text{pa}}^2 + \frac{\kappa_{\text{em}}^2}{4}} \right)^2}. \quad (6.39)$$

a large swap-state cooperativity, $C_{\text{vc}} = \frac{4J_{\text{vc}}(\Delta_{\text{pa}})^2}{\kappa_{q,\text{swap}}\gamma_{m,\text{swap}}}$ with $J_{\text{vc}}(\Delta_{\text{pa}}) = \frac{J_q J_m}{2} \left(\frac{1}{\Delta_{\text{pa}} + J_p} - \frac{1}{\Delta_{\text{pa}} - J_p} \right)$, can be realized in a large detuning regime ($|\Delta_{\text{pa}}| > J_p$). Furthermore, the idle-state damping ($\gamma_{m,\text{idle}}$) of the acoustic memory is rapidly suppressed with a large detuning

according to (6.37). The near-unity state transfer fidelity with suppressed idle-state memory damping rate results in a large AQE for a large Δ_{pa} . After defining the Δ_{pa} and a small J_{m} with design and fabrication that is susceptible to randomness in practice, the electric coupling rate (J_{q}) can be adjusted with an external magnetic flux Φ_{g} to optimize the AQE in-situ.

6.3.4 Ultra-High Fidelity In-Memory Two-Qubit Quantum Gates

The small footprint of acoustic elements allows a transmon to be coupled to multiple single-mode acoustic memory resonators that collectively form a quantum memory bank. Furthermore, the non-linearity of the coupled qubit can act as a four-wave-mixer that effectively implements two-qubit gates for quantum states stored in two detuned acoustic memories when two microwave tones drive it with detuning matching the frequency difference between the two memories [52]. The gates are implemented with the transmon qubit being far detuned from the acoustic cavities. Under this condition, the gates are virtual gates, and the transmon qubit is not excited. Thus, the decoherence due to the energy participation in the transmon qubit during the gate operations is strongly suppressed and the gate fidelity is mostly limited by the decoherence of the acoustic cavities. In the optimal case, the virtual two-qubit gate fidelity can be expressed as (6.40) with $\bar{\gamma}$ being the average damping rate of the acoustic memory modes involved. $c_{\text{v}} = 1$ for a SWAP gate involving two acoustic memory cavities and $c_{\text{v}} = 2$ for a CZ gate involving three acoustic memory cavities. In the expression, $\Delta\nu$ characterizes the scale over which the difference in memory mode frequencies varies as defined in [52]. Since the point defect acoustic memories can have damping rate $\gamma_{\text{m}}/2\pi \sim 1$ Hz with the intermediate system super-modes far detuned from the memories and $\Delta\nu/2\pi \gtrsim 100$ MHz can be realized easily in designing the array of detuned single-mode acoustic memory cavities, the two-qubit gates' fidelities between a pair of detuned memory cavities $\simeq 99.999\%$ for a SWAP-gate and $\simeq 99.998\%$ for a CZ gate. The ultra-high fidelity two-qubit gates implemented in an acoustic memory bank together with ultra-high fidelity single transmon qubit gate can lead to a novel hardware efficient hybrid fault-tolerant quantum computing architecture using engineering feasible electric and acoustic elements.

$$F_{\text{v}} \simeq 1 - \frac{3c_{\text{v}}}{2} \left[\frac{\pi\bar{\gamma}}{\sqrt{2}\Delta\nu} \right]^{\frac{2}{3}} \quad (6.40)$$

6.3.5 Conclusion and Outlook

In this section, we proposed an experimentally realizable architecture with a realistic device design that is robust against fabrication randomness and can transfer, with near unity fidelity, a quantum state between a superconducting qubit and a phononic cavity which can store a quantum state for milliseconds. As mentioned earlier, the small footprint of a phononic memory cavity further allows a qubit to be coupled to multiple detuned single mode phononic memory cavities via one intermediate hybridized system. These phononic cavities can be used to store a large number of quantum states as quantum resources for the coupled quantum logic circuit. Furthermore, ultra-high fidelity two-qubit quantum gates can be directly carried out on a pair of ultra-high coherence phononic cavities by coupling them to a driven detuned transmon that acts as a four-wave-mixer [52]. The abilities to densely store a large number of quantum states by multiplexing multiple single mode acoustic memories around a transmon qubit and to carry out arbitrary ultra-high fidelity two-qubit gates between them lead to a scalable quantum information processing platform for building fault-tolerant quantum computers in a near future. Despite applications in near-term scalable quantum computing systems, the proposed architecture also opens doors to new research routes in manipulating a large number of mesoscopic mechanical objects to test the limit of quantum mechanics [88] and strong coupling of superconducting qubits to highly coherent elastic spins in single crystalline silicon. These purely elastic microwave spins may originate from neutral lattice defects and are only strongly coupled to strain field. They can potentially be used as extremely compact and coherent nonlinear quantum logic units embedded in a phononic crystal.

6.4 Stacked Phononic Piezoacoustic Crystal for Nonlinear Phononics And A New Architecture for Phononic Quantum-Bit

Similar to encoding quantum states in three-dimensional microwave cavities strongly coupled to a detuned superconducting transmon qubit which provides a slight non-linearity to the harmonic modes of the three-dimensional cavities, a mechanical cavity can also be perturbed to act directly as a quantum state storage and computation element by coupling it to a detuned Josephson Junction superconducting qubit. To strongly perturb the harmonic modes of the coupled cavity, it requires that the superconducting qubit and the cavity are strongly coupled to each other. The most efficient coupling can be realized with AlN that has main piezoelectric axis (c-axis) normal to the surface of its substrate using a vertically stacked Mo-AlN-Mo as what was done in the previous section. The mechanical mode that can be

most strongly coupled to the electrodes is the mode that is mostly vertical dilation motion. This means that the structure needs to be thick enough to have the dilation mode within the frequency range of the superconducting Josephson junction qubit \sim GHz. Furthermore, in order to achieve stronger coupling, it is desirable to have the superconducting qubit's electric energy participation (η_q) mostly overlapped with the piezoelectric region to have the largest possible qubit electric field overlap with the piezoacoustic mode electric polarization field. This means that increasing the planar size of the resonator scales up the coupling with increasing capacitance between the two electrodes. However, the increase of resonator size increases the density of mechanical modes that can be coupled to the electrodes strongly. This is similar to the first section where we discussed about the spurious mechanical mode crowding in the Lamb resonator with increasing size. The mechanical state space is direct product of mode space in the planar direction and the vertical dilation motion direction. The crowding of modes in the planar dimensions increase the number of modes near main coupling mode where the whole top surface of the resonator moves in phase and the same can be seen in the lower surface of the resonator. One way to eliminate the planar direction mode space density is to create phononic pattern in planar direction like the one shown in Fig. 6.15**b – d**. The three-dimensional phononic structure shown here is engineered in a way that there are two bandgaps around the vertical dilation motion mode which has an almost flat planar dispersion. As this dilation mode dispersion is isolated from the surrounding bands, the mode is not susceptible to mixing with spurious modes that appear with an increasing planar size of the resonator. The whole resonator will be able to resonate with a mode profile like Fig. 6.15**a**. The unit cell of the structure and the unit cell Γ -point mode of interest is shown in Fig. 6.16. This resonator can be called a phononic Bulk Acoustic Resonator (phBAR). In the following discussions, we assume that the Josephson junction inductance is fixed to about 22 nH.

We can now explore the quantum dynamics of the hybrid system shown in Fig. 6.17**a**. As it was mentioned previously, a piezoacoustic resonator can be modeled in the circuit dynamics as a serially connected large inductance with a small capacitor highlighted in the blue box. The superconducting qubit part of the device is in the red box. This includes the large capacitance provided by the electrodes in the phBAR region and a standard Josephson junction. The quantum degrees of freedom are the phase (ϕ_1) of the superconducting qubit and the phase (ϕ_2) of the piezoacoustic resonator. The Schrodinger equation of the system is shown in (6.41) with quantum

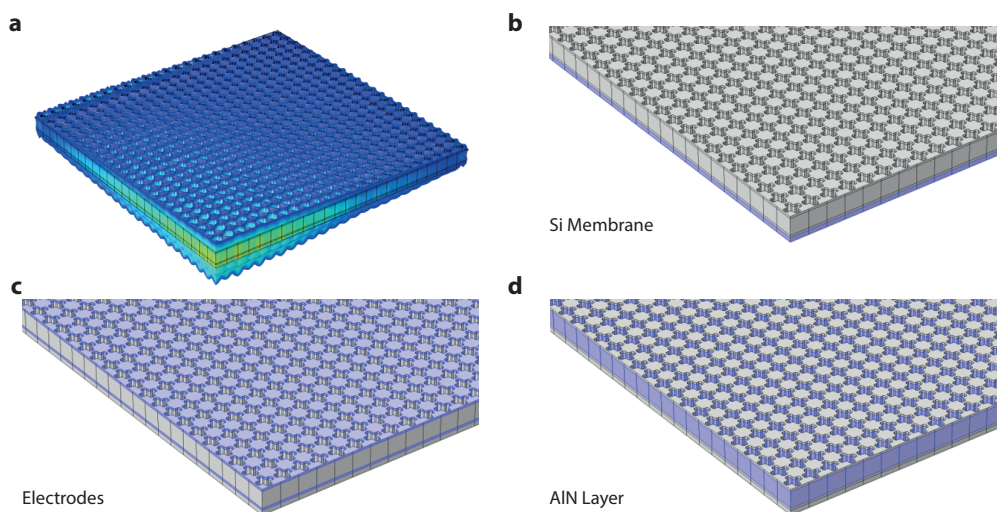


Figure 6.15: **a**, the high piezoelectric coupling thickness dilation bulk acoustic mode in a quarter of the photonic Bulk-Acoustic-Resonator (phBAR). The center of the piezoacoustic resonator deforms the most. **b - d** highlight different material layers of the phBAR which is a sandwich structure having piezoelectric AlN layer between two electrode layers. The sandwich is on top of a suspended silicon layer.

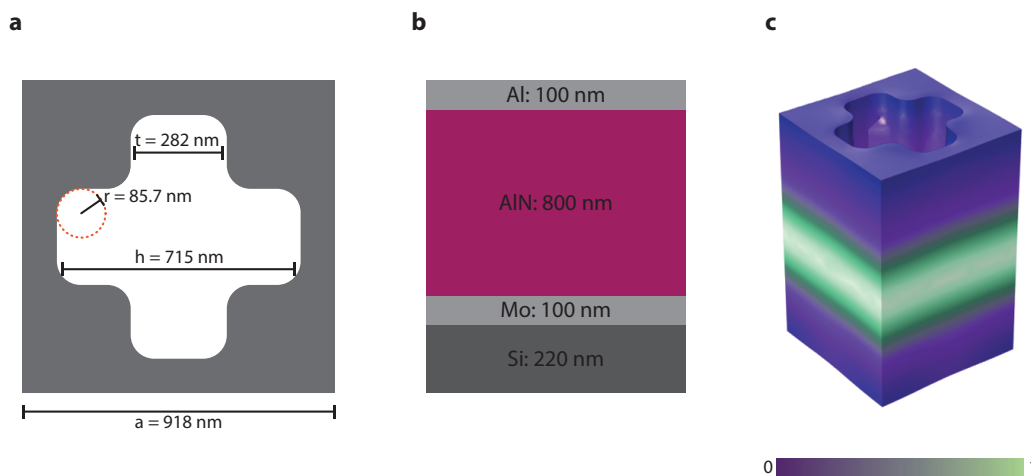


Figure 6.16: **a** shows the top down view of an unit cell of the phBAR. The parameters shown in the figure will eliminate the planar spurious modes around 4 GHz with a wide phononic bandgap for waves propagating in planar directions. **b** shows the vertical composition of an unit cell of the phBAR device and **c** is the normalized mechanical mode profile corresponding to the Γ -point of the band that forms the high piezoelectric coupling dilation phBAR mode shown in Fig. 6.15.

wave-function $\Psi(\phi_1, \phi_2)$ in the two phase variables' basis, $\{|\phi_1, \phi_2\rangle\}$. This is just a linear partial differentiation for a wave-function on a two-dimensional box having periodical boundary conditions as $\Psi(\phi_1 + n\pi, \phi_2 + m\pi) = \Psi(\phi_1, \phi_2)$ for $n, m \in \mathbb{Z}$. It can be easily solved with FEM we have been using for simulating the eigen modes of fields in complicated structures. A straightforward and careful reprogramming of the computational tool we have, we can quickly and accurately solve the eigen wave-functions of the system and their eigen frequencies. The solved wave-function ("boson cloud") can be illustrated in Fig. 6.17c from (1) – (7) for the first 7 modes. It can be identified that the mode 1, 3, 6 are anharmonically perturbed harmonic mechanical modes and the other are qubit-like electric modes of the system. The energy level dispersion of the system with respect to the number of residual charge bias associated with the phase node of the superconducting (charge) qubit in the system is in Fig. 6.18. It can be seen that the charge dispersion of the harmonic modes are flat meaning that they are not susceptible to the charge noise in the circuit on the superconducting qubit degree of freedom. It can also be found that the energy level spacings between the harmonic modes are not equal and they can exhibit aharmonicity ($\chi = \omega_{1 \rightarrow 2} - \omega_{0 \rightarrow 1}$) reaching about 100 MHz for the first three energy levels from the mechanical resonator. These means that it is possible for us to use perturbed energy levels of the mechanical resonator as high quality new mechanical qubit levels and the whole device can be thus called "mechmon".

$$\hat{H}_{\text{phBar}} = \frac{1}{2(C_J + C_m + C_g)} \hat{q}_1^2 - E_J \cos(\hat{\phi}_1) + \frac{1}{2C_m} \hat{q}_2^2 + \frac{1}{2L_m} \hat{\phi}_2^2 + \frac{1}{C_m} \hat{q}_1 \hat{q}_2 \quad (6.41)$$

6.5 Future Directions on Piezoelectric Microwave-Acoustic Transduction

As can be seen in the previous discussions presented in this chapter, the piezoelectric material piezoelectric coefficient and crystallinity are critical for achieving highly efficient and low noise quantum acoustic transduction. In terms of high piezoelectric coupling coefficients, there are a wide variety of materials that can significantly outperform the AlN we have been using. However, most of the materials will have significantly reduced piezoelectric coefficients in low temperatures. This is because as mentioned in the introduction chapter, material piezoelectric commonly has two contributions called intrinsic piezoelectricity and extrinsic piezoelectricity.

The intrinsic piezoelectricity originates from the central symmetric breaking of the material crystal unit cell. This effect directly leads to the electric polarization of the crystal under strain. As this is fundamentally related to the crystal structure

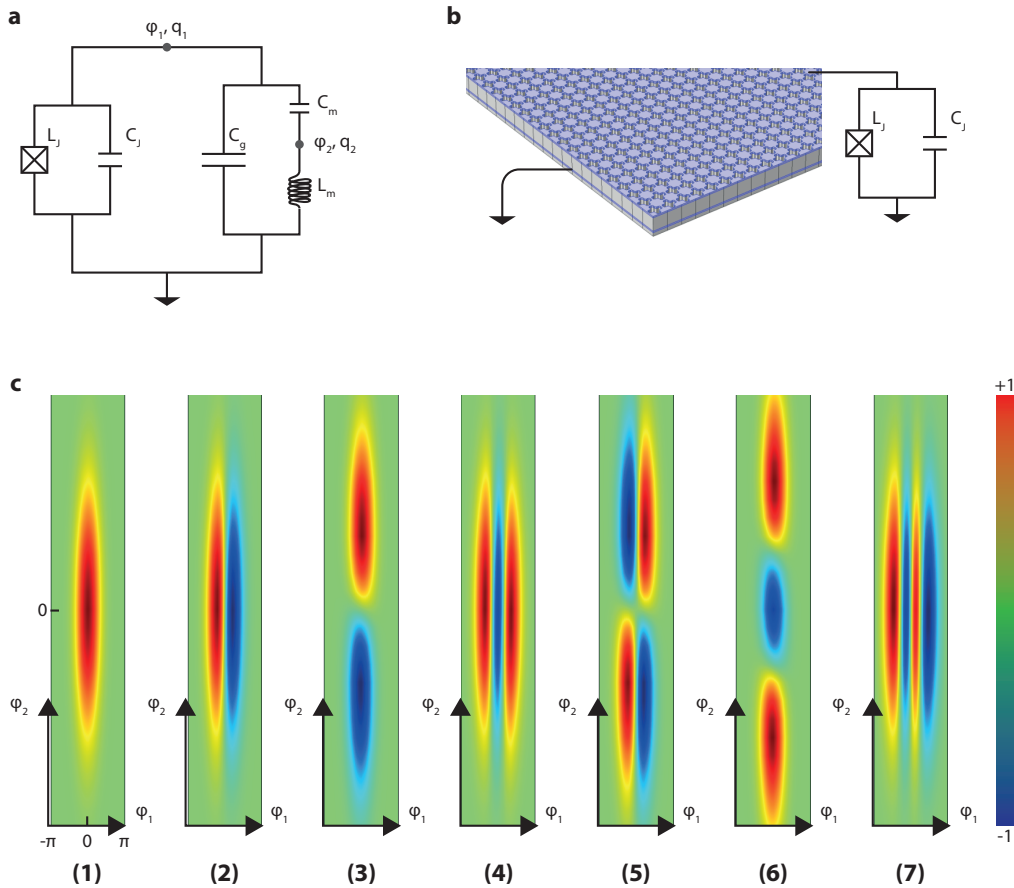


Figure 6.17: **a** illustrates the effective circuit diagram for the system with a Josephson junction characterized by L_J and C_J connected to the phBAR device as further shown in **b**. The phBAR device can be synthesized with an effective serial LC resonator (L_m and C_m) in parallel with a large capacitance provided by the linear dielectric capacitance between the two electrodes of the phBAR device. **c** shows the wave function $\Psi(\phi_1, \phi_2)$ of the lowest 7 eigen states of the anharmonic phBAR system. The third, and the sixth eigen states are perturbed anharmonic acoustic first excited and second excited quantum states. The first one is the system ground state. The qubit-like states in (2), (4), (5), (7) are wave functions of electric modes in the system. It should be noted that the electric modes are periodic in the Josephson junction phase variable ϕ_1 with periodicity 2π .

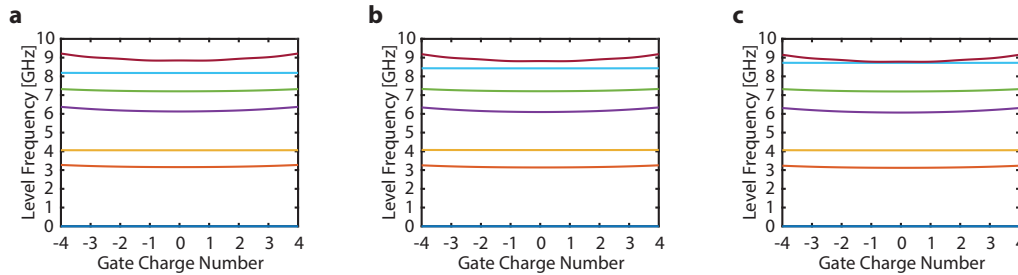


Figure 6.18: The charge dispersion corresponding to different piezoelectric coupling coefficients assuming that the dielectric capacitance $C_J \ll C_g = 100$ fF and junction inductance $L_J = 22$ nH. **a** is for $k_{\text{eff}}^2 = 1\%$. **b** shows the dispersion for $k_{\text{eff}}^2 = 1.5\%$ and this leads to anharmonicity between the lowest three mechanical modes to be around 290 MHz. **c** shows the dispersion for $k_{\text{eff}}^2 = 2\%$ which leads to anharmonicity between the lowest three mechanical modes to be around 600 MHz. The calculated charge dispersions also shows that the mechanical modes even though perturbed by dispersive coupling to nonlinear elements are highly charge fluctuation insensitive as compared to their qubit-like electric mode counterparts. This means that the anharmonic mechanical modes can be great candidates for coherently storing quantum information in a small footprint device.

and unit cell distortion, the intrinsic piezoelectricity is not going to change in low temperature.

The extrinsic piezoelectricity is commonly observed in poly-crystalline bulk piezoelectric materials. In such materials, each small domain with a well defined uniform crystal orientation is coupled to external electric field due to their intrinsic piezoelectricity. under external electric field, the domains are polarized tend to align with electric field. This tendency together with sufficient thermal mobility of the domain walls leads to the electric field induced structural change in the material. Such more drastic and macroscopic change in material structure causes a much larger strain response to the external electric field. Thus this extrinsic piezoelectricity is normally responsible for the large piezoelectric responses of most materials in room temperature. As the temperature is lowered, the domain wall movement is impeded since there is insufficient thermal energy for the domain walls to overcome potential barriers forbidding them from moving. In the mK environment we are concerned with, there can not be extrinsic piezoelectric contribution for any piezoelectric material. For example, the commonly used ceramic piezoelectric material PZT will have a factor of ten reduction in its piezoelectric response. As single crystalline AlN is an intrinsic piezoelectricity dominated material, its piezoelectric coefficients do not change much when the temperature is lowered.

Nevertheless, AlN is still a weak piezoelectric material that only has piezoelectric coupling coefficient $k_{\text{AlN}}^2 = 1\% \sim 4\%$. It is desirable to identify a new single crystalline material that can exhibit ultra-high intrinsic piezoelectric coefficient and perform well at low temperatures. Lithium Niobate (LiNbO_3) has been an emerging popular material to replace AlN in implementing various quantum acoustic transduction as its piezoelectric coefficient can be as large as $k_{\text{LiNbO}_3}^2 = 25\%$ [136, 16] if the electric field can be correctly aligned with its major piezoelectric crystal axis and proper acoustic mode can be engineered to have large elastic energy stored in strain along this major piezoelectric axis. Research efforts have been invested into developing robust nano-fabrication processes for patterning a hard material like LiNbO_3 . These efforts can lead to a new stage of quantum acoustic device research in a near future.

As an even larger leap forward in the coupling coefficient and single crystallinity can enable a variety of ultra-high performance quantum acoustic applications, it is also worth noticing some other single crystalline candidates that have been utilized widely to generate ultra-sound in industry and haven't been carefully looked at in the quantum acoustics community. A potential candidate for realizing such a great leap forward is Lead Magnesium Niobate-lead Titanate (PMN-PT). This single crystalline material has been widely used in medical ultra-sound generation since 1980s and recently various public and private efforts have been invested into micro-machining single crystalline PMN-PT with DRIE ($\text{Ar}+\text{C}_4\text{F}_8$) for MEMS applications [4, 139]. It is intrinsic piezoelectricity dominated and can exhibit piezoelectric coupling coefficient $k_{\text{PMN-PT}}^2 \gtrsim 50\%$ [73] in practice. Single crystalline PMN-PT has been consistently grown in industry by companies including Siemens. The single crystalline material also has the advantage over many other material that its piezoelectric axis is along its main crystal axis meaning that PMN-PT wafers have piezoelectric axis normal to its surface. As it is common in semiconductor industry to bond an ultra-thin (100s nm) layer of single crystalline wafer onto a single crystalline silicon wafer, we can expect to have PMN-PT to be bonded onto our SOI wafers and we can planarly pattern the material to generate highly efficient piezoelectric transduction between a superconducting quantum circuit and a phononic mechanical resonator on SOI in mK environment. To understand the origin of the large piezoelectric coupling presents in PMN-PT, we can look at its crystal structure containing super-cells. A deformation in the super-cell will lead to a large displacement of charges in a super cell formed by two unit cells. This

deformation thus creates a huge electric dipole which can be coupled strongly to the external electric field [124].

Chapter 7

EFFORTS IN GROWING AND CHARACTERIZING PIEZOELECTRIC MATERIAL ALUMINUM NITRIDE

As the piezoelectric material Aluminum Nitride has been the core of the previously discussed works related to transducing electric signal and quantum state into quantum mechanical motion, its material properties including electrical quality, acoustic quality, and piezoelectric coefficients are of primary importance for the works. These properties are fundamentally linked the crystal growth quality of the deposited AlN thin film on a silicon substrate or a Molybdenum substrate. In order to explore the possibilities of growing the high quality AlN thin film of various thickness, we used AlN sputtering and Atomic Layer Deposition (ALD). In the rest of the chapter I will introduce the techniques we used to probe and improve the deposited material's quality.

7.1 Thin Film Quality Characterization

To understand the deposited thin film's quality, it is important to obtain information regarding the film's crystallinity, thickness, chemical composition, and surface topology. The section will introduce the tools we used for characterizing the films we have.

7.1.1 Single Crystalline Thin Film X-ray Diffraction (XRD)

X-ray Diffraction measurement is commonly used in material science to characterize the crystalline phases (periodic alignment of atoms in a direction) in a given solid. The incident X-ray is reflected by different crystal planes as shown in the simplified diagram Fig. 7.1. The phase difference between beams reflected on two nearby planes is (7.1). For a diffraction peak to appear, the condition in (7.2) needs to be satisfied. As can be seen, the diffraction peak reveals the periodic alignment of crystal plane in one direction and its angular position indicates the plane spacing. For a given incident beam (determined by the X-ray source location) and a given detection direction (determined by detector location), the XRD measurement is sensitive to the periodic crystal lattice alignment along the middle of the angle between the incident beam direction and the detection direction as shown in Fig. 7.1 with a yellow

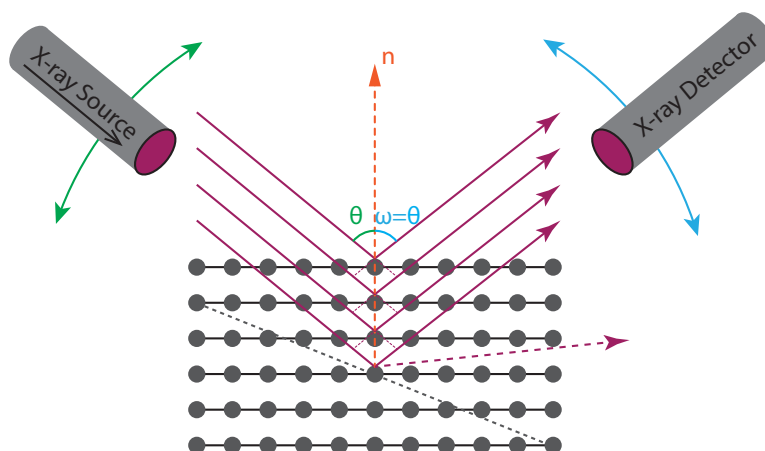


Figure 7.1: The illustration of an X-ray Diffraction (XRD) experiment used in this work to characterize the crystal quality of the deposited thin films used in this work. The X-ray source is located at the angular location θ with respect to the normal direction of the surface of the thin film. The X-ray detector is located at an angular location ω with respect to the surface of the sample under test. For the XRD experiment used to characterize the periodic alignment of crystal planes parallel to the film surface, the detector location ω is chosen such that $\omega = \theta$. This is why this scan is also called "coupled-scan" or $\theta - 2\theta$ scan.

dashed line. The crystal planes of interest is perpendicular to the yellow dashed line.

$$\delta = 2\pi \frac{2d \sin(\theta)}{\lambda} \quad (7.1)$$

$$\delta_m = 2m\pi, m \in Z \quad (7.2)$$

As the X-ray incident beam moves angularly (θ) from 0 degree to 90 degree, if the detector angular location (ω) is adjusted such that the middle of the angle between the two directions are kept normal to the top surface of a thin film sample ($\omega = \theta$), we can keep probing the periodicity in the direction normal to the surface and identify the distance between the crystal planes parallel to the surface by observing the angular positions (θ_i) of the peaks as shown in later measured AlN and Mo XRD curves. This is often called $\theta - 2\theta$ scan or coupled scan. There is another method called ω scan which is used to further understand the quality of crystal plane alignment for existing peak shown in a $\theta - 2\theta$ scan. In this method, the incident beam angular location θ is fixed at the angle where the interested peak was found in a coupled scan. The detector angular location ω is then moved around the θ value to

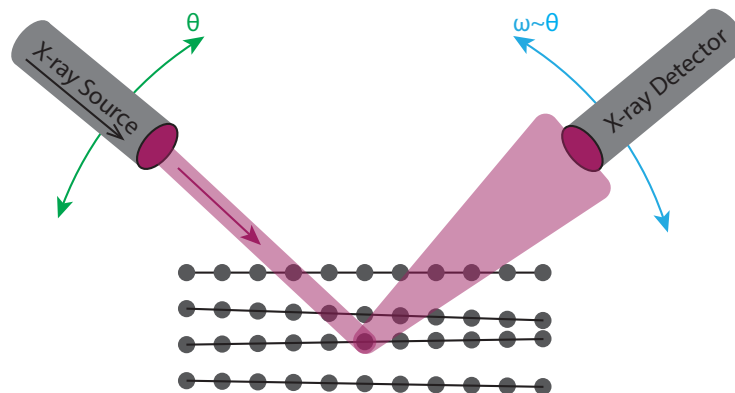


Figure 7.2: This shows another type of X-ray characterization of a thin film's crystal quality. If the thin film's crystal planes, even though periodically aligned in the direction normal to the surface of the sample, are misaligned slightly so that they are not ideally parallel with each other, an incident X-ray with narrow angular spread will be angularly broadened after diffraction on the thin film under test shown here. This spread can be measured precisely by fixing the X-ray source angular position at θ corresponding to a XRD diffraction peak in the previous coupled-scan that corresponds to a periodic alignment of crystal planes. The detector is moved around $\omega \sim \theta$ to measure the reflected X-ray spread caused by the uneven crystal planes in the thin film. This measurement is called $\theta - \omega$ scan or X-ray Rocking Curve.

probe the angular spread of the diffracted X-ray for a given incident angle as shown in Fig. 7.2. This scan is often called the XRD Rocking Curve scan. The spread indicates that the crystal planes are not perfectly parallel to each other.

7.1.2 Measuring the Film Thickness with Ellipsometry

The ellipsometry is used to study the thickness of an ultra-thin film having thickness ranging from a few atomic layers to a few micrometers. A typical setup of a measurement looks like Fig. 7.3. A linearly polarized (by the polarizer in between s and p directions) broadband light is sent onto the surface of the sample and the reflected light is collected by the photo-detector after a rotating polarization analyser. After light incidence on the material, the relative phase between s-component and p-component of the electric field vector leads to a rotating electric field vector in the plane normal to the propagation direction as the light propagates in free space. The electric field vector trajectory formed over an optical field period can be projected onto a plane normal to the propagation direction in general case as an ellipse (line

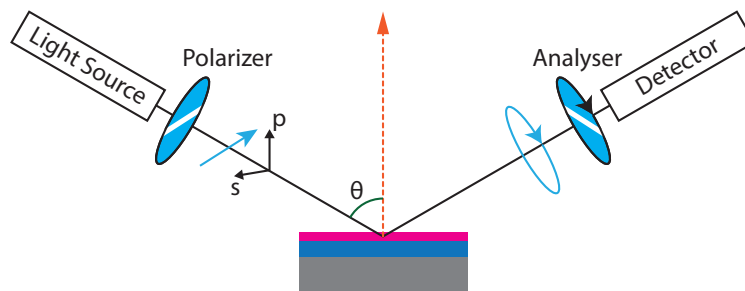


Figure 7.3: The setup for an ellipsometry measurement. The detector and a broadband light source are located with angular positions θ with respect to the normal direction (the dashed orange arrow) of the sample surface. The broadband line is linearly polarized by a polarizer so that it has \vec{s} and \vec{p} components parallel and perpendicular to the sample surface surface respectively. The relative phase between the two component will be changed by the ultra-thin film leading to an elliptically polarized light characterized by the polarization analyser that measures the polarization with a rotating polarizer before the optical detector .

and circle are included as special cases). The shape of the ellipse is determined by the electric field components' phase difference $\Delta\phi_{\text{elip}}$ and amplitude ratio r_{elip} . These parameters depend critically on the thickness and refractive index of different layers of materials. In practice where there are normally multiple layers of dielectric materials, the thickness of the layer of interest can be extracted by a numerical fitting routine that fit thin layer thickness and refractive indexes to the measured $\Delta\phi_{\text{elip}}$ and r_{elip} as functions of photon wavelength. The fitting will work more robustly if all the layers' refractive indexes are known and there is a good initial knowledge about the thickness of the layers.

7.1.3 Measuring Oxygen Contamination with X-ray Photoelectron Spectroscopy

The Chemical composition in the thin film is important for understanding the issue with the film that didn't form good crystals. Particularly, the unintended Chemical contamination of other Chemical species is a sign that the Chamber condition is not ideal and requires attention immediately. The Chemical composition of the thin film can be found by doing the X-ray Photoelectron Spectroscopy (XPS). The setup looks like Fig. 7.4. The focused X-ray is used to bombard the top thin layer

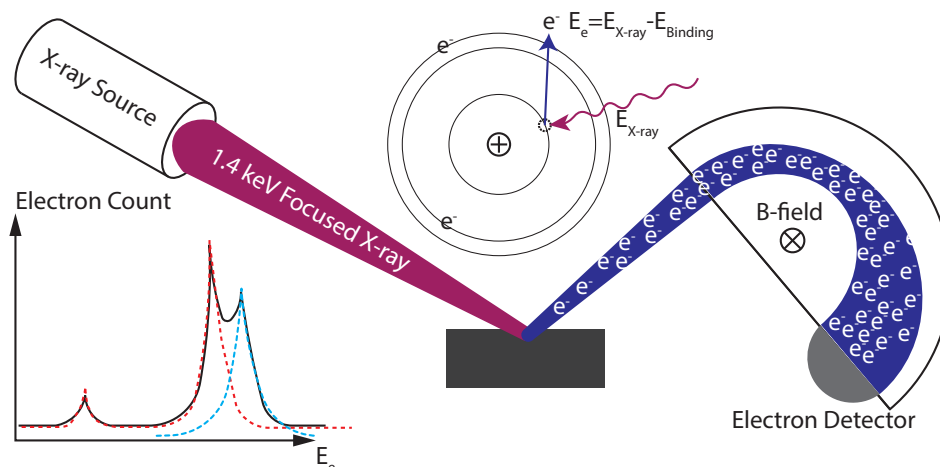


Figure 7.4: The X-ray Photoelectron Spectroscopy (XPS) measurement involved in the work is illustrated here. The XPS utilizes a focused soft X-ray to dissociate inner electrons of elements in the sample. These dissociated inner electrons escape the thin film and become free photoelectrons in an ultra-high vacuum chamber. An photoelectron's kinetic energy E_e is equal to the difference between the known incident X-ray photon energy $E_{X\text{-ray}}$ and the element' characteristic binding energy E_{Binding} . The photoelectrons then enter an kinetic energy analyser that uses magnetic field to steer electrons of different energies to different electron detectors. An example of the measured electron kinetic energy is shown in the lower left corner of the figure. This spectrum can be fitted with different material element composition models (the dashed lines) to determine the elemental composition of the top layer (within 100 nm from the top surface) of the thin film.

of a given sample. It excites photoelectrons in the material and uses the electron spectrometer to obtain the kinetic energy distribution of the ejected electrons in the ultra-high-vacuum (UHV) chamber. This information can be used to extract the binding energy of the electrons in the material. The characteristic binding energy is used to determine the involved Chemical species. As the photoelectrons deep within the material can not propagate out, the XPS is typically most efficient within the top 100 nm surface of the sample.

7.2 Atomic Layer Deposition for Depositing High Quality AlN

Atomic Layer Deposition (ALD) is a layer-by-layer deposit on process that utilizes self-limited material growth to precisely control the uniformity and thickness of the deposited ultra-thin film. The process [117] to deposit the AlN is illustrated in the Fig. 7.5. The tool looks like Fig. 7.6 with different parts involved in the process

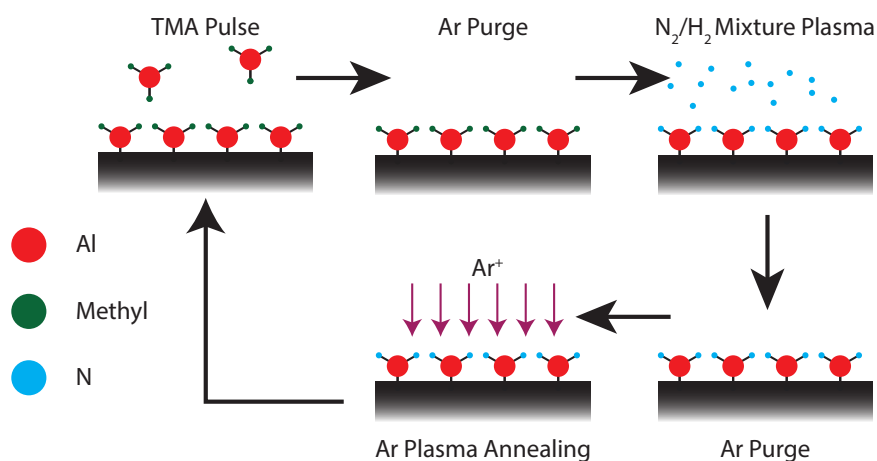


Figure 7.5: The Atomic-Layer-Deposition procedures used to deposit ultra-high quality AlN thin films. The Ar-plasma step is called Atomic-Layer-Annealing that is used to locally heat the atomic layer just deposited to increase surface atoms' mobility and help the layer to reach the ideal crystalline phase thermodynamically.

shown in Fig. 7.7. The system originally uses a Inductively-Coupled-Plasma (ICP) to generate high density reactive H-plasma and N-plasma from the input gas mixture in the ICP tube. Inert Ar gas can also be pumped into the chamber via another gas port to create a low pressure environment to damp the kinetic energy of reactive ions. The plasma power can also be used to tune the plasma ion kinetic energy and density for achieving high quality thin AlN film. As the ALD process is a chemistry dominated process that is driven thermodynamically, temperature of the substrate and reactive ion kinetic energy are critical for achieving uniform self-limited atomic layer-by-layer growth of a thin film as appropriate atom mobility can lead to higher quality crystalline films. This is because the free energy of the desired crystal phase with c-axis normal to the thin film surface is the lowest and thus thermodynamically favored.

We grew multiple thin films initially and obtained high quality materials after fine tuning the kinematics of the chemical process with the pressure and flow rate as well as the plasma power shown in Fig. 7.8 and Fig. 7.9. In Fig. 7.8, it is obvious that all the deposited films on Sapphire-[002] substrates (**i**) are significantly better than the quality of films deposited on a silicon substrate (**ii**) with Si-[001] face. This is because the ALD process is a low kinetic energy Chemical process. As a result, the



Figure 7.6: The Atomic Layer Deposition (ALD) tool we used. The plasma tube is later upgrade with a metal Hollow Cathode Plasma (HCP) tube to eliminate Oxygen contamination due to deteriorating quartz ICP plasma tube.

grown AlN layer quality depends strongly on the lattice match between the substrate surface and the AlN crystal plane of interest at the boundary. In Fig. 7.8a, a higher power ALD process injects larger kinetic energy and mobility to the deposited Al and N atoms. This consistently leads to an improvement in grown film quality. In Fig. 7.8b, the thickness dependence shows that the film's quality improves as the film become thicker. This indicates that the upper layers of the grown thin film is more crystalline than the lower layers of the AlN thin film near the interface between the substrate and the film. This is because the lattice mismatch between the substrate surface and the AlN crystal plane creates faults and disorders in the interface layer of the AlN film. In Fig. 7.8c shows that the Atomic-Layer-Annealing process which is supposed to yield better AlN crystal as it injects kinetic energy to the deposited atomic layer of AlN and provides the Al and N atoms with sufficient mobility to reach the thermodynamically preferred crystalline phase. However, if the Ar-ions have too much kinetic energy, it will also provide too much energy to the atomic layer of AlN and "melts" the crystalline structure of the formed AlN layer. We also observed, in Fig. 7.9, a system drift in chamber conditions that can not be corrected by just flushing the chamber with N-plasma to pre-condition the chamber. Furthermore, the chamber deterioration also become more profound over a month's

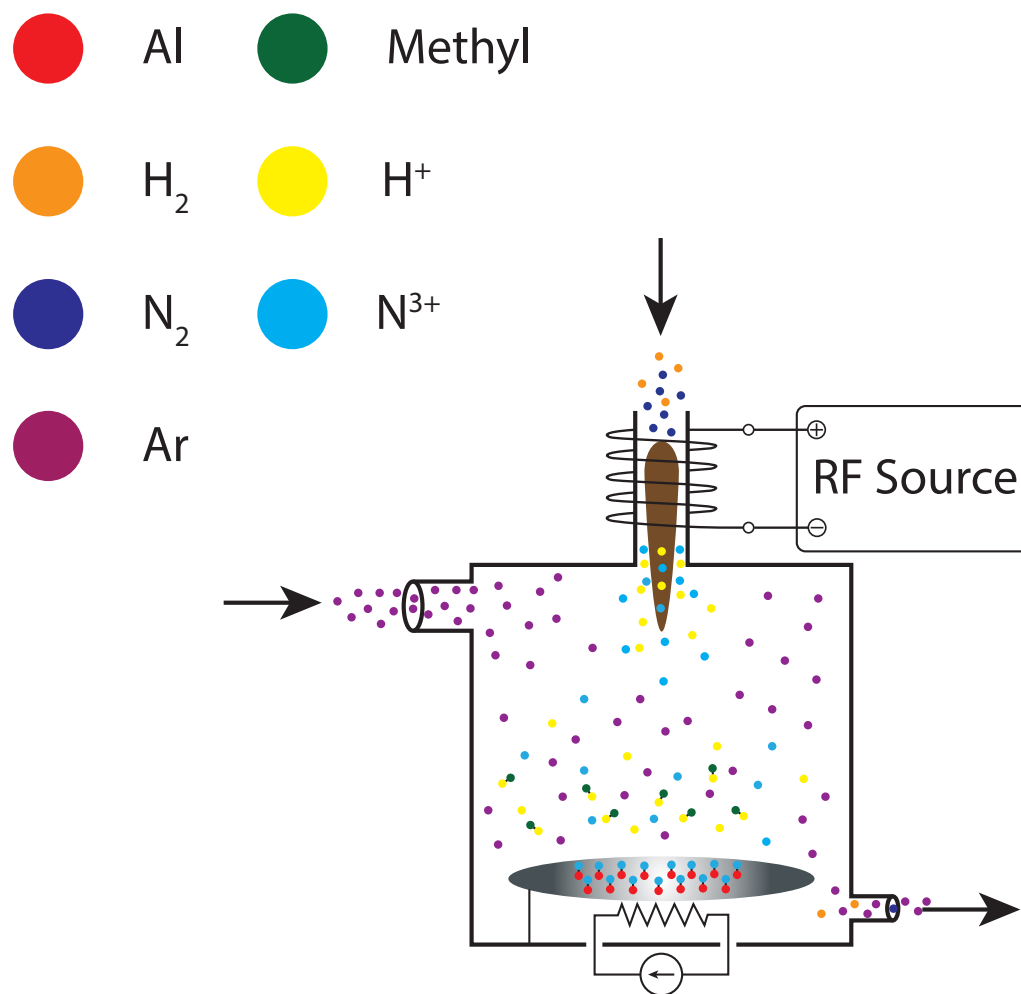


Figure 7.7: An illustration of the ALD deposition process during the H/N-plasma step. Different gas atoms and ions are marked with different colors according to the legends on the upper left. Ar-gas is pumped into the system to serve as either a buffer gas to create a small pressure in the chamber or a purge gas that removes reacted gas from the chamber between two reactive steps. There is also a plasma tube that ionizes gas mixtures going through it. Here in the figure, H₂ and N₂ are injected into the plasma tube and become H-ions and N-ions that can react actively with the atomic layer of reactants deposited by the previous short pulse TMA injection on the surface of the substrate.

time and more high plasma power ALD runs.

We carried out XPS study of the deposited films' Chemical composition and realized a significant increase over time in Oxygen composition level in the film and later realized that the quartz ICP plasma tube we used to generate the Chemically reactive plasma has been ion etched during the process and become dark as shown in Fig. 7.10. Since the tube is made with Oxygen-rich quartz, the Oxygen contamination of the film can be caused by the tube. We replaced the plasma tube with a Hollow-Cathode-Plasma (HCP) source from Meaglow Ltd. and the improvement was significant after we conditioned the chamber with N-plasma for several rounds.

7.3 Sputtering Deposition of AlN Thin Layer and Electrodes

The previously discussed ALD process is a self-limiting Chemical Vapor Deposition (CVD) method. It is a low kinetic energy surface chemistry dominated epitaxial growth process. As a result, the process, even though can potentially create an extremely high quality uniform ultra-thin film on a crystalline substrate, is intrinsically very sensitive to the ALD chamber chemical environment and substrate surface morphology (roughness and crystal structure). Thus, ALD, despite of its high potential, requires challenging fine parameter tuning and deep understanding of chamber history. These practical complications often make it hard for reproducing results reported in literature. A widely adopted alternative method for growing high quality thin films is called sputtering deposition. It is a high kinetic energy physical process dominated epitaxial growth process. Even though this technique is not self-limited and may not produce the ultra-high quality film potentially achievable with more chemical processes, it is relatively more robust in terms of reproducing results presented in literature [61, 1, 68, 78, 77, 80, 59, 40, 55]. In this section we will present our efforts to grow Molybdenum electrode thin film and AlN thin film with sputtering. The tool (AJA Orion Sputtering System) looks like Fig. 7.11. The processes and relevant system parts we used to deposit the Mo and AlN thin film are shown in Fig. 7.12a and b respectively. The commercial magnetron sputtering system we used can operate in three modes (DC, Pulsed-DC, RF) and it has magnetic field generated by electromagnet below the target plate to confine ionizing electrons near the target for increasing the ionization efficiency and local sputtering plasma density. This also has the benefit of avoiding electron charging grown thin film on substrate if it is insulating.

The system operating in the DC mode negatively bias the target such that sputtering

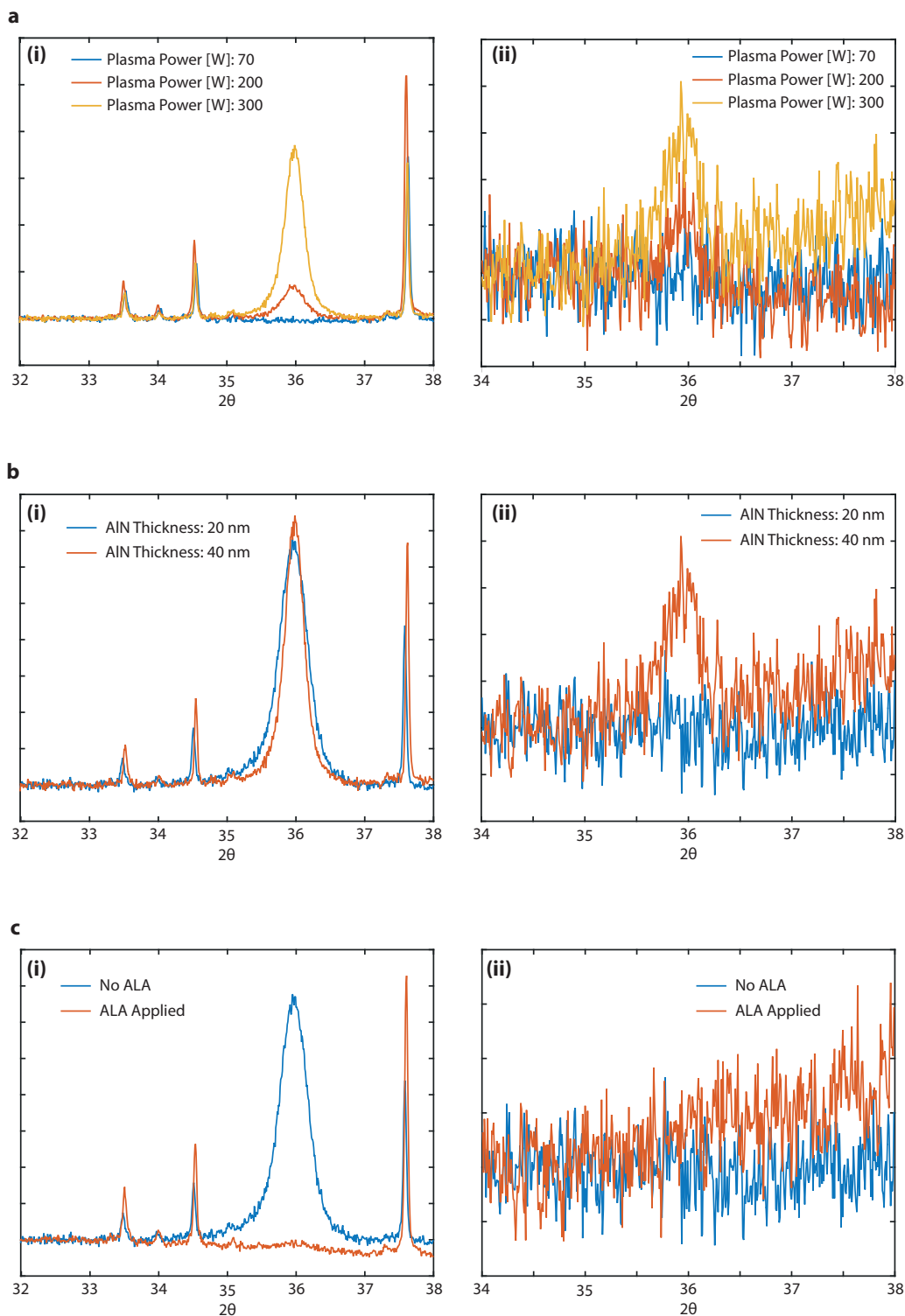


Figure 7.8: **a** shows the plasma power dependence of deposited AlN quality on Sapphire (i) and Si (ii) substrates. **b** shows the thickness dependence of the deposited AlN thin film quality on Sapphire (i) and Si (ii) substrates. **c** is the comparison of ALD process with or without Atomic-Layer-Annealing (ALA) shown in Fig. 7.5 as the Ar-plasma step that transiently heats the newly deposited AlN atomic layer to provide sufficient mobility to the atoms for them to reach the preferred crystalline thermal equilibrium phase.

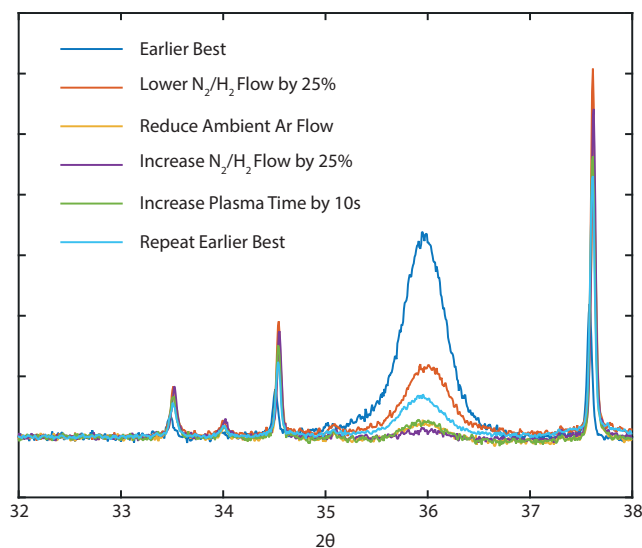


Figure 7.9: This shows some of the later trials we conducted to improve and repeat the previously obtained best result. It shows that non of the parameter tuning leads to a better film quality. In the end, we tried to repeat the recipe for depositing our previously obtained best film, the resulted film quality is still worse than the previous best one obtained using the same parameters. This observation strongly indicates an unknown system deterioration in the deposition chamber quality.

gas (Ar) is ionized and accelerated towards the target. These positively charged ions then transfer their kinetic energy into the target material atoms which are then sputtered out of the target into the vacuum. The sputtered target atoms then arrive at the substrate and are deposited on the surface of the substrate. Such DC operation mode has been widely used for conductive targets as a constant DC bias will accumulate charge on insulating targets. This accumulated charge will cancel the bias voltage eventually and stop the sputtering process. As the target accumulates charge, discharging arcs can also appear near the target which create uncontrolled chemical reactions and contaminating droplets in the plasma leading to poor thin film quality.

In the Pulsed-DC mode, the target plate can be biased with alternating periods of positive and negative voltages. When it is negatively biased, sputtering plasma ions are accelerated towards the target and electrons are driven away. When the target is positively biased, electrons are attracted towards to target and ions are driven away. The positive bias is critical for depositing insulating materials like the AlN. If AlN



Figure 7.10: The burned quartz plasma tube that was etched by the high power plasma and generated excessive Oxygen into the ALD process chamber and contaminated the ultra Oxygen sensitive AlN process and caused deteriorating chamber condition that yielded inconsistent AlN deposition results.



Figure 7.11: The sputtering system we used in the Kaliv Nanoscience Institute (KNI) cleanroom. This system has 8 magnetron guns and correspondingly 8 targets in one chamber. This allows the system to co-sputter alloys and a variety of other compounds. In this system, the distance between the substrate and the guns can also be changed. However, it should be noticed that as the guns are not facing normal to the substrate surface, the closer the substrate gets to the guns the more uniform the sputtered film can be. This system also allows the sputtering to operate in DC mode and RF mode introduced in this text.

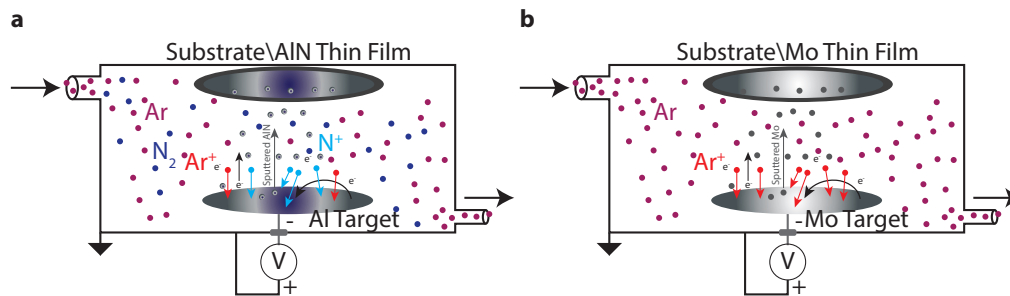


Figure 7.12: **a**, the reactive deposition of AlN thin film using RF sputtering. A mixture of sputtering Ar (purple) and N_2 (deep blue) gases are pumped into the system and ionized near the target. Ar-ions (orange) and N-ions (light blue) sputter the Al target and sputtered Al atoms react with N-ion in the chamber which then fall on the substrate to form the thin layer of AlN. **b**, the DC sputtering of Mo thin film. In this process, pure Ar is pumped into the chamber as sputtering gas. Mo atoms sputtered by the Ar-ions will fall onto the substrate to form the uniform layer of Mo. In contrast to depositing dielectric like AlN where a layer of insulating AlN forms on the Al target and causes charge accumulation and detrimental discharge, Mo deposition does not form this insulating layer and DC sputtering is sufficient for this material.

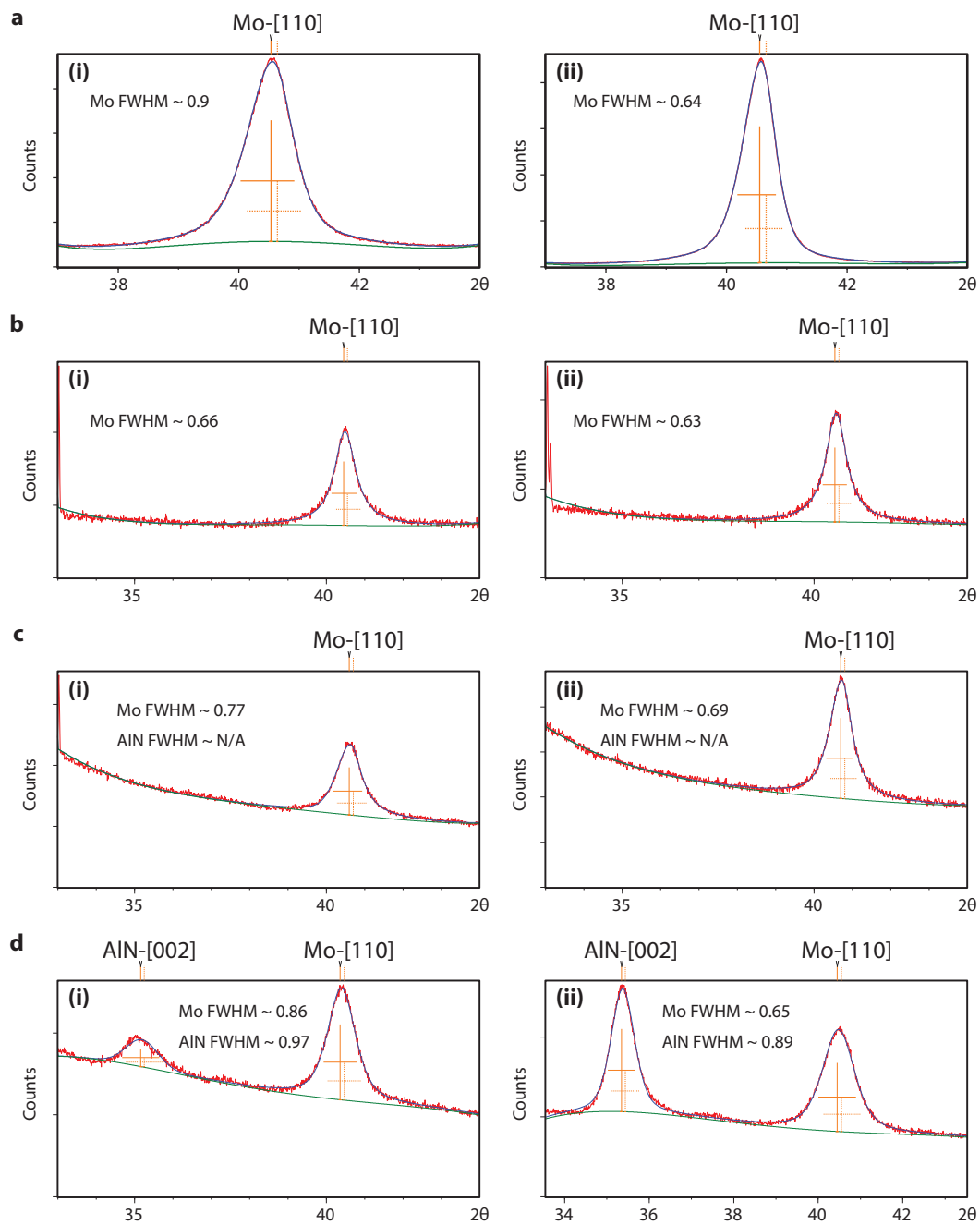
deposition is done with Al target and N-plasma, an insulating AlN layer can form on the target surface. This insulating layer will quickly accumulate charge when the target is negatively biased. If the negative bias period is too long, this charge will build up to a point where either it cancels the electric field of the negative DC bias or causes discharge near the surface of the target. The cancellation of DC bias stops the ionization of sputtering gas. The discharge generates arcs in the plasma. The arcs generate noncrystalline material droplets that significantly contaminates the deposited thin film on the substrate. To avoid these detrimental effects, the length of the negative bias is limited and its is followed by a period of positive bias. Positively biased target attracts electrons towards it to neutralize the positive charge on the insulating surface of the target.

The target can also be driven with an RF source to ionize and accelerate sputtering gas near the target plate. RF drive together with magnetic field near the target keeps a high density of ionizing electrons near the target which efficiently ionize the sputtering gas locally. As the electrons are quickly oscillating back and forth near the target, the accumulated positive charge is neutralized. However, RF operation is significantly more sophisticated as this requires a stable microwave source around

13.56 MHz and a impedance matching network to match the RF drive with the plasma impedance for efficient ionization. We have tried the processes listed in Table.7.1 to deposit the films.

Table 7.1: The processes we tried to deposit AlN and Mo

Label	Material	Plasma Source	Plasma Power [W]	Pressure [mTorr]	$\frac{N_2}{Ar+N_2}$	Heating [°C]
Mo1	Mo	DC	120	3.2	0%	R.T.
Mo2	Mo	DC	200	3.2	0%	R.T.
Mo3	Mo	DC	400	3.2	0%	R.T.
Mo4	Mo	DC	120	2.0	0%	R.T.
Mo5	Mo	DC	120	2.0	0%	250
AlN1	AlN	Pulsed-DC(100 kHz, 3us)	500	1.0	100%	R.T.
AlN2	AlN	Pulsed-DC(45 kHz, 10us)	500	1.0	100%	300
AlN3	AlN	Pulsed-DC(45 kHz, 10us)	500	1.0	100%	200
AlN4	AlN	RF	120	100	75%	300
AlN5	AlN	RF	120	500	75%	300
AlN6	AlN	Pulsed-DC(100 kHz, 3us)	300	28	75%	500



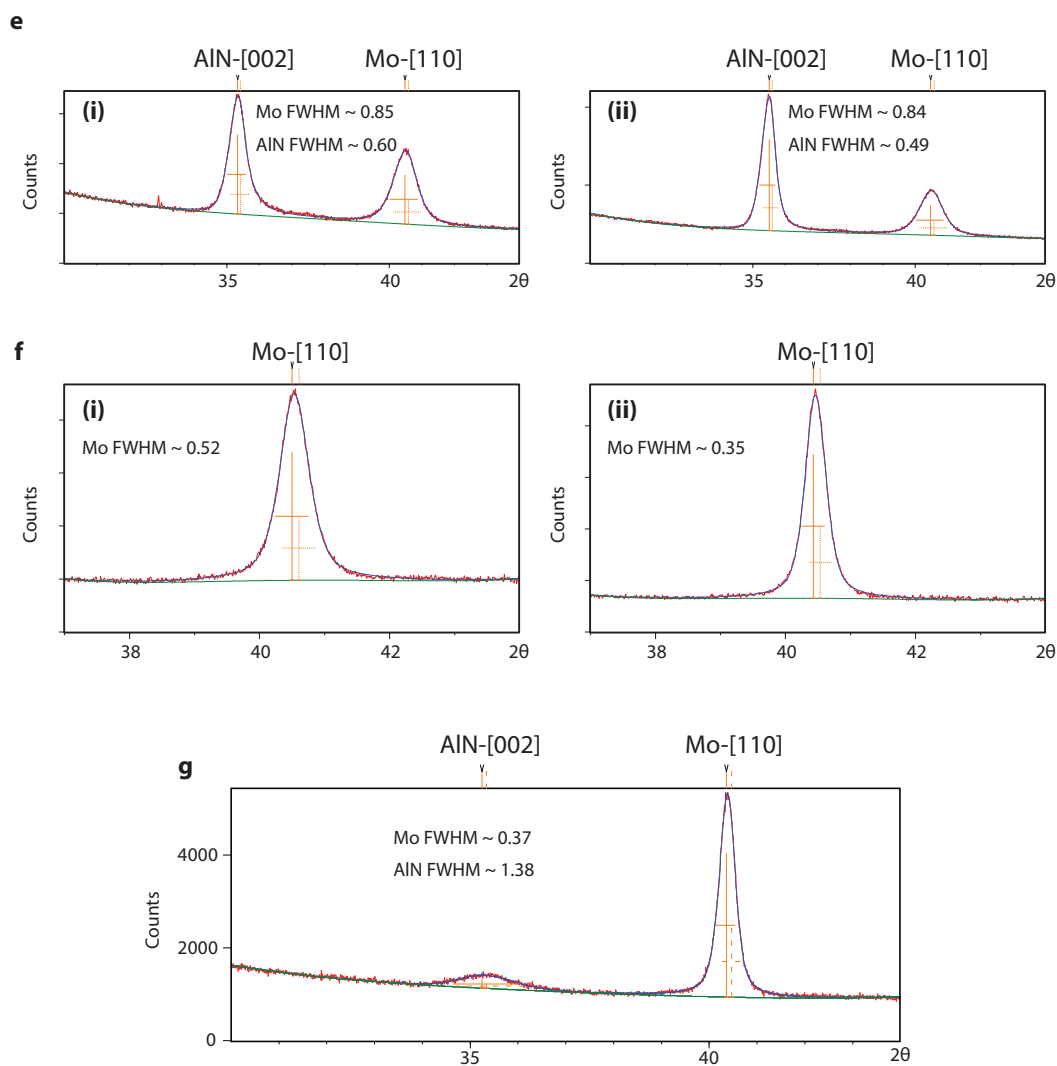


Figure 7.13: The XRD curves of the deposited films using combinations of processes in Table.7.1 on different substrates. The peaks are identified by comparing their θ location with known diffraction angles of AlN-[002] crystal plane ($2\theta_{\text{AlN-002}} \approx 36^\circ$) and Mo-[011] crystal plane ($2\theta_{\text{Mo-011}} \approx 40^\circ$). We characterized AlN and Mo crystal quality using their diffraction peaks' fitted Full-Width-Half-Maximum (FWHM). Raw data of the XRD curves are in red and the fitted curves are in blue with green representing a global slope correction.

Fig. 7.13a.(i) shows the XRD curve corresponding to the process labelled as Mo1 in Table.7.1. This results in a Full-Width-Half-Maximum (FWHM) linewidth of 0.9° . Fig. 7.13a.(ii) is the XRD result for Mo3 which doubled the DC power to 400 W and resulted in a linewidth of 0.64° . Thus, Fig. 7.13a manifests the expected outcome of increasing the DC power for depositing a better quality Mo thin film as the higher kinetic energy of the sputtered atoms, the more compact and uniform the metal film gets. Fig. 7.13b compares the influence of substrate on the quality of deposited films. We experimented with deposition using Mo3 process on Silicon substrate with Si-[001] face and SOI substrate with Si-[001] face. The two substrates show almost identical XRD results with linewidth 0.66° and 0.63° respectively for the Mo-[110] crystal plane. This means that the quality of deposited Mo is very much kinematically define. As we have got a good enough layer of Mo grown on Silicon and SOI substrates, we proceeded to experiment with depositing AlN on sputtered Mo thin film in Fig. 7.13c where we use process AlN1 to deposit AlN on Mo deposited with Mo3. We tested the combination of recipes on both Si and SOI substrates. The room temperature processes didn't lead to observable AlN signature peaks, AlN-[002], on both substrates. The observed Mo-[110] peaks are slightly broadened after the AlN deposition This can be due to the scattering of the amorphous AlN layer on Mo. In Fig. 7.13d, we tried to deposit AlN2 film on Mo1 film on both substrates and expected to see an improved AlN quality. This is because high quality Mo films have rough top surface (large surface height standard deviation in AFM) due to large grains present in a crystalline film. This roughness will disrupt the periodic alignment of AlN crystal in the initial atomic layers of the grown AlN film near the Mo surface even when aligned AlN crystal is thermodynamically favored. Furthermore, as crystalline AlN alignment with c-axis normal to the film surface is thermodynamically favored (this alignment has the lowest energy), sufficient thermal energy is needed for the deposited layers to spontaneously align themselves. As a result, we use Mo1 which lead to a less ideal Mo thin film and AlN2 that is heated and can potentially lead to better thermal dynamical equilibrium (crystalline AlN). The XRD curves in Fig. 7.13d is what we expected. It should be noticed that this group of results reflect the substrate dependence of the deposited films' quality. Fig. 7.13d.(i) is deposition on Si substrate with Si-[001] top face and (ii) is deposition on SOI substrate. The SOI substrate led to a better AlN film quality and this can be caused by the different thermal properties of SOI and Si substrates that led to different Mo surface roughness. In the set of experimentation on two different substrates shown in Fig. 7.13e, we still used the Mo1 process to

grow the Mo layer on top of the substrates. The difference from the previous trials is that we used the process AlN3 to deposit the AlN thin layer. This AlN3 process used lower substrate temperature compared to AlN2 with other parameters kept the same. This is because higher temperature can not only help the formed AlN atomic layers to reach their thermal equilibrium favoring the crystalline formation of the desired AlN-[002] crystal alignment, but also disturb the formed crystal alignment due to excessive thermal kinetic energy. This means that there is a sweep point in temperature that supply sufficient thermal kinetic energy for the AlN atoms to have enough mobility to move away from thermodynamically meta stable alignments and reach global minimum corresponding to the desired crystal phase, but the temperature should be too high that the thermal energy "melts" the crystal phase. As can be shown here, the deposited crystal quality is significantly improved with AlN linewidths being 0.6° and 0.49° respectively on Mo/Si and Mo/SOI substrates. There is still a substrate quality dependence in this set of trials as Mo can have different surface typologies depending on whether it is deposited on Si or SOI. In Fig. 7.13f, this set of experiment is to see if we can significantly improve the Mo layer quality for further confirming that a more crystalline Mo layer leads to a more amorphous AlN layer deposited on top of it. As we observed that high sputtered Mo kinetic energy leads to more compact and thus a more crystalline Mo layer, we decreased the sputtering chamber pressure by reducing the Ar gas flow which not only sputters the Mo target but also buffers the flow of sputtered Mo atoms. This lowered pressure in Mo4 in (i) and Mo5 in (ii) consistently leads to significantly improved Mo crystal quality. Furthermore, we also increased the substrate temperature in Mo5 to provide sufficient mobility to the deposited Mo atoms to reach the thermodynamically favored crystalline phase. As (ii) which used Mo5 showed better crystal quality with FWHM~ 0.52° as compared with (i) with FWHM~ 0.35° , we conclude that an appropriated heated substrate would help create a better Mo crystalline film in sputtering. In Fig. 7.13g, we then deposited the AlN layer using AlN3 onto the Mo film prepared previously with Mo5. This XRD curve showing an AlN peak FWHM reaching 1.38° indicates that a more crystalline Mo layer does create a worse top surface for deposited AlN to crystallize correctly.

The line shape of a XRD curve is determined by various thin film material properties. The width of the crystal axis peak is partially determined by the grain size of the crystal. The area of it corresponds to the fraction of the crystalline phase region in the thin film. It needs to be noted that the line shape can be a superposition of a

narrower peak and a wide peak. This means that there is a high quality crystalline region and a more amorphous region in the thin film. As can be seen in some figures, the line shape can be distorted, and this distortion is a result of internal strain of the film. Material growing on a substrate having different crystal lattice face at the top surface can develop a large strain due to the lattice mismatch. Another factor of intrinsic strain is the dislocation and vacancies in the thin film as a result of nonuniform physical growth and kinetic impact of atoms on grown film. The strain can be tuned by adjusting plasma power and chamber pressure to tune the kinetic energy of impact atoms/molecules. However, this is also coupled with other parameters that determines the film growth rate and crystallinity. For example, higher strain and high crystal quality are achieved with larger plasma power in traditional magnetron sputtering systems. To achieve low strain high quality thin films, a new S-gun magnetron system was recently developed.

In parallel to developing a sputtering process in house, we also purchased S-gun magnetron sputtering services from OEM Inc., who can sputter an ultra-high quality AlN and Mo ultra-thin films on the silicon wafer we provided.

HARDWARE EFFICIENT PROGRAMMABLE MULTI-QUBIT ALL-TO-ALL COUPLING ARCHITECTURE: SPIDERMON

The rapid scaling up of superconducting quantum circuits composed of an increasing number of superconducting Josephson junction qubits have called for innovative methods for engineering hardware-efficient programmable on-demand all-to-all multi-qubit coupling on a planar circuit.

Due to the lack of connectivity in most superconducting qubit architectures, novel quantum programs that could be carried out with a manageable number of two qubit gates between non-nearest-neighbor qubits are always mapped into much deeper quantum circuits involving only two qubit gates between nearest-neighbor qubits. In order to carry out a deep circuit using nearest neighbor interactions, two qubit gates' fidelity between nearest neighbors is required to be almost to unity. This has become one of the major challenges in integrating an increasing number of superconducting qubits onto one chip with high fidelity controls containing single and two-qubit gates implemented using complicate control circuit wiring. Currently, this direction of scaling up superconducting qubit system has led to the noticeable development of three-dimensional integration and packaging in major quantum industry companies and national labs.

Instead of developing complicated three-dimensional systems to wire up multiple qubits that are nearest-neighbor coupled, I devised a way to couple these qubits such that an arbitrary coupling graph between different qubit pairs can be generated pragmatically and controlled in time domain. The scheme of the coupling looks like the one shown in Fig. 8.1. The N qubits in the system are detuned from each other with detuning $\Delta_{ij} = \omega_i - \omega_j$. As they are commonly grounded via a serially connected linear inductor L_g and a SQUID loop with effective Josephson junction inductance L_{gJ} , inductive coupling between the i -th qubit and the j -th qubit is $g_{ij} = (L_g + \frac{L_{gJ}}{\cos \pi \frac{\Phi_{ex}}{\Phi_0}}) \frac{\sqrt{\omega_i \omega_j}}{2\sqrt{L_i L_j}}$, where ω_i and L_i are the frequency and inductance of the i -th qubit. Φ_{ex} is the externally threaded flux through the SQUID loop and Φ_0 is a magnetic flux quanta. We can drive the external magnetic flux such that $\Phi_{ex}(t) = \Phi_{ex}^0 + A_\Phi \Phi_0 \cos \omega_d t$ and obtain (8.1)-(8.4).

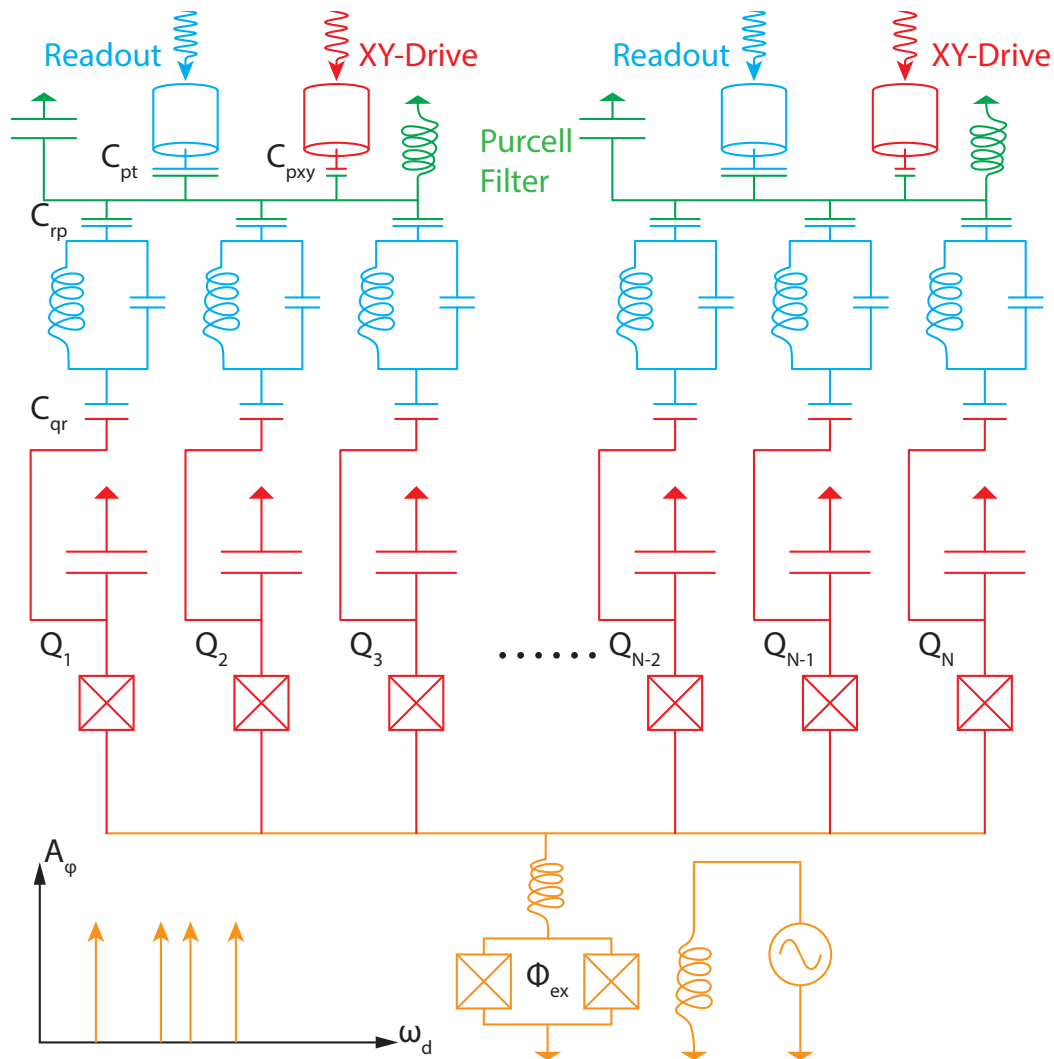


Figure 8.1: The proposed multi-qubit coupling scheme that programmably couples N qubits (in red) together via a common modulated SQUID (yellow) serially connected to a linear inductance (yellow) before going to the ground. The SQUID is externally driven (yellow) with AC flux modulation having multiple frequency components shown in the lower left modulation signal spectrum. All the qubits can be measured and controlled independently via separate readout resonators (blue) and Purcell filters (green).

$$g_{ij}(t) \simeq g_0 + g_1 A_\Phi \Phi_0 \cos(\omega_d t + \phi_{ij}) + g_2 A_\Phi^2 \Phi_0^2 \cos(\omega_d t + \phi_{ij})^2 + O(A_\Phi^3 \Phi_0^3) \quad (8.1)$$

$$g_0 = \frac{\sqrt{\omega_i \omega_j}}{2\sqrt{L_i L_j}} \left(L_g + \frac{L_{gJ}}{\cos \pi \frac{\Phi_{\text{ex}}^0}{\Phi_0}} \right) \quad (8.2)$$

$$g_1 = \frac{L_{gJ}}{2\sqrt{L_i L_j}} \frac{\sqrt{\omega_i \omega_j}}{\Phi_0 \cos \left(\pi \frac{\Phi_{\text{ex}}^0}{\Phi_0} \right)} \frac{\pi \tan \left(\pi \frac{\Phi_{\text{ex}}^0}{\Phi_0} \right)}{\Phi_0 \cos \left(\pi \frac{\Phi_{\text{ex}}^0}{\Phi_0} \right)} \quad (8.3)$$

$$g_2 = \frac{1}{2} \frac{L_{gJ}}{2\sqrt{L_i L_j}} \frac{\sqrt{\omega_i \omega_j}}{\Phi_0 \cos \left(\pi \frac{\Phi_{\text{ex}}^0}{\Phi_0} \right)} \frac{\pi (1 + \sin \left(\pi \frac{\Phi_{\text{ex}}^0}{\Phi_0} \right)^2)}{\Phi_0 \cos \left(\pi \frac{\Phi_{\text{ex}}^0}{\Phi_0} \right)^3} \quad (8.4)$$

We can choose the D.C. bias of the external magnetic flux such that $\Phi_{\text{ex}}^0 = \frac{\Phi_0}{\pi} \arccos \left(-\frac{L_{gJ}}{L_g} \right)$. This choice of external flux bias will lead to $L_g + \frac{L_{gJ}}{\cos \pi \frac{\Phi_{\text{ex}}^0}{\Phi_0}} = 0$. If the linear inductance is designed to have $L_{gJ} \sim L_g$, $\Phi_{\text{ex}}^0 \simeq \Phi_0$. The coupling will become (8.5) and different orders of the coupling coefficients are plotted in Fig. 8.2.

$$g_{ij}(t) \simeq \frac{L_{gJ}}{4\sqrt{L_i L_j}} \sqrt{\omega_i \omega_j} \pi A_\Phi^2 \Phi_0 \cos(\omega_d t + \phi_{ij})^2 + O(A_\Phi^4 \Phi_0^4) \quad (8.5)$$

If the external flux modulation frequency ω_d is chosen such that $\omega_d = \Delta_{ij}$, photon hopping between the i -th qubit and j -th qubit can be effectively induced as shown in the rotational-wave-approximation (RWA) illustrated in (8.6)-(8.8).

$$\hat{H} = \frac{\hbar}{2} \sum_k \omega_k \sigma_{z,k} + \hbar \sum_{ij} g_{ij}(t) (\sigma_{i+} \sigma_{j-} + \sigma_{i-} \sigma_{j+}) \quad (8.6)$$

$$\hat{U}_{\text{int}} = e^{\frac{i\hbar}{2} \sum_k \omega_k \sigma_{z,k}} \quad (8.7)$$

$$\begin{aligned} \hat{H}_{\text{int,RWA}} &= \hbar \sum_{ij} g_{ij}(t) (\sigma_{i+} \sigma_{j-} e^{i(\omega_i - \omega_j)t} + \sigma_{i-} \sigma_{j+} e^{i(\omega_j - \omega_i)t}) \\ &\simeq \frac{L_{gJ}}{16\sqrt{L_i L_j}} \sqrt{\omega_i \omega_j} \pi A_\Phi^2 \Phi_0 (\sigma_{i+} \sigma_{j-} e^{-\phi_{ij}} + \sigma_{i-} \sigma_{j+} e^{-\phi_{ij}}) \end{aligned} \quad (8.8)$$

This technique can clearly be extended to controlling multiple two qubit couplings at the same time by multiplexing in frequency domain multiple phase coherent microwave tones in the coupler SQUID flux modulation as shown in the lower left part

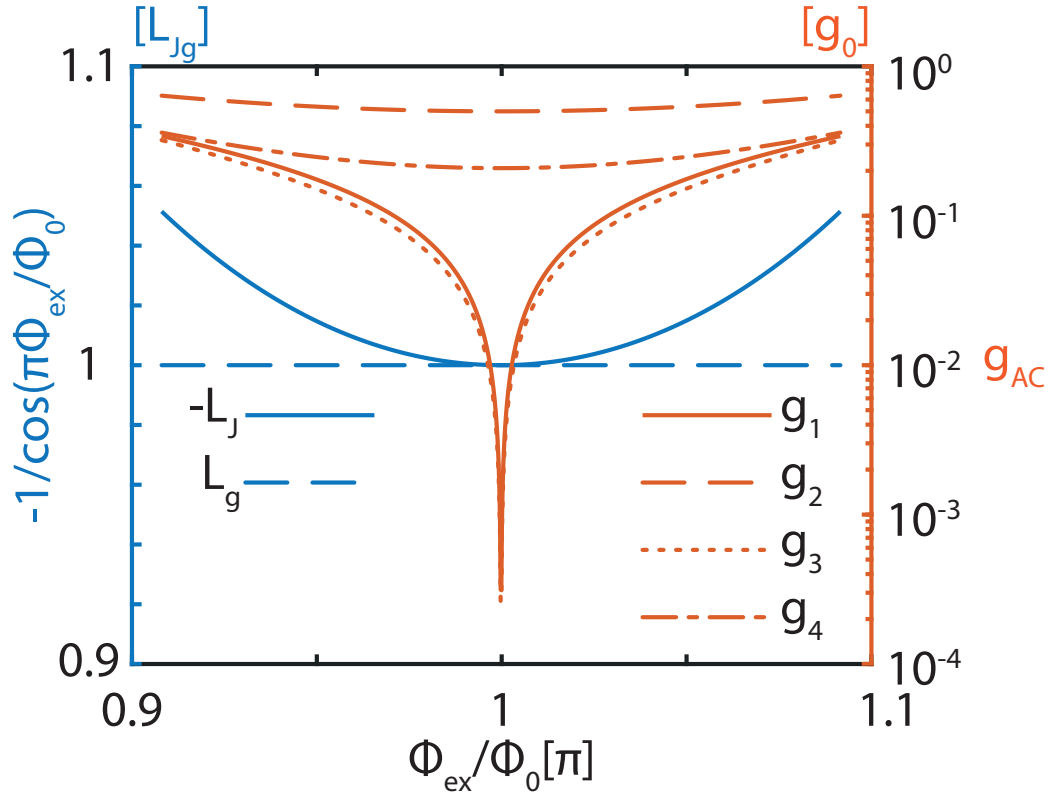


Figure 8.2: The DC parts of the coupling inductance are plotted on against the left (blue) axis. This shows that the Josephson junction inductance (solid blue) cancels the linear inductance (dashed blue) in the unit of SQUID minimum effective Josephson junction inductance (L_{Jg}) around the $\Phi_{\text{ex}}^0 \sim \Phi_0$ bias point. The higher orders of the coupling (g_1, g_2, g_3, g_4) when the flux is modulated slightly around the bias point are plotted against the right (red) axis in the unit of g_0 . It can be seen that the odd orders vanish at the bias point and even orders are non-vanishing.

of Fig. 8.1.

Furthermore, if the coherent modulation tones are phase correlated so that phase difference between any pair of tones is composed of a free time evolution contribution with a constant phase offset, the induced photon hopping will have hopping direction dependent phases that break the time-reversal symmetry of the system. Another aspect of coupling multiple qubit with programmable arbitrary connection graphs is the possibility to synthesize exotic topology in higher dimensions.

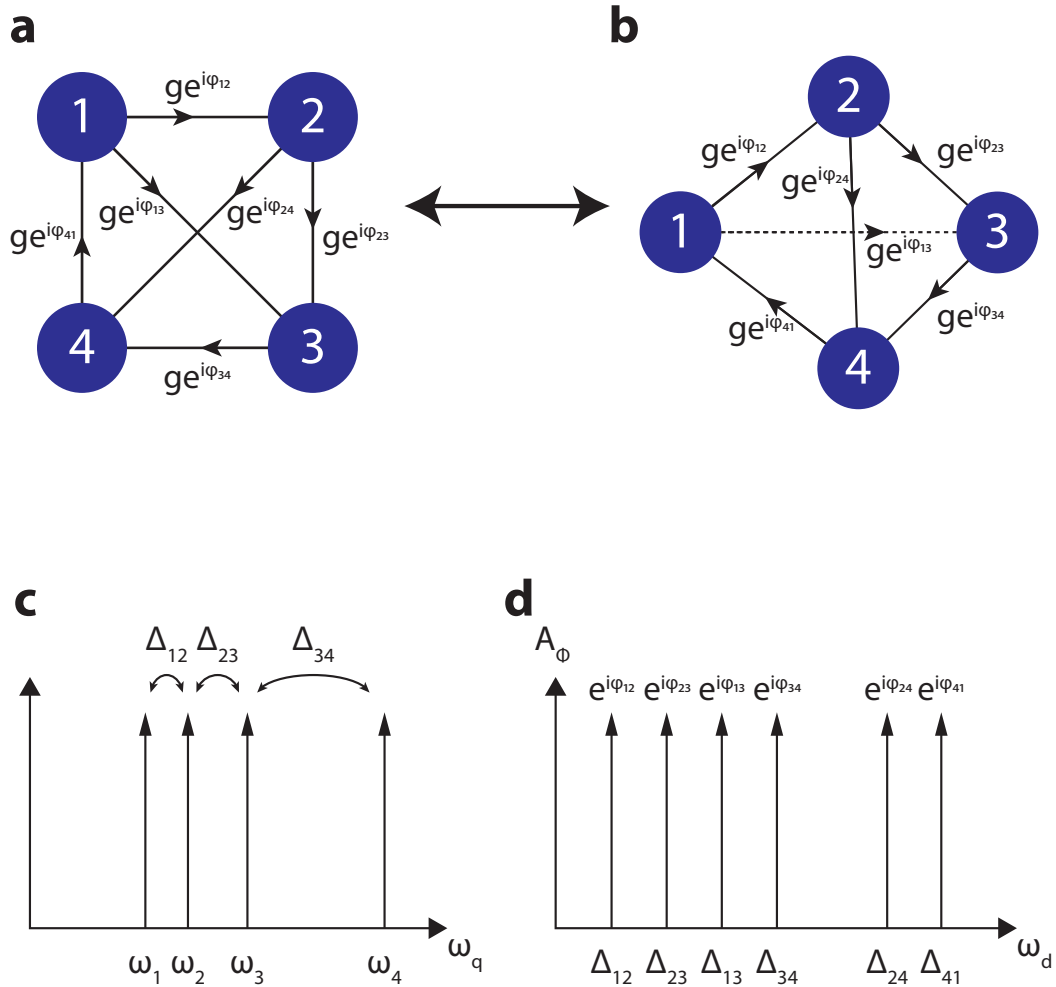


Figure 8.3: **a**, the example application of the hardware efficient programmable multiqubit coupling scheme to a four qubit device. **b**, this system can also be mapped into a quasi-3D tetrahedron connectivity structure where photons flow on the edges of the tetrahedron. **c**, we drive the coupling between four detuned qubits with qubit frequencies in **c** via six external flux drive tones that are phase correlated. The correlated phases can be used to break the time reversal symmetry of photon hopping on between the qubits. Novel applications including cryogenic high efficiency circulator can be realized with this device to realize scalable superconducting quantum network in microwave domain in a DF between multiple qubit chip packages. This can also be used to simulate non-trivial topological photon current in a synthesized high dimensional structure.

8.1 Time-reversal Symmetry Broken Interacting Photonic Tetrahedron Lattice

As a concrete example, Fig. 8.3 shows that we can synthesize a tetrahedron photonic lattice with as few as four qubits that are fully connected in a programmable way. Moreover, the time-reversal symmetry of a photon hopping on the edges of the tetrahedron is broken with phase correlated flux modulation tones. The physics of time reversal symmetry broken tetrahedron photon lattice can be captured with the following Hamiltonian (8.9). This Hamiltonian is written in a form that highlights the slightly anharmonic bosonic resonator nature of transmon qubits. In this form, it is clear that the anharmonicity of a transmon qubit site can be equivalently viewed as a reflection of on-site attractive interaction ($U_k < 0$) between interacting photons in the quantum circuit induced by the Josephson junction that is a nonlinear inductance element. This Hamiltonian can be further transformed into the interaction picture as (8.10) assuming that the coupling coefficients are modulated with phase correlated tones matching the detunings between each qubit pairs with phase factor $e^{i\phi_{p,q}}$. This interaction picture Hamiltonian can be solved to obtain its eigenstates and energies of for a single photon excitation manifold.

$$H_{Aq} = \sum_{k=1}^4 \hbar\omega_k \hat{c}_k^\dagger \hat{c}_k + \hbar U_k \hat{c}_k^\dagger \hat{c}_k \hat{c}_k^\dagger \hat{c}_k + \sum_{p=1, q>p}^4 \hbar \left(g_{p,q}(t) \hat{c}_p^\dagger \hat{c}_q + g_{p,q}(t)^* \hat{c}_p \hat{c}_q^\dagger \right) \quad (8.9)$$

$$H_{Aq,int} = \sum_{p=1, q>p}^4 \hbar \tilde{g}_{p,q} \left(e^{i\phi_{p,q}} \hat{c}_p^\dagger \hat{c}_q + e^{-i\phi_{p,q}} \hat{c}_p \hat{c}_q^\dagger \right) \quad (8.10)$$

The solved energy energies of the single-photon excitation manifold as a function of total photon hopping phase accumulated in a path through all nodes without any self-intersection is shown in Fig. 8.4a assuming that $g_{p,q}(t) = g e^{i\phi_{p,q}}$. We can also measure the photon current flowing through each edge and plot them in Fig. 8.4b – f for $\phi_{tot} = \phi_{41}$ and other $\phi_{pq} = 0$. The colors of the different curves in Fig. 8.4b – f correspond to the energy levels with the same colors in Fig. 8.4a. The photon current can be measured using averaged the Pauli operator correlations $I_{p,q} = \langle \hat{\sigma}_{p,x} \hat{\sigma}_{q,y} \rangle - \langle \hat{\sigma}_{p,y} \hat{\sigma}_{q,x} \rangle$ of nearest qubit sites p, q on the coupling graph Fig. 8.3b. This current variable is in the unit of g which is photon hopping rate between nearest neighbors. A derivation of the form used for photon current can be found in [106]. It should be emphasize that the non-zero photon currents in

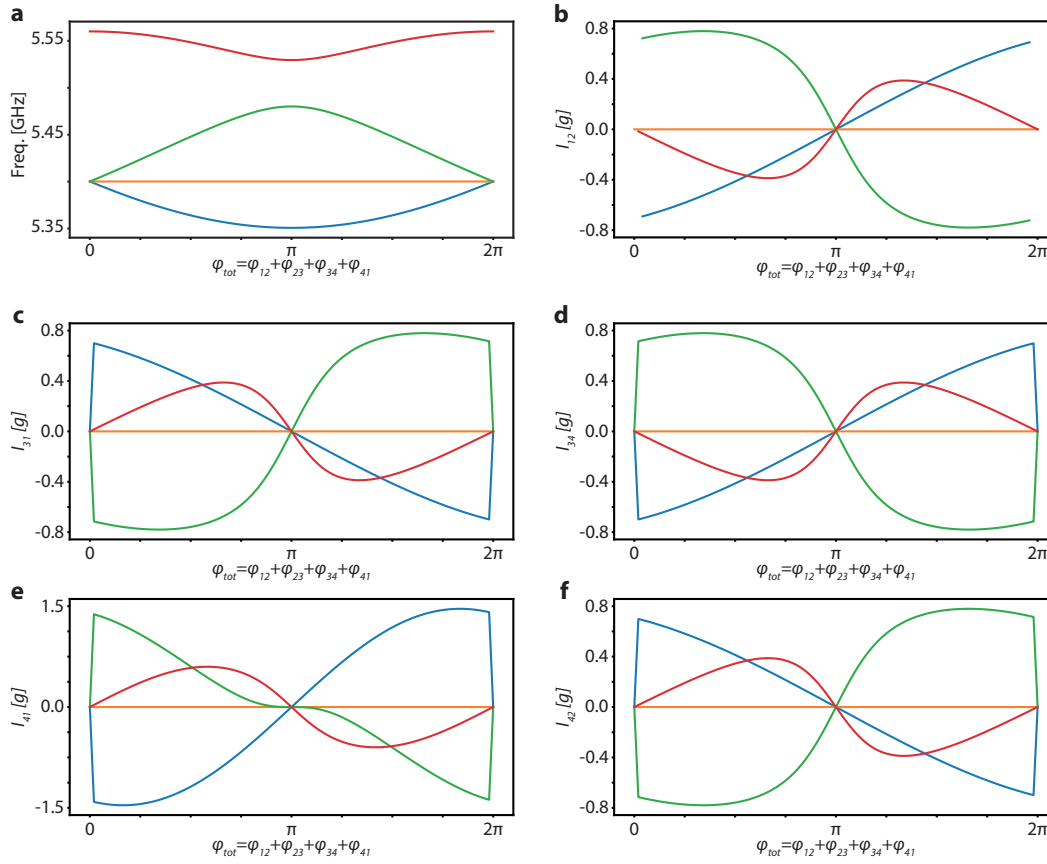


Figure 8.4: **a**, the single photon manifold energy levels of the four qubit spidermon system in time-independent interaction picture frame following from (8.10) for different total photon hopping phase ϕ_{tot} accumulated in a path ($1 \rightarrow 2 \rightarrow 3 \rightarrow 4 \rightarrow 1$) passing all sites without self-intersections. **b – f**, the photon current of each edge in the tetrahedron if $\phi_{\text{tot}} = \phi_{41}$ and other $\phi_{pq} = 0$. Colors of different current curves correspond to different energy levels in **a**. The current $I_{2,3}$ is not plotted as $I_{2,3} = 0$ with the chosen phase (gauge field flux) distribution on the photonic lattice.

Fig. 8.4**b – f** are spontaneous as they are currents flowing in a single photon eigenstate of the four qubit system. These currents are nontrivial since the eigen-states are stationary states of the system and their photon distribution should be time independent. These currents are examples of Chiral edge currents in a topological condensed matter system or a synthetic topological photonic material.

Besides simulating novel physics in a higher dimension with planar structures, this type of device can also be used to build high efficiency cryogenic circulator to route photons between superconducting chips in the same dilution refrigerator. Such circulators will be extremely low loss and are critical for building superconducting quantum network that connects multiple well packaged superconducting quantum

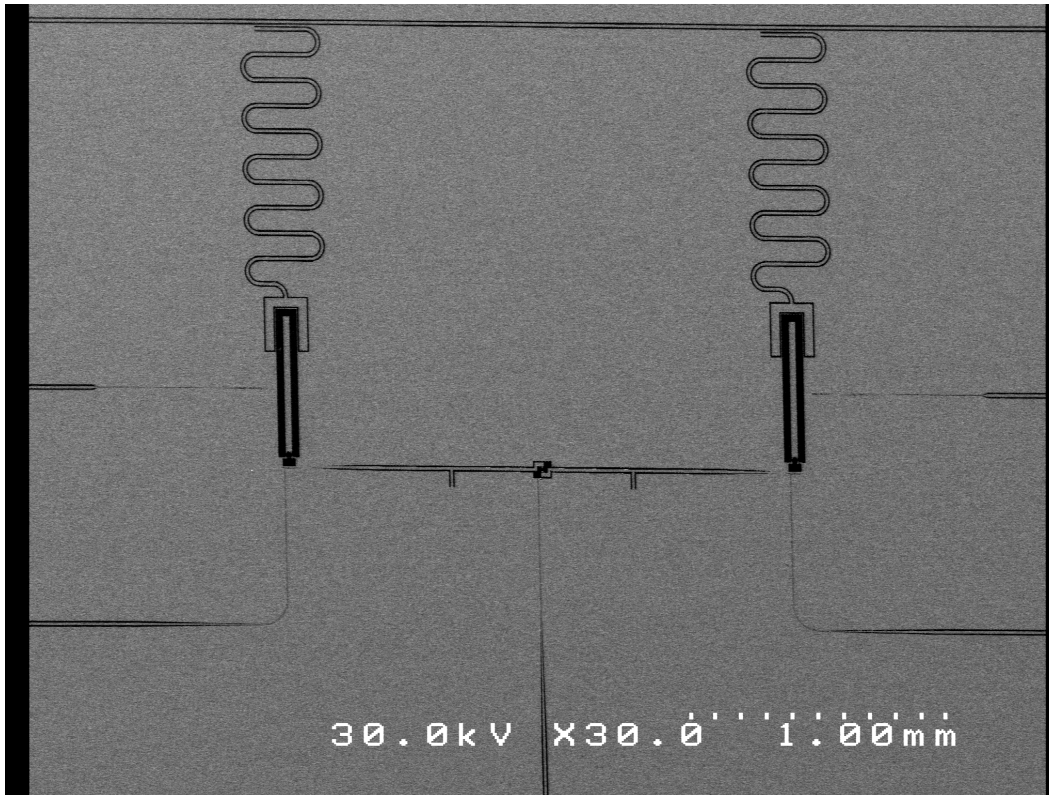


Figure 8.5: The Scanning Electron Microscope (SEM) image of one of the fabricated two qubit device that are coupled together via a tunable coupler to realize photon hopping between detuned qubits assisted with an external flux modulated coupler.

processors into a large quantum system.

Experimentally, we built two generations of test devices to test the idea of inducing photon hopping between detuned qubits via modulating the coupling between them. The first chip is shown in Fig. 8.5. It has two qubit inductively coupled via a common SQUID coupler to the ground and the SQUID in this design is not serially connected to a linear inductor. This results in a non-zero static coupling term $g_0 \neq 0$. The coupling between the two qubits can be written as (8.1) with $L_g = 0$.

To avoid a large static coupling between the two qubit that hybridizes the two qubit unintentionally despite of their large detuning, the coupler SQUID's junctions' inductance needs to be small. However, this introduces two issues. One issue is that the time dependent oscillating part's induced photon hopping rate is also proportional to the SQUID inductance and reducing it will also significantly reduce

the parametrically induced hopping rate for a given flux modulation amplitude. This is a fundamental issue as the flux modulation amplitude is bounded since the SQUID's effective inductance is periodic in the external flux. Driving with flux modulation amplitude greater than $0.5\Phi_0$ is not going to benefit the coupling parametrically induced photon hopping rate. Another more practical issue related to fabrication is that a small Josephson junction inductance corresponds to a large junction area. This is particularly difficult with our current fabrication techniques that are tailored to reliably yield small size junctions suitable for making high quality superconducting transmon qubits as a smaller junction has in general smaller number of two-level-systems (TLSs) that can rapidly decohere the junction's transmon qubit. To be more specific, coupling SQUID's Josephson junctions' areas in our fabrication calibration need to be larger than $1\mu m^2$ while the concurrently fabricated superconducting transmon qubits' Josephson junctions' areas are about $0.07\mu m^2$. The second issue experimentally lowered the fabrication yield of such devices significantly unless we completely alter the fabrication processes which involve replacing the double layer electron resist mask with metal mask or using the Manhattan style junction fabrication process instead of the Dolan-Bridge junctions.

After characterizing this two qubit design in cryogenic environment, we shifted our attention to the design with the coupler SQUID serially connected to a linear inductance. In order to increase our success rate in observing parametrically induced photon hopping between a pair of detuned qubits, we also extended the device to include four single junction superconducting transmon qubits seen in Fig. 8.6.

The DC flux bias was taken to cancel the serial linear inductance. In this scheme, it is critical to have a stable bias current source to generate a stable external magnetic flux for the coupler SQUID to cancel the slightly large linear inductance L_g . The modulation tones were put into the coupler via phase correlated waves synthesized by our keysight AWG cards and mixed to a stable microwave tone generated by an external RF-generator. This mixed microwave flux modulation pulse is further mixed with the DC bias current using a bias-tee in the DF MC stage where the superconducting quantum circuit is located before going into the SQUID coupling flux control line.

8.2 Controlling and Measuring Slightly Hybridized Multiqubit system

In a general multiqubit system, there can be unwanted couplings between qubits that are far detuned. These couplings slightly hybridize the system such that the energy levels of the system used for storing and manipulating quantum information

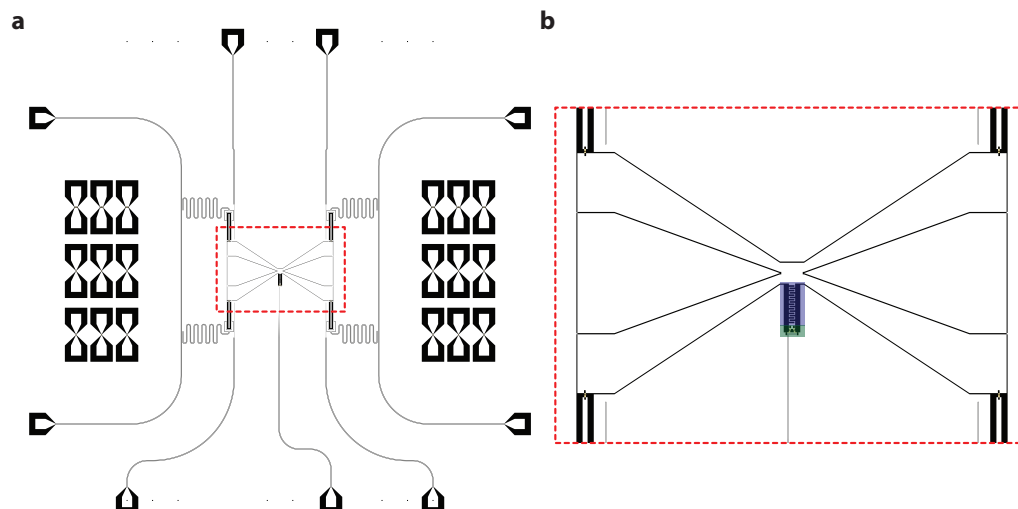


Figure 8.6: **a**, The four qubit spidermon device that has a linear inductance serially connected to a SQUID device. This device has four far detuned single junction transmon qubits that can be individually controlled and read out. The coupler region is highlighted in a red-dashed box. **b**, the zoomed in view of the coupler in the red-dashed box. The linear inductor is highlighted in the blue region and it is serially connected to a SQUID device in the green region.

are supermodes formed by slightly hybridized qubits. If the control and readout schemes, still assume that the far detuned qubits are orthogonal with each other, the qubit gate and readout fidelity will be reduced with reduction positively related to the extent of hybridization which rotates the system Hilbert space's eigen basis away from the basis formed by direct product of eigen states of each qubit. The accidental hybridization can be an important factor to be considered in spidermon system as several qubits are coupled together via a common current path. In this section, I will analysis the influence of such slight hybridization and propose how we can measure and appropriately combine control pulses to directly measure and address the true eigen basis of the system.

As a first step, we can start with analyzing a two qubit system having two far detuned qubits weakly coupled with coupling rate g_{12}^0 . It can be seen that we also included the readout resonators into the system for looking at the hybridization's influence on our qubit state measurement. There are also two XY-drives on the qubits.

The system's Hamiltonian can be written as (8.11).

$$\begin{aligned}
\hat{H}_{2q} = & \frac{1}{2}\hbar\omega_1\hat{\sigma}_{zq1} + \frac{1}{2}\hbar\omega_{q2}\hat{\sigma}_{z2} \\
& + \hbar g_{12}(\sigma_{1+}\sigma_{2-} + \sigma_{1-}\sigma_{2+}) \\
& + \hbar(\omega_{r1} - \chi_1\hat{\sigma}_{zq1})\hat{a}_1^\dagger\hat{a}_1 + \hbar(\omega_{r2} - \chi_2\hat{\sigma}_{zq2})\hat{a}_2^\dagger\hat{a}_2 \\
& + \frac{1}{2}\hbar\Omega_1^0(\sigma_{1+} + \sigma_{1-})\cos(\omega_{d1}t + \phi_1) + \frac{1}{2}\hbar\Omega_2^0(\sigma_{2+} + \sigma_{2-})\cos(\omega_{d2}t + \phi_2)
\end{aligned} \tag{8.11}$$

where the rising and lowering operators for our qubits are $\sigma_{k,\pm} = \sigma_{k,x} \pm i\sigma_{k,y}$ with $k = 1, 2$. We also have that $\hat{\sigma}_{zk} = 2\sigma_{k,+}\sigma_{k,-} - 1$. Notice that the form in the above expression already diagonalized the dispersive interaction between the qubits and the readout resonators. As a result, the qubits and readout resonator frequencies are already renormalized.

Take the following transformations in (8.12) and (8.13).

$$\begin{bmatrix} \sigma_{s-} \\ \sigma_{a-} \end{bmatrix} = \begin{bmatrix} \alpha_1 & \alpha_2 \\ \beta_1 & \beta_2 \end{bmatrix} \begin{bmatrix} \sigma_{1-} \\ \sigma_{2-} \end{bmatrix} \tag{8.12}$$

$$\begin{bmatrix} \sigma_{1-} \\ \sigma_{2-} \end{bmatrix} = \frac{1}{\alpha_1\beta_2 + \alpha_2\beta_1} \begin{bmatrix} \beta_2 & \beta_1 \\ \alpha_2 & -\alpha_1 \end{bmatrix} \begin{bmatrix} \sigma_{s-} \\ \sigma_{a-} \end{bmatrix} = \begin{bmatrix} \beta'_2 & \beta'_1 \\ \alpha'_2 & -\alpha'_1 \end{bmatrix} \begin{bmatrix} \sigma_{s-} \\ \sigma_{a-} \end{bmatrix} \tag{8.13}$$

As the two qubit part of the Hamiltonian in (8.11) can be rewritten as (8.14)

$$\begin{aligned}
\hat{H}_{q-q} = & \begin{bmatrix} \sigma_{1+} & \sigma_{2+} \end{bmatrix} \begin{bmatrix} \omega_{q1} & g_{12} \\ g_{12} & \omega_{q2} \end{bmatrix} \begin{bmatrix} \sigma_{1-} \\ \sigma_{2-} \end{bmatrix} \\
= & \begin{bmatrix} \sigma_{s+} & \sigma_{a+} \end{bmatrix} \begin{bmatrix} \beta'_2 & \beta'_1 \\ \alpha'_2 & -\alpha'_1 \end{bmatrix}^\dagger \begin{bmatrix} \omega_{q1} & g_{12} \\ g_{12} & \omega_{q2} \end{bmatrix} \begin{bmatrix} \beta'_2 & \beta'_1 \\ \alpha'_2 & -\alpha'_1 \end{bmatrix} \begin{bmatrix} \sigma_{s-} \\ \sigma_{a-} \end{bmatrix}
\end{aligned} \tag{8.14}$$

The super-mode transformation should transform the basis into the eigen basis of the qubit-qubit system that diagonalize the qubit-qubit part of the Hamiltonian. By solving the diagonalization problem in (8.15).

$$\begin{bmatrix} \beta'_2 & \beta'_1 \\ \alpha'_2 & -\alpha'_1 \end{bmatrix}^\dagger \begin{bmatrix} \omega_{q1} & g_{12} \\ g_{12} & \omega_{q2} \end{bmatrix} \begin{bmatrix} \beta'_2 & \beta'_1 \\ \alpha'_2 & -\alpha'_1 \end{bmatrix} = \begin{bmatrix} \lambda_+ & 0 \\ 0 & \lambda_- \end{bmatrix} \tag{8.15}$$

We can find diagonalization leads to (8.16) and (8.18) with eigen basis rotational

angle defined by (8.17).

$$\lambda_{\pm} = \frac{(\omega_{q1} + \omega_{q2}) \pm \sqrt{(\omega_{q1} - \omega_{q2})^2 + 4J^2}}{2} \quad (8.16)$$

$$\tan(\theta_{\pm}) = \frac{\lambda_{\pm} - \omega_{q1}}{g_{12}} \quad (8.17)$$

$$\begin{bmatrix} \beta'_2 & \beta'_1 \\ \alpha'_2 & -\alpha'_1 \end{bmatrix} = \begin{bmatrix} \cos(\theta_+) & \cos(\theta_-) \\ \sin(\theta_+) & \sin(\theta_-) \end{bmatrix} \quad (8.18)$$

Applying the above eigen basis rotation matrix to the driving part of the Hamiltonian in (8.11) we can obtain (8.19).

$$\begin{aligned} \hat{H}_{\text{drive}} &= \frac{\hbar}{2} \Omega_1(t) (\sigma_{1+} + \sigma_{1-}) + \frac{\hbar}{2} \Omega_2(t) (\sigma_{2+} + \sigma_{2-}) \\ &= \frac{\hbar}{2} (\Omega_1(t) \beta'_2 + \Omega_2(t) \alpha'_2) (\sigma_{s+} + \sigma_{s-}) + \frac{\hbar}{2} (\Omega_1(t) \beta'_1 - \Omega_2(t) \alpha'_1) (\sigma_{a+} + \sigma_{a-}) \end{aligned} \quad (8.19)$$

$$\begin{bmatrix} \Omega_1(t) \\ \Omega_2(t) \end{bmatrix} = \begin{bmatrix} \beta'_2 & \beta'_1 \\ \alpha'_2 & -\alpha'_1 \end{bmatrix} \begin{bmatrix} \Omega_s(t) \\ \Omega_a(t) \end{bmatrix} \quad (8.20)$$

In (8.19) and (8.20), we assumed that absorbed the time dependence of the XY-Drives such that $\Omega_{k=1,2,a,s}(t) = \Omega_{k=1,2,a,s}^0 \cos(\omega_{d,k}t + \phi_k)$ where $\Omega_{k=1,2}^0$ is the single qubit XY-Drive Rabi frequency.

It can be seen from (8.20) that a simple linear combination of control pulses on the two qubits with appropriate driving frequency, phases, and amplitudes can allow us to directly manipulate the eigen basis of the qubit system with high fidelity. More generally, it can be shown that for a multi-qubit system hybridized in a way that can be represented by a basis transformation matrix \hat{T} in (8.21) the drive is also transformed according to (8.22).

$$\begin{bmatrix} \sigma_{1-} \\ \sigma_{2-} \\ \vdots \\ \sigma_{N-} \end{bmatrix} = \hat{T} \begin{bmatrix} \tilde{\sigma}_{1-} \\ \tilde{\sigma}_{2-} \\ \vdots \\ \tilde{\sigma}_{N-} \end{bmatrix} \quad (8.21)$$

$$\begin{bmatrix} \Omega_1(t) \\ \Omega_2(t) \\ \vdots \\ \Omega_N(t) \end{bmatrix} = \hat{T} \begin{bmatrix} \tilde{\Omega}_1(t) \\ \tilde{\Omega}_2(t) \\ \vdots \\ \tilde{\Omega}_N(t) \end{bmatrix} \quad (8.22)$$

In order to measure the quantum state now stored in the Hilber space with rotated eigen basis due to the hybridization, we need to understand the relation between the projective map on to the eigen basis and the dispersive shifts of the readout resonators. The qubit state dependent dispersive shift of the k -th readout resonator can be written as (8.23) using the transformation matrix defined in (8.21).

$$\Delta\hat{\omega}_{r,k} = -\chi_k\sigma_{z,k} = -\chi_k \left[\sum_j |T_{k,j}|^2 \tilde{\sigma}_{z,j} + \sum_{ij} T_{k,i}^* T_{k,j} \tilde{\sigma}_{i+} \tilde{\sigma}_{j-} \right] \quad (8.23)$$

$$\langle \Delta\hat{\omega}_{r,k} \rangle = -\chi_k \sum_j |T_{k,j}|^2 \langle \tilde{\sigma}_{z,j} \rangle \quad (8.24)$$

The system state measurement is done with averaging the qubit state dependent readout resonator frequency shift as in (8.24). If the mode hybridization is significant, we can extract the coefficients of the transformation matrix T_{ij} using very weak continuous microwave drive to drive the system from different XY-Control ports and measure all the readout resonators' frequency shifts.

The weak drive when resonant with the eigen mode of the system can drive the eigen mode into an equal mixed state of ground and excited states leading to an average occupation number ~ 0.5 , Other modes due to large drive-mode detunings and weak drive amplitude will lead to negligible average populations and contributions to readout resonator frequency shifts for these non-resonant modes. The step-by-step process is as follows:

1. Characterize the readout resonator frequencies without qubit drives.
2. Continuously drive the j -th XY-Control port with sweeping amplitude and frequency around the j -th qubit's designed frequency.
3. Observe the frequency responses of all readout resonators using VNA
4. Identify the XY-Control drive frequency and smallest amplitude that leads to significant frequency shifts in at least one of the readout resonators.
5. Record the frequency shifts of all readout resonators. The i -th readout resonator's frequency shift $\Delta\omega_{r,ij} = -0.5\chi_i|T_{ij}|^2$.
6. Repeat the above steps from Step.2 for the $(j + 1)$ -th XY-Control port until all the XY-Control ports are probed and all $\Delta\omega_{r,ij}$ are obtained.

7. Because \hat{T} is unitary, $\sum_j |T_{ij}| = 1 \forall i = 1, 2, \dots, N$. $\chi_i = -2 \sum_j \Delta\omega_{r,ij}$ and then we can have $|T_{ij}| = \sqrt{-2\Delta\omega_{r,ij}/\chi_i}$.

It should be remarked that the above method for accurately identify amplitudes of the transformation matrix coefficients is most useful when the hybridization is large since readout resonator frequency shifts caused by slight qubit hybridization can be much smaller than the linewidth of the readout resonators. In the case of very slight hybridization, the j -th readout resonator frequency shift can be regarded as a good proxy for measuring the state of the system eigen mode that is almost overlapping with the resonator's directly coupled fabricated qubit. In the case of very slight hybridization, a more general automated machine learning based routine can be used to learn the XY-Control transfer matrix \hat{T} for generating optimal pulse combinations to create gates for the multi-qubit system.

Chapter 9

CONCLUSION

The rapid rise of quantum information technology (QIT) in recent years has signaled the advent of a new stage in technology evolution where the scalability of quantum systems far beyond the existing architectures is at the center of today's quantum technology breakthroughs. In this work, I introduced my efforts in engineering preliminary hybrid quantum devices that can potentially become the foundation of future scalable quantum systems for quantum computation, communication, and sensing.

Using engineered optomechanical interactions between high-finesse optical cavities and mechanical resonators, we created a device that can unidirectional route photons on an integrated photonic microchip composed of patterned suspended crystalline silicon membrane [37]. Such optomechanical interaction is also used to probe and demonstrate that ultra-high quality phononic cavities having mechanical frequency ~ 5 GHz can store the energy of this mechanical mode with relaxation time reaching 1 s in a 10 mK environment [74].

The ultra-high quality phononic cavities created are based on synthetic crystals for trapping the mechanical modes of interest. Such structures that localize mechanical motions into a highly confined volume have an extremely compact footprint on a planar silicon structure. These devices are compatible with the prevailing planar superconducting quantum logic circuits composed of superconducting transmon qubits that operate around 5 GHz with lifetime $\lesssim 100 \mu\text{s}$ [52, 10, 7, 66, 60]. As a scalable quantum computing architecture based superconducting transmon qubits may require a quantum version of Von Neumann Architecture (VNA) [85]. VNA has been commonly used in all current classical computing systems since its introduction in 1940s for efficiently scaling up early computers. This proven path in scalable classical digital computing hints the potential adoption of Quantum Von Neumann Architecture (QVNA) in near future quantum computers. This requires ultra-high coherence quantum memory elements having lifetime much longer than the superconducting qubits and demand close to unity qubit-memory read-write fidelity. The

small footprint and ultra-high quality of phononic quantum acoustic memory can lead to multiplexed quantum memory bank that further boost the functionality of QVNA based on high frequency phononic quantum memories. Ultra-high fidelity two-qubit gates can be carried out in a memory bank [52]. This together with ultra-high single qubit gates in electric domain can lead to a new architecture for building fault-tolerant quantum computers in near future. In order to couple a quantum electric circuit with this promising phononic quantum memory, we choose to use piezoelectric coupling as the transduction mechanism and developed ways to deposit high quality piezoelectric Aluminum Nitride (AlN) layer and electrodes (Mo and Al). We also adopted industrial deposition services that deposit an ultra-high quality thin AlN layer on our supplied SOI wafers.

Using piezoelectric thin film AlN having thickness around 300 nm and novel processing techniques [23, 129], we designed, fabricated, and patterned piezoacoustic Lamb resonators having a 3 GHz piezoacoustic mode optimally matched with interdigitated electrodes. Several Lamb resonator are coupled to a superconducting qubit for hybridizing the qubit with multi-mode acoustic memory bank. Microwave transmission lines are also directly connected to these acoustic resonators to spectroscopically study the coupling spectra of fabricated piezoacoustic Lamb resonators of various sizes. The mode-matched Lamb resonator creates an highly efficient interface between the microwave electric domain and microwave acoustic domain on silicon. The microwave acoustic degree of freedom in a silicon membrane can be further coupled to optical degree of freedom in telecommunication band to assist quantum high-fidelity and high-SNR transduction between microwave photons and telecommunication photons.

Furthermore, I introduced a viable phononic quantum memory architecture based on engineered piezoelectric virtual coupling channels to have an integrated quantum acoustic memory that can dynamically switch between an idle-state and a swap-state. In the idle-state where the virtual coupling is turned off, the ultra-high coherence (relaxation time ~ 1 ms) is achieved in the phononic memory and the superconducting qubit's high bare coherence ($T_1 \sim 10 \mu\text{s}$) is preserved. In the swap-state, high fidelity (~ 1) quantum state transfer is realized between the qubit and the memory via a high cooperativity ($\sim 10^5$) virtual piezoelectric coupling interface.

A scalable quantum computing architecture based on QVNA not only requires high quality on-demand quantum memory but also demands a programmable and scalable quantum logic circuit architecture. Near the end of this dissertation, I introduced my latest work on creating a novel programmable multi-qubit coupling scheme which is hardware-efficient, fast, high-fidelity, and non-nearest neighbor in a planar circuit. The scheme can be used to create in-situ controlled time-dependent couplings between arbitrary qubit pairs in a cluster of qubits. This can for example create a time-reversal symmetry broken photonic lattice that processes nontrivial persistent photon currents in eigen-states of single-photon and two-photon manifolds. This readily allows the creation of a high-efficiency large-bandwidth microwave photon circulator [14] based on time-reversal symmetry broken photon-hopping and parametric amplifications created with phase correlated multi-tone coupling pulses to modulate the couplings of between qubit pairs. The scheme opens doors for a variety of near-term novel experiments including high-connectivity floquet-engineering [34, 140], synthetic high-dimension topological photonic lattices, and demonstrations of small qubit system fault-tolerant protocols [45, 19] with frequency domain multiplexed programmable controls.

In conclusion, this dissertation shows preliminary steps towards building various parts required for constructing scalable quantum systems for the progression of quantum information technology in the near-term Noisy Intermediate-Scale Quantum (NISQ) era.

BIBLIOGRAPHY

- [1] A. Ababneh et al. “The influence of sputter deposition parameters on piezoelectric and mechanical properties of AlN thin films”. In: *Materials Science and Engineering: B* 172.3 (Sept. 2010), pp. 253–258. ISSN: 0921-5107. URL: <http://www.sciencedirect.com/science/article/pii/S0921510710003983>.
- [2] Baleegh Abdo et al. “Directional Amplification with a Josephson Circuit”. In: *Phys. Rev. X* 3 (July 2013), p. 031001.
- [3] Baleegh Abdo et al. “Josephson Directional Amplifier for Quantum Measurement of Superconducting Circuits”. In: *Phys. Rev. Lett.* 112 (Apr. 2014), p. 167701.
- [4] Joel Agnus, Ioan Alexandru Ivan, and S. Queste. *DRY etching of single crystal PMN-PT piezoelectric material*. Feb. 2011, pp. 237–240.
- [5] Y. Aharonov and D. Bohm. “Significance of Electromagnetic Potentials in the Quantum Theory”. In: *Phys. Rev.* 115 (1959), pp. 485–491.
- [6] Thiago P. Mayer Alegre et al. “Quasi-two-dimensional optomechanical crystals with a complete phononic bandgap”. In: *Opt. Express* 19.6 (Mar. 2011), pp. 5658–5669. DOI: 10.1364/OE.19.005658.
- [7] Patricio Arrangoiz-Arriola and Amir Safavi-Naeini. “Engineering interactions between superconducting qubits and phononic nanostructures”. In: *Phys. Rev. A* 94 (July 2016), p. 063864. DOI: 10.1103/PhysRevA.94.063864.
- [8] Patricio Arrangoiz-Arriola and Amir H. Safavi-Naeini. “Engineering interactions between superconducting qubits and phononic nanostructures”. In: *Phys. Rev. A* 94 (6 Dec. 2016), p. 063864. DOI: 10.1103/PhysRevA.94.063864. URL: <https://link.aps.org/doi/10.1103/PhysRevA.94.063864>.
- [9] Patricio Arrangoiz-Arriola et al. “Coupling a Superconducting Quantum Circuit to a Phononic Crystal Defect Cavity”. In: *PRX* 8.3 (July 2018), p. 031007. URL: <https://link.aps.org/doi/10.1103/PhysRevX.8.031007>.
- [10] Patricio Arrangoiz-Arriola et al. “Coupling a Superconducting Quantum Circuit to a Phononic Crystal Defect Cavity”. In: *Phys. Rev. X* 8 (July 2018), p. 031007. DOI: 10.1103/PhysRevX.8.031007.
- [11] M. Aspelmeyer, T. J. Kippenberg, and F. Marquardt. “Cavity optomechanics”. In: *Rev. Mod. Phys.* 86 (2014), pp. 1391–1452.

- [12] Markus Aspelmeyer, Tobias J. Kippenberg, and Florian Marquardt. *Cavity Optomechanics: Nano- and Micromechanical Resonators Interacting with Light*. Springer-Verlag, 2014.
- [13] T. Astner et al. “Solid-state electron spin lifetime limited by phononic vacuum modes”. In: *Nat. Mat.* 17 (Feb. 2018), pp. 313–317. DOI: 10.1038/s41563-017-0008-y.
- [14] S. Barzanjeh et al. “Mechanical on-chip microwave circulator”. In: *Nature Communications* 8.1 (Oct. 2017), p. 953. ISSN: 2041-1723. URL: <https://doi.org/10.1038/s41467-017-01304-x>.
- [15] R. O. Behunin, F. Intravaia, and P. T. Rakich. “Dimensional transformation of defect-induced noise, dissipation, and nonlinearity”. In: *Phys. Rev. B* 93 (June 2016), p. 224110. DOI: 10.1103/PhysRevB.93.224110.
- [16] Syed Bukhari et al. “Shear piezoelectric coefficients of PZT, LiNbO₃ and PMN-PT at cryogenic temperatures”. In: *Journal of Physics: Conference Series* 568.3 (Dec. 2014), p. 032004. ISSN: 1742-6596. URL: <http://dx.doi.org/10.1088/1742-6596/568/3/032004>.
- [17] Jasper Chan. “Laser cooling of an optomechanical crystal resonator to its quantum ground state of motion”. PhD thesis. California Institute of Technology, 2012.
- [18] Jasper Chan et al. “Optimized optomechanical crystal cavity with acoustic radiation shield”. In: *Appl. Phys. Lett.* 101.8 (June 2012), p. 081115. ISSN: 0003-6951. DOI: 10.1063/1.4747726.
- [19] Rui Chao and Ben W. Reichardt. “Fault-tolerant quantum computation with few qubits”. In: *npj Quantum Information* 4.1 (Sept. 2018), p. 42. ISSN: 2056-6387. URL: <https://doi.org/10.1038/s41534-018-0085-z>.
- [20] Ai Min Chen, Sam Young Cho, and Mun Dae Kim. “Implementation of a three-qubit Toffoli gate in a single step”. In: *Phys. Rev. A* 85 (3 Mar. 2012), p. 032326. DOI: 10.1103/PhysRevA.85.032326. URL: <http://link.aps.org/doi/10.1103/PhysRevA.85.032326>.
- [21] Xia Chen, Chao Li, and Hon K. Tsang. “Device engineering for silicon photonics”. In: *NPG Asia Mater.* 3 (2011), pp. 34–40.
- [22] Yu Chen et al. “Qubit Architecture with High Coherence and Fast Tunable Coupling”. In: *Phys. Rev. Lett.* 113 (22 Nov. 2014), p. 220502. DOI: 10.1103/PhysRevLett.113.220502. URL: <https://link.aps.org/doi/10.1103/PhysRevLett.113.220502>.
- [23] Yiwen Chu et al. “Quantum acoustics with superconducting qubits”. In: *Science* (2017). ISSN: 0036-8075. DOI: 10.1126/science.aao1511.
- [24] A.A. Clerk et al. “Introduction to quantum noise, measurement, and amplification”. In: *Rev. Mod. Phys.* 82 (2010), p. 1155.

- [25] L. I. G. O. Scientific Collaboration et al. “Observation of Gravitational Waves from a Binary Black Hole Merger”. In: *PRL* 116.6 (Feb. 2016), p. 061102. URL: <https://link.aps.org/doi/10.1103/PhysRevLett.116.061102>.
- [26] J. Dalibard et al. “Colloquium: Artificial gauge potentials for neutral atoms”. In: *Rev. Mod. Phys.* 83 (2011), p. 1523.
- [27] Dragan Damjanovic. “Ferroelectric, dielectric and piezoelectric properties of ferroelectric thin films and ceramics”. In: *Reports on Progress in Physics* 61.9 (Sept. 1998), pp. 1267–1324. ISSN: 1361-6633. URL: <http://dx.doi.org/10.1088/0034-4885/61/9/002>.
- [28] L. Deák and T. Fülöp. “Reciprocity in quantum, electromagnetic and other wave scattering”. In: *Ann. Phys.* 327 (2012), pp. 1050–1077.
- [29] M. H. Devoret and R. J. Schoelkopf. “Superconducting Circuits for Quantum Information: An Outlook”. In: *Science* 339.6124 (2013), pp. 1169–1174. ISSN: 0036-8075. DOI: 10.1126/science.1231930.
- [30] Marc-Alexandre Dubois and Paul Muralt. “Properties of aluminum nitride thin films for piezoelectric transducers and microwave filter applications”. In: *Appl. Phys. Lett.* 74.20 (Dec. 2018), pp. 3032–3034. ISSN: 0003-6951. DOI: 10.1063/1.124055. URL: <https://doi.org/10.1063/1.124055>.
- [31] Marc-Alexandre Dubois and Paul Muralt. “Stress and piezoelectric properties of aluminum nitride thin films deposited onto metal electrodes by pulsed direct current reactive sputtering”. In: *Journal of Applied Physics* 89.11 (Dec. 2018), pp. 6389–6395. ISSN: 0021-8979. DOI: 10.1063/1.1359162. URL: <https://doi.org/10.1063/1.1359162>.
- [32] Matt Eichenfield et al. “A picogram- and nanometre-scale photonic-crystal optomechanical cavity”. In: *Nature* 459 (2009), pp. 550–555.
- [33] M. Eichenfield et al. “Optomechanical crystals”. In: *Nature* 462 (2009), pp. 78–82.
- [34] Dominic V. Else et al. *Discrete Time Crystals*. May 2019. URL: <https://ui.adsabs.harvard.edu/abs/2019arXiv190513232E>.
- [35] K. Fang, Z. Yu, and S. Fan. “Photonic Aharonov-Bohm Effect Based on Dynamic Modulation”. In: *Phys. Rev. Lett.* 108 (2012), p. 153901.
- [36] K. Fang, Z. Yu, and S. Fan. “Realizing effective magnetic field for photons by controlling the phase of dynamic modulation”. In: *Nature Photon.* 6 (2012), pp. 782–787.
- [37] Kejie Fang et al. “Generalized non-reciprocity in an optomechanical circuit via synthetic magnetism and reservoir engineering”. In: *Nature Physics* 13 (Jan. 2017), p. 465.

- [38] Kejie Fang et al. “Optical transduction and routing of microwave phonons in cavity-optomechanical circuits”. In: *Nature Photon.* 10 (June 2016), pp. 489–496.
- [39] K. Fang et al. In: *in preparation* ().
- [40] V. V. Felmetzger, P. N. Laptev, and S. M. Tanner. “Innovative technique for tailoring intrinsic stress in reactively sputtered piezoelectric aluminum nitride films”. In: *Journal of Vacuum Science & Technology A* 27.3 (Aug. 2009), pp. 417–422. ISSN: 0734-2101. DOI: 10.1116/1.3089242. URL: <https://doi.org/10.1116/1.3089242>.
- [41] Serge Galliou et al. “Extremely Low Loss Phonon-Trapping Cryogenic Acoustic Cavities for Future Physical Experiments”. In: *Scientific Reports* 3 (July 2013), p. 2132. DOI: 10.1038/srep02132.
- [42] Jiansong Gao. “The Physics of Superconducting Microwave Resonators”. PhD thesis. California Institute of Technology, 2008.
- [43] A. H. Ghadimi et al. “Elastic strain engineering for ultralow mechanical dissipation”. In: *Science* 360 (6390 May 2018), pp. 764–768. DOI: 10.1126/science.aar6939.
- [44] J. Gomis-Bresco et al. “A one-dimensional optomechanical crystal with a complete phononic band gap”. In: *Nat. Commun.* 5 (2014), p. 4452.
- [45] Daniel Gottesman. *Quantum fault tolerance in small experiments*. Oct. 2016. URL: <https://ui.adsabs.harvard.edu/abs/2016arXiv161003507G>.
- [46] Simon Gröblacher et al. “Highly efficient coupling from an optical fiber to a nanoscale silicon optomechanical cavity”. In: *App. Phys. Lett.* 108 (2013), p. 181104.
- [47] Martin V. Gustafsson et al. “Propagating phonons coupled to an artificial atom”. In: *Science* 346.6206 (2014), pp. 207–211. DOI: 10.1126/science.1257219. URL: <http://www.sciencemag.org/content/346/6206/207.abstract>.
- [48] S. J. M. Habraken et al. “Continuous mode cooling and phonon routers for phononic quantum networks”. In: *New J. Phys.* 14 (2012), p. 115004.
- [49] Mohammad Hafezi and Peter Rabl. “Optomechanically induced non-reciprocity in microring resonators”. In: *Opt. Express* 20.7 (Mar. 2012), pp. 7672–7684.
- [50] M. Hafezi et al. “Robust optical delay lines with topological protection”. In: *Nat. Phys.* 7 (2011), p. 907.
- [51] M. Selim Hanay et al. “Inertial imaging with nanomechanical systems”. In: *Nature Nanotech.* 10 (Mar. 2015), pp. 339–344. DOI: 10.1038/NNANO.2015.32.

- [52] Connor T. Hann et al. “Hardware-efficient quantum random access memory with hybrid quantum acoustic systems”. In: *arXiv* (2019). URL: <https://arxiv.org/abs/1906.11340>.
- [53] A. Hardy and W. Streifer. “Coupled mode theory of parallel waveguides”. In: *Journal of Lightwave Technology* 3.5 (Oct. 1985), pp. 1135–1146. ISSN: 0733-8724. DOI: 10.1109/JLT.1985.1074291.
- [54] B. D. Hauer et al. “Two-level system damping in a quasi-one-dimensional optomechanical resonator”. In: *Phys. Rev. B* 98 (Dec. 2018), p. 214303. DOI: 10.1103/PhysRevB.98.214303.
- [55] Cheng-Liang Huang, Kok-Wan Tay, and Long Wu. “Aluminum nitride films deposited under various sputtering parameters on molybdenum electrodes”. In: *Solid-State Electronics* 49.2 (Feb. 2005), pp. 219–225. ISSN: 0038-1101. URL: <http://www.sciencedirect.com/science/article/pii/S003811010400276X>.
- [56] T. Ikeda. *Fundamentals of Piezoelectricity*. Oxford University Press, 1996. URL: <https://books.google.com/books?id=TrFvQgAACAAJ>.
- [57] Evan Jeffrey et al. “Fast Accurate State Measurement with Superconducting Qubits”. In: *PRL* 112.19 (May 2014), p. 190504. URL: <https://link.aps.org/doi/10.1103/PhysRevLett.112.190504>.
- [58] Mahmoud Kalae et al. “Quantum electromechanics of a hypersonic crystal”. In: *arXiv:1808.04874* (2018).
- [59] Abd El-Hady B. Kashyout et al. “Preparation and characterization of DC sputtered molybdenum thin films”. In: *Alexandria Engineering Journal* 50.1 (Mar. 2011), pp. 57–63. ISSN: 1110-0168. URL: <http://www.sciencedirect.com/science/article/pii/S1110016811000172>.
- [60] Andrew J. Keller et al. “Al transmon qubits on silicon-on-insulator for quantum device integration”. In: *Appl. Phys. Lett.* 111.4 (June 2017), p. 042603. ISSN: 0003-6951. DOI: 10.1063/1.4994661.
- [61] Majid Khan and Mohammad Islam. “Deposition and characterization of molybdenum thin films using dc-plasma magnetron sputtering”. In: *Semiconductors* 47.12 (Dec. 2013), pp. 1610–1615. ISSN: 1090-6479. URL: <https://doi.org/10.1134/S1063782613140017>.
- [62] JunHwan Kim et al. “Non-reciprocal Brillouin scattering induced transparency”. In: *Nat. Phys.* 11 (Jan. 2015), pp. 275–280.
- [63] R. N. Kleiman, G. Agnolet, and D. J. Bishop. “Two-Level Systems Observed in the Mechanical Properties of Single-Crystal Silicon at Low Temperatures”. In: *Phys. Rev. Lett.* 59 (18 Nov. 1987), pp. 2079–2082. DOI: 10.1103/PhysRevLett.59.2079.
- [64] Jens Koch et al. “Introducing the Transmon: a new superconducting qubit from optimizing the Cooper Pair Box”. In: *cond-mat/0703002v1* (2007).

- [65] J. Koch et al. “Time-reversal-symmetry breaking in circuit-QED-based photon lattices”. In: *Phys. Rev. A* 82 (2010), p. 043811.
- [66] P. Krantz et al. “A quantum engineer’s guide to superconducting qubits”. In: *Applied Physics Reviews* 6.2 (June 2019), p. 021318. DOI: 10.1063/1.5089550. URL: <https://doi.org/10.1063/1.5089550>.
- [67] Alexander G. Krause et al. “A high-resolution microchip optomechanical accelerometer”. In: *Nature Photonics* 6 (Oct. 2012), p. 768. URL: <https://doi.org/10.1038/nphoton.2012.245>.
- [68] Tomoyuki Kumada, Makoto Ohtsuka, and Hiroyuki Fukuyama. “Influence of substrate temperature on the crystalline quality of AlN layers deposited by RF reactive magnetron sputtering”. In: *AIP Advances* 5.1 (Aug. 2019), p. 017136. DOI: 10.1063/1.4906796. URL: <https://doi.org/10.1063/1.4906796>.
- [69] L. Landau and G. Rumer. “Über Schallabsorption in festen Körpern”. In: *Phys. Z. Sowjet.* 11 (18 1937).
- [70] Sheng-Kai Liao et al. “Satellite-to-ground quantum key distribution”. In: *Nature* 549 (Aug. 2017), p. 43. URL: <https://doi.org/10.1038/nature23655>.
- [71] Y.-J. Lin et al. “Synthetic magnetic fields for ultracold neutral atoms”. In: *Nature* 462 (2009), p. 628.
- [72] L. Lu, J.D. Joannopoulos, and M. Soljačić. “Topological photonics”. In: *Nat. Photonics*. 8 (2014), p. 821.
- [73] L. Luo, X. Zhao, and H. Luo. “7 - Single crystal PZN-PT, PMN-PT, PSN-PT and PIN-PT-based piezoelectric materials”. In: *Advanced Piezoelectric Materials*. Ed. by Kenji Uchino. Woodhead Publishing, Jan. 2010, pp. 239–286. URL: <http://www.sciencedirect.com/science/article/pii/B9781845695347500078>.
- [74] Gregory S. MacCabe et al. “Phononic bandgap nano-acoustic cavity with ultralong phonon lifetime”. In: (2019). eprint: arXiv:1901.04129.
- [75] Riccardo Manenti et al. “Circuit quantum acoustodynamics with surface acoustic waves”. In: *Nat. Commun.* 8 (Oct. 2017), p. 975. DOI: 10.1038/s41467-017-01063-9.
- [76] Sasikanth Manipatruni, Jacob T. Robinson, and Michal Lipson. “Optical Nonreciprocity in Optomechanical Structures”. In: *Phys. Rev. Lett.* 102 (May 2009), p. 213903.
- [77] F. Martin, P. Mural, and M.-A. Dubois. “Process optimization for the sputter deposition of molybdenum thin films as electrode for AlN thin films”. In: *Journal of Vacuum Science & Technology A* 24.4 (Dec. 2018), pp. 946–952. ISSN: 0734-2101. DOI: 10.1116/1.2201042. URL: <https://doi.org/10.1116/1.2201042>.

- [78] F. Martin et al. “Thickness dependence of the properties of highly c-axis textured AlN thin films”. In: *Journal of Vacuum Science & Technology A* 22.2 (Dec. 2018), pp. 361–365. ISSN: 0734-2101. DOI: 10.1116/1.1649343. URL: <https://doi.org/10.1116/1.1649343>.
- [79] John M. Martinis and A. Megrant. “UCSB final report for the CSQ program: Review of decoherence and materials physics for superconducting qubits”. In: *arXiv:1410.5793* (Oct. 2014).
- [80] F. Medjani et al. “Effect of substrate temperature and bias voltage on the crystallite orientation in RF magnetron sputtered AlN thin films”. In: *Thin Solid Films* 515.1 (Sept. 2006), pp. 260–265. ISSN: 0040-6090. URL: <http://www.sciencedirect.com/science/article/pii/S0040609005024193>.
- [81] Seán M. Meenehan et al. “Pulsed Excitation Dynamics of an Optomechanical Crystal Resonator near Its Quantum Ground State of Motion”. In: *Phys. Rev. X* 5 (4 Oct. 2015), p. 041002. DOI: 10.1103/PhysRevX.5.041002.
- [82] A. Metelmann and A. A. Clerk. “Nonreciprocal Photon Transmission and Amplification via Reservoir Engineering”. In: *Phys. Rev. X* 5 (2015), p. 021025.
- [83] Mohammad Mirhosseini et al. “Superconducting metamaterials for waveguide quantum electrodynamics”. In: *Nature Communications* 9.1 (Sept. 2018), p. 3706. ISSN: 2041-1723. URL: <https://doi.org/10.1038/s41467-018-06142-z>.
- [84] Bradley A. Moores et al. “Cavity Quantum Acoustic Device in the Multimode Strong Coupling Regime”. In: *Phys. Rev. Lett.* 120 (May 2018), p. 227701. DOI: 10.1103/PhysRevLett.120.227701.
- [85] R. K. Naik et al. “Random access quantum information processors using multimode circuit quantum electrodynamics”. In: *Nature Communications* 8.1 (Dec. 2017), p. 1904. ISSN: 2041-1723. URL: <https://doi.org/10.1038/s41467-017-02046-6>.
- [86] C. Neill et al. “A blueprint for demonstrating quantum supremacy with superconducting qubits”. In: *Science* 360.6385 (2018), pp. 195–199. ISSN: 0036-8075. DOI: 10.1126/science.aao4309.
- [87] C. Neill et al. “Ergodic dynamics and thermalization in an isolated quantum system”. In: *Nature Physics* 12 (July 2016), p. 1037.
- [88] Stefan Nimmrichter, Klaus Hornberger, and Klemens Hammerer. “Optomechanical Sensing of Spontaneous Wave-Function Collapse”. In: *Phys. Rev. Lett.* 113 (2 July 2014), p. 020405. DOI: 10.1103/PhysRevLett.113.020405. URL: <https://link.aps.org/doi/10.1103/PhysRevLett.113.020405>.
- [89] A. D. O’Connell et al. “Quantum ground state and single-phonon control of a mechanical resonator”. In: *Nature* 464 (Mar. 2010), p. 697. ISSN: 1476-4687. URL: <http://dx.doi.org/10.1038/nature08967>.

- [90] A. D. O’Connell et al. “Quantum ground state and single-phonon control of a mechanical resonator”. In: *Nature* 464 (Mar. 2010), p. 697.
- [91] Gottlieb S. Oehrlein. “Dry Etching Damage of Silicon: A Review”. In: *Materials Science and Engineering: B* 4 (Oct. 1989), pp. 441–450. DOI: 10.1016/0921-5107(89)90284-5.
- [92] Hanhee Paik et al. “Observation of High Coherence in Josephson Junction Qubits Measured in a Three-Dimensional Circuit QED Architecture”. In: *Phys. Rev. Lett.* 107 (24 Dec. 2011), p. 240501. DOI: 10.1103/PhysRevLett.107.240501.
- [93] Vittorio Peano et al. “Topological quantum fluctuations and travelling wave amplifiers”. In: *arXiv:1604.04179* (Apr. 2016).
- [94] V. Peano et al. “Topological phase transitions and chiral inelastic transport induced by the squeezing of light”. In: *Nat. Commun.* 7 (2016), p. 10779.
- [95] V. Peano et al. “Topological Phases of Sound and Light”. In: *Phys. Rev. X* 5 (2015), p. 031011.
- [96] W. A. Phillips. “Two-level states in glasses”. In: *Rep. Prog. Phys.* 50 (12 Dec. 1987), pp. 1657–1708. DOI: 10.1088/0034-4885/50/12/003.
- [97] G. Piazza. *Piezoelectric Aluminum Nitride Vibrating RF MEMS for Radio Front-end Technology*. University of California, Berkeley, 2005. URL: <https://books.google.com/books?id=ej1NwAACAAJ>.
- [98] J.-M. Pirkkalainen et al. “Hybrid circuit cavity quantum electrodynamics with a micromechanical resonator”. In: *Nature* 494 (Feb. 2013), pp. 211–215. DOI: 10.1038/nature11821.
- [99] Tomás Ramos et al. “Nonlinear Quantum Optomechanics via Individual Intrinsic Two-Level Defects”. In: *Phys. Rev. Lett.* 110 (May 2013), p. 193602. DOI: 10.1103/PhysRevLett.110.193602.
- [100] M. W. Ray et al. “Observation of Dirac monopoles in a synthetic magnetic field”. In: *Nature* 505 (2014), p. 657.
- [101] M.C. Rechtsman et al. “Photonic Floquet topological insulators”. In: *Nature* 496 (2013), p. 196.
- [102] Ji-Gang Ren et al. “Ground-to-satellite quantum teleportation”. In: *Nature* 549 (Aug. 2017), p. 70. URL: <https://doi.org/10.1038/nature23675>.
- [103] Jessie Rosenberg, Qiang Lin, and Oskar Painter. “Static and dynamic wavelength routing via the gradient optical force”. In: *Nature Photon.* 3 (Aug. 2009), pp. 478–483.
- [104] K. Rostem, P. J. de Visser, and E. J. Wollack. “Enhanced quasiparticle lifetime in a superconductor by selective blocking of recombination phonons with a phononic crystal”. In: *Phys. Rev. B* 98 (1 July 2018), p. 014522. DOI: 10.1103/PhysRevB.98.014522.

- [105] P. Roushan et al. “Chiral groundstate currents of interacting photons in a synthetic magnetic field”. In: (2016), arXiv:1606.00077.
- [106] P. Roushan et al. “Chiral ground-state currents of interacting photons in a synthetic magnetic field”. In: *Nature Physics* 13 (Oct. 2016), p. 146. URL: <https://doi.org/10.1038/nphys3930>.
- [107] Freek Ruesink et al. “Nonreciprocity and magnetic-free isolation based on optomechanical interactions”. In: *arXiv:1607.07180* (July 2016).
- [108] S. Sadat-Saleh et al. “Tailoring simultaneous photonic and phononic band gaps”. In: *J. Appl. Phys.* 106 (2009), p. 074912.
- [109] A. H. Safavi-Naeini and O. Painter. “Design of optomechanical cavities and waveguides on a simultaneous bandgap phononic-photonic crystal slab”. In: *Opt. Express* 18 (2010), pp. 14926–14943.
- [110] Amir H. Safavi-Naeini et al. “Electromagnetically induced transparency and slow light with optomechanics”. In: *Nature* 472 (2011), pp. 69–73. DOI: [10.1038/nature09933](https://doi.org/10.1038/nature09933).
- [111] Amir H. Safavi-Naeini et al. “Two-Dimensional Phononic-Photonic Band Gap Optomechanical Crystal Cavity”. In: *Phys. Rev. Lett.* 112 (15 Apr. 2014), p. 153603. DOI: [10.1103/PhysRevLett.112.153603](https://doi.org/10.1103/PhysRevLett.112.153603).
- [112] Y. Sato et al. “Strong coupling between distant photonic nanocavities and its dynamic control”. In: *Nature Photon.* 6 (2012), pp. 56–61.
- [113] K. J. Satzinger et al. “Quantum control of surface acoustic wave phonons”. In: *arXiv:1804.07308* (Apr. 2018).
- [114] M. Schmidt et al. “Optomechanical creation of magnetic fields for photons on a lattice”. In: *Optica* 2 (2015), pp. 635–641.
- [115] Eyob A. Sete, John M. Martinis, and Alexander N. Korotkov. “Quantum theory of a bandpass Purcell filter for qubit readout”. In: *PRA* 92.1 (July 2015), p. 012325. URL: <https://link.aps.org/doi/10.1103/PhysRevA.92.012325>.
- [116] Z. Shen et al. “Experimental realization of optomechanically induced non-reciprocity”. In: *arXiv:1604.02297* (2016).
- [117] Huan-Yu Shih et al. “Low-temperature atomic layer epitaxy of AlN ultrathin films by layer-by-layer, in-situ atomic layer annealing”. In: *Scientific Reports* 7 (Jan. 2017), p. 39717. URL: <https://doi.org/10.1038/srep39717>.
- [118] K.M. Sliwa et al. “Reconfigurable Josephson Circulator/Directional Amplifier”. In: *Phys. Rev. X* 5 (2015), p. 041020.
- [119] Young-Ik Sohn et al. “Controlling the coherence of a diamond spin qubit through its strain environment”. In: *Nat. Commun.* 9 (1 May 2018), p. 2012. DOI: [10.1038/s41467-018-04340-3](https://doi.org/10.1038/s41467-018-04340-3).

- [120] Xiufeng Song, Renli Fu, and Hong He. “Frequency effects on the dielectric properties of AlN film deposited by radio frequency reactive magnetron sputtering”. In: *Microelectronic Engineering* 86.11 (Nov. 2009), pp. 2217–2221. ISSN: 0167-9317. URL: <http://www.sciencedirect.com/science/article/pii/S0167931709002159>.
- [121] G. P. Srivastava. *The Physics of Phonons*. Taylor & Francis Group, 1990. ISBN: 978-0852741535.
- [122] S. Strite and H. Morkoç. “GaN, AlN, and InN: A review”. In: *Journal of Vacuum Science & Technology B: Microelectronics and Nanometer Structures Processing, Measurement, and Phenomena* 10.4 (Dec. 2018), pp. 1237–1266. ISSN: 1071-1023. DOI: 10.1116/1.585897. URL: <https://avs.scitation.org/doi/abs/10.1116/1.585897>.
- [123] S. Tadigadapa and K. Mateti. “Piezoelectric MEMS sensors: state-of-the-art and perspectives”. In: *Measurement Science and Technology* 20.9 (2009), p. 092001. ISSN: 0957-0233. URL: <http://stacks.iop.org/0957-0233/20/i=9/a=092001>.
- [124] Hengxin Tan et al. “First-principles studies of the local structure and relaxor behavior of $\text{Pb}(\text{Mg}_{1/3}\text{Nb}_{2/3})\text{O}_3$ – PbTiO_3 -derived ferroelectric perovskite solid solutions”. In: *Phys. Rev. B* 97.17 (May 2018), p. 174101. URL: <https://link.aps.org/doi/10.1103/PhysRevB.97.174101>.
- [125] The LIGO Scientific Collaboration. “A gravitational wave observatory operating beyond the quantum shot-noise limit”. In: *Nature Phys.* 7 (2011), pp. 962–965.
- [126] L.D. Tzuang et al. “Nonreciprocal phase shift induced by an effective magnetic flux for light”. In: *Nature Photons* 8 (2014), p. 701.
- [127] R.O. Umucalılar and I. Carusotto. “Artificial gauge field for photons in coupled cavity arrays”. In: *Phys. Rev. A* 84 (2011), p. 043804.
- [128] Quirin P. Unterreithmeier, Thomas Faust, and Jorg P. Kotthaus. “Damping of Nanomechanical Resonators”. In: *Phys. Rev. Lett.* 105 (July 2010), p. 027205.
- [129] Amit Vainsencher et al. “Bi-directional conversion between microwave and optical frequencies in a piezoelectric optomechanical device”. In: *Appl. Phys. Lett.* 109.3 (July 2016), p. 033107. ISSN: 0003-6951. DOI: 10.1063/1.4955408. URL: <https://doi.org/10.1063/1.4955408>.
- [130] Wolfram Wersing Walter. Heywang Karl. Lubitz, ed. *Piezoelectricity: Evolution and Future of a Technology*. Springer-Verlag Berlin Heidelberg, Nov. 3, 2008. ISBN: 978-3-540-68680-4.
- [131] Stefan Walter and Florian Marquardt. “Dynamical Gauge Fields in Optomechanics”. In: *arXiv:1510.06754* (Oct. 2015).

- [132] Zheqi Wang et al. “Optical Nonreciprocity in Asymmetric Optomechanical Couplers”. In: *Scientific Reports* 5 (Mar. 2015), p. 8657.
- [133] T. O. Woodruff and H. Ehrenreich. “Absorption of Sound in Insulators”. In: *Phys. Rev.* 123 (5 Sept. 1961), pp. 1553–1559. DOI: 10.1103/PhysRev.123.1553.
- [134] A. Barg Y. Tsaturyan, E. S. Polzik, and A. Schliesser. “Ultracoherent nanomechanical resonators via soft clamping and dissipation dilution”. In: *Nature Nanotech.* 12 (June 2017), pp. 776–783. DOI: 10.1038/nnano.2017.101.
- [135] Norikuni Yabumoto et al. “Surface Damage on Si Substrates Caused by Reactive Sputter Etching”. In: *Jpn. J. Appl. Phys.* 20 (5 May 1981), pp. 893–900. DOI: 10.1143/JJAP.20.893.
- [136] T. Yamada, N. Niizeki, and H. Toyoda. “Piezoelectric and Elastic Properties of Lithium Niobate Single Crystals”. In: *Japanese Journal of Applied Physics* 6 (Feb. 1967), p. 151. DOI: 10.1143/JJAP.6.151.
- [137] E. Yarar et al. “Low temperature aluminum nitride thin films for sensory applications”. In: *AIP Advances* 6.7 (Dec. 2016), p. 075115. DOI: 10.1063/1.4959895. URL: <https://doi.org/10.1063/1.4959895>.
- [138] P.-L. Yu et al. “A phononic bandgap shield for high-Q membrane microresonators”. In: *App. Phys. Lett.* 104 (Jan. 2014), p. 023510.
- [139] Junshan Zhang et al. “Deep Reactive Ion Etching of PZT Ceramics and PMN-PT Single Crystals for High Frequency Ultrasound Transducers”. In: *Ceramics International* 41 (Apr. 2015).
- [140] J. Zhang et al. “Observation of a discrete time crystal”. In: *Nature* 543 (Mar. 2017), p. 217. URL: <https://doi.org/10.1038/nature21413>.

Appendix A

DETAILS ON DESIGNING ULTRA-HIGH COHERENCE MICROWAVE PHONONIC QUANTUM RANDOM ACCESS MEMORY

A.1 Finite-element Simulations and Device Parameters

Due to the complexity of piezoelectric field distributions for different piezoacoustic modes, analytic computation of the coupling strength between different modes and the electric circuit is in general not feasible. Finite-element-method (FEM) numerical simulations can be very efficient in solving frequency-domain responses of the structure. Sec. A.1.1 discusses a method utilizing field overlap integral [53] to calculate the piezoelectric coupling rate of a piezoacoustic eigenmode to an electromagnetic mode in an external electric circuit. Sec. A.1.2 introduces another method to synthesis an equivalent circuit and calculate its piezoelectric coupling rate to the rest of the microwave circuit. This method relies on the simulated frequency-domain admittance response of a piezoelectric system.

A.1.1 Coupling Rate Via Field Overlap Integral

Due to the broken central symmetry in a piezoelectric material crystal structure, deformation will significantly impact its charge distribution, leading to electric polarization. The mechanically induced polarization density in the dielectric can be described as (A.1),

$$\vec{P}_m = [d]\vec{\sigma}. \quad (\text{A.1})$$

where $[d]$ is a 3×6 matrix called piezoelectric coupling coefficient matrix and $\vec{\sigma}$ is the mechanical stress field written as a vector of 6 elements. External electric field (\vec{E}_e) can also generate trivial linear dielectric polarization field expressed in (A.2),

$$\vec{P}_e = ([\epsilon] - \epsilon_0 I)\vec{E}_e, \quad (\text{A.2})$$

with permittivity matrix, $[\epsilon]$, and identity matrix, I . As a result, the total displacement field generated by a given stress field and an external electric field is (A.3). Similarly, the strain field can also have an external electric field contribution due to

the inverse coupling matrix as in the second term of (A.4).

$$\vec{D} = [d]\vec{\sigma} + [\epsilon]\vec{E}_e \quad (\text{A.3})$$

$$\vec{s} = [c]\vec{\sigma} + [d]'\vec{E}_e \quad (\text{A.4})$$

They form a set of coupled equations that determine the mechanical and electrical responses of the piezoelectric material. In weak coupling limit, energy transfer between external electric field \vec{E}_e and stress field $\vec{\sigma}$ can be understood with perturbation theory leading to the overlap integral (6.12) discussed in the main text.

A.1.2 Coupling Strength via Circuit Equivalence

Piezoelectric devices have been widely used in integrated microwave circuits as compact filters due to their electrical response. For an electric circuit, the piezoacoustic resonator can be equivalently viewed as a lump electric resonator with effective inductance L_{pa} and capacitance C_{pa} [130, 90, 8]. The simulated admittance of the piezoelectric mode of interest is shown in Fig. A.1. There are different ways of synthesizing an equivalent circuit corresponding to a simulated admittance. The most commonly used is a serial circuit model where the piezoacoustic mode is mapped into serially connected motional inductance L_{pa} and motional capacitance C_{pa} . The mechanical mode corresponds to an admittance pole. In the serial equivalent circuit model, the effective inductance can be intuitively understood as a representation of a mechanical resonator mass inertia. This equivalent serial LC resonator is further parallelly connected to the linear capacitance C_{g} , which corresponds to the motion independent capacitance between the electrodes. It represents the low-frequency electric response of the system. A fit to the admittance as shown in Fig. A.1 extracts the effective inductance and capacitance.

The equivalent model can be used to determine the coupling rate (J_{p}) between the piezoacoustic resonator with frequency ω_{m} and a resonant electric resonator having total capacitance $C_{\mu} = (C_{\text{l}} + C_{\text{g}})$ as:

$$J_{\text{p}} = \frac{\omega_{\text{m}}}{2} \sqrt{\frac{C_{\text{pa}}}{(C_{\mu} + C_{\text{pa}})C_{\text{pa}}}}. \quad (\text{A.5})$$

Furthermore, the equivalent circuit model can be readily used to extract the piezoacoustic resonator's external coupling rate, $\kappa_{\text{ex}} = Z_0/L_{\text{pa}}$, to a microwave transmission line by comparing (A.6) and (A.7) for transmission line coupled to an one-side res-

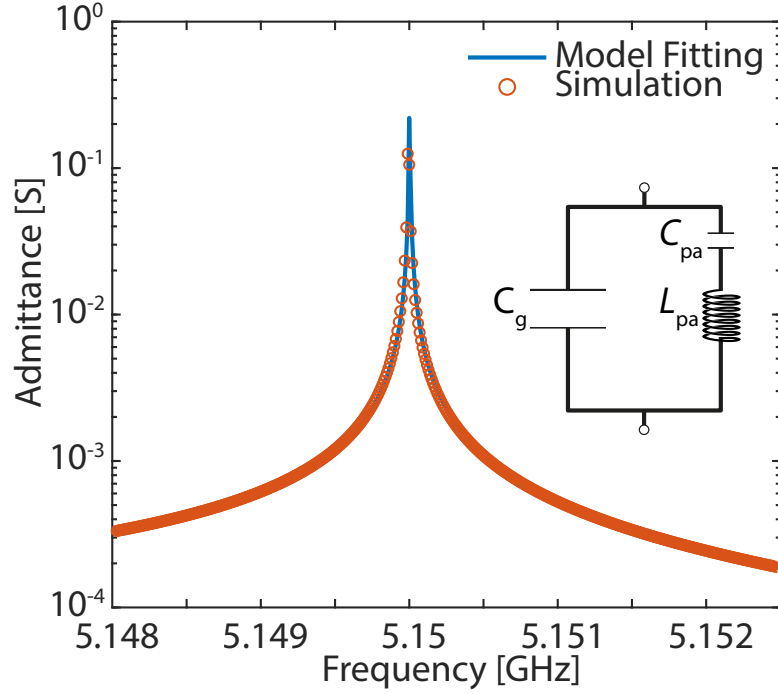


Figure A.1: The admittance of the proposed piezoelectric resonator in the intermediate system. The simulated data is fitted with a serial resonator model that is illustrated as an inset. The equivalent circuit variables are defined in the inset as dielectric linear capacitance C_g , the motional inductance L_{pa} and capacitance C_{pa} . The piezoacoustic resonance is $\omega_{pa} = \frac{1}{\sqrt{L_{pa}C_{pa}}}$.

onator.

$$S_{11} = \frac{Z_{pa} - Z_0}{Z_{pa} + Z_0} \quad (\text{A.6})$$

$$S_{11} = \frac{(\kappa_0 - \kappa_{ex})/2 - i(\omega - \omega_{pa})}{(\kappa_0 + \kappa_{ex})/2 - i(\omega - \omega_{pa})} \quad (\text{A.7})$$

where the $Z_{pa} = 1/Y_{pa}$ is the frequency-dependent impedance of the piezoelectric resonator and Z_0 is the characteristic impedance of the transmission line used to couple the mechanical resonator. To have a better comparison with the single side coupled cavity response (A.7) for extracting corresponding parameters, an arbitrarily small resistance, R , serially connected with the serial-LC resonator can be assumed. It is straightforward to show that $\kappa_{ex}/2\pi = 57$ kHz for direct transmission line coupling to the mechanical resonator assuming $Z_0 = 50 \Omega$.

A.2 Derivation of Multi-channel Virtual Coupling

In general, the coupling between a cavity and a qubit via multiple intermediate levels can be written in the following Hamiltonian (A.8) and (A.9),

$$\hat{H}_{\text{sys}} = \hbar\omega_m \hat{a}^\dagger \hat{a} + \hbar\omega_q \frac{\hat{\sigma}_z}{2} + \sum_k \hbar\omega_k \hat{b}_k^\dagger \hat{b}_k + \hat{H}_{\text{int}}, \quad (\text{A.8})$$

$$\begin{aligned} \hat{H}_{\text{int}} = \sum_k \hbar \left(g_k^* \hat{b}_k^\dagger \hat{a} + g_k \hat{b}_k \hat{a}^\dagger \right) \\ + \hbar \left(J_k^* \hat{b}_k^\dagger \hat{\sigma}_- + J_k \hat{b}_k \hat{\sigma}_+ \right), \end{aligned} \quad (\text{A.9})$$

where all the involved intermediate bosonic levels are labeled as \hat{b}_k in the Hamiltonian. J_k and g_k are coupling of the k -th intermediate level with the qubit and memory cavity respectively.

The four-body dynamics of the system can be simplified by eliminating the intermediate system's degrees of freedom. The first step is to transfer the system in to an approximately diagonalized frame via the unitary transformation (A.10) assuming that $\omega_m \simeq \omega_q$,

$$\hat{U} = \exp \left(\sum_k \frac{\begin{pmatrix} (g_k \hat{a}^\dagger + J_k \hat{\sigma}_+) \hat{b}_k \\ - (g_k^* \hat{a} + J_k^* \hat{\sigma}_-) \hat{b}_k^\dagger \end{pmatrix}}{\omega_m - \omega_k} \right). \quad (\text{A.10})$$

In the dispersive limit where $|\omega_k - \omega_m| \gg |J_k|, |g_k|$, the transformed system Hamiltonian can be simplified after ignoring higher order terms into (A.11),

$$\hat{H}_{\text{eff}} = \hbar\omega'_m \hat{a}^\dagger \hat{a} + \hbar\omega'_q \frac{\hat{\sigma}_z}{2} + \hbar(J_{\text{vc}}^* \hat{a}^\dagger \hat{\sigma}_- + J_{\text{vc}} \hat{a} \hat{\sigma}_+), \quad (\text{A.11})$$

where ω'_m and ω'_q are renormalized frequencies of the two resonant cavities. The frequency shifts are small in this limit and we can always tune the qubit frequency slightly such that $\omega'_m = \omega'_q$. The effective coupling rate, J_{vc} , can be expressed as follows in (A.12),

$$J_{\text{vc}} = \sum_k \frac{g_k^* J_k}{\omega_k - \omega_m}. \quad (\text{A.12})$$

In the case where the intermediate system contains two strongly coupled resonant cavities, the two hybridized levels are symmetric and anti-symmetric superpositions of the two cavity modes. We can analysis the effective dynamics by going into

the frequency-domain considering that diagonalizing the intermediate double cavity first in (6.23) and (6.24) will reveal a correspondence that $g_{\pm} = \pm J_m/\sqrt{2}$ and $J_{\pm} = J_q/\sqrt{2}$ for symmetric (+) and anti-symmetric (-) super-modes. Starting from the four-body system Hamiltonian in (A.13),

$$H_{4-body} = \hbar\omega_m \hat{a}^\dagger \hat{a} + \hbar\omega_q \frac{\hat{\sigma}_z}{2} + \sum_{k=\pm} \hbar\omega_k \hat{b}_k^\dagger \hat{b}_k + \left(\sum_{k=\pm} \hbar \left(g_k^* \hat{b}_k^\dagger \hat{a} + g_k \hat{b}_k \hat{a}^\dagger \right) + \sum_{k=\pm} \hbar \left(J_k^* \hat{b}_k^\dagger \hat{\sigma}_- + J_k \hat{b}_k \hat{\sigma}_+ \right) \right), \quad (\text{A.13})$$

we obtain the following quantum master equations of motion (EOMs) in (A.14)–(A.16).

$$\dot{\hat{\sigma}}_- = -\omega_q i \hat{\sigma}_- - \frac{J_q}{\sqrt{2}} i \hat{b}_+ - \frac{J_q}{\sqrt{2}} i \hat{b}_- \quad (\text{A.14})$$

$$\dot{\hat{a}} = -\omega_m i \hat{a} - \frac{J_m}{\sqrt{2}} i \hat{b}_+ + \frac{J_m}{\sqrt{2}} i \hat{b}_- \quad (\text{A.15})$$

$$\dot{\hat{b}}_{\pm} = -\omega_{\pm} i \hat{b}_{\pm} \mp \frac{J_m}{\sqrt{2}} i \hat{a} - \frac{J_q}{\sqrt{2}} i \hat{\sigma}_- \quad (\text{A.16})$$

The time-domain EOMs can be further Fourier-Transformed into their dual frequency-domain forms as a set of simple linear equations in (A.17)–(A.19).

$$-\omega i \tilde{\sigma}_- = -\omega_q i \tilde{\sigma}_- - \frac{J_q}{\sqrt{2}} i \tilde{b}_+ - \frac{J_q}{\sqrt{2}} i \tilde{b}_- \quad (\text{A.17})$$

$$-\omega i \tilde{a} = -\omega_m i \tilde{a} - \frac{J_m}{\sqrt{2}} i \tilde{b}_+ + \frac{J_m}{\sqrt{2}} i \tilde{b}_- \quad (\text{A.18})$$

$$-\omega i \tilde{b}_{\pm} = -\omega_{\pm} i \tilde{b}_{\pm} \mp \frac{J_m}{\sqrt{2}} i \tilde{a} - \frac{J_q}{\sqrt{2}} i \tilde{\sigma}_- \quad (\text{A.19})$$

To eliminate the detuned intermediate system degrees of freedom and extract the two-body dynamics between the near resonant resonant qubit and memory, we can solve for the intermediate system's \tilde{b}_{\pm} as functions of $\tilde{\sigma}_-$ and \tilde{a} in (A.20).

$$-\omega i \tilde{b}_{\pm} = \frac{-\frac{J_q}{\sqrt{2}} \tilde{\sigma}_- \mp \frac{J_m}{\sqrt{2}} \tilde{a}}{\omega_{\pm} - \omega} \quad (\text{A.20})$$

Plugging the solution back into (A.17) and (A.18), we can solve for the $\tilde{\sigma}_-$ and \tilde{a} as follows in (A.21) and (A.22), respectively.

$$\begin{aligned}
-\omega i \tilde{\sigma}_- &= - \left(\omega_{\text{q}}^- - \frac{J_{\text{q}}^2}{2} \left(\frac{1}{\omega_+ - \omega} + \frac{1}{\omega_- - \omega} \right) \right) i \tilde{\sigma}_- \\
&\quad - \frac{J_{\text{q}} J_{\text{m}}}{2} i \left(\frac{1}{\omega_- - \omega} - \frac{1}{\omega_+ - \omega} \right) \tilde{a}
\end{aligned} \tag{A.21}$$

$$\begin{aligned}
-\omega i \tilde{a} &= - \left(\omega_{\text{m}}^- - \frac{J_{\text{m}}^2}{2} \left(\frac{1}{\omega_+ - \omega} + \frac{1}{\omega_- - \omega} \right) \right) i \tilde{a} \\
&\quad - \frac{J_{\text{q}} J_{\text{m}}}{2} i \left(\frac{1}{\omega_- - \omega} - \frac{1}{\omega_+ - \omega} \right) \tilde{\sigma}_-
\end{aligned} \tag{A.22}$$

The effective virtual coupling rate (J_{vc}) and renormalized effective qubit and memory frequencies (ω'_{q} and ω'_{m}) can be extracted from the above solutions and arrive at (A.23)–(A.24) shown below.

$$J_{\text{vc}} = \frac{J_{\text{q}} J_{\text{m}}}{2} \left(\frac{1}{\omega_- - \omega_{\text{m}}} - \frac{1}{\omega_+ - \omega_{\text{m}}} \right) \tag{A.23}$$

$$\omega'_{\text{q}} = \omega_{\text{q}} - \frac{J_{\text{q}}^2}{2} \left(\frac{1}{\omega_+ - \omega_{\text{q}}} + \frac{1}{\omega_- - \omega_{\text{q}}} \right) \tag{A.24}$$

$$\omega'_{\text{m}} = \omega_{\text{m}} - \frac{J_{\text{m}}^2}{2} \left(\frac{1}{\omega_+ - \omega_{\text{m}}} + \frac{1}{\omega_- - \omega_{\text{m}}} \right) \tag{A.25}$$

The frequency shifts in (A.25) and (A.24) are proportional to J_{m}^2 and J_{q}^2 respectively. The qubit bare frequency, ω_{q} (Φ_{ex}), can always be tuned by external flux, Φ_{ex} , to match effective frequencies of the qubit and memory ($\omega'_{\text{q}} = \omega'_{\text{m}}$). Thus, a high state-transfer fidelity swap-state can always be reached. AQE optimization for a given Δ_{pa} which is defined by design and fabrication can always be done in an experiment by adjusting J_{q} using external magnetic flux, Φ_{g} , through the tunable coupler.

A.3 Idle-State Noise Propagation and Decoherence Suppression

To study the additional decoherence of the ultra high-Q defect phononic cavity due to its mechanical coupling (J_{m}) to the lossy intermediate system, a simplified model of three coupled cavities is studied here. Cavity-A₁ ($\hat{a}_1, \hat{a}_1^\dagger$) and Cavity-A₂ ($\hat{a}_2, \hat{a}_2^\dagger$) are the lossy cavities belonging to the intermediate system. The Cavity-B (\hat{b}, \hat{b}^\dagger) corresponds to the low loss mechanical cavity. The system Hamiltonian can be written as (A.26),

$$\hat{H} = \hbar \omega_{\text{a}} \hat{a}_1^\dagger \hat{a}_1 + \hbar \omega_{\text{a}} \hat{a}_2^\dagger \hat{a}_2 + \hbar \omega_{\text{b}} \hat{b}^\dagger \hat{b} + \hat{H}_{\text{int}}, \tag{A.26}$$

and the interaction part is (A.27),

$$\hat{H}_{\text{int}} = \hbar J_a \left(\hat{a}_1^\dagger \hat{a}_2 + \hat{a}_1 \hat{a}_2^\dagger \right) + \hbar J_b \left(\hat{a}_2^\dagger \hat{b} + \hat{a}_2 \hat{b}^\dagger \right). \quad (\text{A.27})$$

The dynamics of the system can be derived from solving the system master equation in the frequency-domain. The equation of motion (EOM) for the system can be written as (A.28) - (A.30).

$$\dot{\hat{a}}_1 = -i(\omega_{a1} - \frac{\gamma_{a1}}{2}i)\hat{a}_1 - iJ_a\hat{a}_2 + \sqrt{\gamma_{a1}}\hat{a}_{1e} \quad (\text{A.28})$$

$$\dot{\hat{a}}_2 = -i(\omega_{a2} - \frac{\gamma_{a2}}{2}i)\hat{a}_2 - iJ_a\hat{a}_1 - iJ_b\hat{b} + \sqrt{\gamma_{a2}}\hat{a}_{2e} \quad (\text{A.29})$$

$$\dot{\hat{b}} = -i\omega_b\hat{b} - iJ_b\hat{a}_2 \quad (\text{A.30})$$

where the \hat{a}_{1e} and \hat{a}_{2e} represent the continuum environmental bath modes and they are normalized into photon number flux.

They can be transformed into the frequency-domain as (A.31) - (A.33)

$$-i\omega\tilde{a}_1 = -i(\omega_{a1} - \frac{\gamma_{a1}}{2}i)\tilde{a}_1 - iJ_a\tilde{a}_2 + \sqrt{\gamma_{a1}}\tilde{a}_{1e} \quad (\text{A.31})$$

$$\begin{aligned} -i\omega\tilde{a}_2 &= -i(\omega_{a2} - \frac{\gamma_{a2}}{2}i)\tilde{a}_2 - iJ_a\tilde{a}_1 \\ &\quad - iJ_b\tilde{b} + \sqrt{\gamma_{a2}}\tilde{a}_{2e} \end{aligned} \quad (\text{A.32})$$

$$-i\omega\tilde{b} = -i\omega_b\tilde{b} - iJ_b\tilde{a}_2 \quad (\text{A.33})$$

To understand how the decoherence noises in the lossy cavities (A_1 and A_2) perturb the high-Q mode (B), the noise spectral power density of Cavity- A_2 when it is decoupled from the high-Q mode needs to be calculated as (A.34).

$$S_{\hat{a}_2\hat{a}_2}[\omega] = \int \left\langle \tilde{a}_2^\dagger[\omega]\tilde{a}_2[\omega] \right\rangle d\omega' \quad (\text{A.34})$$

The average is over the state of the lossy cavities and their environment where $\tilde{a}_2^\dagger[\omega] = (\tilde{a}_2[-\omega])^\dagger$. The environment noise on A_1 and A_2 has the following properties:

$$\langle \tilde{a}_{1e}^\dagger[\omega]\tilde{a}_{1e}[\omega'] \rangle = \langle n_1 \rangle \delta(\omega + \omega') \quad (\text{A.35})$$

$$\langle \tilde{a}_{2e}^\dagger[\omega]\tilde{a}_{2e}[\omega'] \rangle = \langle n_2 \rangle \delta(\omega + \omega') \quad (\text{A.36})$$

$$\langle \tilde{a}_{1e}[\omega]\tilde{a}_{1e}^\dagger[\omega'] \rangle = (\langle n_1 \rangle + 1)\delta(\omega + \omega') \quad (\text{A.37})$$

$$\langle \tilde{a}_{2e}[\omega]\tilde{a}_{2e}^\dagger[\omega'] \rangle = (\langle n_2 \rangle + 1)\delta(\omega + \omega') \quad (\text{A.38})$$

where $\langle n_1 \rangle$ and $\langle n_2 \rangle$ are equilibrium bath mode occupations at the given frequency, ω .

Combining the results from (A.31)–(A.38) and in the limit where $J_b = 0$, it is straightforward to show the spectral power densities of the Cavity-A₂ are (A.39),

$$S_{\hat{a}_2 \hat{a}_2}[\omega] = \frac{\langle n_2 \rangle \gamma_{a2} + \frac{\langle n_1 \rangle J_b^2 \gamma_{a1}}{(\omega_{a1} + \omega)^2 + \frac{\gamma_{a1}^2}{4}}}{\left(\omega_{a2} + \omega - \frac{J_b^2 (\omega_{a1} + \omega)}{(\omega_{a1} + \omega)^2 + \frac{\gamma_{a1}^2}{4}} \right)^2 + \left(\frac{\gamma_{a2}}{2} + \frac{J_b^2 \gamma_{a1}}{(\omega_{a1} + \omega)^2 + \frac{\gamma_{a1}^2}{4}} \right)^2}, \quad (\text{A.39})$$

and its reversed dual in (A.40),

$$S_{\hat{a}_2^\dagger \hat{a}_2^\dagger}[\omega] = \frac{\langle n_2 \rangle \gamma_{a2} + \frac{\langle n_1 \rangle J_b^2 \gamma_{a1}}{(\omega_{a1} - \omega)^2 + \frac{\gamma_{a1}^2}{4}}}{\left(\omega_{a2} - \omega - \frac{J_b^2 (\omega_{a1} - \omega)}{(\omega_{a1} - \omega)^2 + \frac{\gamma_{a1}^2}{4}} \right)^2 + \left(\frac{\gamma_{a2}}{2} + \frac{J_b^2 \gamma_{a1}}{(\omega_{a1} - \omega)^2 + \frac{\gamma_{a1}^2}{4}} \right)^2}. \quad (\text{A.40})$$

Below 10 mK, $\langle n_1 \rangle$ and $\langle n_2 \rangle \sim 0$ for the 5 GHz mode. As a result, the Cavity-B will only see the noise in $S_{\hat{a}_2^\dagger \hat{a}_2^\dagger}$ and the additional decay rate, γ_{ab} , is (A.41),

$$\begin{aligned} \gamma_{ab} &= J_b^2 (S_{\hat{a}_2^\dagger \hat{a}_2^\dagger}[\omega_b] - S_{\hat{a}_2 \hat{a}_2}[-\omega_b]) \\ &\simeq J_b^2 S_{\hat{a}_2^\dagger \hat{a}_2^\dagger}[\omega_b] \end{aligned} \quad (\text{A.41})$$

Appendix B

EFFICIENT OPTIC-MICROWAVE QUANTUM
TRANSDUCTION VIA ACOUSTIC CHANNEL

Quantum communication and distributed quantum system over a vast distance have been recently attracted significant amount of attention among the quantum science and technology community due to both its potential in constructing a secure communication network and realizing a quantum Internet between quantum computers. Previous work in demonstrating successful intercontinental quantum key distribution was based on free space optical channel between a satellite and ground stations. However, scalability of this approach is limited due to the high costs of constructing a new constellation of quantum satellites and compatible ground stations. Another approach more feasible for economically scaling up the quantum communication network is based on quantum repeaters and routers that can be used for upgrading existing telecommunication fiber-optical network to be compatible with quantum communication. Quantum repeaters and routers can be realized in various architectures. One candidate requires the incorporation of superconducting quantum circuit that is efficient in carrying out deterministic quantum operations which can enable high speed long distance quantum communication in an extended fiber-optical network. This implementation requires a high efficiency coherent transduction between a telecommunication band photon in the optical fiber and a microwave frequency photon in the superconducting circuit. A transducer with unity efficiency can be realized with an optomechanical crystal coupled to a microwave circuit. In the rest of this section, we will present the analysis of the proposed optomechanical crystal quantum transducer.

Fig. B.1 shows the scheme we have for the transduction. Microwave frequency mechanical mode of the optomechanical crystal is coupled to a tunable superconducting microwave resonator with rate J_{pa} . The optical cavity is coupled to the input fiber with coupling rate κ_{oe} and it suffers from intrinsic loss to environment with rate κ_{oi} . The superconducting microwave resonator is coupled to a transmission line with rate $\kappa_{\mu e}$ and it has intrinsic loss rate $\kappa_{\mu i}$ to the environment. The system Hamiltonian for the open quantum system can be written as (B.1)-(B.6). The intrinsic loss channels will introduce environmental noises ($a_{in}^n, b_{in}^n, c_{in}^n$) into the system along with signals ($a_{in,out}$ and $c_{in,out}$) coupled into the system via external coupling channels to

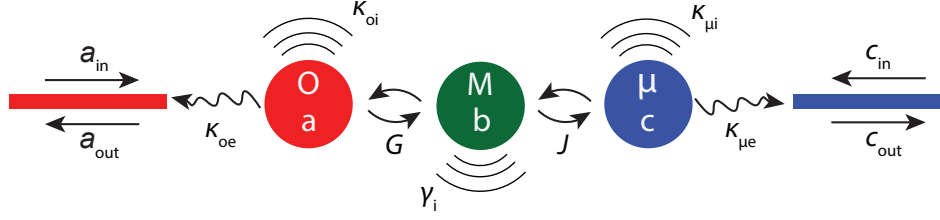


Figure B.1: The red mode on the left is the optical cavity mode that is dispersively coupled to the mechanical mode (green) via the optomechanical coupling. The mechanical mode (green) is strongly resonantly coupled to a tunable superconducting microwave resonator/qubit (blue) in a single photon level.

the fiber and superconducting transmission line.

$$H = H_0 + H_{\text{Drive}} + H_{\text{Signal}} + H_{\text{Noise}} \quad (\text{B.1})$$

$$H_0 = \hbar(\omega_o - \frac{\kappa_o}{2}i)\hat{a}^\dagger\hat{a} + \hbar(\omega_m - \frac{\gamma}{2}i)\hat{b}^\dagger\hat{b} + \hbar(\omega_\mu - \frac{\kappa_\mu}{2}i)\hat{c}^\dagger\hat{c} \quad (\text{B.2})$$

$$H_{\text{Int}} = \hbar g_0 \hat{a}^\dagger \hat{a} (\hat{b}^\dagger + \hat{b}) \quad (\text{B.3})$$

$$H_{\text{Drive}} = -\hbar\sqrt{\kappa_{oe}}i(\alpha_{\text{in}}^*(t)\hat{a} + \alpha_{\text{in}}(t)\hat{a}^\dagger) \quad (\text{B.4})$$

$$H_{\text{Signal}} = -\hbar\sqrt{\kappa_{oe}}i(\hat{a}_{\text{in}}^\dagger\hat{a} + \hat{a}_{\text{in}}\hat{a}^\dagger) - \hbar\sqrt{\kappa_{\mu e}}i(\hat{c}_{\text{in}}^\dagger\hat{c} + \hat{c}_{\text{in}}\hat{c}^\dagger) \quad (\text{B.5})$$

$$H_{\text{Noise}} = -\hbar\sqrt{\kappa_{oi}}i(\hat{a}_n^\dagger\hat{a} + \hat{a}_n\hat{a}^\dagger) - \hbar\sqrt{\gamma}i(\hat{b}_n^\dagger\hat{b} + \hat{b}_n\hat{b}^\dagger) - \hbar\sqrt{\kappa_{\mu i}}i(\hat{c}_n^\dagger\hat{c} + \hat{c}_n\hat{c}^\dagger) \quad (\text{B.6})$$

where $\alpha(t) = \alpha_0 \exp(-\omega_d t i)$ is the optical pumping field at ω_d . Taking the time dependant unitary transformation to a rotating frame with the driving field shown in $\hat{U} = \exp(-\omega_d \hat{a}^\dagger \hat{a} t i)$ and then linearize the Hamiltonian using $\hat{a} = \bar{a} + \delta \hat{a}$ with coherent cavity amplitude \bar{a} , we can obtain the standard optomechanical interaction Hamiltonian after rotation-wave-approximation assuming $\Delta_o = \omega_o - \omega_d > 0$

$$H' = H'_0 + H'_{\text{Signal}} + H'_{\text{Noise}} \quad (\text{B.7})$$

$$H'_0 = \hbar(\Delta_o - \frac{\kappa_o}{2}i)\hat{a}^\dagger\hat{a} + \hbar(\omega_m - \frac{\gamma}{2}i)\hat{b}^\dagger\hat{b} + \hbar(\omega_\mu - \frac{\kappa_\mu}{2}i)\hat{c}^\dagger\hat{c} \quad (\text{B.8})$$

$$H'_{\text{Int}} = \hbar G(\hat{b}^\dagger\hat{a} + \hat{b}\hat{a}^\dagger) \quad (\text{B.9})$$

$$H'_{\text{Signal}} = -\hbar\sqrt{\kappa_{oe}}i(\hat{a}_{\text{in}}^\dagger\hat{a} + \hat{a}_{\text{in}}\hat{a}^\dagger) - \hbar\sqrt{\kappa_{\mu e}}i(\hat{c}_{\text{in}}^\dagger\hat{c} + \hat{c}_{\text{in}}\hat{c}^\dagger) \quad (\text{B.10})$$

$$H'_{\text{Noise}} = -\hbar\sqrt{\kappa_{oi}}i(\hat{a}_n^\dagger\hat{a} + \hat{a}_n\hat{a}^\dagger) - \hbar\sqrt{\gamma}i(\hat{b}_n^\dagger\hat{b} + \hat{b}_n\hat{b}^\dagger) - \hbar\sqrt{\kappa_{\mu i}}i(\hat{c}_n^\dagger\hat{c} + \hat{c}_n\hat{c}^\dagger) \quad (\text{B.11})$$

We relabelled $\delta \hat{a} \rightarrow \hat{a}$, $\hat{a}_{\text{in}} \exp((\omega_d t i)) \rightarrow \hat{a}_{\text{in}}$, and $\hat{a}_n \exp((\omega_d t i)) \rightarrow \hat{a}_n$. Define $G = \sqrt{n_c} g_0$ as the optomechanical coupling rate with intra-cavity photon occupancy $n_c = |\bar{a}|^2$.

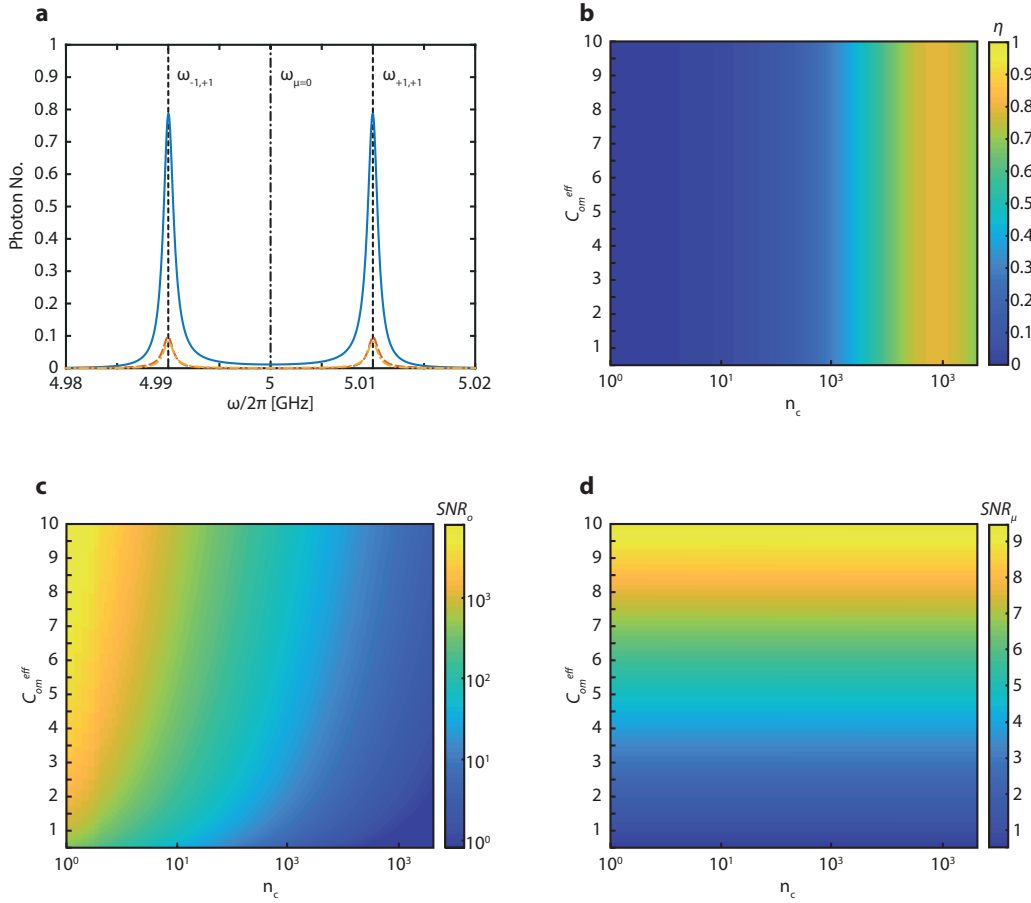


Figure B.2: **a**, the transduction number efficiency (η) as a function of signal frequency (ω) with typical system parameters with a high power optical drive leading to an intra-cavity photon number $n_c \approx 1000$. The dashed black lines are the $\omega = \omega_{\mu=\pm 1, \nu=1}$ and the central dot-dashed line is $\omega = \omega_{\mu=0}$. The blue-solid line is the transduction number efficiency η . The red-dashed line is the noise optical photon number that is transduced into the optical output channel from the microwave photon noise, mechanical phonon bath noise, and optical cavity photon noise. The yellow-dot-dashed line is the noise microwave photon number transduced into the microwave transmission line output from optical photon noise, mechanical phonon bath noise, and microwave cavity photon noise. **b – d** assume that $\omega = \omega_{\mu=\pm 1, \nu=1}$ which leads to the largest transduction number efficiency for different effective optomechanical cooperativity $C_{\text{om}}^{\text{eff}}$ and intra-cavity photon number n_c driven by the strong detuned pump laser. Laser heating effect leading to the elevated phonon number and acoustic damping rate is taken into consideration with the heating curves extracted from experimental data in [Hengjiang2019]. **b**, the transduction number efficiency as a function of effective optomechanical cooperativity ($C_{\text{om}}^{\text{eff}}$) and pump intra-cavity photon number (n_c) in the optomechanical cavity. **c**, the microwave-to-optics transduction signal-to-noise (SNR_o) that is always much larger than unity over a wide range of optomechanical cooperativity and pump laser power. This is because, in this direction of transduction, the important piezoacoustic cooperativity $C_{\mu\text{m}}^{\text{eff}} \gg 1$. **d**, the optics-to-microwave transduction signal-to-noise (SNR_μ). This highlights that $C_{\text{om}}^{\text{eff}} \gg 1$ is necessary to have an ultra-low noise transduction from an optical photon to a microwave photon.

Using relation $\hat{O} = \frac{i}{\hbar} [H', \hat{O}]$

$$\dot{a} = -i(\Delta_o - \frac{\kappa_o}{2}i)\hat{a} - iG\hat{b} + \sqrt{\kappa_{oe}}\hat{a}_{in} + \sqrt{\kappa_{oi}}\hat{a}_n \quad (\text{B.12})$$

$$\dot{b} = -iG\hat{a} - i(\omega_m - \frac{\gamma}{2}i)\hat{b} - iJ\hat{c} + \sqrt{\gamma}\hat{b}_n \quad (\text{B.13})$$

$$\dot{c} = -iJ\hat{b} - i(\omega_\mu - \frac{\kappa_\mu}{2}i)\hat{c} + \sqrt{\kappa_{\mu e}}\hat{c}_{in} + \sqrt{\kappa_{\mu i}}\hat{c}_n \quad (\text{B.14})$$

Transforming the equations into frequency domain.

$$-i\omega\tilde{a} = -i(\Delta_o - \frac{\kappa_o}{2}i)\tilde{a} - iG\tilde{b} + \sqrt{\kappa_{oe}}\tilde{a}_{in} + \sqrt{\kappa_{oi}}\tilde{a}_n \quad (\text{B.15})$$

$$-i\omega\tilde{b} = -iG\tilde{a} - i(\omega_m - \frac{\gamma}{2}i)\tilde{b} - iJ\tilde{c} + \sqrt{\gamma}\tilde{b}_n \quad (\text{B.16})$$

$$-i\omega\tilde{c} = -iJ\tilde{b} - i(\omega_\mu - \frac{\kappa_\mu}{2}i)\tilde{c} + \sqrt{\kappa_{\mu e}}\tilde{c}_{in} + \sqrt{\kappa_{\mu i}}\tilde{c}_n \quad (\text{B.17})$$

Writing this system of equations in matrix form:

$$\begin{bmatrix} \Delta_o - \omega - \frac{\kappa_o}{2}i & G & 0 \\ G & \omega_m - \omega - \frac{\gamma}{2}i & J \\ 0 & J & \omega_\mu - \omega - \frac{\kappa_\mu}{2}i \end{bmatrix} \begin{bmatrix} \tilde{a} \\ \tilde{b} \\ \tilde{c} \end{bmatrix} = -i \begin{bmatrix} \sqrt{\kappa_{oe}}\tilde{a}_{in} + \sqrt{\kappa_{oi}}\tilde{a}_n \\ \sqrt{\gamma}\tilde{b}_n \\ \sqrt{\kappa_{\mu e}}\tilde{c}_{in} + \sqrt{\kappa_{\mu i}}\tilde{c}_n \end{bmatrix} \quad (\text{B.18})$$

Inverting the coefficient matrix on the left, we will obtain

$$\begin{bmatrix} \tilde{a} \\ \tilde{b} \\ \tilde{c} \end{bmatrix} = -iD[T] \begin{bmatrix} \sqrt{\kappa_{oe}}\tilde{a}_{in} + \sqrt{\kappa_{oi}}\tilde{a}_n \\ \sqrt{\gamma}\tilde{b}_n \\ \sqrt{\kappa_{\mu e}}\tilde{c}_{in} + \sqrt{\kappa_{\mu i}}\tilde{c}_n \end{bmatrix} \quad (\text{B.19})$$

$$[T] = \begin{bmatrix} (\omega_m - \omega - \frac{\gamma}{2}i)(\omega_\mu - \omega - \frac{\kappa_\mu}{2}i) - J^2 & -G(\omega_\mu - \omega - \frac{\kappa_\mu}{2}i) & GJ \\ -G(\omega_\mu - \omega - \frac{\kappa_\mu}{2}i) & (\Delta_o - \omega - \frac{\kappa_o}{2}i)(\omega_\mu - \omega - \frac{\kappa_\mu}{2}i) & -J(\Delta_o - \omega - \frac{\kappa_o}{2}i) \\ GJ & -J(\Delta_o - \omega - \frac{\kappa_o}{2}i) & (\Delta_o - \omega - \frac{\kappa_o}{2}i)(\omega_m - \omega - \frac{\gamma}{2}i) \end{bmatrix} \quad (\text{B.20})$$

$$D = \left((\Delta_o - \omega - \frac{\kappa_o}{2}i)(\omega_m - \omega - \frac{\gamma}{2}i)(\omega_\mu - \omega - \frac{\kappa_\mu}{2}i) - G^2(\omega_\mu - \omega - \frac{\kappa_\mu}{2}i) - J^2(\Delta_o - \omega - \frac{\kappa_o}{2}i) \right)^{-1} \quad (\text{B.21})$$

For input signal from microwave transmission line (\tilde{c}_{in}) we can obtain the signal in the optical fiber from input-output theorem.

$$\tilde{a}_{out}^{signal} = D\sqrt{\kappa_{oe}\kappa_{\mu e}}GJ\tilde{c}_{in} \quad (B.22)$$

$$\begin{aligned} \tilde{a}_{out}^{noise} = D & \left(\sqrt{\kappa_{oe}\kappa_{oi}} \left((\omega_m - \omega - \frac{\gamma}{2}i)(\omega_\mu - \omega - \frac{\kappa_\mu}{2}i) - J^2 \right) \tilde{a}_n \right. \\ & \left. - \sqrt{\gamma\kappa_{oe}}G(\omega_\mu - \omega - \frac{\kappa_\mu}{2}i)\tilde{b}_n + GJ\sqrt{\kappa_{\mu i}\kappa_{oe}}\tilde{c}_n \right) \end{aligned} \quad (B.23)$$

The conversion number efficiency η can be shown in (B.24)

$$\eta = \frac{\langle \tilde{a}_{out}^{signal\dagger} \tilde{a}_{out}^{signal} \rangle}{\langle \tilde{c}_{in}^\dagger \tilde{c}_{in} \rangle} = |D\sqrt{\kappa_{oe}\kappa_{\mu e}}GJ|^2 \quad (B.24)$$

$$\begin{aligned} SNR_o &= \frac{\langle \tilde{a}_{out}^{signal\dagger} \tilde{a}_{out}^{signal} \rangle}{\langle \tilde{a}_{out}^{noise\dagger} \tilde{a}_{out}^{noise} \rangle} \\ &= \frac{\kappa_{\mu e}G^2J^2}{\kappa_{oi} \left| (\omega_m - \omega - \frac{\gamma}{2}i)(\omega_\mu - \omega - \frac{\kappa_\mu}{2}i) - J^2 \right|^2 \bar{n}_{ob} \\ & \quad + \gamma G^2 \left| \omega_\mu - \omega - \frac{\kappa_\mu}{2}i \right|^2 \bar{n}_{mb} + G^2 J^2 \kappa_{\mu i} \bar{n}_{\mu b}} \end{aligned} \quad (B.25)$$

$$\begin{aligned} SNR_\mu &= \frac{\langle \tilde{c}_{out}^{signal\dagger} \tilde{c}_{out}^{signal} \rangle}{\langle \tilde{c}_{out}^{noise\dagger} \tilde{c}_{out}^{noise} \rangle} \\ &= \frac{\kappa_{oe}G^2J^2}{\kappa_{\mu i} \left| (\omega_m - \omega - \frac{\gamma}{2}i)(\omega_o - \omega - \frac{\kappa_o}{2}i) - G^2 \right|^2 \bar{n}_{\mu b} \\ & \quad + \gamma J^2 \left| \Delta_o - \omega - \frac{\kappa_o}{2}i \right|^2 \bar{n}_{mb} + G^2 J^2 \kappa_{oi} \bar{n}_{ob}} \end{aligned} \quad (B.26)$$

Note that the denominator of the conversion efficiency can be minimized with respect to the frequency ω by looking for the extrema points of the denominator in (B.28) according to (B.29) with solutions in (B.32) and (B.33) assuming the resonant condition that $\Delta_0 = \omega_m = \omega_\mu$.

$$\begin{aligned} d &= (\Delta_o - \omega - \frac{\kappa_o}{2}i)(\omega_m - \omega - \frac{\gamma}{2}i)(\omega_\mu - \omega - \frac{\kappa_\mu}{2}i) \\ & \quad - G^2(\omega_\mu - \omega - \frac{\kappa_\mu}{2}i) - J^2(\Delta_o - \omega - \frac{\kappa_o}{2}i) \end{aligned} \quad (B.27)$$

$$D = |d|^2 \quad (B.28)$$

$$0 = \frac{\partial D}{\partial \omega} = 2Re \left[\frac{\partial d}{\partial \omega} d^* \right] \quad (B.29)$$

$$\begin{aligned} \zeta = & \left(16G^4 + 32G^2J^2 + 16J^4 - 16G^2\gamma^2 - 16J^2\gamma^2 + \gamma^4 \right. \\ & - 24G^2\gamma\kappa_o - 16G^2\kappa_o^2 + 8J^2\kappa_o^2 - \gamma^2\kappa_o^2 \\ & + \kappa_o^4 - 24J^2\gamma\kappa_u + 8G^2\kappa_u^2 - 16J^2\kappa_u^2 \\ & \left. - \gamma^2\kappa_u^2 - \kappa_o^2\kappa_u^2 + \kappa_u^4 \right)^{1/2} \end{aligned} \quad (\text{B.30})$$

$$\beta = 8G^2 + 8J^2 - \gamma^2 - \kappa_o^2 - \kappa_u^2 \quad (\text{B.31})$$

$$\omega_{\mu=\pm 1, \nu=\pm 1} = \omega_m + \mu \frac{\sqrt{\beta + \nu\zeta}}{2\sqrt{3}} \quad (\text{B.32})$$

$$\omega_{\mu=0} = \omega_m \quad (\text{B.33})$$

For expressions in (B.32), we can notice that typical parameters have $\kappa_o \sim 2\pi \times 1$ GHz, $\kappa_u \sim 2\pi \times 10$ kHz, $\gamma \sim 2\pi \times 1$ kHz, $J \sim 2\pi \times 10$ MHz, and $G = g_0\sqrt{n_c} \sim 2\pi \times 10$ MHz. These typical parameters lead to $b < 0$. Thus only $\omega_{\mu=\pm 1, \nu=1}$ and $\omega_{\mu=0}$ are valid real solutions. It can also be shown that $\omega_{\mu=0}$ leads to a maximal point of D and a local minimal point in (B.24). $\omega_{\mu=\pm 1, \nu=1}$ are the maximal points of (B.24).

To highlight the importance of effective cooperatives for optomechanical and piezo-electric interactions defined as $C_{\mu m}^{\text{eff}} = \frac{C_{\mu m}}{\bar{n}_{mb}}$ and $C_{om}^{\text{eff}} = \frac{C_{om}}{\bar{n}_{mb}}$ with $C_{\mu m} = \frac{4J^2}{\gamma\kappa_\mu}$, $C_{om} = \frac{4G^2}{\gamma\kappa_o}$, we can look at the case where $\omega = \omega_m$ and have (B.34) – (B.36).

$$\eta = \frac{\kappa_{oe}\kappa_{\mu e}G^2J^2}{\left(\frac{\kappa_o\gamma\kappa_\mu}{8} + \frac{G^2\kappa_\mu}{2} + \frac{J^2\kappa_o}{2}\right)^2} \quad (\text{B.34})$$

$$SNR_o \simeq \frac{1}{C_{\mu m}^{\text{eff}}} + \frac{\kappa_{oi}}{\kappa_o} \frac{\bar{n}_{ob}}{C_{om}} \left(\frac{1}{C_{\mu m}} + C_{\mu m} + 2 \right) \quad (\text{B.35})$$

$$SNR_\mu \simeq \frac{1}{C_{om}^{\text{eff}}} + \frac{\kappa_{\mu i}}{\kappa_\mu} \frac{\bar{n}_{\mu b}}{C_{\mu m}} \left(\frac{1}{C_{om}} + C_{om} + 2 \right) \quad (\text{B.36})$$

As both of these noise photon numbers need to be much smaller than 1 for high fidelity transduction, cryogenic temperature will be needed for eliminating the GHz microwave bath noise photon occupation. This readily eliminates the second term of (B.36). The second term of (B.35) is also vanishing as the telecommunication band optical bath occupation is zero. But the first terms may not be vanishing as the mechanical bath phonon occupation is larger than one due to the parasitic heating effect of the laser on the silicon material. Since $C_{\mu m}^{\text{eff}} \gg 1$ has been shown to be

achievable with the state-of-art electromechanical-crystal (EMC), the work shown in [Hengjiang2019] demonstrating the possibility to have $C_{\text{om}}^{\text{eff}} \gg 1$ has made it possible for future opto-electro-mechanical-crystal (OEMC) quantum transducers to achieve unity transduction number efficiency together with vanishing noise.

The analysis above is for the system operating in the case where $\omega = \omega_{\mu=0}$ which is a local minimum for the transduction number efficiency. The maximal efficiency points are harder to draw insights without using numerical tools to study the transductions in two directions (optics-to-microwave and microwave-to-optics). For typical system parameters and experimentally probed laser heating curves for two dimensional optomechanical crystals [Hengjiang2019], the transduction number efficiency and transduced noise photon numbers are shown in Fig. B.2a assuming $n_c = 1000$. Fig. B.2b–d show transduction number efficiency and signal-to-noises (SNRs) as functions of effective optomechanical cooperativity ($C_{\text{om}}^{\text{eff}}$) and the intra-cavity photon number (n_c) driven by the pump laser. As it is shown in Fig. B.2d, the optical to microwave transduction signal to noise (SNR_{μ}) strongly depends on $C_{\text{om}}^{\text{eff}}$. $SNR_{\mu} \gg 1$ requires $C_{\text{om}}^{\text{eff}} \gg 1$. Furthermore, SNR_{μ} is independent of the pump laser power (n_c). The later observation is because the experimentally extracted heating curves reveal that the mechanical decoherence rate due to laser heating is proportional to n_c and this leads to a laser power independent effective cooperativity as $G \propto \sqrt{n_c}$. Figures showing the dependence on $C_{\mu\text{m}}$ is not shown as it can be shown for a large range of typical system parameters $C_{\mu\text{m}} \gg 1$ is always true and transduction quality is not limited by it. This is very evident in the $C_{\mu\text{m}} \gg 1$ sensitive microwave-to-optics transduction $SNR_o \gg 1$ illustrated in Fig. B.2c.